Title
The Effects of Coulomb Stress Change on Southern California Earthquake Forecasting

Author
Strader, Anne Elizabeth

Publication Date
2014

Peer reviewed|Thesis/dissertation

UNIVERSITY OF CALIFORNIA

Los Angeles

The Effects of Static Coulomb Stress Change on Southern California Earthquake Forecasting

A dissertation submitted in partial satisfaction of the requirements for the degree

Doctor of Philosophy in Geophysics and Space Physics

by

Anne Elizabeth Strader

2014

ABSTRACT OF THE DISSERTATION

The Effects of Coulomb Stress Change on Southern California Earthquake Forecasting

by

Anne Elizabeth Strader

Doctor of Philosophy in Geophysics and Space Physics

University of California, Los Angeles, 2014

Professor David. D. Jackson, Chair

I investigate how inclusion of static Coulomb stress changes, caused by tectonic loading and previous seismicity, contributes to the effectiveness and reliability of prospective earthquake forecasts. Several studies have shown that positive static Coulomb stress changes are associated with increased seismicity, relative to stress shadows. However, it is difficult to avoid bias when the learning and testing intervals are chosen retrospectively. I hypothesize that earthquake forecasts based on static Coulomb stress fields may improve upon existing earthquake forecasts based on historical seismicity. Within southern California, I have confirmed the aforementioned relationship between earthquake location and Coulomb stress change, but found no identifiable triggering threshold based on static Coulomb stress history at individual earthquake locations. I

have also converted static Coulomb stress changes into spatially-varying earthquake rates by optimizing an index function and calculating probabilities of cells containing at least one earthquake based on Coulomb stress ranges. Inclusion of Coulomb stress effects gives an improvement in earthquake forecasts that is significant with 95% confidence, compared to smoothed seismicity null forecasts. Because of large uncertainties in Coulomb stress calculations near faults (and aftershock distributions), I combine static Coulomb stress and smoothed seismicity into a hybrid earthquake forecast. Evaluating such forecasts against those in which only Coulomb stress or smoothed seismicity determines earthquake rates indicates that Coulomb stress is more effective in the far field, whereas statistical seismology outperforms Coulomb stress near faults. Additionally, I test effects of receiver plane orientation, stress type (normal and shear components), and declustering receiver earthquakes. While static Coulomb stress shows significant potential in a prospective earthquake forecast, simplifying assumptions compromise its effectiveness. For example, we assume that crustal material within the study region is isotropic and homogeneous and purely elastic, and that pore fluid pressure variations do not significantly affect the static Coulomb stress field. Such assumptions require further research in order to detect direct earthquake triggering mechanisms.

The dissertation of Anne Elizabeth Strader is approved.

_____

Peter Bird

_____

Caroline Beghein

_____

Rick Schoenberg

_____

David D. Jackson, Committee Chair

University of California, Los Angeles

2014

To Virginia and Clifton Strader

TABLE OF CONTENTS

ACKNOWLEDGEMENTS

The research conducted throughout my academic career has been one of the greatest, and rewarding, challenges I have faced. This work and dissertation would not have been possible without the support and guidance of many people.

I would like to thank my advisor, Prof. Dave Jackson, for his unending guidance, support, and patience throughout my time at UCLA. Thank you for helping me to interpret my results objectively, without introducing bias based on results I might have expected. With your guidance, I learned to explore new ideas and possibilities for future research, even when earthquake forecasts I expected to be successful failed. The concepts you taught me will prove crucial in my future scientific career. I could not have asked for a better mentor.

I would like to thank Dr. Kathy Jackson for moral support throughout my graduate career, as well as guidance in improving my writing. Your encouragement means so much to me, and has helped me to work through the more difficult aspects of research, as well as life as a graduate student.

I also want to thank Prof. Paul Davis, Prof. Caroline Beghein, Prof. Peter Bird, and Prof. Rick Schoenberg for being part of my dissertation and qualifying exam committees, and providing indispensable advice throughout my graduate career. You have helped me to view my work from many different perspectives, and provided numerous valuable suggestions regarding future research.

Thank you to all EPSS staff for your support, encouragement, and enthusiasm, which made this department one of the most supportive, friendly academic departments in which I have had the privilege to work.

I am incredibly grateful to all of my fellow graduate students and friends, with whom I greatly enjoyed working. Whether we struggled with physics problem sets, or prepared for qualifying exams, or listened to each other's seminars and conference presentations, I truly appreciate having had the chance to exchange knowledge and scientific perspectives with all of you, as well as get to know you. I would especially like to thank Debbie Weiser for her support and advice throughout my academic career. From the day I first visited the UCLA campus as a prospective student, you made me feel welcome in the EPSS community, and are a true role model, both as a scientist and as a person. To all of my colleagues and friends, I wish you much success and funding!

Finally, thank you to the two best parents in the entire universe, Ginny and Cliff Strader! I could not have asked for more supportive, loving, caring parents than you. Thank you for encouraging my interest in seismology from an early age, and for showing me so many incredible geologic sites during all these years. You both always encourage me to grow as a scientist and as a person, even when I am very stressed and full of complaints, for which I am extremely grateful. You make me the luckiest person in the world.

VITA

2006-2010: Bachelor of Science in Geology with Honors, with minors in Math and Physics, from Bucknell University

2010-2013: Master of Science in Geophysics and Space Physics, from the University of California, Los Angeles

2013: Teaching Assistant, UCLA Department of Earth, Planetary and Space Sciences

PUBLICATIONS

Strader, A., and D. D. Jackson (2014), Near-prospective test of Coulomb stress triggering, *Journal of Geophysical Research – Solid Earth*, *119*, doi: 10.1002/2013JB010780.

Strader, A., and D. D. Jackson (2014), Static Coulomb stress-based southern California earthquake forecasts: a pseudo-prospective test, to be submitted to *Journal of Geophysical Research – Solid Earth*.

CHAPTER 1

Introduction

While statistical seismology often indicates probabilities of aftershock locations and times, reliable prospective earthquake forecasts require a physical explanation of earthquake distribution. Understanding how static stress accumulates over time through tectonic plate motion or co- and postseismic slip may provide a basis for determining earthquake probabilities over time windows extending beyond typical aftershock duration times (Freed et al., 2007). Through identifying potential physical triggering mechanisms, foreshock sequences become unnecessary to forecast large mainshocks that typically do not follow seismic precursors. Previous studies find a strong association between the static Coulomb Failure Function (ΔCFF) and earthquake location, where earthquakes tend to nucleate in areas of positive ΔCFF. However, such studies do not account for ΔCFF variation in areas with few earthquakes. The purpose of my study is to determine the extent to which static aseismic and coseismic ΔCFF is reliable as an indicator of future earthquake locations and times.

1.1 Background Research

My research begins as an extension of research by Deng & Sykes (1997a,b) focusing on ΔCFF and seismicity distributions from 1812 until the time of publication. Deng and Sykes observe that, within southern California, 95% of M≥6 earthquakes from 1852-1997 (Deng & Sykes, 1997a) and 85% of M≥5 earthquakes from 1932-1995 (Deng & Sykes, 1997b) occur in areas with positive ΔCFF, which comprise on average 65% of the study area. They hypothesize that stress shadows, areas of negative cumulative ΔCFF, have been shrinking since the 1812 Wrightwood earthquake due to insufficient seismic moment releasing accumulated aseismic ΔCFF. However, there exist large areas with positive ΔCFF and few recent earthquakes,

primarily in areas with coseismic stress contributions from paleoseismic events. Such areas of seismic quiescence suggest that the extent to which Coulomb stress affects seismicity rates evolves over time, eventually approaching background rates. Stein et al. (1997) observed a similar ΔCFF sequence along the North Anatolian fault, where nine M≥6.7 earthquakes ruptured within areas of recently elevated static Coulomb stress, indicating that static ΔCFF significantly brings faults closer to failure. Because coseismic ΔCFF from larger earthquakes displays a better fit than smaller earthquakes to seismicity rates, Stein et al. hypothesize that only large earthquakes contribute to the permanent, or static, Coulomb stress field that may trigger future large earthquakes. By contrast, transient seismicity rate variation lasts 5-10 years following both large and small earthquakes, during which the stress perturbations trigger aftershocks. Lin and Stein (2004) argue that static ΔCFF may trigger large earthquakes within subduction zones and near the San Andreas fault, due to an apparent relationship between static ΔCFF and earthquake location.

Complexities in the stress field caused by variations in crustal material and coseismic stress changes often challenge the assumption, used in several retrospective forecasts, that earthquakes nucleate at regular recurrence intervals (seismic "gaps"). Rong et al. (2003) tested the seismic gap hypothesis against a Poissonian null hypothesis for M≥7.0 earthquakes occurring within the Pacific Rim. Likelihood ratio tests indicated a 5% chance of a Type I error, and a 20% probability of a Type II error. The 2004 Parkfield earthquake corroborates these results, as the M6.0 earthquake failed to nucleate within the 95% characteristic time window, 1985-1993 (Jackson and Kagan, 2006). Deviations from the characteristic earthquake cycle may indicate irregular stressing rates, varying the times at which stress reaches a necessary triggering threshold. The seismic gap hypothesis assumes that stress contributions are limited to fault

sections, and neglects to take coseismic stress changes into account. The static ΔCFF model that I test allows for off-fault mainshocks, and does not require ΔCFF to accumulate at a constant rate at a given location. To some extent, one may forecast earthquake clustering patterns through the Epidemic Type Aftershock Sequence (ETAS) model, which assigns expected seismicity rates as a function of locations, times, and magnitudes of preceding earthquakes (Zhuang et al., 2002). Time-independent seismicity rate distributions similarly base future earthquake locations upon a linear combination of recent earthquake locations and mapped fault locations (Hiemer et al., 2013). Expected seismicity rates are modeled as functions of distances from previous earthquakes and from mapped faults, with seismicity rate contributions from source earthquakes proportional to source magnitudes and probability of independence. Smoothed seismicity-based earthquake forecasts support previous findings that most earthquakes occur near locations of recent events; however, these forecasts fail to anticipate independent earthquakes not located on or near previously known faults. Similarly, ETAS forecasts are based upon incomplete historical seismicity, as well as assumptions that oversimplify variations in physical properties throughout the earth's crust. Earthquakes outside of a given study area may significantly influence optimal ETAS parameter values, as shown by varying auxiliary windows and optimizing individual ETAS parameters within southern California (Wang et al., 2010). Similarly, the static Coulomb stress field is incomplete, due to crustal heterogeneities and incomplete records of paleoseismic earthquakes. The nature of observed earthquake clustering patterns may delineate potential triggering mechanisms, such as fluid signals observed in swarms (Daniel et al., 2011; Hainzl and Ogata, 2005), whereas seismicity characterized by Omori aftershock decay is indicative of varying static Coulomb stress. Parsons et al. (2012) and Parsons and Segou (2014) find that the prospective potential of static Coulomb stress in forecasting microearthquakes is limited by

secondary aftershock triggering, effectively represented by ETAS. However, moderate to large earthquakes tend to nucleate in areas of recently elevated ΔCFF, consistent with studies by Deng and Sykes (1997a,b) and Stein et al. (1997). Such forecasts are most commonly evaluated, prospectively or retrospectively, through log likelihood tests (Ogata et al., 2013, Rong et al., 2003) which take into account numbers of earthquakes as well as their spatiotemporal distribution.

Because recent seismicity appears to depend mostly upon recent stress transfer, a prospective Coulomb stress-based forecast must take into account postseismic, or quasi-static stress evolution to reliably forecast temporal earthquake distributions. Laboratory experiments indicate that seismicity is highly sensitive to small changes in normal and shear stress, yielding the rate-and-state constitutive formulation for seismicity rate evolution as a function of Coulomb stress perturbations (Cocco et al., 2010; Dieterich and Kilgore, 1996). Hainzl et al. (2010) retrospectively employed rate-and-state theory to estimate aftershock density as a function of distance from the nearest fault, following the 1992 M7.3 Landers earthquake. Toda et al. (2005) retrospectively tested a rate-and-state Coulomb stress-based earthquake forecast within the spatiotemporal window containing the Landers earthquake, demonstrating that consecutive mainshocks may elevate seismicity rates for decades before returning to background seismicity rates. Additionally, Toda and Enescu (2011) are currently testing a prospective rate-and-state seismicity forecast for Japan, through the Collaboratory for the Study of Earthquake Prediction (CSEP). Through representing off-fault aftershock zones as finite fault sources, Toda and Enescu allowed for mainshocks in their model, and their subsequent aftershock sequences, to occur away from major faults. Differences between observed and expected seismicity may be partially due to assumed receiver plane orientation. The prospective Japan earthquake forecast is

based upon receiver plane orientations derived from thrust faults at the convergent margin. However, rate-and-state models often underestimate seismicity rates, which indicates a greater range of receiver plane orientations than previously assumed (Hainzl et al., 2010). Conversely, receiver plane orientations similar to optimally oriented planes may indicate direct triggering from static ΔCFF, depending on regional stress uncertainty (Steacy et al., 2005).

1.2 Study Area and Outline of Research

I select southern California (32° to 37° latitude, -122° to -114° longitude) as my study area (Figure 1.1), as high seismicity rates easily allow for short-term prospective and pseudo-prospective testing. Assuming zero ΔCFF just before the 1812 Wrightwood earthquake, I use the cumulative static ΔCFF field, calculated from tectonic plate motion and historical seismicity, to first confirm the association observed between ΔCFF and recent (during 1999-2010) earthquake locations. Earthquakes assumed to contribute to the static ΔCFF field are termed "source" earthquakes, and occur during the "learning period," a time window where the static ΔCFF may evolve. At the beginning of the "target period," or time window where I evaluate the earthquake forecast, I pause the static ΔCFF evolution and use the resulting probability field to determine how effectively it forecasts target, or "receiver" earthquakes. To identify whether or not there exists a clearly defined static ΔCFF triggering threshold, I calculated the stress histories at each receiver earthquake location and determine the percentage of events that occur at their respective historic stress maxima. I also determined whether a relationship exists between static ΔCFF magnitude and receiver earthquake magnitude. These results are further described in the article "Near-Prospective Test of Coulomb Stress Triggering," published in the Journal of Geophysical Research, Solid Earth.

I then evaluated the effectiveness of earthquake forecasts based on probability distributions derived from static ΔCFF fields just after the 1999 M7.1 Hector Mine earthquake. In one forecast, I fit a normalized arctangent index function to the ΔCFF and seismicity distributions to directly infer normalized seismicity rates from ΔCFF. Using a smoothed seismicity-based earthquake forecast as a null hypothesis, I statistically compared each forecast's efficacy for multiple target and learning period time windows. I considered the static ΔCFF-based forecast an improvement over the smoothed seismicity-based forecast if I could reject the null hypothesis for numerical (N), spatial log likelihood (S) and log likelihood ratio (R) tests in favor of the alternate hypothesis. The tests evaluate numbers of earthquakes or amount of seismically active area, spatial seismicity distribution, and relative effectiveness, respectively (Rong et al., 2003). I tested two types of spatially varying static Coulomb stress forecasts. The first ΔCFF-based forecast directly infers seismicity rates from ΔCFF through a normalized index function. The other indicates the probability of a cell containing least one earthquake, through dividing static ΔCFF into quantiles and calculating the fraction of "activated" cells. I describe the results from the forecast that indicates the distribution of activated cells in the article "Static Coulomb Stress-Based Southern California Earthquake Forecasts: a Pseudo-Prospective Test," submitted to the Journal of Geophysical Research: Solid Earth (Chapter 4). The results from the arctangent ΔCFF-based probability distributions are given in Chapter 5

.

Through rate-and-state quasi-static ΔCFF evolution, I permitted the modeled stress field to evolve independently of coseismic stress changes, altering the shear stress necessary for fault rupturing to occur. I pseudo-prospectively tested two time-dependent rate-and-state-based forecasts: one deriving cell activation probabilities from seismicity rates calculated from the

forward model, and one deriving cell activation probabilities from ΔCFF inferred from inverting observed seismicity rate changes. As a null hypothesis, I selected an ETAS model with cell activation probabilities derived from the Landers earthquake aftershock sequence. I then applied the aforementioned likelihood tests to each earthquake forecast to evaluate the extent to which ΔCFF-based forecasts improve upon those based on statistical seismology.

Given that static ΔCFF is calculated from rectangular fault patches, stress singularities often obscure ΔCFF at fault section edges, where aftershock sequences frequently occur. The numerical approximation allows for constant slip rates along each fault section, but does not represent the complete ΔCFF variation along faults, or reliably constrain fault asperities. I tested the relative effectiveness of physics-based and statistics-based forecasts, for both time-dependent and time-independent cases, by forming hybrid probability forecasts. For each set of earthquake forecasts, the null and alternate probabilities are weighted as a function of distance to the nearest fault segment. Because static ΔCFF decays with distance from faults as a power law, at approximately r^{-2}, stress-based probabilities are less influenced by stress singularities with increasing distance from faults. Therefore, I hypothesize that, for both spatial and spatiotemporal forecasts, static ΔCFF improves upon statistical seismicity-based forecasts farther away from faults, while seismicity-based probabilities mitigate the stress uncertainties within areas near aftershock sequences. I also investigate how declustering the earthquake catalog affects each probability distribution's relative effectiveness.

1.3 Earthquake and Fault Data

Aseismic stress sources include all 98 aseismic rectangular fault dislocations from Deng and Sykes's studies (1997a,b). Similar to their research, I used a steady backslip approximation of the interseismic intervals. I modeled the earth's crust as an elastic half-space, locking the

upper 15 km and allowing for constant deformation beneath the seismogenic zone. The "creeping zone" on the San Andreas fault is assumed to accumulate no tectonic ΔCFF. Each fault patch was assumed to slip at a constant rate, yielding constant ΔCFF/year. The backslip approximation does not take into account instability at fault intersection points, or account for faults not included in Deng and Sykes' displacement model. I included $M \geq 5.0$ earthquakes as coseismic ΔCFF sources, including all seismic sources from Deng and Sykes' studies as well as the Hector Mine displacement field (Ji et al., 2002). For time-independent forecasts, I define two time intervals: the learning and target periods. The learning period is defined as the eleven years preceding the Hector Mine earthquake, and the target period is defined as the time between the Hector Mine earthquake and just before the M7.2 El Mayor Cucapah earthquake, containing 2764 $M \geq 2.8$ earthquakes from the focal mechanism catalog by Yang et al. (2012). For the time-dependent (rate-and-state) forecasts, I define a learning, target, and "accumulation" period. The accumulation period extends from six years before to eight weeks before the Hector Mine earthquake. During this time, source earthquakes may contribute to the quasi-static ΔCFF field, but the time window is not used to derive cell activation probabilities. I define the learning period as the eight weeks before the Hector Mine earthquake, during which I empirically determine cell activation probabilities from observed ΔCFF evolution. The target period, during which I evaluate the rate-and-state forecast, is defined as the eight weeks after the Hector Mine earthquake. All earthquake data are available at the Southern California Earthquake Center data website: http://www.data.scec.org/research-tools/alt-2011-yang-hauksson-shearer.html.

1.4 Figures

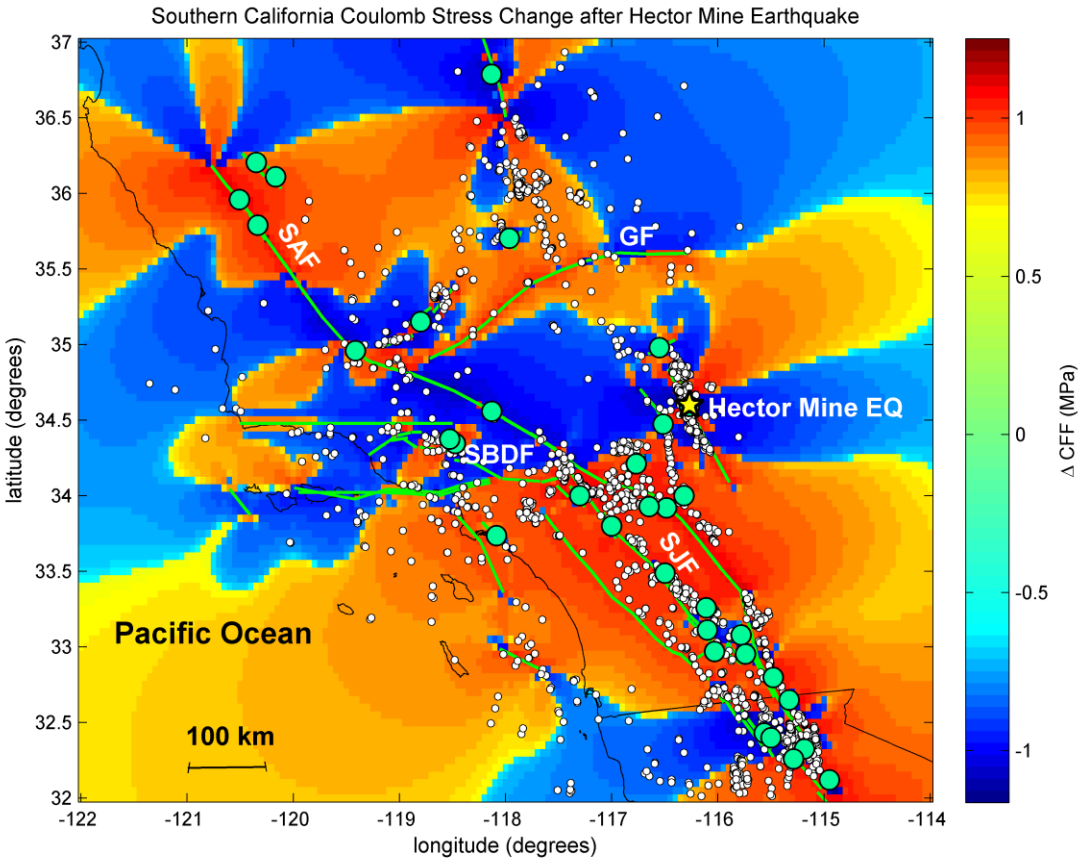

Figure 1.1: ΔCFF field calculated from uniform vertical, right-lateral strike-slip planes striking 321° just after the 1999 Hector Mine earthquake. Small white dots indicate locations of receiver earthquakes used in our study, large green dots indicate source earthquake locations, and green lines indicate faults that contribute to aseismic stress accumulation. Major faults are labeled as follows: SAF = San Andreas fault, SJF = San Jacinto fault, GF = Garlock fault, and SBDF = San Bernardino fault. The yellow star indicates the Hector Mine earthquake epicenter.

1.5 Tables

M ≥ 5 Coseismic Stress Sources												
Year	**Month**	**Day**	**Hour**	**Minute**	**Second**	**Lat**	**Lon**	**Depth**	**Mw**	**Strike**	**Dip**	**Rake**
1812	12	8	15	0		34.37	-117.65	0	7.5	295	90	180
1812	12	21	19	0		34.20	-119.90	0	7.1	280	26	57
1852	11	29	20	0		32.50	-115.00	0	6.5	312	88	179
1855	7	11	4	15		34.10	-118.10	0	6	310	90	180
1857	1	9	8	12		35.30	-119.80	0	7.9	321	90	180
1858	12	16	10	0		34.00	-117.50	0	6	321	90	180
1862	5	27	20	0		32.70	-117.20	0	5.9	336	90	180
1872	3	26	10	30		36.70	-118.10	0	7.8	340	80	-171
1872	3	26	14	6		36.90	-118.20	0	6.5	340	80	-171
1872	4	3	12	15		37.00	-118.20	0	6.1	340	80	-171
1875	11	15	22	30		32.50	-115.50	0	6.2	327	90	180
1883	9	5	12	30		34.20	-119.90	0	6			
1885	4	12	4	5		36.57	-120.65	0	6.5	132	25	101
1890	2	9	12	6		33.40	-116.30	0	6.3	305	90	180
1890	4	24	11	36		36.90	-121.60	0	6	314	90	180
1892	2	24	7	20		32.55	-115.63	0	7.2	328	90	180
1892	5	28	11	15		33.20	-116.20	0	6.3	315	90	180
1894	7	30	5	12		34.30	-117.60	0	6	305	90	180
1897	6	20	20	14		37.00	-121.50	0	6.2	321	90	180
1899	7	22	20	32		34.30	-117.50	0	6.5	305	90	180
1899	12	25	12	25		33.80	-117.00	0	6.7	309	90	180
1901	3	3	7	45		36.00	-120.50	0	5.8	327	90	180
1906	4	19	0	30		32.90	-115.50	0	5.8	327	90	180
1907	9	20	1	54		34.20	-117.10	0	6	317	90	180
1908	11	4	8	37		36.00	-117.00	0	6.5			
1910	5	15	15	47		33.70	-117.40	0	6	308	90	180
1915	6	23	3	59		32.80	-115.50	0	6.3	327	90	180
1915	6	23	4	56		32.80	-115.50	0	6.3	327	90	180
1915	11	21	0	13		32.00	-115.00	9	6.6	312	88	179
1916	10	23	2	44		34.90	-118.90	0	6			
1916	11	10	9	11		36.00	-117.00	0	6.1			
1918	4	21	22	32		33.80	-117.00	7	6.8	150	87	-176
1922	3	10	11	21		36.00	-120.50	0	6.3	327	90	180
1923	7	23	7	30		34.00	-117.30	12	6.3	320	85	180
1925	6	29	14	42		34.30	-119.80	0	6.3	280	26	57
1927	11	4	13	50		34.35	-120.90	10	6.6	340	66	95
1933	3	11	1	54		33.66	-117.97	13	6.4	315	80	-170

1933	10	2	9	10		33.78	-118.13	0	5.4	315	90	180
1934	6	5	21	48		35.80	-120.33	0	5	327	90	180
1934	6	8	4	30		35.80	-120.33	0	5	327	90	180
1934	6	8	4	47		35.80	-120.33	0	6.4	327	90	180
1934	11	25	8	18		32.08	-116.67	0	5			
1934	12	24	16	26		35.93	-120.48	0	5	327	90	180
1934	12	30	13	52		32.25	-115.50	10	6.5	311	88	180
1934	12	31	18	45		32.00	-114.75	12	7	317	89	180
1935	10	24	14	48		34.10	-116.80	0	5.1			
1935	12	20	7	45		33.17	-115.50	0	5.2	321	90	180
1937	3	25	16	49		33.47	-116.41	3	5.6	309	83	-136
1938	5	31	8	34		33.70	-117.51	10	5.2	321	90	180
1938	9	27	12	23		36.30	-120.90	0	5			
1939	5	1	23	53		32.00	-117.50	0	5			
1939	5	4	20	44		35.97	-114.82	0	5			
1939	6	24	13	1		36.40	-121.00	0	5.5			
1939	6	24	16	27		32.00	-117.50	0	5			
1940	3	10	18	1		37.00	-115.00	0	5			
1940	5	18	5	3		34.08	-116.30	0	5.3	345	45	-170
1940	5	19	4	36		32.87	-115.48	7	7	325	90	180
1941	7	1	7	50		34.37	-119.58	0	5.5	280	26	57
1941	9	21	19	53		34.87	-118.93	0	5.1			
1942	3	3	1	3		34.00	-115.75	0	5	350	90	180
1942	5	23	15	47		32.98	-115.98	0	5.1	321	90	180
1942	10	21	16	22		32.97	-116.03	7	6.3	61	88	10
1942	10	22	1	50		33.23	-115.72	0	6.1	321	90	180
1943	8	29	3	45		34.27	-116.97	0	5.3	310	90	180
1943	12	22	15	50		34.33	-115.80	0	5.3	331	72	154
1944	6	12	10	45		33.98	-116.72	10	5	222	67	-81
1944	6	12	11	16		33.99	-116.71	10	5.2	142	80	-170
1945	4	1	23	43		34.00	-120.02	0	5.1	280	14	45
1945	8	15	17	56		33.22	-116.13	0	5.7	330	90	135
1946	1	8	18	54		33.00	-115.83	0	5.4	321	90	180
1946	3	15	13	21		35.75	-117.99	0	5.5	315	71	-164
1946	3	15	13	49		35.73	-118.05	22	6	346	45	-117
1946	7	18	14	27		34.53	-115.98	0	5.5	180	80	180
1947	4	10	15	58		34.98	-116.55	5	6.5	65	85	8
1947	7	24	22	10		34.02	-116.50	0	5.3			
1947	11	18	21	59		33.27	-119.45	0	5	170	30	-180
1948	2	24	8	15		32.50	-118.55	0	5.3	350	90	130
1948	12	4	23	43		33.92	-116.48	12	6.2	305	65	169

1949	3	9	12	28		36.02	-121.48	0	5.2	297	80	-118
1949	5	2	11	25		34.02	-115.68	0	5.8	350	90	180
1949	11	4	20	42		32.20	-116.55	0	5.7	135	40	170
1950	7	28	17	50		33.12	-115.57	0	5.4	321	90	180
1950	7	29	14	36		33.12	-115.57	0	5.5	321	90	180
1951	1	24	7	17		32.98	-115.73	0	5.8	324	82	145
1951	7	29	10	53		36.58	-121.18	0	5			
1951	12	26	0	46		32.82	-118.35	0	5.9	321	90	180
1952	7	21	11	52		35.00	-119.02	16	7.5	73	75	50
1952	7	29	7	3		35.38	-118.85	0	6.3	53	90	
1952	8	23	10	9		34.52	-118.20	13.1	5.1			
1952	11	22	7	46		35.77	-121.15	10	6	309	66	145
1953	6	14	4	17		32.95	-115.72	0	5.5	321	90	180
1954	1	12	23	33		35.00	-119.02	0	5.6			
1954	1	27	14	19		35.15	-118.63	0	5			
1954	2	1	4	23		32.30	-115.30	0	5.2			
1954	2	1	4	32		32.30	-115.30	0	5.6			
1954	3	19	9	54		33.29	-116.18	9	6.1	307	85	175
1954	4	25	20	33		36.93	-121.68	0	5.3			
1954	5	23	23	52		34.98	-118.98	0	5.1			
1955	4	25	10	43		32.33	-115.00	0	5.2			
1955	11	2	19	40		36.00	-120.92	0	5.2	327	90	180
1955	12	17	6	7		33.00	-115.50	0	5.2	321	90	180
1956	11	16	3	23		35.95	-120.47	0	5	327	90	180
1957	4	25	21	57		33.22	-115.81	0.3	5.2	321	90	180
1957	5	26	15	59		33.23	-116.00	15.1	5	321	90	180
1958	12	1	3	21		33.23	-115.75	0	5.8			
1959	3	2	23	27		36.98	-121.58	0	5.3			
1960	1	20	3	25		36.78	-121.43	0	5	305	85	-130
1961	1	28	8	12		35.78	-118.05	5.5	5.3	335	45	-140
1961	4	9	7	23		36.68	-121.30	0	5.6			
1961	10	19	5	9		35.83	-117.76	2	5.4	140	88	94
1962	9	16	5	36		35.75	-118.04	3.8	5	289	51	-133
1962	10	29	2	42		34.33	-116.87	8.6	5	330	85	-130
1963	9	14	19	46		36.89	-121.60	3.4	5.4	306	60	180
1963	9	23	14	41		33.71	-116.93	16.5	5.1	145	73	-148
1965	9	25	17	43		34.71	-116.50	10.6	5.2	317	60	174
1965	9	26	7	0		34.71	-116.03	8.3	5.1	302	51	167
1966	6	28	4	26		35.92	-120.53	18.6	6.4	327	90	-160
1968	4	9	2	28		33.19	-116.13	10	6.7	311	78	179
1968	7	5	0	45		34.12	-119.70	5.9	5.3	280	26	57

1969	1	23	23	1		33.89	-116.04	17.7	5	160	81	-150
1969	4	28	23	20		33.34	-116.35	12	5.6	295	69	169
1969	10	22	22	51		34.58	-121.62	10	5.4	340	66	95
1969	10	24	8	29		33.29	-119.19	10	5.1	321	90	180
1969	10	27	10	59		36.90	-121.34	10	5			
1969	11	5	17	54		34.61	-121.44	10	5.6	340	66	95
1970	9	12	14	30		34.27	-117.54	8	5.3	334		
1971	2	9	14	0		34.41	-118.40	8.4	6.7	293	52	72
1971	9	30	22	46		33.03	-115.82	8	5	321	90	180
1972	2	24	15	56		36.62	-121.18	8	5			
1973	2	21	14	45		34.06	-119.04	8	5.5	260	36	55
1973	8	6	23	29		33.99	-119.48	16.9	5	280	26	57
1974	11	28	23	1		36.90	-121.61	7	5	300	90	180
1975	6	1	1	38		34.52	-116.50	4.5	5	158	80	180
1976	1	10	12	58		32.08	-115.47	12.3	5	313	80	170
1976	11	4	10	41		33.13	-115.62	0	5	145	75	140
1978	5	5	21	3		32.21	-115.30	6	5.2	349	40	172
1978	8	13	22	54		34.40	-119.68	12.7	5.8	280	26	57
1979	1	1	23	14		33.95	-118.69	9.6	5.2	280	60	85
1979	3	15	21	7		34.33	-116.44	2.5	5.5	168	79	-170
1979	10	15	23	16		32.61	-115.32	12.3	6.4	323	90	180
1980	2	25	10	47		33.50	-116.51	13.6	5.5	309	63	-152
1980	6	9	3	28		32.19	-115.08	5	6.4	318	90	180
1981	4	26	12	9	28.36	33.09	-115.63	9.29	5.75	158	86	-151
1981	9	4	15	50	50.47	33.68	-119.08	15	5.45	134	77	169
1982	10	1	14	29	1.59	35.74	-117.75	5.66	5.12	315	75	-152
1986	7	8	9	20	44.35	34.01	-116.61	10.85	5.65	298	38	-177
1986	7	13	13	47	8.76	32.99	-117.85	21.44	5.45	359	72	-167
1987	2	7	3	45	14.5	32.37	-115.31	10.29	5.38	235	87	98
1987	10	1	14	42	19.66	34.07	-118.09	15.04	5.9	262	23	83
1987	10	4	10	59	37.82	34.08	-118.09	9.78	5.25	152	69	161
1987	11	24	1	54	14.34	33.08	-115.78	8.2	6.2	280	86	171
1987	11	24	13	15	56.29	33.01	-115.83	5.45	6.6	127	72	-159
1988	6	10	23	6	42.84	34.94	-118.74	8.2	5.37	162	83	176
1988	12	3	11	38	26.26	34.14	-118.14	12.6	5.02	157	86	169
1988	12	16	5	53	4.77	33.99	-116.68	8.68	5.03	292	41	148
1990	2	28	23	43	36.61	34.14	-117.70	4.87	5.51	132	89	167
1991	6	28	14	43	54.47	34.26	-117.99	7.82	5.8	56	25	74
1992	4	23	4	50	23.02	33.97	-116.31	12.03	6.1	344	85	171
1992	6	28	17	5	57.2	34.26	-116.90	11.36	5.26	123	83	-166
1992	6	28	12	36	39.95	34.17	-116.42	11.62	5.49	296	46	-75

1992	6	28	14	43	21.67	34.17	-116.85	11.36	5.53	299	72	165
1992	6	28	15	5	30.29	34.21	-116.82	10.52	6.3	309	88	-180
1992	6	28	11	57	33.98	34.20	-116.43	2.79	7.3	173	85	-177
1992	6	29	14	13	38.46	34.11	-116.40	9.16	5.08	145	78	-167
1992	6	29	14	8	37.39	34.11	-116.40	9.64	5.69	160	58	-157
1992	7	1	7	40	29.46	34.35	-116.45	10.64	5.34	16	83	-146
1992	7	5	21	18	27.14	34.58	-116.32	1.79	5.42	344	54	153
1992	7	11	18	14	15.98	35.21	-118.06	12.77	5.67	292	71	177
1992	8	17	20	41	51.84	34.20	-116.86	12.37	5.23	257	45	111
1992	9	15	8	47	11.03	34.07	-116.36	7.28	5.26	139	88	-175
1992	11	27	16	0	57.39	34.34	-116.89	0.07	5.29	128	88	167
1992	12	4	2	8	57.33	34.37	-116.89	0	5.26	123	88	159
1993	5	28	4	47	40.37	35.14	-119.11	23.96	5.19	114	71	170
1993	8	21	1	46	38.13	34.03	-116.32	9.16	5	349	36	-144
1994	1	17	23	33	30.01	34.34	-118.70	12.02	5.58	118	36	86
1994	1	17	12	30	54.96	34.21	-118.55	21.07	6.7	113	36	106
1994	1	18	0	43	8.23	34.37	-118.71	7.94	5.24	280	38	104
1994	1	19	21	9	28.23	34.37	-118.71	12.86	5.06	276	32	68
1994	1	19	21	11	44.49	34.37	-118.64	15.02	5.07	310	36	89
1994	1	29	11	20	35.27	34.32	-118.58	1.82	5.06	330	82	-166
1994	3	20	21	20	12	34.24	-118.50	12.83	5.24	325	60	139
1995	6	26	8	40	28.54	34.39	-118.68	10.78	5.02	263	35	67
1995	8	17	22	39	58.82	35.77	-117.66	6.69	5.36	274	21	-100
1995	9	20	23	27	36.12	35.76	-117.64	5.72	5.75	157	69	-177
1996	1	7	14	32	52.91	35.77	-117.65	6.17	5.17	160	82	-173
1996	11	27	20	17	24.18	36.07	-117.66	3.93	5.3	139	71	175
1997	3	18	15	24	47.7	34.97	-116.82	4.02	5.26	154	75	-163
1997	4	26	10	37	30.38	34.38	-118.67	13.67	5.07	358	52	-141
1998	3	6	5	47	40.12	36.08	-117.64	7.17	5.23	126	82	155
1998	3	7	0	36	46.57	36.09	-117.62	6.99	5.04	348	82	-158
1999	10	16	12	57	21.02	34.44	-116.25	7.75	5.37	185	90	150
1999	10	16	9	59	35.14	34.67	-116.31	11.92	5.77	330	72	171
1999	10	16	9	46	43.96	34.60	-116.27	1.18	7.1	5	90	159

Table 1: $M \geq 5$ coseismic stress sources used in all research are displayed, ranging from the 1812 Wrightwood earthquake to the 1999 Hector Mine earthquake. Columns from left to right indicate earthquake year, month, day, hour, minute, second, latitude (N), longitude (W), depth (km), magnitude, strike, dip and rake. For sources without fault plane orientation information, I assumed a plane orientation of 321° strike, 90° dip, and 180° rake.

CHAPTER 2

Methods and Theory

2.1 Coulomb Failure Function and Stress Calculations

The Coulomb Failure Function (CFF) quantifies Coulomb stress state as a function of normal and shear stress, in which the relative influence of each depends on the frictional properties of a given material:

$$CFF = \mu\sigma + \tau \quad (1)$$

where CFF is Coulomb stress, μ is the coefficient of friction. σ is the normal stress on a pre-designated receiver plane (denoted positive for tension and negative for compression), and τ is the magnitude of shear traction on the same plane. Given a measured amount of slip along a fault plane, the resulting Coulomb stress change is expressed as:

$$\Delta CFF = \mu\Delta\sigma + \Delta\tau, \quad (2)$$

where I assume that $\Delta\mu = 0$ in all time-independent forecasts. I calculate the normal and shear stress at 8km depths and hypocentral earthquake depths as follows:

$$\sigma = S\hat{n} \cdot \hat{n} \quad (3)$$

$$\tau = -cos(\xi) * (S\hat{n} \cdot \hat{t_1}) - sin(\xi) * (S\hat{n} \cdot \hat{t_2}) \quad (4)$$

where S is the three-dimensional stress tensor, **n** is the normal (with respect to fault orientation) unit vector, $\mathbf{t_1}$ is the shear unit vector parallel to fault strike, $\mathbf{t_2}$ is the shear unit vector

perpendicular to fault strike but parallel to fault dip, and ξ is the rake angle. I define the unit vectors, using Cartesian coordinates, as:

$$\hat{n} = (cos(\theta)sin(\beta), -sin(\theta)sin(\beta), cos(\beta)) \quad (5)$$

$$\hat{t_1} = (-sin(\theta), -cos(\theta), 0) \quad (6)$$

$$\hat{t_2} = (cos(\theta)cos(\beta), -sin(\theta)cos(\beta), -sin(\beta)) \quad (7)$$

where θ is the strike angle and β is the dip angle. Using fault angle conventions from Aki and Richards (1980), I define the dip angle as $0° \leq \beta \leq 90°$ and the strike vector such that the fault dips to the right of it. The results I present are based on stress calculations that assume right-lateral receiver planes, and therefore positive right-lateral shear stress throughout the southern California study area. For the general case, it is necessary to calculate Coulomb stress considering both positive and negative shear stress change for right-lateral slip.

To ensure that earthquakes with similar fault plane orientations to Pacific-North American plate motion release seismic moment accumulated from aseismic slip, I modeled tectonic stress evolution using the backslip projection method described by Deng and Sykes (1997a, Figure 2). Modeling the crust as an elastic half-space, I assumed that the seismogenic zone, or uppermost 15 km of the earth's crust, is relatively rigid compared to the lower crust and asthenosphere. The seismogenic zone is assumed "locked," and only permitted to slip coseismically, with the exception of creeping regions. Below the seismogenic zone, increased temperatures lower the viscosity, decreasing the amount of shear stress that may accumulate before deformation occurs. Over long periods of time, moment accumulated through tectonic plate motion must equal released seismic moment in the upper crust; therefore, I introduced a left-lateral dislocation along major southern California faults, equivalent to plate movement

inferred from GPS data. Accumulated aseismic ΔCFF then gradually brings locked faults closer to failure, when the ΔCFF is released.

I assumed the earth's crust in southern California is homogeneous and isotropic. Using the program Coulomb 3.3 (Toda et al., 2011), I calculated strain tensors from rectangular fault dislocation patches as follows:

$$\left[\varepsilon_{ij}\right] = \begin{bmatrix} \frac{\partial u_1}{\partial x_1} & \frac{1}{2}\left(\frac{\partial u_1}{\partial x_2} + \frac{\partial u_2}{\partial x_1}\right) & \frac{1}{2}\left(\frac{\partial u_1}{\partial x_3} + \frac{\partial u_3}{\partial x_1}\right) \\ \frac{1}{2}\left(\frac{\partial u_2}{\partial x_1} + \frac{\partial u_1}{\partial x_2}\right) & \frac{\partial u_2}{\partial x_2} & \frac{1}{2}\left(\frac{\partial u_2}{\partial x_3} + \frac{\partial u_3}{\partial x_2}\right) \\ \frac{1}{2}\left(\frac{\partial u_3}{\partial x_1} + \frac{\partial u_1}{\partial x_3}\right) & \frac{1}{2}\left(\frac{\partial u_3}{\partial x_2} + \frac{\partial u_2}{\partial x_3}\right) & \frac{\partial u_3}{\partial x_3} \end{bmatrix} \quad (8)$$

where $[\epsilon_{ij}]$ is the three-dimensional strain tensor and $\mathbf{u_i}$ is the set of displacement vectors in the Cartesian coordinate system. I used the Okada dislocation method (Okada, 1992) to calculate the strain field as a function of contributions from each displaced fault patch, then converted the resulting strain tensor to a stress tensor with Hooke's Law:

$$\Delta\sigma_{ij} = C_{ijkl}\Delta\varepsilon_{kl} \quad (9)$$

where $\Delta\sigma_{ij}$ is the change in the three-dimensional stress tensor, C_{ijkl} is a fourth-order tensor of elastic coefficients that describe physical properties of the earth's crust, and $\Delta\varepsilon_{kl}$ is the change in the three-dimensional strain tensor. For an isotropic medium, the tensor is defined as:

$$C = \begin{bmatrix} 2\mu+\lambda & \lambda & \lambda & 0 & 0 & 0 \\ \lambda & 2\mu+\lambda & \lambda & 0 & 0 & 0 \\ \lambda & \lambda & 2\mu+\lambda & 0 & 0 & 0 \\ 0 & 0 & 0 & \mu & 0 & 0 \\ 0 & 0 & 0 & 0 & \mu & 0 \\ 0 & 0 & 0 & 0 & 0 & \mu \end{bmatrix} \quad (10)$$

where μ and λ are Lamé parameters, which may be expressed in terms of elastic moduli. I assumed a constant rigidity of 33 GPa, Young's modulus of 82.5 GPa, and Poisson's ratio of 0.25.

2.2 Coulomb Stress Index Function

For a spatially-variant Coulomb stress-based earthquake forecast that directly takes into account seismicity rates, I initially assumed that seismicity rates must increase monotonically with ΔCFF. Given that earthquake probabilities of zero or one hundred percent completely invalidate earthquake forecasts with one or zero earthquakes in a given area, respectively, I assigned the additional constraint that the probability of an earthquake falls within the range $0 < p < 1$. Due to singularities at fault section ends with strain discontinuities, calculated stress may approach negative or positive infinity, causing points where the static ΔCFF may be unrealistic. If the static ΔCFF at a point exceeds 2 MPa or drops below -2 MPa, I assigned a value of 2 or -2 MPa, respectively, under the assumption that ΔCFF values outside of the acceptable range do not represent the stress field at actual fault asperities, are artefacts from the backslip projection method (Stein et al., 1997). I modeled earthquake probability variation as a function of ΔCFF with a normalized arctangent function:

$$p = 0.5 + \frac{1}{\pi}\arctan\left(\frac{\Delta CFF - a}{d}\right) \quad (11)$$

where a and d are the function's median and width, respectively. To best fit the index function to the study area's earthquake distribution, I counted the number of receiver earthquakes for a given time window in each cell, and calculated the optimal median and function width through optimizing a log likelihood function:

$$L = \sum_{i=1}^{M} n_i \ln\left(p_i\right) - \left\langle N \right\rangle \quad . \tag{12}$$

L is the log likelihood, M is the total number of cells in the study area, n_i is the number of receiver earthquakes in cell i, p_i is the normalized earthquake probability in cell i and N is the expected number of earthquakes throughout the study area, equal to one when normalized. I then incorporated the optimal parameters (Figure 2.1) into the index function when calculating normalized earthquake probabilities throughout the study area (Figure 2.2). For all likelihood tests, I assume every earthquake is independent, and therefore does not require a conditional probability.

2.3 Smoothed Seismicity

For spatially-variant earthquake statistics-based earthquake forecasts, I modeled earthquake probabilities as a function of distance from previous source earthquakes (Hiemer et al., 2013), with seismicity rates inversely proportional to source distances:

$$k\left(r\right) = \frac{C}{r^2 + d^2} \tag{13}$$

where k(r) is the seismicity rate contribution from one source earthquake as a function of distance to a given point, r is the distance from the earthquake to the given location, d is the

smoothing kernel distance, and C is a normalizing constant. The smoothing kernel may be optimized by measuring probability gain as follows:

$$G = \exp\left(\frac{\log(L) - \log(L_0)}{N}\right) \tag{14}$$

where log(L) is the log likelihood of the smoothed seismicity model, $\log(L_0)$ is the log likelihood of a uniform seismicity model, and N is the total number of receiver earthquakes within the study area during the tested time window.

Other variations of the smoothed seismicity model take into account earthquake magnitude and probability of independence (whether or not the earthquake was triggered by a previous event):

$$k(r) = \frac{C'M}{r^2 + d^2} \tag{15}$$

$$k(r) = \frac{C''\varphi}{r^2 + d^2} \tag{16}$$

where M and φ are seismic moment and probability of independence, respectively.

2.4 Stochastic Earthquake Declustering

Earthquake clustering potentially plays an important role in evaluating earthquake forecasts' relative effectiveness when forecasting seismicity rate magnitudes, rather than distributions of activated cells. Although ideally earthquake forecasts should indicate future aftershock sequence locations, such clustering may distort evidence of triggered independent

events. The ETAS declustering method proposed by Zhuang et al. (2002) describes a method for calculating the probability of an earthquake being independent of prior events:

$$\varphi_j = 1 - \rho_j = \frac{\mu\left(x_j, y_j | H_{t_j}\right)}{\lambda\left(t_j, x_j, y_j | H_{t_j}\right)} \tag{17}$$

where ρ is the probability that an earthquake was triggered by a previous event, μ is the background intensity and λ is the conditional intensity, or contributed seismicity rate from previous earthquakes. The conditional intensity at an earthquake hypocenter increases when previous, relatively large earthquakes have occurred recently and within a small radius – for example, during an aftershock sequence:

$$\lambda\left(t, x, y, M | H_t\right) = \mu\left(x, y\right) + \sum_{\{k: t_k < t\}} \kappa\left(M_k\right) g\left(t - t_k\right) f\left(x - x_k, y - y_k | M_k\right) \tag{18}$$

where H_t refers to historical seismicity, μ(x,y) is the background intensity, and $\kappa(M_k)$, $g(t-t_k)$ and $f(x-x_k,y-y_k|M_k)$ are magnitude, time and spatial functions. They are defined as follows:

$$\kappa\left(M\right) = Ae^{\alpha\left(M - M_0\right)} \tag{19}$$

$$g\left(t\right) = \left(p - 1\right) c^{p-1} \left(t + c\right)^{-p}, t > 0 \tag{20}$$

$$f\left(x, y | M\right) = \frac{1}{2\pi d e^{\alpha\left(M - M_0\right)}} exp\left\{-\frac{1}{2}\frac{x^2 + y^2}{d e^{\alpha\left(M - M_0\right)}}\right\} \tag{21}$$

where A, α, c and p are constants, M_0 is the lower magnitude threshold, and d is the spatial kernel bandwidth, which may remain constant or vary for each earthquake via adaptive smoothing.

Background intensity is a function of spatial distribution of historical seismicity, and is calculated as follows:

$$\mu(x,y) \approx m_1(x,y) - \frac{1}{T} \sum_{\{k:t_k<T\}} \kappa(M_k) f(x-x_k, y-y_k|M_k) \tag{22}$$

$$m_1(x,y) = \frac{1}{T} \sum_{j=1}^{N} k_d(x-x_j, y-y_j) \tag{23}$$

where T is the entire duration of the earthquake catalog and k_d is the Gaussian kernel function:

$$k_d(x,y) = \frac{1}{2\pi d} exp\left\{-\frac{x^2+y^2}{2d^2}\right\}. \tag{24}$$

In order to optimize the relative effects of conditional and background intensity on future earthquake locations, I rewrote the background seismicity with a constant multiplier ν:

$$\mu(x,y) = \nu u(x,y) \tag{25}$$

which I optimized through a log likelihood test, with u(x,y) initially set to one throughout the entire study area:

$$logL(\underline{\Theta}) = \sum_{k=1}^{N} log\lambda_{\underline{\Theta}}(t_k, x_k, y_k|H_k) - \int_0^T \iint_S \lambda_{\underline{\Theta}}(t,x,y|H_t)\, dxdydt \tag{26}$$

$$\underline{\hat{\Theta}} = \left(\hat{v}, \hat{A}, \hat{\alpha}, \hat{c}, \hat{p}, \hat{d}\right). \tag{27}$$

From the optimized ν value, I calculate the probability of triggering for each earthquake, then calculate the background seismicity. Setting u(x,y) = μ(x,y), I repeat the optimization until it

converges, and ν becomes stable. I use the resulting earthquake independence probabilities to stochastically classify each earthquake as an independent event or as an aftershock.

2.5 Rate-and-State Theory

Temporal dependence may be introduced into static ΔCFF-based earthquake forecasts through rate-and-state friction. Based on empirical observations, the coefficient of friction of a material varies as a function of normal stress, displacement and time (Cocco et al., 2010; Dieterich and Kilgore, 1996):

$$\tau = \sigma\left[\mu_0 + A\ln\left(\dot{\delta}/\dot{\delta}^*\right) + B\ln\left(\theta/\theta^*\right)\right] \tag{28}$$

where τ is the shear stress necessary for sliding, σ is effective normal stress, μ_0, A and B are empirically determined constants, δ-dot is sliding speed, θ is a state variable, and δ*-dot and θ* are normalizing constants. Shear and normal stress have been shown to significantly alter slip speed in small quantities. If one expresses seismicity rate as a function of static ΔCFF, the state variable will be greater in areas of low seismicity and decrease following a jump in static ΔCFF from a prior earthquake (Hainzl, 2010; Toda and Enescu, 2011):

$$\gamma_0 = 1/\dot{\tau} \tag{29}$$

$$\gamma_n = \gamma_{n-1} exp(-\Delta CFF/A\sigma) \tag{30}$$

where γ_0 represents steady state, and is equal to the inverse of shear tectonic stress rate τ-dot. γ_n is the state variable for given iteration n just after a source earthquake occurs, with γ_{n-1} being the previous state variable value. A is a constitutive parameter multiplied by σ, the pre-existing

normal stress. Over time, the static ΔCFF iteration exerts less influence over the seismicity rate, and the state variable returns to steady state:

$$\gamma_{n+1} = (\gamma_n - \gamma_0) * exp(-\Delta t \dot{\tau}/A\sigma) + \gamma_0 \quad (31)$$

where γ_{n+1} is the state variable value after an elapsed time, Δt, since the last source earthquake. For a given time and historic stress sequence, I then calculate the seismicity rate in a given cell:

$$R = r/\gamma\dot{\tau} \quad (32)$$

where R is the total seismicity rate and r is the background seismicity rate, inferred from either the tectonic stress rate or historical seismicity and Gutenberg-Richter slope values throughout the study area.

The expected number of aftershocks, N_a, over time T and above a defined magnitude threshold M_{min} may be calculated by integrating the difference between the total and background seismicity rates:

$$N_a(T) = \int_0^T R(t)\,dt - rT \quad (33)$$

to yield

$$N_a = \frac{V}{\langle M_0 \rangle} \Delta CFF \quad (34)$$

where $\langle M_0 \rangle$ (with units Nm) is the average seismic moment of earthquakes within the study area:

$$\langle M_0 \rangle = 10^{9.1+1.5M_{min}} \frac{b}{1.5-b} \frac{10^{(1.5-b)(M_{max}-M_{min})}-1}{1-10^{-b(M_{max}-M_{min})}} \quad . \qquad (35)$$

M_{max} is the largest expected earthquake within the study area, and b is the Gutenberg-Richter slope, or magnitude-frequency distribution.

2.6 Rate-and-State ΔCFF Inversion

Stress singularities tend to artificially inflate calculated seismicity rates near ends of fault sections that experience consecutive source earthquakes with overestimated coseismic ΔCFF. Assuming observed seismicity should delineate stress field evolution, Dieterich et al. (2000) inverted the forward rate-and-state equation to obtain ΔCFF as a function of seismicity rates over two defined time intervals:

$$\Delta CFF = A\sigma \ln\left\{\frac{\dot{S}\left[\exp\left(N_2 \dot{S}_r t_1 / N_1 A\sigma\right)-1\right]}{\dot{S}_r\left[\exp\left(\dot{S}t_2 / A\sigma\right)-1\right]}\right\} \qquad (36)$$

where S-dot and S_r-dot are the total and tectonic stress rates, respectively, and N_1 and N_2 are the numbers of earthquakes occurring during time intervals t_1 and t_2, respectively. Aftershock sequences elevate ΔCFF considerably, but not to the extent forecasted at dislocation patch corners by physically unreasonable stress change.

If few or no earthquakes nucleate in or near a cell, then the inversion method cannot yield physically realistic stress steps; therefore, the method is limited to areas and time intervals of elevated seismicity, compared to seismically quiescent areas. Because a prospective earthquake forecast must effectively forecast areas of seismic quiescence as well as earthquake locations and times, I modified Dieterich's stress inversion equation to allow areas with relatively low

seismicity to be included. To include the entire southern California study region, I substituted the Poissonian cumulative probability of observed seismicity for the actual numbers of earthquakes in each time interval:

$$\Delta CFF = A\sigma \ln\left\{\frac{\dot{S}\left[\exp\left(p_2\dot{S}_r t_1 / p_1 A\sigma\right)-1\right]}{\dot{S}_r\left[\exp\left(\dot{S}t_2 / A\sigma\right)-1\right]}\right\} \tag{37}$$

where p_1 and p_2 are the cumulative Poissonian probabilities of the observed numbers of earthquakes occurring in a cell, given a uniform seismicity rate λ, which I derived from smoothed seismicity:

$$p = F\left(x \mid \lambda\right) = \exp\left(-\lambda\right)\sum_{i=0}^{floor(x)}\frac{\lambda^i}{i!}. \tag{38}$$

2.7 Optimally Oriented Plane Calculations

With reliable constraint of the regional stress field, optimally oriented planes yield the strongest association between earthquake locations and ΔCFF (Steacy et al., 2005). The program Coulomb 3.3 currently employs a grid search method to estimate three-dimensional optimally oriented planes. I presented an analytical method for calculating optimal plane orientations with improved precision and efficiency, which will be incorporated in the next iteration of Coulomb software (R. Stein and S. Toda, personal communication).

Given the regional stress tensor [R], the stress tensor containing contributions from seismicity and tectonic loading [S], and the coefficient of friction μ, one may calculate the optimal receiver plane orientation through the use of Mohr's circles (Newman, 2012). First, I combined the regional and source stress tensors into a total stress tensor, [T]:

$$[T] = \begin{bmatrix} R_{11} + S_{11} & R_{12} + S_{12} & R_{13} + S_{13} \\ R_{21} + S_{21} & R_{22} + S_{22} & R_{23} + S_{23} \\ R_{31} + S_{31} & R_{32} + S_{32} & R_{33} + S_{33} \end{bmatrix}. \tag{39}$$

The eigenvalues of stress tensor [T] yield the principal stresses, from greatest to least: σ_1, σ_2, and σ_3. Tension is considered positive, while compression is considered negative. These values and the coefficient of friction may be used to obtain the normal (σ_N) and shear (σ_s) stresses corresponding to the point at which the Mohr's circle intersects the line tangent to it, with a slope defined by μ:

$$\sigma_N = \left(\frac{\sigma_1 + \sigma_3}{2}\right) + \left(\sigma_1 - \left(\frac{\sigma_1 + \sigma_3}{2}\right)\right)\cos\varphi \tag{40}$$

$$\sigma_S = \left|\left(\sigma_1 - \left(\frac{\sigma_1 + \sigma_3}{2}\right)\right)\sin\varphi\right| \tag{41}$$

$$\varphi = \tan^{-1}\mu \tag{42}$$

where φ is the angle between the line tangent to the Mohr's circle and the x-axis.

Components of the vector normal to the fault plane, **n**, are calculated as functions of σ_N, σ_S, and the principal stresses:

$$n_1^2 = \frac{(\sigma_N - \sigma_2)(\sigma_N - \sigma_3) + \sigma_S^2}{(\sigma_1 - \sigma_2)(\sigma_1 - \sigma_3)} \tag{43}$$

$$n_2^2 = \frac{(\sigma_N - \sigma_3)(\sigma_N - \sigma_1) + \sigma_S^2}{(\sigma_2 - \sigma_3)(\sigma_2 - \sigma_1)} \tag{44}$$

$$n_3^2 = \frac{(\sigma_N - \sigma_1)(\sigma_N - \sigma_2) + \sigma_S^2}{(\sigma_3 - \sigma_1)(\sigma_3 - \sigma_2)}. \tag{45}$$

The positive and negative square roots of each component of **n** yield eight possible normal vectors. For each vector, it is necessary to calculate the corresponding receiver plane orientation, onto which the tectonic and seismic stress changes, [S], are resolved.

Unit vectors parallel to fault strike ($\mathbf{f_s}$) and to fault dip ($\mathbf{f_d}$) are calculated as follows:

$$\hat{\underline{f_s}} = \frac{\underline{k} \times \hat{\underline{n}}}{|\underline{k} \times \hat{\underline{n}}|} \tag{46}$$

$$\hat{\underline{f_d}} = \hat{\underline{n}} \times \hat{\underline{f_s}} \tag{47}$$

$$\underline{k} = (0, 0, 1) \tag{48}$$

where unit vectors are specified by index notation ($\mathbf{f_{si}}$, $\mathbf{f_{di}}$). The strike and dip angles, θ and β, are then derived from $\mathbf{f_s}$ and $\mathbf{f_d}$:

$$\theta = \sin^{-1}(-f_{s1}) \tag{49}$$

$$\beta = \cos^{-1}\left(\frac{f_{d1}}{\cos\theta}\right). \tag{50}$$

The rake angle ξ is then calculated from the traction vector **t**, total stress tensor [T], and the unit vectors parallel to the fault plane:

$$\xi = \cos^{-1}\left(\frac{a}{\sqrt{a^2 + b^2}}\right) \tag{51}$$

$$a = \underline{t} \cdot \underline{f_s} \tag{52}$$

$$b = \underline{t} \cdot \underline{f_d} \tag{53}$$

$$\underline{t} = [T]\,\underline{\hat{n}}. \tag{54}$$

The optimally oriented plane is defined as the receiver plane that yields the greatest static ΔCFF as a function of [S] and μ (Equations 2-7).

2.8 Likelihood Testing

N-Test

The N, or "number" test, compares the observed number of earthquakes or activated cells to the numbers the null and alternate probability models tend to construct. I evaluated the null and alternate hypotheses by generating a large number of synthetic earthquake maps from each probability distribution, and computing the percentage of synthetic earthquake maps containing fewer earthquakes or activated cells than the observed number. I defined a p-value as the percentage of synthetic earthquake maps with fewer earthquakes or activated cells. Because a forecast that over- or underestimates seismicity rates is ineffective, I employed a two-tailed test where I did not reject the hypothesis if $0.025 < p < 0.975$. If $p < 0.025$, the probability distribution yielded seismicity maps with more earthquakes than anticipated, and fewer earthquakes for $p > 0.975$, and I rejected the hypothesis at the 95% confidence interval.

S-Test

The spatial log likelihood test, or S-test, individually evaluates spatial seismicity rates or activated cell distribution for the null and alternate forecasts. I based the S-test on the probability of a specific area containing at least one earthquake. When taking into account seismicity rates variation for cells containing earthquakes, I calculated the L statistic as follows:

$$L = \sum_{i=1}^{N} n_i \ln(p_i) - 1 \tag{55}$$

where L is the log likelihood, N is the total number of cells in the study area, n_i is the number of earthquakes in cell i, and p_i is the relative probability of a cell containing earthquakes relative to other cells. When only considering whether the cell is "activated," or whether the cell contains at least one earthquake, the log likelihood becomes:

$$L = \sum_{i=1}^{N} c_i \ln(p_i) + \sum_{i=1}^{N} (1 - c_i) \ln(1 - p_i) \tag{56}$$

where p_i is the probability of a cell containing at least one earthquake during a specified time window, and c_i is equal to either zero or one, indicating whether I observed at least one earthquake in the cell during the test period (Rong et al., 2003). Because cell activation probabilities do not depend on the locations or times of previously activated cells, only independent earthquakes should be used in the S-test and R-tests.

Similar to the N-test, I construct many synthetic seismicity maps from the null and alternate probability distributions, and calculate their respective L statistics. I used a two-tailed test, defined two critical L values, L_1 and L_2. L_1 was the log likelihood value exceeding 2.5%, and L_2 was the log likelihood value exceeding 97.5% of the synthetic log likelihood distribution. If the observed log likelihood score fell below L_1 or was greater than L_2, the forecast either anticipated earthquakes in areas where few are predicted to occur, or failed to anticipate earthquakes in areas with elevated ΔCFF or conditional intensity.

R-Test

The log likelihood ratio test, or R-test, allows for direct comparison of the null and alternate earthquake forecasts by assessing the probability of falsely rejecting either hypothesis. Methodology is very similar to the S-test: I simulated a large number of earthquake catalogs for each probability distribution, and calculated the log likelihood ratio, or R-value, for the observed and synthetic earthquake catalogs as follows:

$$R_1 = L_{11} - L_{21} \tag{57}$$

$$R_2 = L_{12} - L_{22} \tag{58}$$

$$R_o = L_{1o} - L_{2o} \tag{59}$$

where the subscript for the R values indicates the earthquake catalog type, the first subscript for the L values indicates the type of probability distribution, and the second subscript indicates the earthquake catalog type. Subscripts 1, 2 and o indicate Coulomb stress (alternate), smoothed seismicity or ETAS (null), and the receiver earthquake catalog (observed value). I defined a critical value, R_1, as the log likelihood ratio exceeding 95% of the synthetic log likelihood ratio distributions generated from ΔCFF-based cell activation probabilities. If the observed R value was greater than R_1, I rejected the ETAS forecast in favor of the ΔCFF-based forecast. I defined the second critical value, R_2, as the log likelihood ratio exceeding 5% of the synthetic log likelihood ratio distributions generated from ETAS-based cell activation probabilities. If the observed R value fell below R_2, I rejected the ΔCFF-based forecast in favor of the ETAS forecast.

The R-test measures the overall relative effectiveness of each forecast, but does not indicate specific areas where one forecast may outperform the other. Log likelihood residual

maps, where I calculate the log likelihood ratio for each cell, indicate the areas in which either the physics-based or statistics-based forecast is most reliable.

Information Scores

Information statistics are used to evaluate any probability distribution by calculating its probability gain throughout the study area. A forecast may be evaluated by calculating the "success" and "specificity" scores, I_1 and I_0. I_1 evaluates the information gain against a uniform probability distribution as follows:

$$I_1 = \frac{1}{n}\sum_{i=1}^{n}\log_2\frac{\lambda_i}{\xi} \tag{60}$$

where in the context of an earthquake forecast, n is the number of receiver earthquakes, λ_i is the normalized seismicity rate density in cell i, and ξ is the normalized uniform seismicity rate within the study area. I_0 evaluates I_1 for longer tests, if the given forecast is exactly correct:

$$I_0 = \sum_{i=1}^{N}\nu_i\log_2\frac{\nu_i}{\tau_i} \tag{61}$$

where N is the total number of cells in the study area, ν_i is the normalized seismicity rate in cell i, and τ_i is the normalized cell area in cell i. The tests are comparable to spatial log likelihood tests (S-tests), in that the log likelihood is defined as the sum of the log likelihood, or log(probability), contributions from each earthquake. However, S-tests do not evaluate a forecast relative to uniform seismicity, or take into account differences in cell area.

2.9 Hybrid Earthquake Forecasts

Information statistics allow for the optimization of hybrid earthquake forecasts with linear combinations of ΔCFF and statistics-based earthquake probabilities as a function of

distance from the nearest fault section. Given that stress singularities introduce large uncertainties in the stress field near faults, I gave ΔCFF more influence over earthquake probabilities in the far field, and statistical earthquake probabilities more influence near faults. The linear combination of each probability distribution, P, is defined as follows:

$$P = aC + (1-a)S \quad . \tag{62}$$

C is the physics-based earthquake probability in a given location, S is the statistics-based earthquake probability, and a is a mixing parameter that indicates the percentage weight given to physics-based earthquake probabilities.

Similar to the arctangent index function used to calculate seismicity rates as a function of ΔCFF, the mixing parameter may be expressed as a function of distance from the nearest fault:

$$a = 0.5 + \frac{1}{\pi}\tan^{-1}\left(\frac{f-\sigma}{d}\right) \tag{63}$$

where f is the distance to the nearest fault, and σ and d are the function median and width, respectively. Using equation 12, I optimized the mixing parameter by calculating the maximum likelihood from combinations of the index function's median and function width.

2.10 Figures

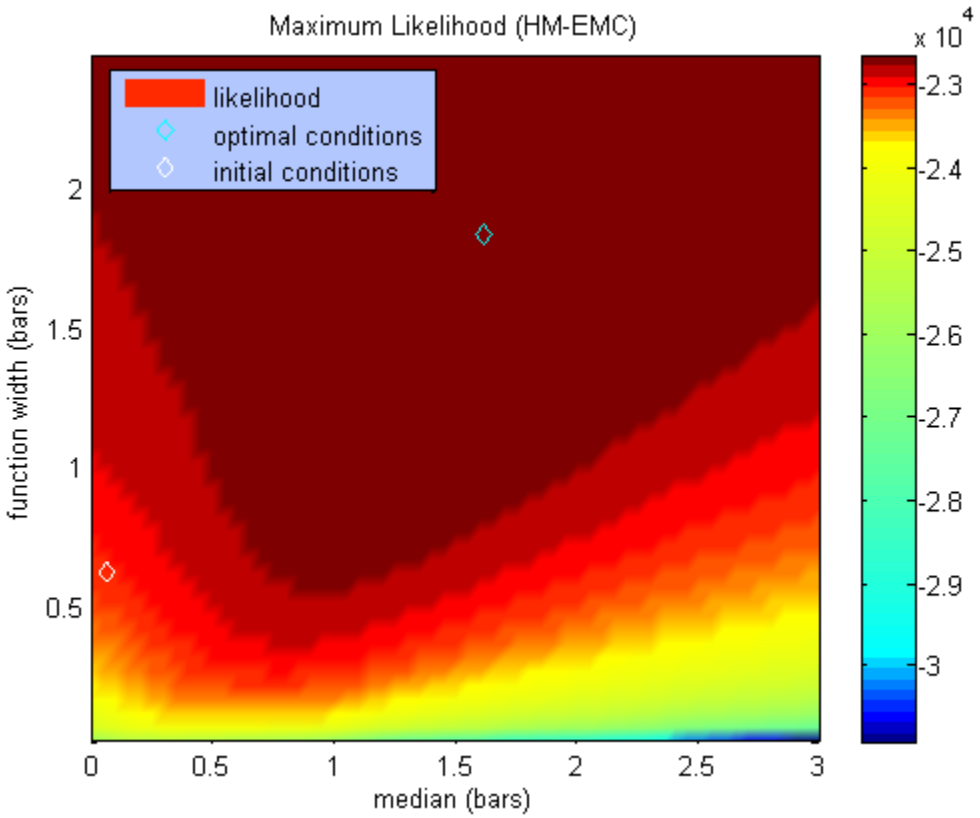

Figure 2.1: Log likelihood as a function of median and function width from equation 12. Red areas indicate combinations of median and function width with relatively large likelihood scores, whereas yellow, green and blue indicate combinations with lower likelihood scores. The white diamond indicates the initial function median and width, and the cyan diamond indicates the optimal function median and width.

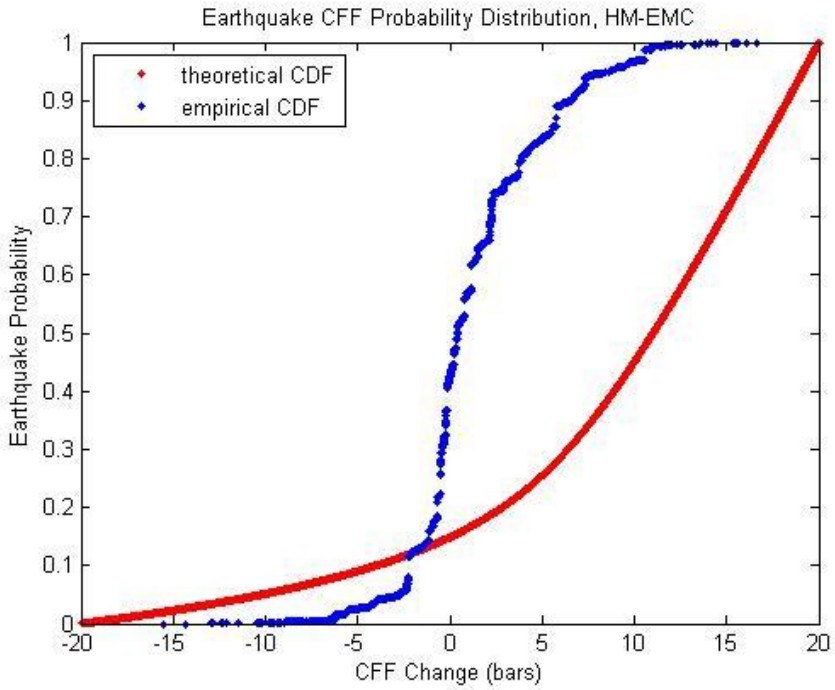

Figure 2.2: Theoretical and empirical cumulative seismicity with ascending ΔCFF. The blue curve displays observed cumulative seismicity with ΔCFF, and the red curve displays cumulative seismicity derived from the arctangent index function. The index function anticipates that seismicity rates increase monotonically with ΔCFF, whereas most observed seismicity occurs at small, positive ΔCFF values.

CHAPTER 3

Near-Prospective Test of Coulomb Stress Triggering

3.1 Abstract

Numerous studies retrospectively observed a strong association between earthquake location and increased static Coulomb stress. In addition to confirming these results for southern California seismicity, we observed prospective forecasting potential in static stress evolution. With 141 seismic and 98 aseismic stress sources, we considered alternate choices of stress components and receiver fault orientations, examined the effect of Coulomb triggering on earthquake magnitude, calculated stress histories for receiver quakes to see if some occurred after their stress had peaked, examined whether stress changes from the Hector Mine earthquake alone changed the earthquake rate as expected, and estimated the conditional distribution of earthquake occurrence given resolved Coulomb stress change. We found that, with 95% confidence, more $M \geq 2.8$ receiver earthquakes nucleate often in areas of shear or Coulomb stress change increase than in stress shadows. On average, 59% of earthquakes occurred within stress-enhanced zones, regardless of the choice of rupture plane or type of stress change. Given that approximately 60% of the study area displayed cumulative positive ΔCFF, we tested the reverse conditional hypothesis: that given a stress-enhanced zone, seismicity rates should be elevated. The 1999 Hector Mine, California earthquake increased the seismicity in regions of positive and negative stress change, but more so in the positive regions. Earthquakes frequently occur after their calculated peak stress has occurred, indicating that elastic calculations don't tell the whole story. We found no significant evidence that stress change affects the magnitude of

receiver quakes. Thus, instantaneous Coulomb and shear stress change apparently influence the locations but not the magnitudes of future earthquakes.

3.2 Introduction

Deng and Sykes [1997a,b] compared earthquake locations and focal mechanisms with the elastic Coulomb Failure Function (CFF):

$$CFF = \mu\sigma + \tau \quad (1)$$

where CFF, σ and τ correspond to Coulomb, normal and shear stress respectively, and μ is the coefficient of friction. They estimated ΔCFF, the total accumulated Coulomb stress change, as a function of location and time by summing the tensor stress effects of previous earthquakes and tectonic plate motion since 1812. ΔCFF was resolved onto the assumed fault plane of a receiver earthquake in its assumed rake direction. Deng and Sykes found that 95% of $M > 6$ and 85% of $M \geq 1.8$ earthquakes occurred where the ΔCFF was positive, as calculated at the time of the receiver event. Their ΔCFF maps (Figure 3.1), calculated on uniformly oriented right-lateral strike-slip vertical planes striking at 321°, also indicate that the "stress shadows" (regions of negative ΔCFF) resulting from the great California earthquakes of 1812 and 1857 [*Harris and Simpson*, 1996] have been shrinking as a result of stress accumulation, with approximately 75% of the area displaying elevated cumulative positive ΔCFF by the time the study was published. Such shrinkage might suggest that moderate to large earthquakes will occur at an accelerated rate until a future earthquake strikes. They also calculated ΔCFF fields from thrust receiver planes, and observed an association between positive ΔCFF and earthquakes nucleating along similarly oriented faults. Their conclusions did not constitute a formal forecast because they gave no quantitative estimate of future earthquake rates, nor did they suggest a specific test that could be applied using subsequent earthquakes. They did provide specific formulae to reproduce their

calculations and to extend them by including subsequent earthquakes. Their most important conclusion, that a strong majority of earthquakes occurred at positive ΔCFF, is essentially a statement about the stress distribution given the locations and times of earthquakes. A forecast useful for earthquake risk management would have to be based on the reverse conditional distribution: that of earthquake times and places given the evolving stress map. Here we examine both distributions: ΔCFF given earthquakes, and earthquakes given ΔCFF.

We extended Deng and Sykes' 1997 studies by conducting pseudo-prospective tests within the same study area using both source and receiver earthquakes in California after 1997. We define "source" earthquakes as those assumed to change the stress environment for future events. Receiver earthquakes were candidates for being triggered, and for which we calculated the immediate prior stress. The lower magnitude thresholds for source and receiver earthquakes were 5.8 and 2.8, respectively. Most source events also served as receivers. We only added the 1999 M7.1 Hector Mine, California earthquake to the source receiver earthquake catalog because no $M \geq 5.8$ earthquakes occurred within the study area between Deng and Sykes' study and that event.

We also isolated and tested the normal and shear stress components of the ΔCFF to ascertain if either shows a greater tendency to trigger earthquakes. To remain consistent with the prior study, we resolved stress onto uniformly oriented planes. We also tested three additional sets of receiver planes, with orientations interpolated from (a) all known earthquake focal mechanisms in the study area, (b) local fault orientation, and (c) the preferred nodal planes of the receiver earthquakes, for which the resolved Coulomb stress was most positive.

If Coulomb stress discourages earthquake nucleation, seismicity should decrease when Coulomb stress decreases [*Harris*, 1998, 2000]. Previous research suggests that, for a variety of

tectonic settings, aftershocks tend to occur where the mainshock increased the static Coulomb stress change [*Stein et al.*, 1997; *Papadimitriou et al.*, 2001; *Wang and Chen*, 2001; *Shan et al.*, 2011], and static Coulomb stress along one fault may bring neighboring faults closer to failure [*Ghisetti*, 2000; *King and Cocco*, 2001; *Papadimitriou*, 2002; *Robinson*, 2004]. We tested for such a correlation, assuming zero stress change just before the 1812 Wrightwood earthquake, on the San Andreas fault. For each recent receiver earthquake, we calculated the $\Delta\sigma$ (normal stress change), $\Delta\tau$ (shear stress change) and ΔCFF history, that included tectonic loading, at the event's location for each year since 1812 to determine the percentage of events that occur at the time of maximum stress change. The maximum stress magnitude could be influenced by deep fault slip rates as well as upper fault boundaries of deep dislocation; therefore, we expect maximum stress to vary throughout the study region. If a strong majority of receiver earthquakes occur at the historic stress maxima since 1812 at their locations, mapping Coulomb stress relative to its previous maximum might have promise for forecasting. Finally, we tested for an association between static Coulomb stress and receiver earthquake magnitude, to determine whether static stress evolution influences dynamic rupture propagation.

3.3 Earthquake and Fault Selection

Similar to *Deng and Sykes* [1997a,b], we used a study area covering 32°-37°N latitude and 114°-122°W longitude. Our complete receiver earthquake catalog included 2764 M2.8-M7.2 events reported in the southern California focal mechanism catalog of *Yang et al.* [2012]. The magnitude distribution, which maintains a constant Gutenberg-Richter slope down to magnitude 2.8, suggests that the catalog is complete at that level. We included a total of 141 source earthquakes in the stress change model, of which 140 occurred prior to 1997 and were

included in Deng and Sykes's study. We calculated stress changes for that earthquake using a model by *Ji et al.* [2002], who assumed slip on a collection of sub-parallel rectangular fault patches. We included tectonic stresses from the same 98 fault slip sources used by Deng and Sykes. We both used a coefficient of friction of 0.6 ($\Delta\mu = 0$ for the entire study), Poisson's ratio of 0.25, rigidity of 33 GPa, and Young's modulus of 82.5 GPa. Stress contributions from both aseismic and seismic sources are consistent with Deng and Sykes's findings until 1997. After this time, we added recent source earthquakes to the stress change field and tectonic stress contributions increased in magnitude due to the extended time period.

We calculated stress tensors at each receiver earthquake location for both hypocentral and uniform 8km depths and generated stress change field maps using the program Coulomb 3.3 [*Lin and Stein,* 2004; *Toda et al.,* 2011]. We calculated Coulomb stress changes using the Coulomb Failure Function:

$$\Delta CFF = \mu\Delta\sigma + \Delta\tau \tag{2}$$

where μ is the coefficient of friction, $\Delta\sigma$ the normal stress change on a pre-designated receiver plane, and $\Delta\tau$ the magnitude of shear traction, assuming right-lateral receiver planes – most, but not all receiver earthquake focal mechanisms are right-lateral strike-slip. We calculated the normal and shear stress components as follows:

$$\sigma = \mathbf{S}\hat{\mathbf{n}} \cdot \hat{\mathbf{n}} \tag{3}$$

$$\tau = -\cos\theta * \left(\mathbf{S}\hat{\mathbf{n}} \cdot \hat{\mathbf{t}}_1\right) - \sin\xi * \left(\mathbf{S}\hat{\mathbf{n}} \cdot \hat{\mathbf{t}}_2\right) \tag{4}$$

where S is the stress tensor at a given earthquake location, $\hat{\mathbf{n}}$ is the unit vector normal to the assumed receiver fault, $\hat{\boldsymbol{t}}_1$ is the horizontal unit vector parallel to receiver fault strike, $\hat{\boldsymbol{t}}_2$ is the shear unit vector perpendicular to receiver fault strike but parallel to receiver fault dip, and ξ is the receiver fault rake angle. We defined the strike vector such that the fault always dips to the right [*Aki and Richards*, 1980]. We calculated the unit vectors, using Cartesian coordinates, as follows:

$$\hat{\mathbf{n}} = \left(\cos\theta\sin\beta, -\sin\theta\sin\beta, \cos\beta\right) \tag{5}$$

$$\hat{\mathbf{t}}_1 = \left(-\sin\theta, -\cos\theta, 0\right) \tag{6}$$

$$\hat{\mathbf{t}}_2 = \left(\cos\theta\cos\beta, -\sin\theta\cos\beta, -\sin\beta\right) \tag{7}$$

where θ is the receiver fault strike and β is the receiver fault dip, within the $0° \leq \beta \leq 90°$ range.

We interpreted positive normal stress as unclamping, and positive shear stress as right-lateral [*Aki and Richards*, 2002]. Faults and earthquake rupture surfaces were represented by collections of rectangular patches with uniform slip rate or coseismic slip. We then used the program Coulomb 3.3 [*Lin and Stein*, 2004; *Toda et al.*, 2011], which implements the calculations described by *Okada* [1992] to sum the strain and stress tensors for all the patches. To promote the right-lateral slip characteristic of most southern California earthquake displacement, we modeled interseismic stress accumulation through the backslip projection method, introducing left-lateral aseismic (tectonic) displacement for all right-lateral aseismic

fault segments and vice versa. Deng and Sykes' study [1997a] describes the backslip projection method in more detail. Our results are shown in Figure 3.2.

3.4 Testing Methods

For each of the assumed receiver plane choices, we calculated the Coulomb stress accumulated since 1812 at the location and time of each receiver earthquake. We then used the binomial test for positivity of the median and the t-test to determine whether the mean Coulomb stress at the earthquake locations was significantly positive. The cumulative binomial test, which does not assume a specific distribution, gives the probability P of achieving n or fewer successes in N trials, if each trial has a probability of success equal to p. Here N is the number of earthquakes, and n is the number for which the ΔCFF is positive. Our null hypothesis that p=0.5 (positive and negative ΔCFF equally likely) could be rejected with 95% confidence if $P<0.025$ or $P>0.975$ (Tables 1 and 2).

The t-test assumes a normal distribution of values with unknown mean and variance. For this test the null hypothesis is that the mean is zero. The null hypothesis is rejected at 95% confidence if the cumulative probability P of drawing the observed ratio of mean to standard is less than 0.025 or more than 0.975. The null hypotheses imply that the median and mean ΔCFF at earthquake locations should converge to zero for infinitely many earthquakes. Rejecting the null hypothesis at the 95% confidence level would provide evidence that earthquake location depends on accumulated stress change.

We refer to these tests as "pseudo-prospective" because they were computed after the receiver quakes had occurred, but all the details of the stress model were determined from the 1997 studies of Deng and Sykes. For a test to be truly prospective, we would wait for future earthquakes to occur; however, our test is pseudo-prospective in that we use earthquakes that

have occurred since Deng and Sykes's study to test their hypothesis. Do earthquakes tend to locate in stress-enhanced zones? Deng and Sykes did not specify a particular distribution of pre-earthquake ΔCFF, and their main conclusions rested on the fraction of earthquakes for which ΔCFF was positive. Thus, the binomial test is more appropriate for their hypothesis. In using the t-test, we examine a slightly different hypothesis than considered by Deng and Sykes.

3.5 Direct Tests of Deng and Sykes' Hypothesis

To be consistent with Deng and Sykes' work, we also determined, for each stress change distribution and receiver plane orientation, the percentage of receiver earthquakes that occurred in areas with positive pre-earthquake stress. We tested the hypothesis with both the complete stress change field from 1812 until and including the Hector Mine earthquake, and the isolated Hector Mine earthquake stress change field. We defined the "learning period" as the interval before the Hector Mine earthquake coseismic stress changes. The "target period" is an equivalent period of time after the stress field was altered.

When we did not take into account the stress change magnitude, most distributions resulted in a majority of receiver earthquakes occurring in stress-enhanced zones (Table 1). Out of twelve tested distributions with stress changes calculated at hypocentral earthquake depths, one resulted in more receiver earthquakes occurring in stress shadows than in stress-enhanced zones: normal stress change resolved onto smoothed seismicity-based planes. The highest percentage of receiver earthquakes, 78%, occurred in stress-enhanced zones when resolving normal stress onto the first set of nodal planes. However, all other receiver plane orientations yielded considerably lower percentages of earthquakes in areas of increased normal stress. ΔCFF resolved onto uniformly oriented planes resulted in 66% of receiver events occurring in

stress-enhanced zones. Over half of receiver earthquakes consistently occurred in ΔCFF-enhanced zones, regardless of receiver plane orientation.

We tested the significance of these results against the null hypothesis that the sign or magnitude of the stress changes had no effect on earthquake occurrence, so that the differences in activity between the regions of positive and negative stress were simply due to random variations. We defined a test statistic favorable to the Coulomb hypothesis, and estimated P, the complement of the probability that the observed test statistic could occur if the null hypothesis were true. Thus, there were three possible outcomes. If $P \geq 0.975$, we rejected the null hypothesis in favor of the Coulomb hypothesis. If $P \leq 0.025$, we rejected the null hypothesis in favor of the antithesis of the Coulomb hypothesis, that earthquakes prefer stress shadows, where the stress decreased. For $0.025 \leq P \leq 0.975$, we can't reject the null hypothesis with 95% confidence. For brevity, we'll describe the results as favoring the Coulomb, the null, and the antithesis respectively for high, intermediate, and low values of P.

Median stress change values at earthquake hypocenters were significantly positive for most combinations of stress type and receiver plane orientation (Table 2). Our results do not yield as strong an association between earthquake location and static pre-stress as Deng and Sykes found. They showed that 95% of $M \geq 6$ and 85% of $M \geq 1.8$ receiver earthquakes occurred in areas where the ΔCFF was positive. However, our findings do support their general conclusion that earthquakes tend to nucleate in stress-enhanced zones.

For the two-tailed t-test, we defined the p-value as the probability of randomly obtaining the mean receiver earthquake pre-stress given an unknown variance and true mean of zero. In addition to testing uniformly oriented planes, we tested three other sets of planes: smoothed seismicity, mapped faults, and the preferred nodal planes. We calculated stress changes from

both original hypocentral depths and uniform 8km depths. For the t-test, we reject the null in favor of the Coulomb hypothesis at the 95% confidence interval in all but two cases: resolving normal stress onto smoothed seismicity-based receiver planes, and resolving shear stress onto preferred nodal planes. The other combinations of stress components and receiver plane orientations yielded p-values lower than 0.025. This result indicates a significantly negative mean stress change. Because earthquakes occurring near stress singularities may exhibit stress changes up to thousands of MPa, outlier events may have made the mean hypocentral stress change artificially negative.

3.6 Stress History

At each receiver earthquake location, we calculated stress changes from 1812 until the year of the event's occurrence to determine the percentage of receiver events occurring at the time of maximum stress accumulation. Historic stress changes included both constant tectonic stress rates and immediate stress jumps caused by source earthquakes. A majority of receiver earthquakes occurring when stress change is maximum would support the ability of increased stress to trigger future events. Furthermore, if pre-earthquake stress values equal historic stress maxima and these values are within a consistent range, there might exist a triggering threshold for each type of stress change at which earthquakes tend to nucleate [*Du and Sykes*, 2001].

For most tested plane orientation and stress type combinations, no more than half of all receiver earthquakes occurred at the time of maximum stress (Table 3). The exceptions were normal stress resolved onto the first set of nodal planes, shear stress resolved onto fault-based and uniformly oriented planes, and Coulomb stress resolved onto uniformly oriented planes and the first set of nodal planes. The greatest percentage of earthquakes nucleating at historic stress maxima, 55%, occurred when resolving shear and Coulomb stress onto uniformly oriented

planes. Normal stress histories resolved onto the second set of moment tensor nodal planes resulted in the lowest percentage of earthquakes occurring when stress change was maximum: only 15%. Receiver event stress histories varied considerably, based on whether aseismic stress change rates were positive or negative as well as proximity to source earthquake rupture planes (Figure 3.3).

We divided the stress history range at the location of each receiver earthquake into equally spaced quartiles, and recorded the quartile in which the event occurred. For example, if a receiver quake occurred near the historic low stress, it would fall into the first quartile, a receiver earthquake occurring at its historic maximum would fall into the fourth quartile, etc. Events tended to occur in the fourth quartile (Table 4) near the maximum historic stress, consistent with a relatively large percentage of receiver events nucleating in areas of positive stress change for most stress change distributions. The second most frequently selected quartile was the first, with relatively few earthquakes occurring in the second and third quartiles. We observed that receiver earthquakes were more likely to nucleate at their historic stress maximum with increasing hypocentral pre-stress.

3.7 Magnitude-Stress Testing

We considered an additional hypothesis that static stress change controls earthquake rupture extent once the earthquake has nucleated. If true, there should exist a positive correlation between receiver earthquake magnitude and static stress change. We divided $M \geq 2.8$ and $M \geq 4$ receiver earthquake magnitudes into quartiles, with the first quartile corresponding to the 25% of events with the lowest magnitudes. We calculated the cumulative number of earthquakes with respect to static pre-stress for each magnitude quartile to check for such dependence. For $M \geq 2.8$ earthquakes, the magnitude ranges for each quartile, from lowest to greatest, were 2.8-2.94, 2.94-

3.11, 3.11-3.42, and 3.42-7.2. For M≥4 earthquakes, the magnitude ranges for each quartile were 4-4.11, 4.11-4.3, 4.31-4.59, and 4.59-7.2.

To evaluate the effect of pre-stress on receiver earthquake magnitude, we divided the earthquake catalog into two components: events occurring in stress-enhanced zones, and events occurring in stress shadows. Using maximum likelihood estimation, we calculated b-values for either group. To determine whether the difference in b-values for earthquakes occurring in positive and negative areas of static stress change is statistically significant, we devised a null hypothesis by randomly assigning events to both groups. For 5000 earthquake randomizations, we recalculated and found the difference between b-values for the positive and negative stress groups. We defined the p-value as the probability that the b-value difference is less or greater than the expected value between two random sets of earthquakes. Using a two-tailed test, we asked whether the difference in b-values between events in stress-enhanced zones and those in stress shadows was significant at the 95% confidence interval.

For both M≥2.8 and M≥4 thresholds, we observed no association between magnitude quartiles and stress change distributions for any combination of stress type and receiver plane orientation (Table 5). Neither mean nor median stress change systematically increased with ascending magnitude quartiles (Figure 3.4). Increasing the lower magnitude threshold did not affect stress distribution with respect to magnitude. However, such results may be misleading due to the small magnitude ranges in the lower quartiles. The difference between the upper and lower magnitude in the first quartile, 0.11, is comparable to the magnitude uncertainty. If we were to apply a similar Gaussian error distribution to the magnitude distribution, any observed correlation between stress change and magnitude would likely disappear. Therefore, we found no evidence that the amount of stress change controls the triggered earthquake magnitude. For

earthquakes occurring in stress-enhanced zones or in stress shadows, we calculated b-values of 0.9630 and 0.9845, respectively. The difference between the b-values, 0.0215, is insignificant at the 95% confidence interval.

3.8 Reverse Conditional Earthquake Distribution

For the binomial tests applied to the entire study area, we defined two test hypotheses: (1) given an earthquake, its location is more likely than not to be within a stress-enhanced zone, and (2) given a stress-enhanced zone, it is more likely to contain earthquakes. The second hypothesis takes into account the relative area for which the ΔCFF is positive. We categorized 0.05° by 0.05° cells by their stress change sign and whether or not they contained at least one receiver earthquake. We varied the time windows for the target and learning period intervals, testing one, five and eleven year windows, and tested the isolated Hector Mine earthquake stress field.

Contingency tables indicate that, for most combinations of stress type and receiver plane orientation, the majority of cells do not contain earthquakes and are located within stress shadows (Table 6). For most cases, a greater percentage of cells within stress-enhanced zones contain at least one earthquake. When isolating the Hector Mine earthquake stress field, we see earthquakes tending to nucleate in stress-enhanced zones during the target period rather than in the learning period for shorter target and learning period intervals, corroborating results from *Ogata et al.* [2003]. If we resolve stress changes onto uniformly oriented planes, earthquakes do not, with 95% confidence, occur more often in areas of positive stress change during the learning period. However, they do during the target period (Table 7). Stress-enhanced zones are significantly more likely to contain events during the target period than during the learning period, when resolving shear and Coulomb stress change onto fault-based and uniformly oriented planes (Table 8).

3.9 Discussion and Conclusions

In general, the simple hypothesis of *Deng and Sykes* [1997a,b], that southern California earthquakes tend to occur preferentially in where Coulomb stress has increased, has survived the test of time. They only resolved stresses onto uniformly oriented planes, but considering alternatives based on nearby fault orientation, averaged focal mechanisms of previous earthquakes, or focal mechanisms of the receiver earthquakes did not change the results substantially. The lack of improvement using more detailed receiver planes seems counter-intuitive, but perhaps the alternatives would show advantages if the stress calculations were more accurate.

We found that relative earthquake magnitudes do not vary much with cumulative Coulomb stress increment, and what variations we did observe were not consistent with the idea that increasing stress would result in larger magnitudes. Thus, the Coulomb stress influence appears local, near the hypocenter, rather than distributed over the rupture zone of an earthquake. For earthquake forecasting, one needs to know whether increased Coulomb stress will result in an increase in earthquake rate, which we observed following the Hector Mine event.

Our results depend on a multitude of assumptions regarding stress calculation, uniform physical parameters, and uniform slip distribution. For example, we assumed a uniform coefficient of friction, and that all ruptured materials are rheologically uniform and behave as a homogeneous elastic half space. We did not take pore fluid pressure into account, and we assumed that rupture plane physical properties do not change with depth, as might be expected from temperature and pressure variation. Without physical property variation with depth, there is no significant difference in our results when calculating stress changes at hypocentral earthquake depths or uniform 8km depths. Furthermore, aseismic stress accumulation rates may vary over

time due to events on neighboring faults [*Papadimitriou and Sykes*, 2001; *Luo and Liu*, 2012], affecting stress evolution. Coseismic stress sources just outside the study area boundaries may also contribute to the stress field and potential triggering threshold. We neglected postseismic stress changes from large events outside our study area which might trigger locations inside it [*Marzocchi and Selva*, 2003]. Including postseismic deformation may also improve correlation between Coulomb stress changes and earthquake location near faults [*Harris and Simpson*, 1998; *Nostro et al.*, 2001; *Viti et al.*, 2003; *Selva and Marzocchi*, 2005; *Freed et al.*, 2007]. Despite these enumerated simplifying assumptions, static Coulomb stress passes most statistical tests and shows potential in at least contributing to a prospective earthquake forecast.

Along the fault segments, unmodeled stress concentrations may partially explain earthquake clustering that sometimes occurs in apparent stress shadows [*Smith and Dieterich*, 2010]. To avoid selection bias, we did not decluster the earthquake catalog or impose a stress magnitude limit at earthquake hypocenters. For the binomial tests which required the average stress change in each cell of the study area, we imposed a ±2 MPa limit on stress at any given point within the cell, so one point located at a concentration would not significantly skew the average stress throughout.

Incomplete knowledge of the current stress field and stress evolution limits what we may infer from our results. Given a history of Pacific-North American plate strike-slip motion lasting millions of years, we know that the assumption of zero stress before 1812 is unrealistic, and that stress contributions not included in our calculations may have impacted recent seismicity. Local seismicity catalogs are certainly incomplete before 1812, and fault maps may omit many faults overlain by recent sediment deposits, or faults that do not break the surface. Additionally, we only considered $M \geq 5.8$ source earthquakes in our static ΔCFF field. However, *Parsons et al.*

[2012] suggest that large (M≥6.5) rupture planes yield a relatively strong association between stress change sign and earthquake location compared to smaller ruptures. Similarly, *Parsons and Segou* [2014] indicate that large receiver earthquakes yield improved stress-location association compared to smaller earthquakes. Approximating receiver earthquake rupture plane orientations with respect to general plate motion orientation, instead of a relatively short timespan of fault or earthquake data, may prove most effective in correlating stress change with earthquake location. Static stress contributions before 1812, not included in our study, may encourage fault displacement at receiver plane orientations similar to plate motion along the San Andreas fault. Stress estimates for the oldest included earthquakes, such as the 1812 Wrightwood and 1857 Fort Tejon earthquakes, are also highly uncertain. Rate-and-state stress evolution [*Dieterich and Kilgore*, 1996] may mitigate the effects of an incomplete stress field on earthquake forecasting, however, since observed seismicity appears to depend more on recent stress jumps, decaying in an Omori-like fashion.

Our assumption that all earthquakes within the southern California study area tend to nucleate on right-lateral receiver planes, while consistent with Deng and Sykes, may have resulted in false stress change values for some receiver earthquake locations. Most seismicity within southern California occurs along receiver planes similar to tectonic plate motion along the San Andreas Fault (northwest strike, right-lateral strike-slip). However, in areas like those near the Garlock fault, fault motion is left lateral strike-slip, striking northeast. Other areas, such as near the Oakridge fault, are characterized mainly by east-west striking thrust faults. Because we assume that right-lateral shear stress changes are always positive, areas with different faulting mechanisms may falsely display negative shear and Coulomb stress changes. The assumption may also have affected how we distinguished between the fault and auxiliary planes in the case

of fault-based and smoothed seismicity-based receiver plane orientation [*Hiemer et al.*, 2013]. The lack of association between normal stress change and earthquake location suggests a lower coefficient of friction than assumed, given prior evidence that seismicity distribution is dependent on normal stress change [*Parsons et al.*, 1999, 2002]. Pre-earthquake stress change distribution indicates that pre-earthquake static stress influences where a receiver earthquake nucleates, but not its size or length (Table 6). Our results suggest significant potential for earthquakes occurring before they reach their historical static stress maxima. The lack of an apparent earthquake triggering stress threshold [*Ziv and* Rubin, 2000] indicates that, even if a location is currently at maximum or minimum stress, how the stress change amount shapes earthquake likelihood is unknown.

3.10 Tables

Table 3.1: Percentage of Receiver Earthquakes in Stress-Enhanced Zones (EQ Depths)[a]				
	Uniform	**Seismicity**	**Fault**	**NP1**
Coulomb	66	59	65	77
Shear	66	62	65	65
Normal	50	44	56	78

[a] Percentages of receiver earthquakes that occur within stress-enhanced zones for each combination of stress change type and receiver plane orientation. "Uniform" means that the assumed receiver plane orientation is right-lateral strike-slip and strikes 321 degrees. "Seismicity" and "Fault" mean that the assumed receiver planes were derived from interpolated earthquake focal mechanisms and interpolated fault section orientations, respectively. "NP1" means that the stress was resolved onto the more favorable nodal plane of the receiver earthquake.

Table 3.2: Two-Tailed Binomial Test P-Values (Hypocentral EQ Depths)[a]				
	Uniform	**Seismicity**	**Fault**	**NP1**
Coulomb	1.0000	1.0000	1.0000	1.0000
Shear	1.0000	1.0000	1.0000	1.0000
Normal	0.6691	0.0000	1.0000	1.0000

[a] P-values for the hypothesis that earthquakes are equally likely to nucleate within stress-enhanced zones and stress shadows. For the two-tailed 95% confidence interval, p-values above 0.975 indicate that earthquakes are more likely to nucleate within stress-enhanced zones, whereas p-values below 0.025 indicate that earthquakes prefer stress shadows.

Table 3.3: Percentage of Receiver Earthquakes Occurring at Maximum Historic Stress: Hypocentral Depths[a]				
	Uniform	**Seismicity**	**Fault**	**NP1**
Coulomb	55	37	48	54
Shear	55	44	50	46
Normal	36	28	35	50

[a] Percentages of receiver earthquakes that occurred when total accumulated hypocentral stress since 1812 was at a maximum.

Table 3.4: Percentage of Earthquakes Occurring in Stress History Quartiles (Hypocentral Depths)[a]				
	Q1	**Q2**	**Q3**	**Q4**
Uniform, Coulomb	27	6	3	64
Uniform, Shear	30	3	3	63
Uniform, Normal	40	9	4	48
Seismicity, Coulomb	34	5	4	57
Seismicity, Shear	33	3	4	61
Seismicity, Normal	50	6	4	40
Fault, Coulomb	28	6	5	61
Fault, Shear	31	3	5	62
Fault, Normal	38	7	6	49
NP1, Coulomb	19	4	4	73
NP1, Shear	29	5	5	61
NP1, Normal	18	5	6	72

[a] Percentages of receiver earthquakes with pre-stress values in each quartile of their stress history according to their respective receiver plane pre-stress changes. Q1 corresponds to the lowest stress quartile, while Q4 corresponds to the greatest. "NP1" refers to the first set of nodal planes, or the nodal planes that yield greater positive Coulomb stress change at earthquake hypocenters.

Table 3.5: Median Stress Change (MPa) by Magnitude Quartile: M≥4.0 (Hypocenters)[a]				
	Q1	**Q2**	**Q3**	**Q4**
Uniform, Coulomb	0.121	0.132	0.085	**0.231**
Uniform, Shear	0.147	0.070	0.135	**0.228**
Uniform, Normal	-0.085	-0.039	**-0.009**	-0.114
Seismicity, Coulomb	0.092	0.084	**0.300**	0.099
Seismicity, Shear	0.153	0.079	0.144	**0.159**
Seismicity, Normal	-0.070	-0.181	**-0.036**	-0.252
Fault, Coulomb	**0.091**	0.076	0.036	0.036
Fault, Shear	**0.105**	0.094	0.079	0.057
Fault, Normal	-0.018	**0.018**	0.012	-0.130
NP1, Coulomb	0.378	0.288	**0.834**	0.482
NP1, Shear	0.138	0.034	**0.398**	0.176
NP1, Normal	0.566	0.437	**0.742**	0.635

[a] Median stress change for each magnitude quartile. The first quartile, "Q1," corresponds to the quartile with the lowest magnitudes, and the fourth quartile, "Q4," corresponds to the quartile with the largest magnitudes. "NP1" corresponds to the set of nodal planes that yields greater positive Coulomb stress change at earthquake hypocenters. The largest median pre-stress values for each set of magnitude quartiles are shown in bold font.

Table 3.6a: 1-Year Learning Period[a]			
	Positive	**Negative**	**Row Total**
Earthquake	55	66	121
No Earthquake	6724	9155	15879
Column Total	6779	9221	

Table 3.6b: 1-Year Target Period			
	Positive	**Negative**	**Row Total**
Earthquake	86	77	163
No Earthquake	6693	9144	15837
Column Total	6779	9221	

[a] Contingency tables categorizing study area cells according to the sign of the stress change caused by the Hector Mine earthquake, and whether or not they contain at least one earthquake. Both contingency tables represent Coulomb stress change resolved onto uniformly oriented planes during 1-year time intervals, using only the Hector Mine earthquake stress field. (a) Learning period (one year before Hector Mine earthquake). (b) Target period (one year after Hector Mine earthquake).

Table 3.7: P(positive|earthquake): Hector Mine Stress Field, 1-Year Learning Period[a]			
	Uniform	**Seismicity**	**Fault**
Coulomb	0.7825	0.9998	0.9912
Shear	0.6608	0.9999	0.9932
Normal	0.9653	0.9999	0.9997
P(positive|earthquake): Hector Mine Stress Field, 1-Year Target Period			
	Uniform	**Seismicity**	**Fault**
Coulomb	0.9970	1.0000	0.9999
Shear	0.9962	1.0000	0.9999
Normal	0.9904	1.0000	1.0000

[a] P-values for the null hypothesis that, given an earthquake, it is equally likely to occur in a stress-enhanced zone or stress shadow. P-values exceeding 0.9750 indicate that earthquakes, at the 95% confidence interval, are significantly more likely to nucleate in a stress-enhanced zone. P-values lower than 0.025 indicate that earthquakes, at the 95% confidence interval, are significantly more likely to nucleate in a stress shadow. Top: earthquakes within the learning period (one year before the Hector Mine earthquake). Bottom: earthquakes within the target period (one year after the Hector Mine earthquake).

Table 3.8: P(earthquake|positive): Hector Mine Stress Field, 1-Year Learning Period[a]			
	Uniform	**Seismicity**	**Fault**
Coulomb	0.7286	0.9933	0.9529
Shear	0.6338	0.8499	0.9554
Normal	0.9294	0.9962	0.9958

P(earthquake|positive): Hector Mine Stress Field, 1-Year Target Period			
	Uniform	**Seismicity**	**Fault**
Coulomb	0.9797	0.9980	0.9952
Shear	0.9798	0.9526	0.9937
Normal	0.9704	1.0000	0.9995

[a] P-values for the null hypothesis that, given a stress-enhanced zone or stress shadow, spatial seismicity rates do not depend on the sign of static stress change. P-values exceeding 0.9750 indicate that stress-enhanced zones, at the 95% confidence interval, have significantly greater seismicity rates than stress shadows. Top: earthquakes within the learning period (one year before the Hector Mine earthquake). Bottom: earthquakes within the target period (one year after the Hector Mine earthquake).

3.11 Figures

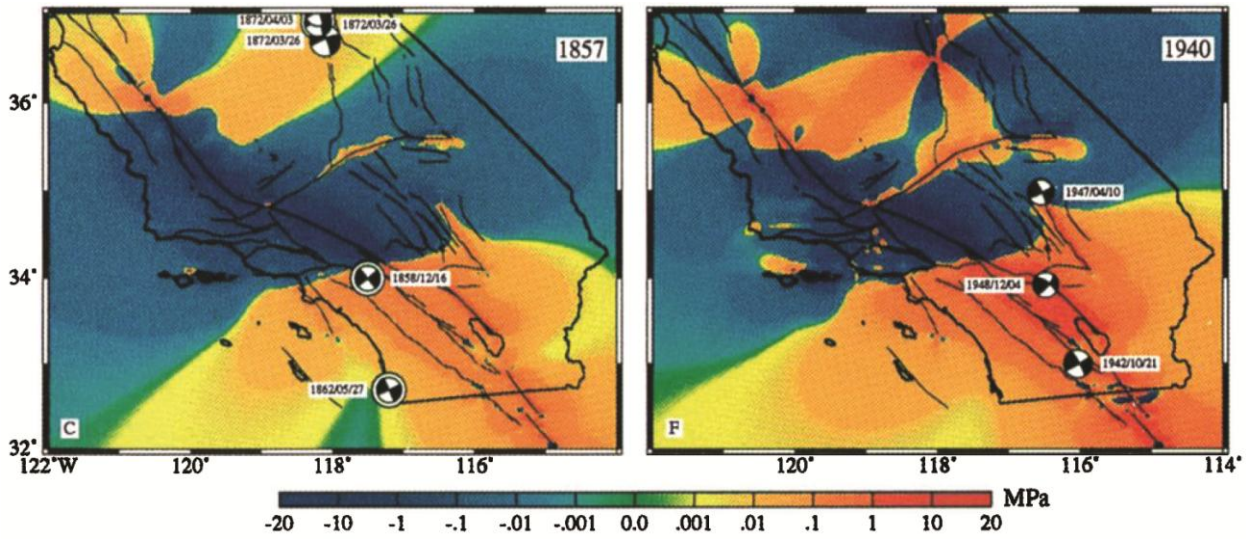

Figure 3.1: From the study by *Deng and Sykes* [1997a]. The figures display the cumulative ΔCFF fields from 1812 until just after the (left) 1857 Fort Tejon earthquake and (right) 1940 Imperial Valley earthquake. For these examples, Deng and Sykes calculated the stress field from uniform right-lateral strike-slip planes striking 321°. Red/yellow zones and blue zones represent areas where Coulomb stress increased and decreased, respectively. $M \geq 6$ focal mechanisms are displayed for each time interval, corroborating the association between earthquake location and stress-enhanced zones.

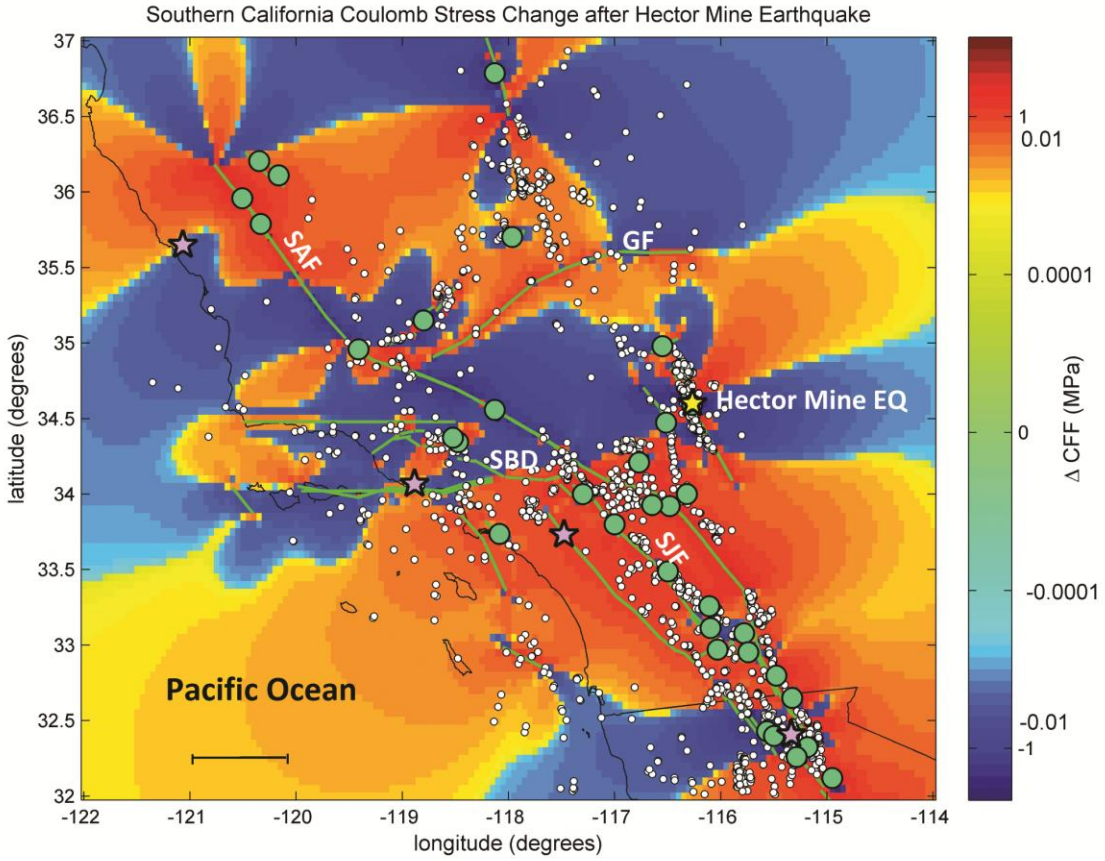

Figure 3.2: ΔCFF field calculated from uniform vertical, right-lateral strike-slip planes striking 321° just after the 1999 Hector Mine earthquake. Small white dots indicate locations of receiver earthquakes used in our study, large green dots indicate source earthquake locations, and green lines indicate faults. Major faults are labeled as follows: SAF = San Andreas Fault, SJF = San Jacinto Fault, GF = Garlock Fault, and SBD = San Bernardino Fault. Purple stars indicate locations where we calculated ΔCFF evolution, shown in Figure 3.3. The yellow star indicates the Hector Mine earthquake location.

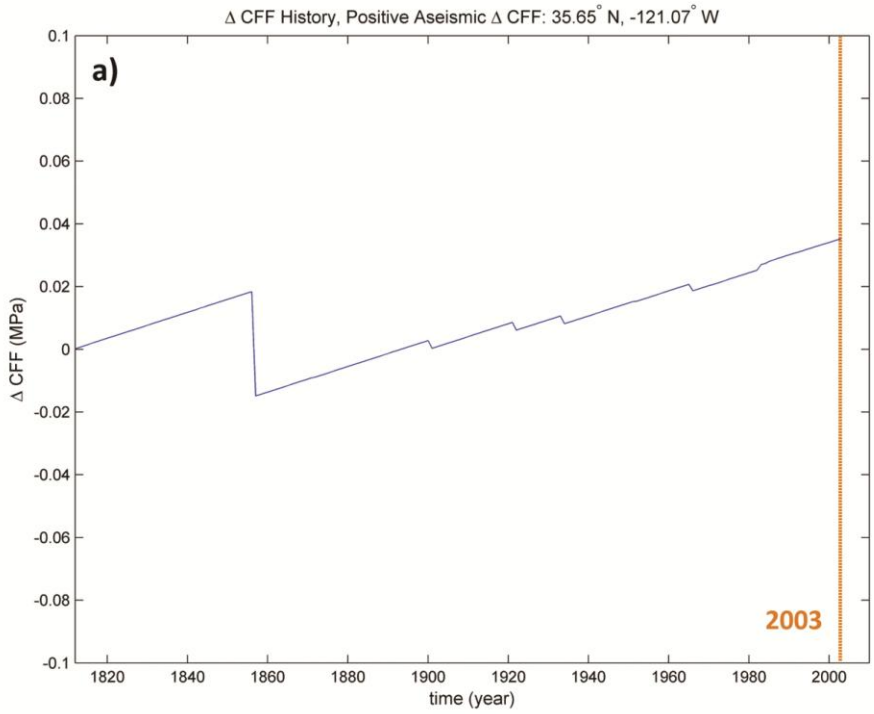
Δ CFF History, Positive Aseismic Δ CFF: 35.65° N, -121.07° W
a)
Δ CFF (MPa)
time (year)
2003

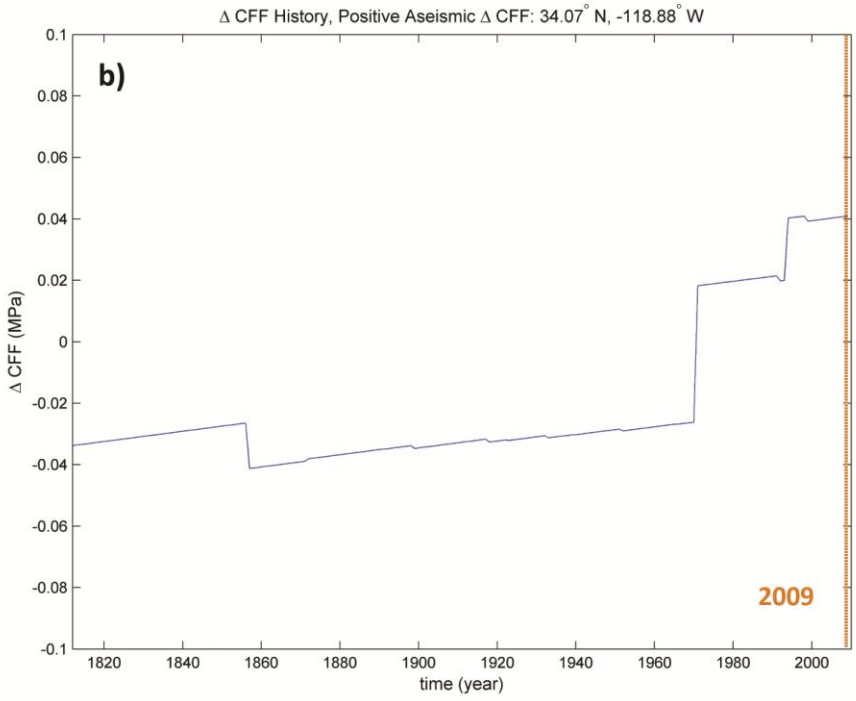
Δ CFF History, Positive Aseismic Δ CFF: 34.07° N, -118.88° W
b)
Δ CFF (MPa)
time (year)
2009

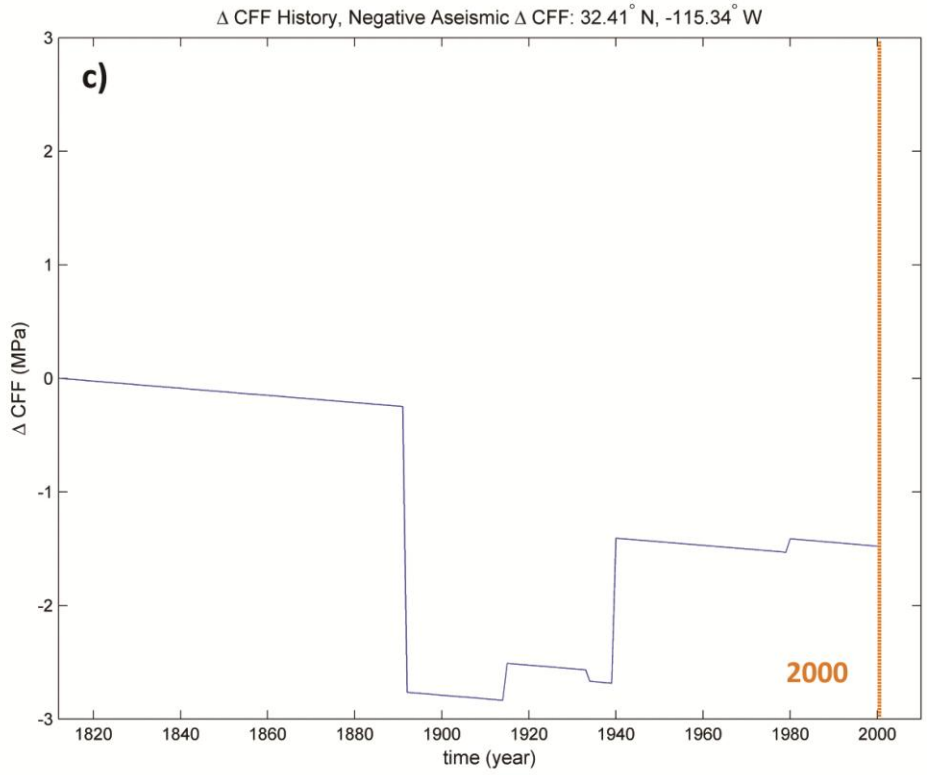
Δ CFF History, Negative Aseismic Δ CFF: 32.41° N, -115.34° W
c)
Δ CFF (MPa)
time (year)
2000
3
2
1
0
-1
-2
-3
1820
1840
1860
1880
1900
1920
1940
1960
1980
2000

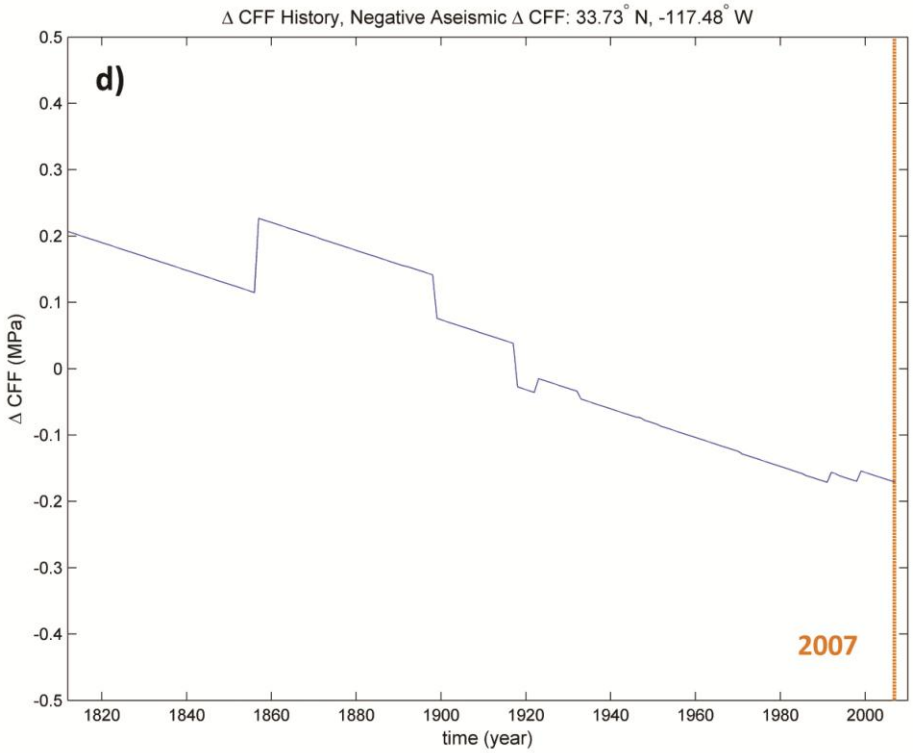
Δ CFF History, Negative Aseismic Δ CFF: 33.73° N, -117.48° W
d)
Δ CFF (MPa)
time (year)
2007
0.5
0.4
0.3
0.2
0.1
0
-0.1
-0.2
-0.3
-0.4
-0.5
1820
1840
1860
1880
1900
1920
1940
1960
1980
2000

Figure 3.3: Stress histories at receiver earthquake locations, using Coulomb stress resolved onto uniformly oriented planes. (a) Receiver earthquake located at 35.651° N latitude and -121.072° W longitude, where the aseismic stress rate is positive. The event occurred on 22 December 2003 near the rupture plane of the 1857 Fort Tejon earthquake and experienced a significant stress drop during that year. (b) Receiver earthquake located at 34.07° N latitude and -118.88° W, which occurred on 2 May 2009 in an area with a positive aseismic stress rate. The location experienced minor stress jumps during the 1971 San Fernando earthquake and the 1992 Landers earthquake. (c) Receiver earthquake occurring on 6 November 2000, located at 32.41° N latitude and -115.34° W longitude, where the aseismic stress rate is negative. The location experienced a significant stress drop following the 1892 Laguna Salada earthquake, as well as a stress jump following the 1940 Imperial Valley earthquake. (d) Receiver earthquake located at 33.73° N latitude and -117.48° W longitude, which occurred on 2 September 2007. The aseismic stress rate is negative, with multiple small stress perturbations and a stress jump following the 1858 San Bernardino earthquake.

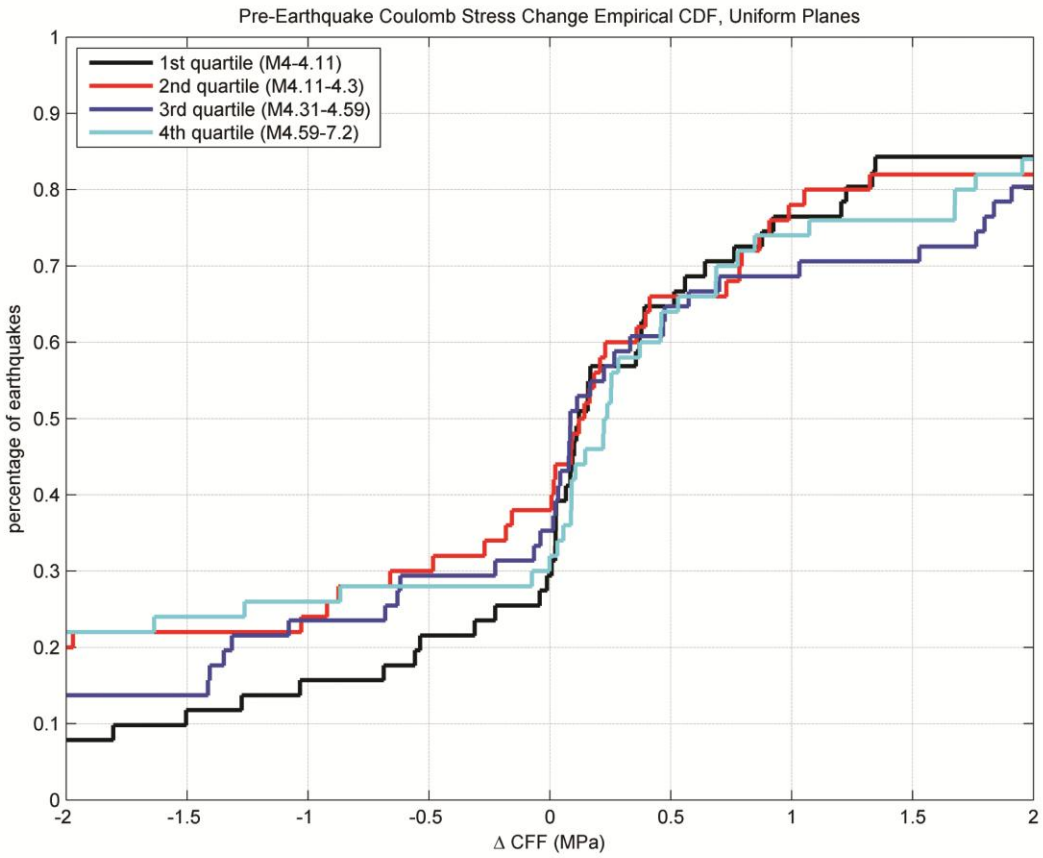

Figure 3.4: Cumulative fraction of $M \geq 4$ receiver earthquakes with respect to prestress for each magnitude quartile (magnitude ranges indicated in legend), plotted against pre-earthquake Coulomb stress change resolved onto uniformly oriented receiver planes, at hypocentral earthquake depths.

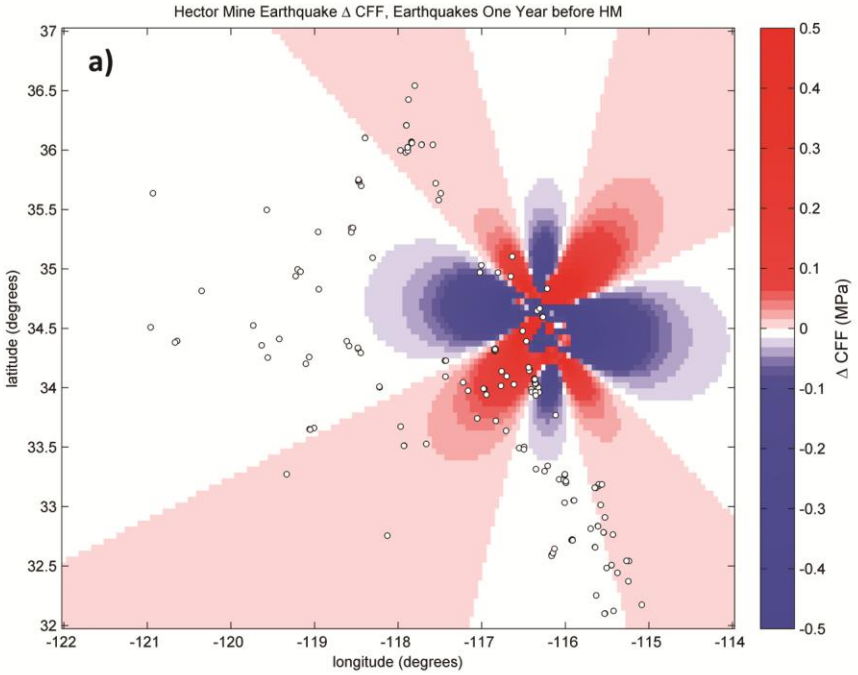

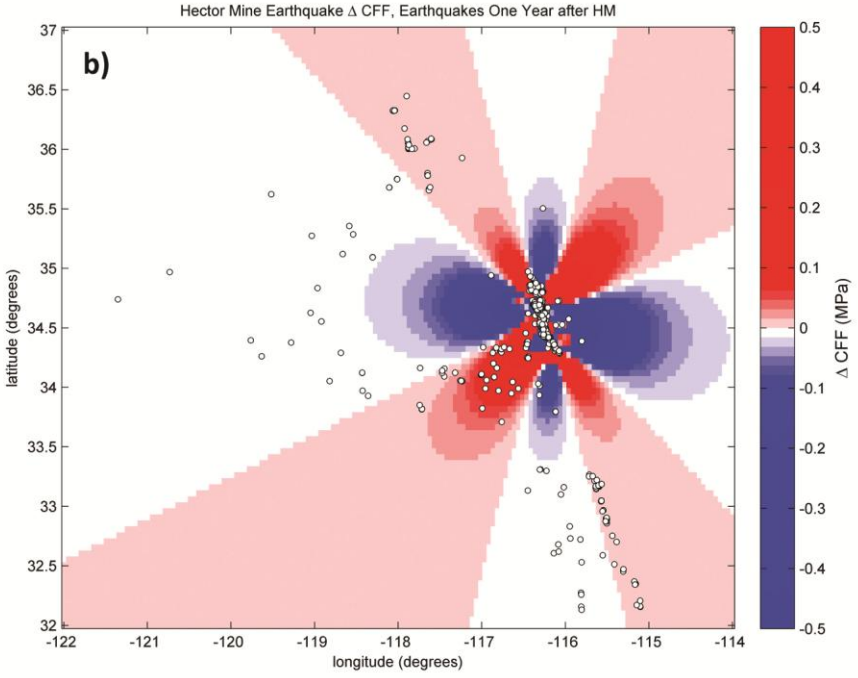

Figure 3.5: Static coseismic Coulomb stress change, resolved onto uniformly oriented receiver planes, following the 1999 Hector Mine earthquake. $M \geq 2.8$ earthquake locations during the (a) year before the Hector Mine earthquake and (b) year after the Hector Mine earthquake are displayed.

CHAPTER 4

Static Coulomb Stress-Based Southern California Earthquake Forecasts: a Pseudo-Prospective Test

4.1 Abstract

Many studies support the hypothesis that where earthquakes occur, recent changes in resolved Coulomb stress tend to be positive. How about the converse hypothesis, that where resolved Coulomb stress recently increased, earthquakes are more likely to occur? Successful earthquake forecasting by Coulomb stress changes requires the converse. To test this, we calculate stress everywhere in our study area, not just at earthquake locations. We model stress accumulation in southern California since 1812 from both the elastic effect of slip below locked faults and from M≥5 "source" earthquakes up to any given date. To minimize the effect of secondary aftershocks unrelated to the source earthquakes, we measure seismicity using a gridded binary map, in which a 0.1°x0.1° cell is activated if it contains one or more "receiver" earthquakes of magnitude 2.8 or larger. We then construct an empirical relationship between resolved Coulomb stress and seismicity within regions with similar stress values, defining probabilities of activated cells during the "test" period, within 11 years of the M7.1 Hector Mine earthquake. We find that the bias in future earthquake locations predicted by Coulomb stress changes exists, with 95% confidence. However, smoothed seismicity forecasts outperform Coulomb forecasts in most areas due to aftershock clustering. Most earthquakes tend to nucleate in areas with large Coulomb stress magnitudes (±0.5 MPa). Within areas with increased Coulomb stress from older earthquakes, fewer earthquakes occur than anticipated. The Coulomb

forecast may be improved by introducing quasi-static stress evolution, as well as combining the Coulomb stress and seismicity forecasts into a hybrid model.

4.2 Introduction

Retrospective and pseudo-prospective studies indicate a statistically significant association between earthquake location and the sign of static Coulomb stress change (Deng and Sykes, 1997a,b; and Stein et al., 1997):

$$CFF = \mu\sigma + \tau \tag{1}$$

where CFF is known as the Coulomb Failure Function, μ is the coefficient of friction, and σ and τ are the normal and shear stress, respectively, resolved onto an assumed fault plane. Deng and Sykes found that earthquakes tend to nucleate in areas where the instantaneous Coulomb Failure Function is positive at the time of the receiver event, and that seismicity rates increase in areas of increased ΔCFF following large earthquakes. They calculated ΔCFF, the cumulative change in CFF, at earthquake locations from 1812 until 1997, resolving combined tectonic and coseismic stress tensors onto uniformly oriented planes that approximated southern California tectonic plate motion. Stein et al. (1997) observed that nine out of ten M≥6.7 earthquakes within the North Anatolian fault occurred in areas of positive ΔCFF, when resolving stress tensors of previous events onto the focal mechanisms of current earthquakes. We extended Deng and Sykes' study, finding that most southern California earthquakes between the times of the 1999 Hector Mine and 2010 El Mayor Cucapah events occurred in areas of positive ΔCFF (Strader and Jackson, 2013). Such results are consistent for uniformly oriented planes, focal mechanisms,

and fault plane orientations based on smoothed seismicity and interpolated fault locations (Hiemer et al., 2013).

We further investigate the effects of static Coulomb stress changes on seismicity rates by deriving future earthquake rates from static Coulomb stress evolution. Although previous studies suggest that ΔCFF may at least partially control future earthquake locations, they do not estimate future seismicity rates that can be incorporated into a formal earthquake forecast. Similar to our previous research, we calculate the cumulative ΔCFF from the 1812 Wrightwood earthquake until and including the 1999 Hector Mine earthquake, resolving stress tensors onto uniformly oriented, northwest striking right-lateral strike-slip planes. We derive an empirical index function to determine earthquake probability from ΔCFF by quantizing the ΔCFF distribution, and calculating the fractional area of grid cells within each stress quantile that contain at least one earthquake during the eleven years preceding the Hector Mine earthquake.

To determine whether physics-based earthquake forecasts significantly improve upon those based purely on statistical seismology, we choose a smoothed seismicity earthquake forecast as our null hypothesis. We select the target period as the time interval between the Hector Mine and El Mayor Cucapah earthquakes, evaluating the locations of 2764 M≥2.8 receiver earthquakes. We define smoothed seismicity probabilities from M≥2.8 source earthquakes during the eleven year time interval before the Hector Mine event (Yang et al., 2010). If seismicity rates vary proportionally with ΔCFF (Harris, 1998; Harris, 2000; Ghisetti, 2000; King and Cocco, 2001; Papadimitriou, 2002; and Robinson, 2004), then spatial earthquake distribution should not be isotropic near source earthquakes, as smoothed seismicity-based earthquake probabilities would indicate.

4.3 Earthquake and Fault Selection

We defined our southern California study area similarly to Deng and Sykes' (1997a,b), encompassing the region from 32°-37°N latitude and 114°-122°W longitude (Figure 4.1). Our receiver earthquake catalog includes M≥2.8 events from the focal mechanism catalog compiled by Yang et al. (2010), from just after the 1999 Hector Mine earthquake until the 2010 El Mayor Cucapah earthquake. The earthquake catalog maintains a constant Gutenberg-Richter slope down to M=2.8, suggesting that the catalog is complete at that level. We calculated stress tensors from 98 aseismic fault sections with assumed uniform slip rates (Deng and Sykes, 1997a) and 141 M≥5 source earthquakes, 140 of which occurred prior to 1997, and were included in Deng and Sykes' study (1997b). For the Hector Mine earthquake, we calculated Coulomb stress changes from a slip distribution model by Ji et al. (2002), who assumed uniform slip on a collection of sub-parallel rectangular fault patches. We assumed that the earth's crust was homogeneous and isotropic, assigning the following constant physical parameters: 0.6 coefficient of friction, 0.25 Poisson's ratio, 33 GPa rigidity, and 82.5 GPa Young's modulus.

At a constant depth of 8km, we calculated average stress tensor components for each 0.1°x0.1° cell within the study area, and generated stress change field maps using the program Coulomb 3.3 (Lin and Stein, 2004; Toda et al., 2005). We then calculated Coulomb stress changes by resolving each stress tensor onto uniformly oriented right-lateral strike-slip planes striking 321°, using the Coulomb Failure Function:

$$\Delta CFF = \mu\Delta\sigma + \Delta\tau \qquad (2)$$

where μ is the coefficient of friction, Δσ the normal stress change on a pre-designated receiver plane, and Δτ the magnitude of shear traction, assuming right-lateral receiver planes. We calculated the normal and shear stress components as follows:

$$\sigma = \mathbf{S}\hat{\mathbf{n}} \cdot \hat{\mathbf{n}} \tag{3}$$

$$\tau = -\cos\theta\left(\mathbf{S}\hat{\mathbf{n}} \cdot \hat{\mathbf{t}}_1\right) - \sin\xi\left(\mathbf{S}\hat{\mathbf{n}} \cdot \hat{\mathbf{t}}_2\right) \tag{4}$$

where S is the stress tensor at a given location, $\hat{\mathbf{n}}$ is the unit vector normal to the assumed receiver fault, $\hat{\boldsymbol{t}}_1$ is the horizontal unit vector parallel to receiver fault strike, $\hat{\boldsymbol{t}}_2$ is the shear unit vector perpendicular to receiver fault strike but parallel to receiver fault dip, and ξ is the receiver fault rake angle. We defined the strike vector such that the fault always dips to the right (Aki and Richards, 2002). We calculated the unit vectors, using Cartesian coordinates, as follows:

$$\hat{\mathbf{n}} = \left(\cos\theta\sin\beta, -\sin\theta\sin\beta, \cos\beta\right) \tag{5}$$

$$\hat{\mathbf{t}}_1 = \left(-\sin\theta, -\cos\theta, 0\right) \tag{6}$$

$$\hat{\mathbf{t}}_2 = \left(\cos\theta\cos\beta, -\sin\theta\cos\beta, -\sin\beta\right) \tag{7}$$

where θ is the receiver fault strike and β is the receiver fault dip, within the $0° \leq \beta \leq 90°$ range.

We interpreted positive normal stress as tension, and positive shear stress as right-lateral (Aki and Richards, 2002). Faults and earthquake rupture surfaces were represented by

collections of rectangular patches with uniform slip rate or coseismic slip. We then used the program Coulomb 3.3, which implements the calculations described by Okada (1992) to sum the strain and stress tensors for all the patches. To promote the right-lateral slip characteristic of most southern California earthquake displacement, we modeled interseismic stress accumulation through the backslip projection method, introducing left-lateral aseismic (tectonic) displacement for all aseismic fault segments (Deng and Sykes, 1997a). Given that stress singularities occur at the ends of fault sections with uniform slip, we imposed a ± 2 MPa constraint on average stress change within each cell. Cumulative ΔCFF, faults, and source/receiver earthquake locations are shown in Figure 4.1.

4.4 Earthquake Probability Distributions

A successful prospective spatial earthquake forecast must not only be able to indicate future earthquake locations, but future areas of seismic quiescence. Therefore, instead of solely evaluating ΔCFF at receiver earthquake locations to derive earthquake probabilities, we took into account seismicity rates throughout the entire study area. For a 0.1°x0.1° resolution grid, we calculated the average cumulative ΔCFF in each cell just before the Hector Mine earthquake. If the ΔCFF in a cell was greater than 2 MPa or smaller than -2 MPa, we set the average ΔCFF to 2 or -2 MPa, respectively. We based earthquake probabilities on the locations of 4898 $M \geq 2.8$ earthquakes that occurred throughout the southern California study area during the "learning period" from 8/4/1988 until just before the Hector Mine earthquake. To mitigate the effects of aftershock clustering on the ΔCFF-based earthquake probability distribution, we only took into account whether or not at least one earthquake occurred in a given cell, rather than including the total number of earthquakes.

We divided the average ΔCFF distribution into 40 quantiles, each including 100 cells within the study area. Because most cells are located in the "far field", away from rupture zones, stress ranges decreased considerably near zero MPa compared to quantiles containing larger positive or negative ΔCFF magnitudes, but the area contained within each quantile did not vary. We calculated the fraction of activated cells (those that contained at least one receiver earthquake) in each stress quantile, assigning the resulting values as probabilities that a cell within a given ΔCFF range would contain at least one earthquake during the "test period" between the Hector Mine and El Mayor Cucapah earthquakes (Figure 4.2). For positive ΔCFF quantiles, we observed that the fractional area of activated zones increased monotonically with ΔCFF, as expected. Surprisingly, the activation rate also increased for increasingly negative ΔCFF. However, the probability distribution was asymmetrical. Overall, activation rates in positive ΔCFF quantiles exceeded those in negative ΔCFF quantiles, although we observed a similar pattern of increased earthquake probability with increasingly negative ΔCFF magnitude. Within stress-enhanced zones, 13.8% of cells contained at least one earthquake, whereas only 10.6% of cells contained at least one earthquake within stress "shadows" (Harris and Simpson, 1996). Previous studies corroborate these findings, indicating that aftershocks tend to occur in coseismic stress-enhanced zones (Ogata et al., 2003).

Defining our null hypothesis as the smoothed seismicity forecast, we calculated earthquake probabilities from 48 $M \geq 5$ earthquakes, from 1981 until the Hector Mine earthquake. To remain consistent with ΔCFF-based earthquake probabilities, we did not assign time decay to smoothed seismicity-based probabilities. We modeled earthquake probabilities as a function of distance from previous source earthquakes (Hiemer et al., 2013), such that expected seismicity rates were inversely proportional to distances from previous earthquakes:

$$k(r) = \frac{C}{r^2 + d^2} \tag{8}$$

where k is the seismicity rate contribution from one source event, r is the distance from a given location to that event, d is the smoothing kernel distance, and C is a normalizing constant. By measuring probability gain as a function of smoothing kernel distance, we determined that the optimal smoothing kernel distance was approximately 3 km by maximizing the probability gain, G:

$$G = \exp\left(\frac{\log(L) - \log(L_0)}{N}\right) \tag{9}$$

where log(L) is the log likelihood of the smoothed seismicity probability model, $\log(L_0)$ is the log likelihood of the uniform seismicity model, and N is the total number of receiver earthquakes. As for the ΔCFF-derived earthquake probabilities, we divided the smoothed seismicity-based earthquake rates into quantiles, assigning probabilities based on seismicity distribution during the learning period. Earthquake probability maps for ΔCFF and smoothed seismicity are displayed in Figures 4.3a and 4.3b, respectively.

4.5 Likelihood Testing

We tested static ΔCFF-based earthquake forecasts against those derived from smoothed seismicity, to evaluate whether physics-based earthquake forecasts were significantly more reliable than those based on statistics. Our null hypothesis stated that earthquake forecasts based

on ΔCFF did not indicate future earthquake locations more effectively than forecasts based on smoothed seismicity. By contrast, we defined an alternate hypothesis that ΔCFF-based earthquake forecasts significantly improved upon smoothed seismicity-based forecasts. We evaluated each forecast's ability to detect future earthquake locations by testing their ability to indicate 1) the number of "activated" zones containing at least one earthquake, and 2) the activated zones' locations. We based each test on a defined statistic, for which we compared observed seismicity with synthetic earthquakes constructed by both hypotheses. To evaluate the forecasts' relative performance throughout the study region, we calculated log likelihood ratios, or likelihood "residuals", for each cell.

To determine whether the observed number of activated zones during the test period was sufficiently similar to what each forecast would construct, we employed the "N-test," or "number of activated cells" test. We generated 1000 synthetic seismicity distributions, with each cell assigned as containing zero or at least one earthquake. For each cell within the study area, we generated a random probability between zero and one, comparing it to both forecasts' probabilities of the cell being filled during the test period. If the random probability was less than the calculated probability, we assigned the cell as containing at least one earthquake, and zero earthquakes if the random probability exceeded the calculated probability. Because of the hypotheses' potential to over- or under-estimate the number of filled zones, we chose a two-tailed test, defining the p-value as the percentage of synthetic seismicity distributions with fewer filled zones than observed. If $p \leq 0.025$, we rejected the hypothesis at the 95% confidence interval due to underestimating the number of filled zones, and overestimating the number of filled zones for $p \geq 0.975$. Both the ΔCFF and smoothed seismicity-based forecasts passed the N-test at the 95% confidence interval (Figure 4.4).

We based the spatial likelihood test, or "S-test," on the probability of a specific set of zones containing at least one earthquake. Similar to the N-test, we generated 1000 synthetic seismicity distributions each from ΔCFF- and smoothed seismicity-based probabilities of filled zones. For both the observed and synthetic seismicity distributions, we calculated the cumulative log likelihood, or "L" statistic:

$$L = \sum_{i=1}^{N'} c_i \ln(p_i) + \sum_{i=1}^{N'} (1 - c_i) \ln(1 - p_i) \quad (10)$$

where "L" is the log likelihood, "N' " is the total number of cells in the study area, "i" is the specified cell, "p" is the probability of the cell containing at least one earthquake, and "c" is equal to either zero or one, indicating whether we observed at least one earthquake in the cell during the test period (Rong et al., 2003). We defined a test statistic "p" as the percentage of synthetic log likelihood values exceeding the observed log likelihood. Because an observed log likelihood exceeding the majority of synthetic likelihood values indicates a deficiency of the forecast model, we chose a two-tailed test, rejecting either hypothesis at the 95% confidence interval if $p \leq 0.025$ or $p \geq 0.975$. With these criteria, we did not reject the ΔCFF-based forecast, but rejected the smoothed seismicity hypothesis at the 95% confidence interval, as the observed likelihood was far below the theoretical distribution approximated by the simulations (blue curve, Figure 4.5).

We investigated the spatial variation in each forecast's effectiveness during the test period by computing the log likelihood ratio, or residual, for each cell:

$$R_i = L_{1i} - L_{2i} = \ln\left(\frac{1-p_{1i}}{1-p_{2i}}\right) + c_i \ln\left(\frac{p_{1i}(1-p_{2i})}{p_{2i}(1-p_{1i})}\right) \quad (11)$$

where "R_i" is the log likelihood ratio in a given cell. "L_{1i}" and "L_{2i}" are log likelihood values in a given cell derived from the ΔCFF and smoothed seismicity forecasts, respectively. Similarly, "p_{1i}" and "p_{2i}" indicate probabilities of a given cell containing at least one earthquake based on ΔCFF and smoothed seismicity. A positive residual indicates that the ΔCFF forecast more reliably indicated seismicity during the test period than the smoothed seismicity forecast, and vice versa. Despite being rejected by the S-test, the smoothed seismicity-based forecast outperforms the ΔCFF-based forecast in most zones within the study area, as the observed cumulate log likelihood exceeds that of the ΔCFF-based forecast. Within the region encompassing the Northridge earthquake epicenter, the log likelihood residual is significantly negative, illuminating areas of recent aftershock clustering. However, the ΔCFF-based forecast more effectively locates the Hector Mine aftershock sequence, where ΔCFF is within 0.2-0.3 MPa. In the far field, log likelihood residuals are negligible, with the exception of far field earthquake locations, which are more likely to nucleate according to the ΔCFF-based earthquake forecast.

4.6 Discussion and Conclusions

Overall, the spatially varying Coulomb stress-based forecast consistently indicated earthquake locations between the Hector Mine and El Mayor Cucapah events, but the smoothed seismicity-based forecast did not. Earthquake clustering decreased the reliability of the ΔCFF-based forecast relative to the smoothed seismicity-based forecast in previous mainshock

locations, due to recent aftershock clustering from source earthquakes included in the seismicity model. Conversely, the smoothed seismicity-based model inadequately forecasted earthquakes within the far field, due to its small spatial kernel distance. At the 95% confidence interval, we rejected the smoothed seismicity-based earthquake forecast, but not the ΔCFF-based forecast, although smoothed seismicity proved more reliable in regions with mainshocks occurring several years prior to the test period.

We hypothesized that accumulated positive ΔCFF should bring faults closer to failure. Such an assumption suggests that positive coseismic stress changes should in turn trigger future earthquakes, while stress shadows delay or suppress them (Harris and Simpson, 1998). Although ruptured faults form stress shadows in most of the surrounding area, stress increases at the ends of fault sections, potentially triggering aftershock sequences. Strain discontinuities result from modeling fault dislocation on discretized patches, causing ΔCFF at the ends of fault sections to approach positive or negative infinity. Fault heterogeneities, which may further concentrate ΔCFF within small areas and indicate receiver earthquake magnitude (Heatherington and Steacy, 2007), are not adequately represented by current slip dislocation models. ΔCFF magnitude, though uncertain near fault sections, decays as a power law with distance from faults. Therefore, ΔCFF tends to forecast earthquakes more reliably in the far field. However, we observed a potential ΔCFF triggering threshold between 0.2-0.3 MPa where the probability of a zone containing earthquakes sharply increases (Figure 4.2). The peak in probability persisted when changing the number of ΔCFF quantiles from 40 to 16 or to 100, indicating that the increased probability was not an artefact of noise within the empirical ΔCFF distribution.

Some zones, typically near earthquakes long before 1997, had enhanced stress but low seismicity during the test period. Such zones were often the result of older events, such as the

1812 Wrightwood earthquake. A lack of earthquakes in areas of elevated, but not recent ΔCFF, provided potential evidence for postseismic deformation (Nostro et al., 2001, Marzocchi and Selva, 2003; Viti et al., 2003; Selva and Marzocchi, 2005; Freed et al., 2007), or stress relaxation, that should be incorporated into the stress model. Stress sources adjacent to study area boundaries may also influence seismicity rates within the study area. Either these stress contributions should be included in the stress model, or an auxiliary window should be defined within the study area where stress sources, but no receiver earthquakes, are considered in evaluating earthquake forecasts (Smith and Dieterich, 2010; Wang et al., 2010).

The smoothed seismicity earthquake forecast, though more reliable than the ΔCFF forecast near mainshocks during the learning period, also failed to consistently indicate receiver earthquake locations in far field regions. By changing the source earthquake magnitude threshold from $M \geq 2.8$ to $M \geq 5$ and using a consistent smoothing kernel distance of 3km, smoothed seismicity-based earthquake probabilities were concentrated within relatively small areas compared to the ΔCFF probability distribution. Earthquakes occurring more than ten years before the beginning of the target period were considered equally likely to trigger earthquakes as earthquakes occurring days before the time interval. Although many receiver earthquakes during the target period were clustered within areas where source earthquakes had occurred during the learning period, smoothed seismicity remained ineffective in forecasting receiver earthquake locations in areas of recently elevated ΔCFF. Therefore, a hybrid smoothed seismicity/ΔCFF may improve upon both the null and alternate hypotheses. The empirical ΔCFF-based earthquake probability distribution may be further improved by introducing rate/state seismicity evolution as a function of ΔCFF (Dieterich, 1996; Cocco, 2010). Rather than completely controlling seismicity rates, ΔCFF may act as a multiplier to variable

background seismicity rates, which may be represented through smoothed seismicity (Hainzl et al., 2010; Toda and Enescu, 2011).

A truly prospective ΔCFF-based earthquake forecast requires both prior knowledge of how stress change magnitude varies seismicity rates, and complete knowledge of the stress field itself. As Coulomb stress magnitudes become increasingly uncertain near faults, smoothed seismicity may contribute more to earthquake probabilities than Coulomb stress, and vice versa with increasing distance from faults. Earthquake locations that fall within stress shadows tend to be located near active faults, suggesting fault locations should be combined with ΔCFF in determining cell activation probabilities. Large areas of seismic quiescence within stress-enhanced zones indicate that recent stress evolution should exert a greater influence on seismicity rates, compared to coseismic static stress from older earthquakes. Within the smoothed seismicity-based forecast, recent earthquakes may also be associated with elevated seismicity rates, according to the Omori power law for aftershock sequence decay. Based on log likelihood residual variation with time since previous mainshocks, we conclude that Coulomb stress variation significantly alters aftershock rates from what smoothed seismicity models would forecast.

4.7 Figures

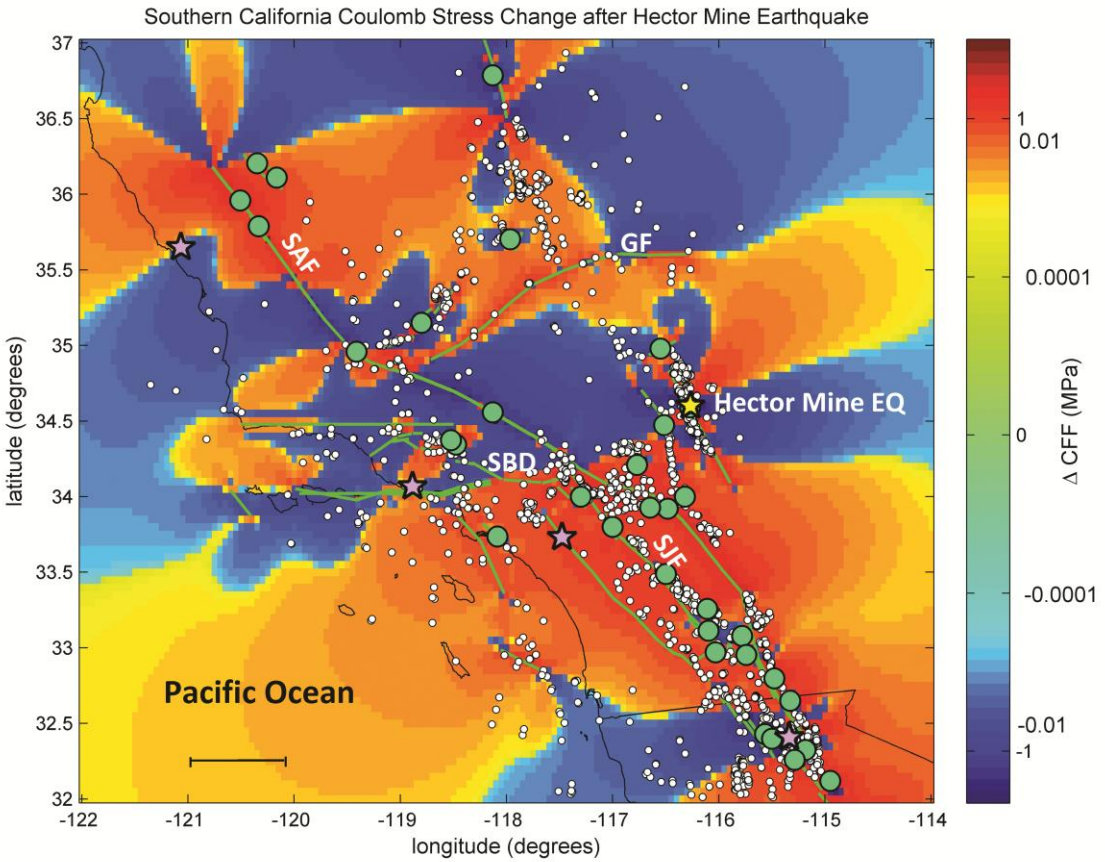

Figure 4.1. ΔCFF field calculated from uniform vertical, right lateral strike-slip planes striking 321° just after the 1999 Hector Mine earthquake. Small white dots indicate locations of receiver earthquakes used in our study, large green dots indicate source earthquake locations, and green lines indicate faults. Major faults are labeled as follows: SAF = San Andreas Fault, SJF = San Jacinto Fault, GF = Garlock Fault, and SBD = San Bernardino Fault. Purple stars indicate locations where we calculated ΔCFF evolution, shown in Figure 3 of Strader and Jackson (2013). The yellow star indicates the Hector Mine earthquake location.

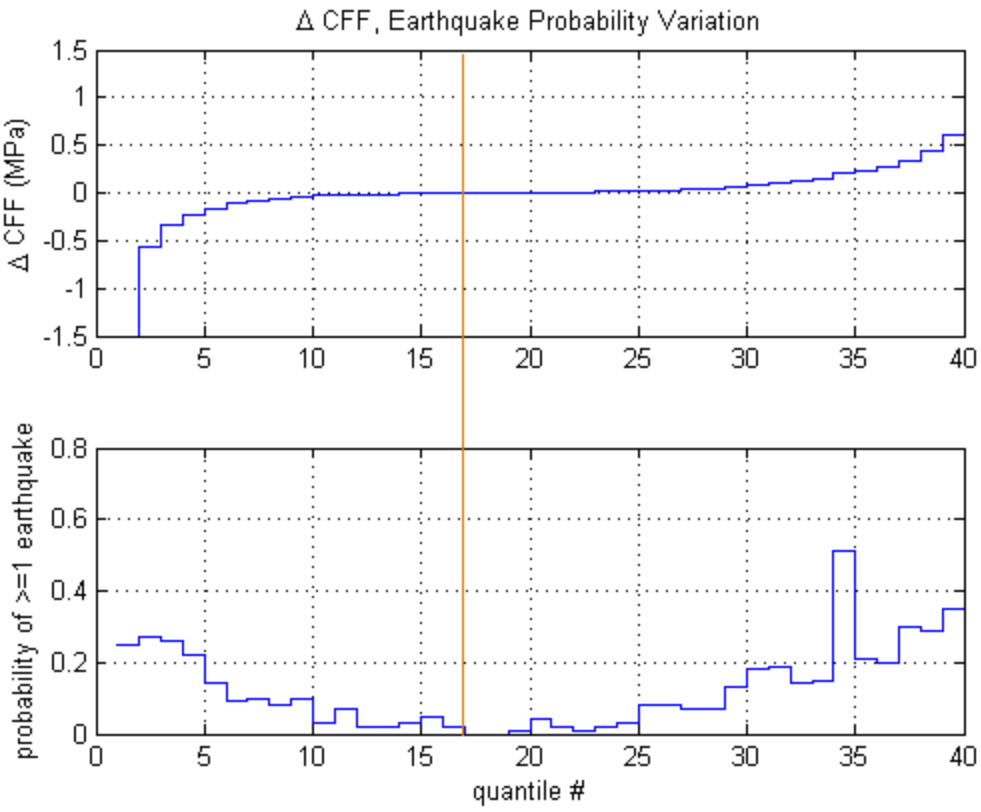

Figure 4.2. Top: ΔCFF bounds for each stress quantile. Bottom: Probability of a cell within each ΔCFF quantile containing at least one earthquake. The orange line marks the seventeenth ΔCFF quantile, within which ΔCFF = 0.

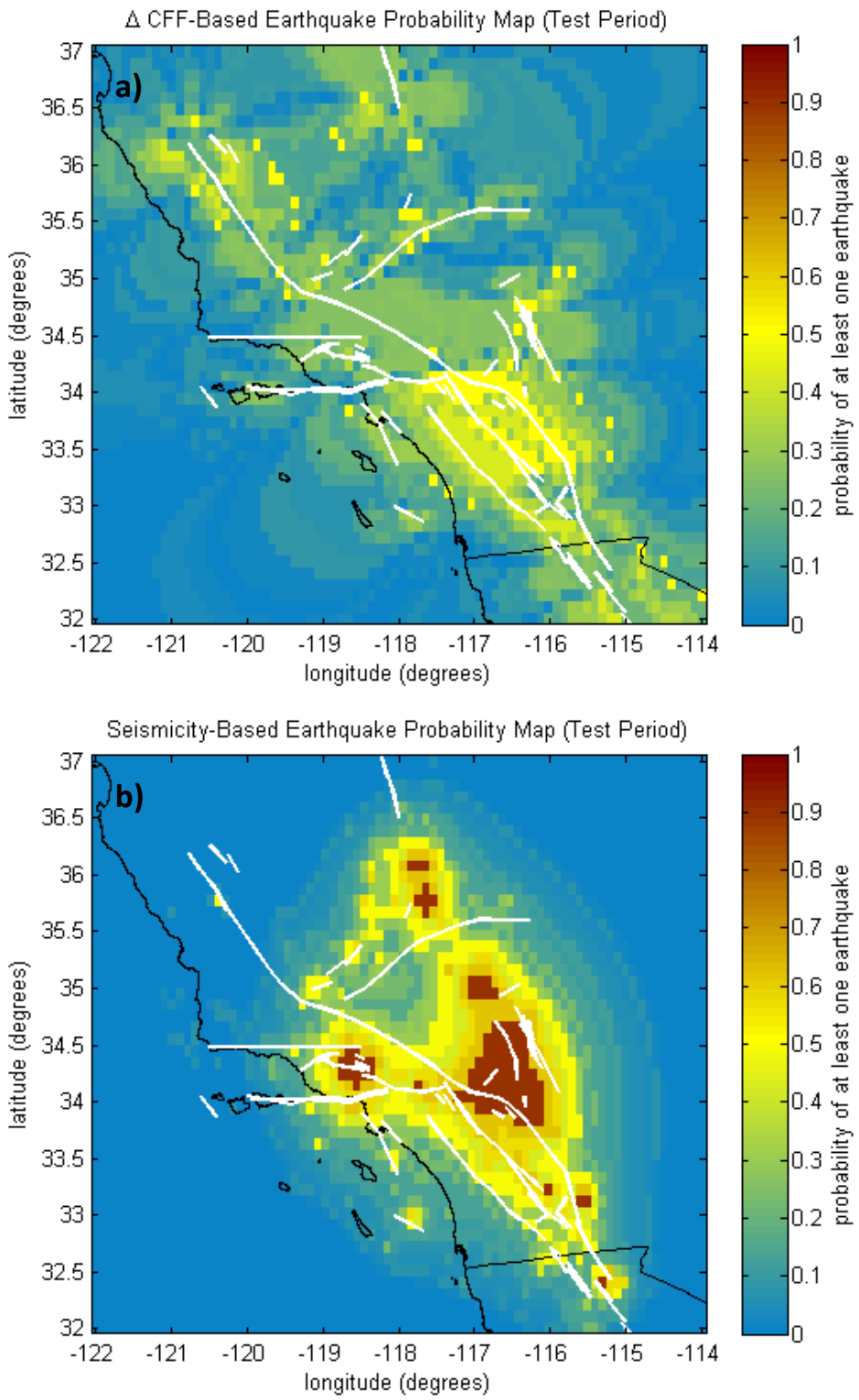

Figure 4.3: Probabilities of each cell containing at least one earthquake for earthquake forecasts based on a) ΔCFF and b) smoothed seismicity. White lines indicate major fault locations, similar to those in Figure 1.

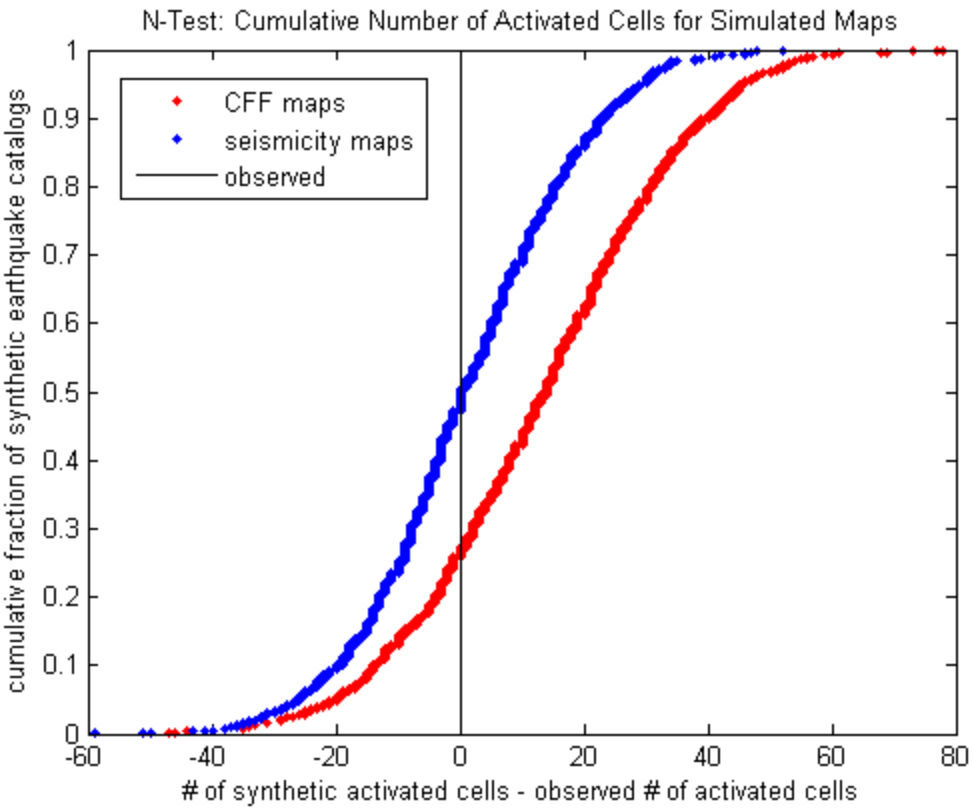

Figure 4.4. N-test results for ΔCFF-based and smoothed seismicity-based earthquake forecasts. The x-axis displays the difference between the number of activated cells in the synthetic and observed earthquake maps. The black line indicates where the number of activated cells is equal to the observed number (N = 0). The red and blue curves display the cumulative fraction of synthetic earthquake catalogs by ascending number of activated cells, constructed from ΔCFF and smoothed seismicity probabilities, respectively.

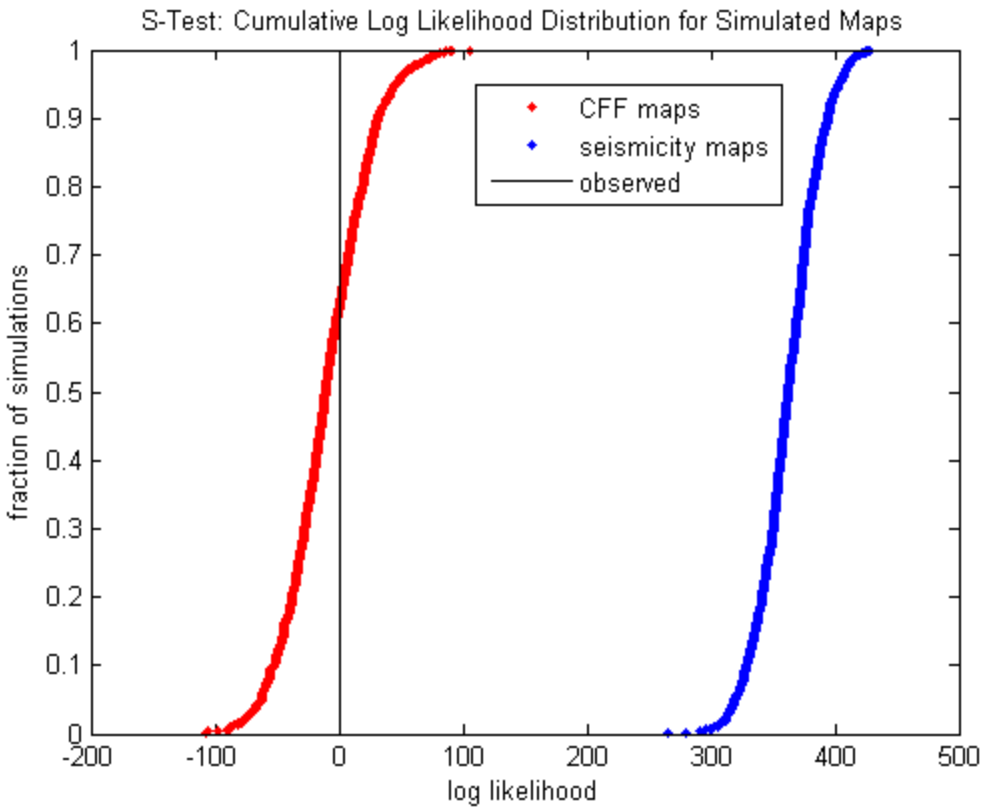

Figure 4.5. S-test results for ΔCFF-based and smoothed seismicity-based earthquake forecasts. The x-axis displays the difference between the log likelihood scores in the synthetic and observed earthquake maps. The black line indicates where the difference between the synthetic and observed log likelihood scores is zero. The red and blue curves display the cumulative fraction of synthetic earthquake catalogs by ascending log likelihood, constructed from ΔCFF and smoothed seismicity probabilities, respectively.

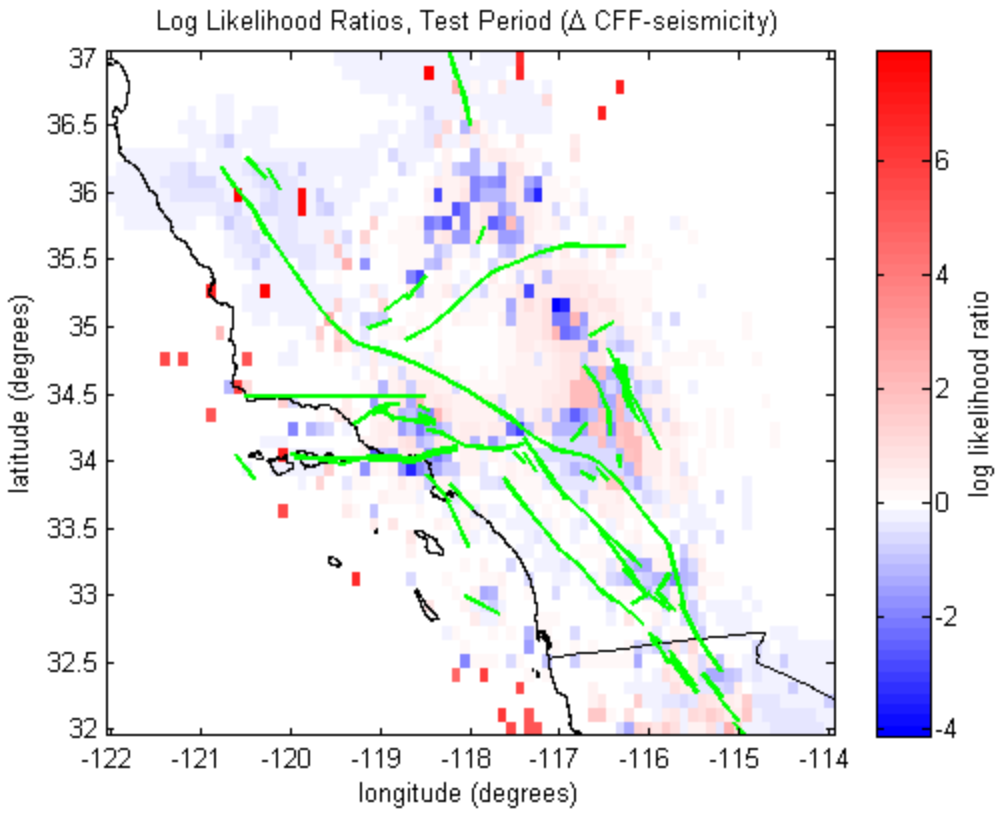

Figure 4.6. Spatial log likelihood residual map, displaying the difference between log likelihood values calculated from ΔCFF- and smoothed seismicity-based earthquake forecasts. Red areas indicate where the ΔCFF based forecast outperforms the smoothed seismicity forecast, and are prominent in the far field and near the Hector Mine earthquake epicenter. Blue areas display where smoothed seismicity more effectively indicates earthquake locations during the test period, which is the case for areas near mainshocks occurring before the Hector Mine earthquake. White regions indicate a negligible difference between the two forecasts' reliability. Green lines outline the major faults displayed in Figure 1.

CHAPTER 5

Testing Assumptions

5.1 Forecasting Time-Independent Spatial Seismicity Rates

In Chapter 4, I presented a spatial earthquake forecast of cell activation probabilities, or the probabilities of cells containing at least one earthquake, as a function of cumulative ΔCFF. Here, I tested a pseudo-prospective forecast that takes into account varying seismicity rates among activated cells. Using the same tectonic and coseismic stress sources as in Chapter 4, I chose a test period from just after the 1999 Hector Mine earthquake to just before the 2010 El Mayor Cucapah earthquake, and a learning period including the 11 years before the Hector Mine earthquake. To determine whether Coulomb stress-based forecasted seismicity rates significantly improve upon those based on historical seismicity, I chose a smoothed seismicity earthquake forecast as my null hypothesis, consistent with the activated cell forecast.

I assigned two criteria to the Coulomb stress-based probability density function: 1) earthquake probabilities must be between zero and one, but never equal to zero and one, and 2) earthquake probability must increase monotonically with ΔCFF. First, I calculated the average ΔCFF within each cell of the study area from points at 0.05° intervals. If the static ΔCFF at a point exceeded 2MPa (20 bars) or drops below -2 MPa (-20 bars), I assigned a value of 2 or -2 MPa, respectively. For each cell, I counted the number of receiver earthquakes between the Hector Mine and El Mayor earthquakes, and fit the number of earthquakes vs. static ΔCFF to an arctangent index function (Figure 5.1 and Chapter 2, Equation 7). I then normalized the earthquake probability distribution such that the total probability over the study area was equal to

one. To best fit the function to the earthquake data, I optimized the function's median and width through maximizing a likelihood function explained in Chapter 2, Equation 8. The optimization yielded a function median of 0.16 MPa and a function width of 0.18 MPa (Chapter 2, Figure 2.1).

Likewise, I calculated smoothed seismicity probabilities from 48 $M \geq 5$ earthquakes, from 1981 until and including the Hector Mine earthquake. To remain consistent with ΔCFF-based earthquake probabilities, I did not assign time decay to smoothed seismicity-based probabilities. I modeled earthquake probabilities as a function of distance from previous source earthquakes (Hiemer et al., 2013; Ogata et al., 2013; Kagan, 2009) such that the probability of a future earthquake was inversely proportional to distance from previous earthquakes (Chapter 2, Equation 13). To optimize the function to best represent seismicity distribution as a function of source earthquake distance, I maximized the function's probability gain (Chapter 2, Equation 14). Earthquake probability maps for ΔCFF and smoothed seismicity are displayed in Figure 5.2.

I evaluated both forecasts using the similar methods to those applied to cell activation forecasts (Chapter 4), for both the original and declustered receiver earthquake catalog (the declustering method is described in Chapter 2). Because I took into account spatially-varying seismicity rates instead of whether or not a cell contains at least one receiver earthquake, I evaluated the log likelihood score using Equation 55 (Chapter 2). My null hypothesis stated that earthquake forecasts based on ΔCFF do not indicate future earthquake locations more effectively than forecasts based on smoothed seismicity. By contrast, I defined an alternate hypothesis that ΔCFF-based seismicity rate forecasts significantly improved upon smoothed seismicity-based forecasts. I defined a critical value for each forecast, p, as the percentage of synthetic log

likelihood scores below the observed log likelihood. Appling a one-tailed spatial likelihood test (S-test), I rejected either hypothesis at the 95% confidence interval if $p < 0.05$. Under such criteria, both forecasts fail the S-test, regardless of whether or not the earthquake catalog was declustered (Figures 5.3 and 5.4, respectively).

I also employed the log likelihood ratio test (R-test) to evaluate the probability of falsely rejecting the smoothed seismicity forecast in favor of the ΔCFF forecast, or vice versa. Similar to the S-test, I defined my test statistic, p, as the percentage of R values below the log likelihood ratio calculated from receiver earthquakes. For a one-tailed test at the 95% confidence interval, I rejected the smoothed seismicity forecast in favor of the ΔCFF forecast if $p < 0.95$ for the synthetic ΔCFF earthquakes, and vice versa if $p > 0.95$ for the synthetic smoothed seismicity events. The S-test and R-test procedures are explained in more detail in Chapter 2. For both the original and declustered receiver earthquake catalogs, I rejected ΔCFF in favor of smoothed seismicity at the 95% confidence interval (Figures 5.5 and 5.6, respectively), as well as rejected smoothed seismicity in favor of ΔCFF. Although the smoothed seismicity forecast failed the S-test while the ΔCFF forecast did not, the log likelihood for observed events was greater when evaluated from smoothed seismicity probabilities. There was a nearly zero percent chance of a Type I error for either forecast as shown in the cross-likelihood plots (Figures 5.5 and 5.6); therefore, the R-test results were inconclusive regarding the relative effectiveness of each forecast.

Neither the ΔCFF nor smoothed seismicity-based forecasts proved reliable indicators of future seismicity rates, at the 95% confidence interval. Additionally, the ΔCFF forecast was significantly less indicative of future earthquake locations and seismicity rates than the smoothed seismicity forecast. While declustering the receiver earthquake catalog improved consistency

between earthquake locations and ΔCFF probability distribution, it also improved consistency with smoothed seismicity probabilities. Therefore, declustering had no discernible effect on the relative effectiveness of either forecast.

I hypothesized that accumulated positive ΔCFF should bring faults closer to failure. Such an assumption suggests that positive coseismic stress changes should in turn trigger future earthquakes, while stress shadows delay or suppress them (Harris and Simpson, 1998). Although ruptured faults decreased ΔCFF, forming stress shadows in most of the surrounding area, stress increased at the ends of fault sections, potentially triggering aftershock sequences. Strain discontinuities resulted from modeling fault dislocations on discretized patches, causing ΔCFF at the ends of fault sections to approach physically impossible quantities. Furthermore, fault heterogeneities may have concentrated ΔCFF within asperities not accurately modeled by fault dislocation patches (Heatherington and Steacy, 2007). Therefore, I hypothesized that ΔCFF more reliably forecasts seismicity rates and earthquake locations in the far field, rather than aftershock clusters, as shown by the increase in log likelihood when declustering the receiver earthquake catalog (Figure 5.7).

Although I did not identify a specific threshold at which ΔCFF triggers earthquakes, I observed that most earthquakes occurred within areas with small, positive ΔCFF, as described in Chapter 3. The arctangent function I chose not only poorly fit the ΔCFF/receiver earthquake distribution after optimization, but implied that maximum earthquake probability corresponds to maximum ΔCFF. There also existed large, seismically quiescent stress-enhanced zones that lowered the ΔCFF-based log likelihood, rendering the forecast ineffective compared to the smoothed seismicity forecast. Stress in such zones might have been relaxed by viscoelastic or plastic deformation, causing a difference between observed and expected seismicity rates.

5.2 Hybrid Spatially-Dependent Earthquake Forecast

I observed a tradeoff in relative forecast reliability with distance from fault sections. Smoothed seismicity more accurately indicated earthquake locations near faults, whereas ΔCFF more accurately indicated earthquake locations in the far field. Therefore, a hybrid smoothed seismicity/ΔCFF probability model may improve upon either forecast alone. The index function anticipated sharp increases in seismicity rates with ΔCFF, which I did not consistently observe. Therefore, the function may be improved by combining the smoothed seismicity probability distribution as a function of fault distance.

Here, I tested the effects of large stress uncertainties near fault sections through optimizing hybrid earthquake probabilities as a function of distance to the nearest fault section, where smoothed seismicity was given more weight near faults and Coulomb stress was given more weight in the far field. Similar to previous research, the resulting earthquake probability distributions were evaluated with both the original and declustered receiver earthquake catalogs (Figure 5.8). I defined hybrid earthquake probabilities as a linear combination of Coulomb stress-based and smoothed seismicity-based earthquake probabilities, as explained in Chapter 2 (Equation 62). Using an arctangent index function to calculate the mixing parameter as a function of minimum cell-fault distance, I optimized the function as described by Equation 63 in Chapter 2. To determine how earthquake clustering influenced the relative effectiveness of each forecast, I optimized the mixing parameter using both the original and declustered earthquake catalogs.

Declustering the receiver earthquake catalog significantly altered the relative effectiveness of ΔCFF and smoothed seismicity-based probabilities, given distance from the

nearest fault (Figure 5.9). A pure smoothed seismicity-based model best fit the complete earthquake catalog with no declustering (Figures 5.10a,5.11), whereas the best fit to the declustered catalog was a combination of smoothed seismicity-based probabilities near faults and Coulomb stress-based probabilities in the far field (Figures 5.10b,5.11). When using the declustered earthquake catalog, Coulomb stress controlled most of the earthquake probability distribution at 50 km or greater distances from faults (Figure 5.11). Given stress uncertainties near the ends of fault patches, smoothed seismicity was consistently the more reliable indicator of seismicity rates and future earthquake locations in areas near faults.

I tested the dependence of forecast effectiveness on distance to the nearest fault by calculating two information scores, the "success" and "specificity" statistics (Kagan, 2009), as a function of mixing parameter values (Chapter 2, Equations 60-61). In doing so, I kept the mixing parameter constant throughout the study area, disregarding cell-fault distance at any given location. When not taking into account cell-fault distance, the smoothed seismicity forecast best fit both the complete and declustered earthquake catalogs (Figure 5.9). Because the smoothing kernel distance for the ΔCFF-based earthquake forecast exceeded the optimal kernel distance for the smoothed seismicity forecast (Equation 14), earthquake probability was concentrated in smaller areas (Figure 5.7). Receiver earthquakes tended to nucleate in areas of mid- to high probability, though a significant percentage did not avoid areas of low probability, and the earthquake aftershock cluster locations heavily influenced the relative effectiveness of Coulomb stress and smoothed seismicity-based earthquake forecasts. Earthquake clusters often occurred close to fault sections, encouraging purely smoothed seismicity earthquake forecasts over hybrid forecasts, and therefore have the potential to bias hybrid forecast optimization results regardless of their proximity to major fault sections.

5.3 Figures

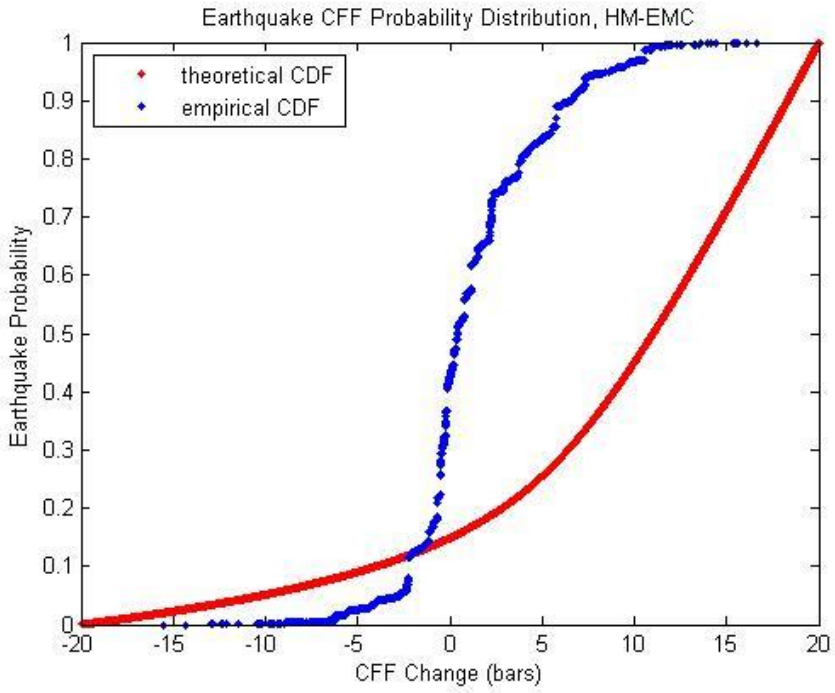

Figure 5.1: Theoretical and empirical cumulative seismicity with ascending ΔCFF. The blue curve displays observed cumulative seismicity with ΔCFF, and the red curve displays cumulative seismicity derived from the arctangent index function. The index function anticipates that seismicity rates increase monotonically with ΔCFF, whereas most observed seismicity occurs at small, positive ΔCFF values.

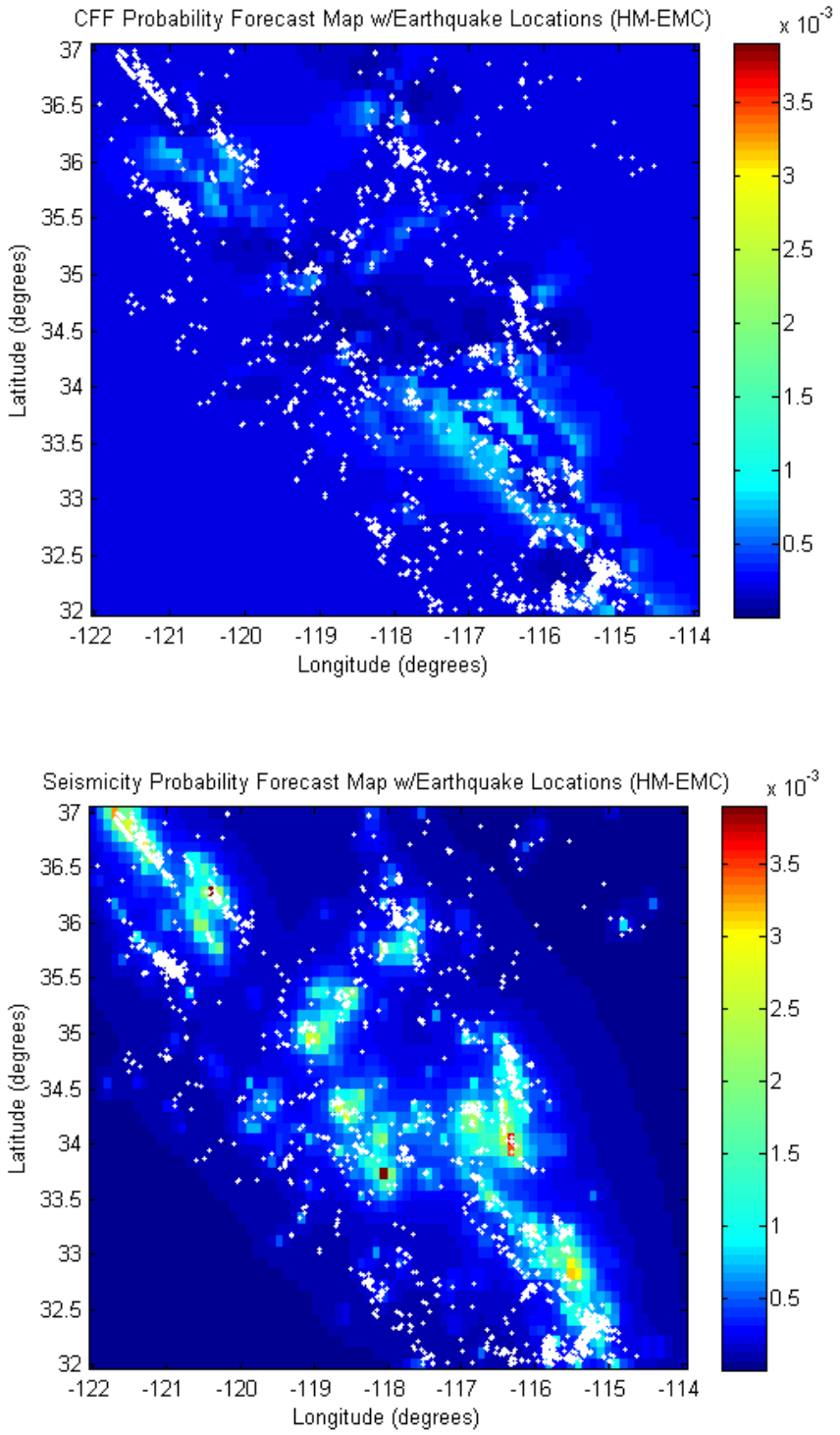

Figure 5.2: Normalized probability forecast maps for ΔCFF-based probabilities (top) and smoothed seismicity-based probabilities (bottom). Red and yellow regions indicate areas of high seismicity rates, light blue areas indicate areas of moderate seismicity, whereas dark blue regions denote regions with low expected seismicity rates. White dots display receiver earthquake epicenter locations.

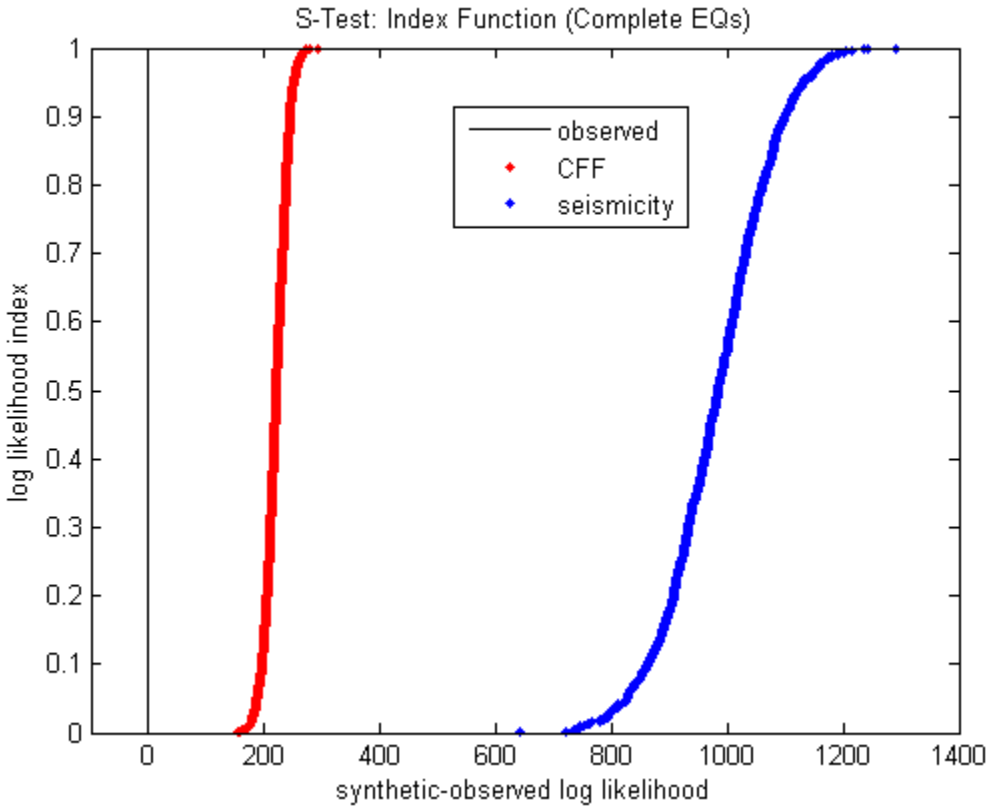

Figure 5.3: S-test results, using the complete receiver earthquake catalog, for ΔCFF-based earthquake probabilities (red curve) and smoothed seismicity-based probabilities (blue curve). The red and blue curves represent cumulative differences between synthetic and observed log likelihood scores, and the black line indicates where the synthetic and observed log likelihood scores are equal.

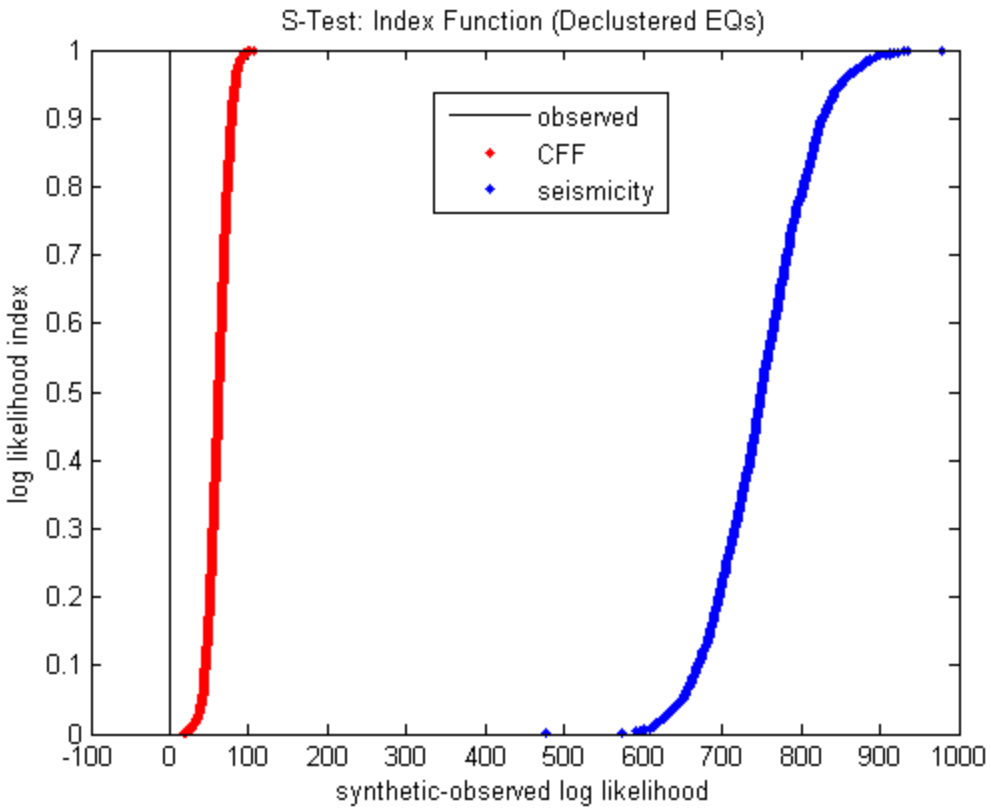

Figure 5.4: S-test results, using the declustered receiver earthquake catalog, for ΔCFF-based earthquake probabilities (red curve) and smoothed seismicity-based probabilities (blue curve). The red and blue curves represent cumulative differences between synthetic and observed log likelihood scores, and the black line indicates where the synthetic and observed log likelihood scores are equal.

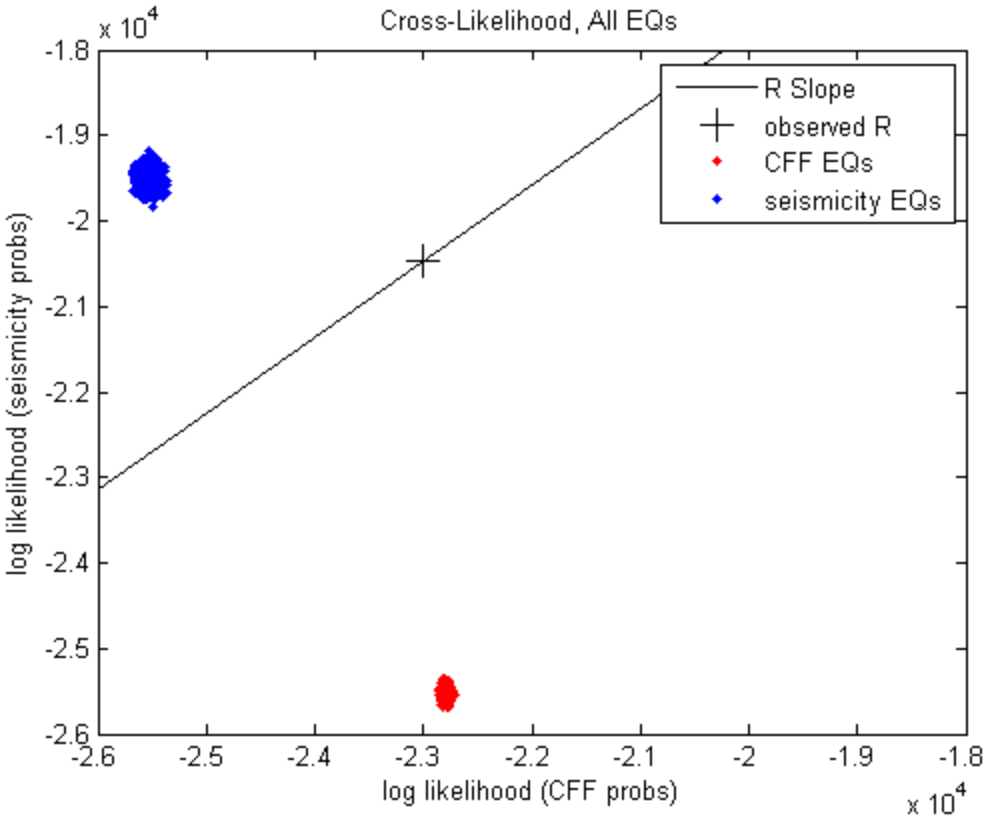

Figure 5.5: Cross-likelihood plot displaying R-test results from the complete receiver earthquake catalog. The x-axis displays log likelihood values calculated from ΔCFF-based earthquake probabilities, while the y-axis displays log likelihood values calculated from smoothed seismicity-based earthquake probabilities. Log likelihood values for ΔCFF and smoothed seismicity-based synthetic earthquake catalogs are shown by red and blue dots, respectively. The black cross indicates log likelihood values corresponding to the receiver earthquake catalog, while the black line plots all possible log likelihood combinations given the R-value derived from receiver earthquakes.

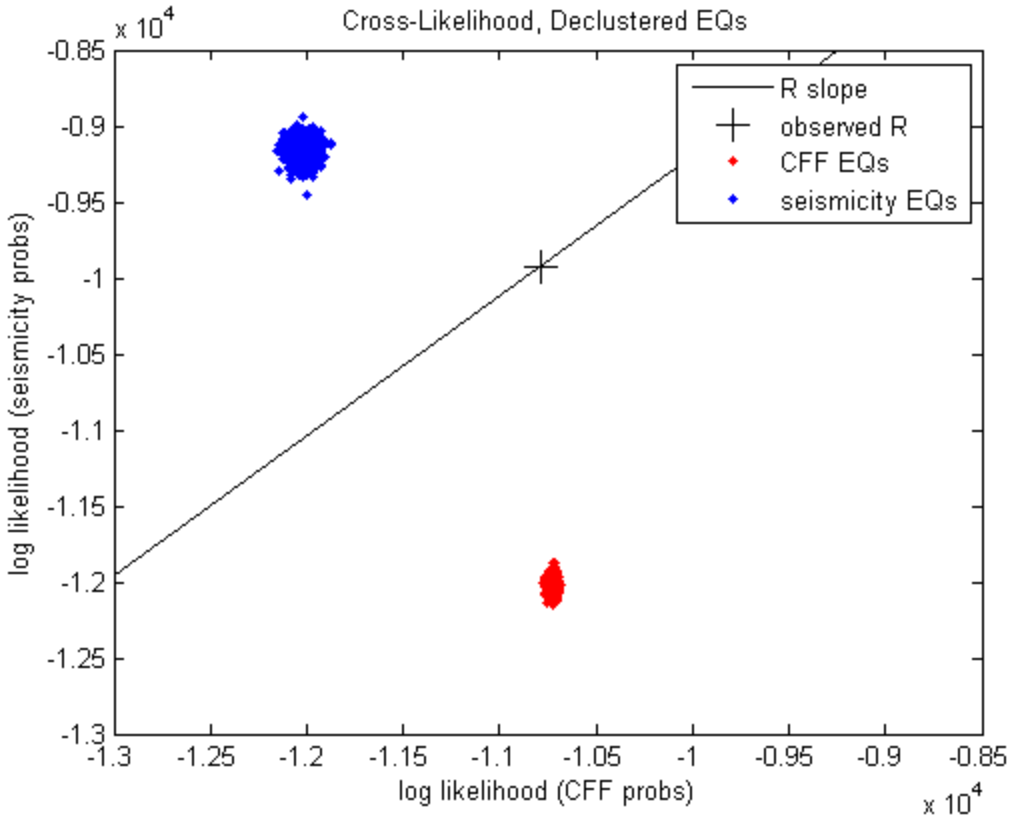

Figure 5.6: Cross-likelihood plot displaying R-test results from the declustered receiver earthquake catalog. The x-axis displays log likelihood values calculated from ΔCFF-based earthquake probabilities, while the y-axis displays log likelihood values calculated from smoothed seismicity-based earthquake probabilities. Log likelihood values for ΔCFF and smoothed seismicity-based synthetic earthquake catalogs are shown by red and blue dots, respectively. The black cross indicates log likelihood values corresponding to the receiver earthquake catalog, while the black line plots all possible log likelihood combinations given the R-value derived from receiver earthquakes.

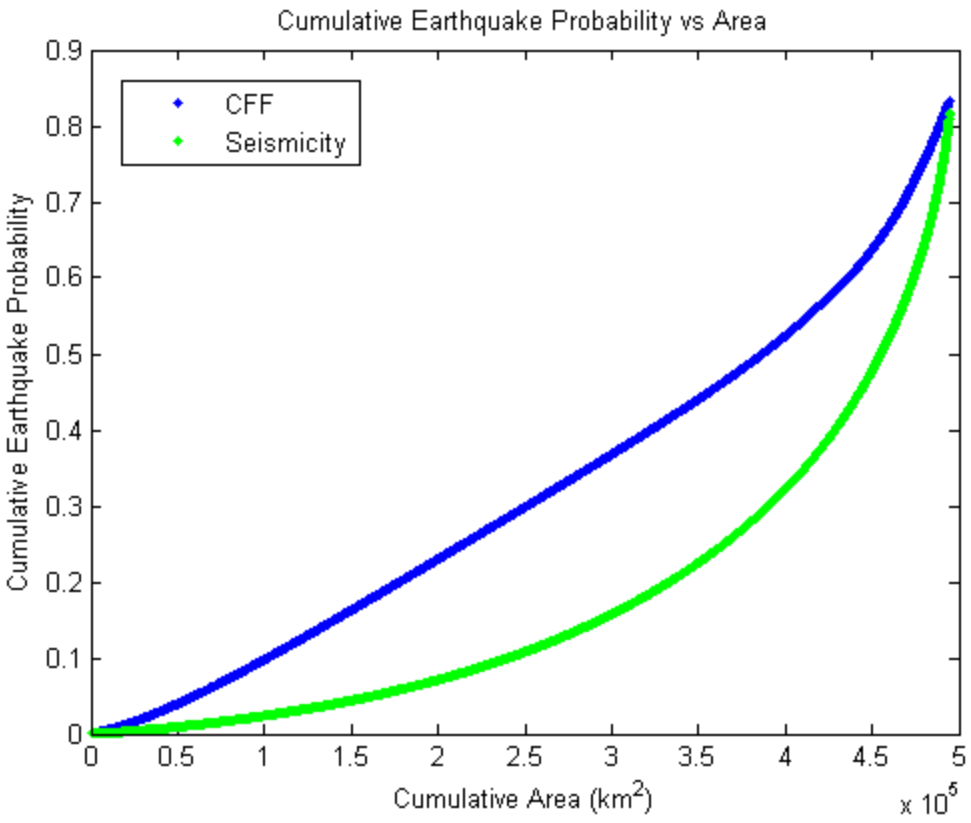

Figure 5.7: Cumulative earthquake probability vs. cumulative area for the ΔCFF-based (blue curve) and smoothed seismicity-based (green curve) earthquake forecasts. The cells were sorted in order of increasing probability, as determined by CFF or smoothed seismicity. 50% of smoothed seismicity probability is concentrated in approximately 10% of the study area, while 50% of CFF probability is contained in 22% of the study area.

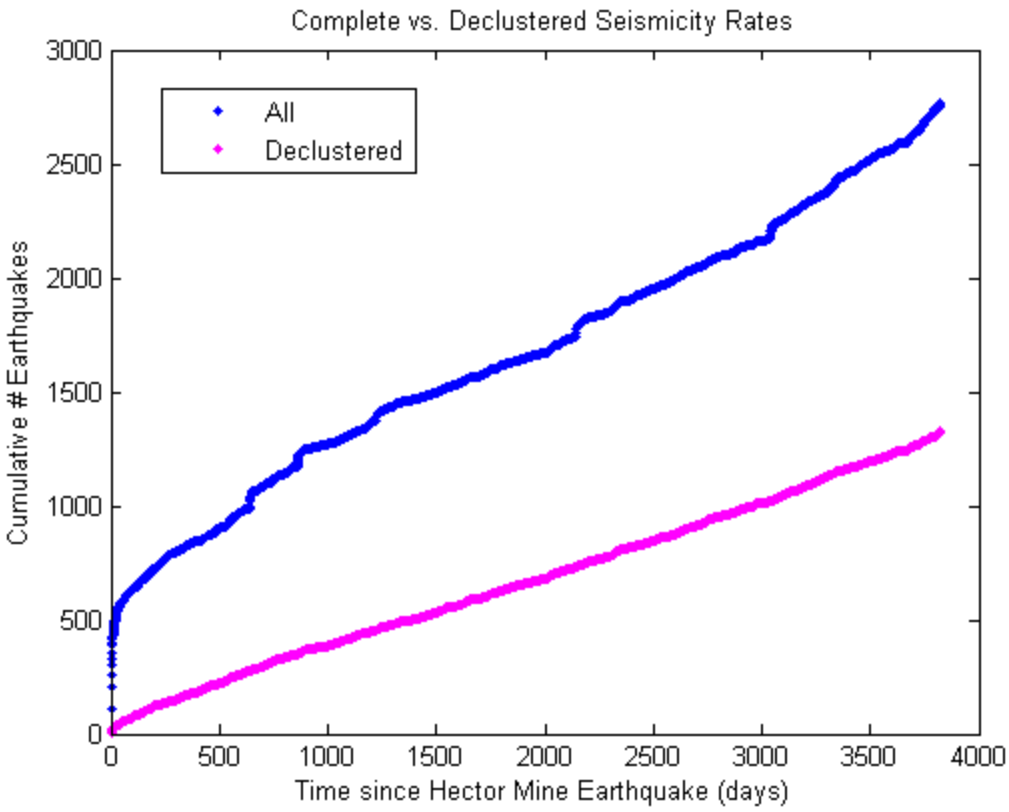

Figure 5.8: Cumulative numbers of receiver earthquakes are plotted against the number of days since the Hector Mine earthquake, which occurred on October 16, 1999. The time interval ends just before the April 4, 2010 El Mayor Cucapah earthquake. The blue curve represents the complete earthquake catalog, and the magenta curve represents the declustered earthquake catalog.

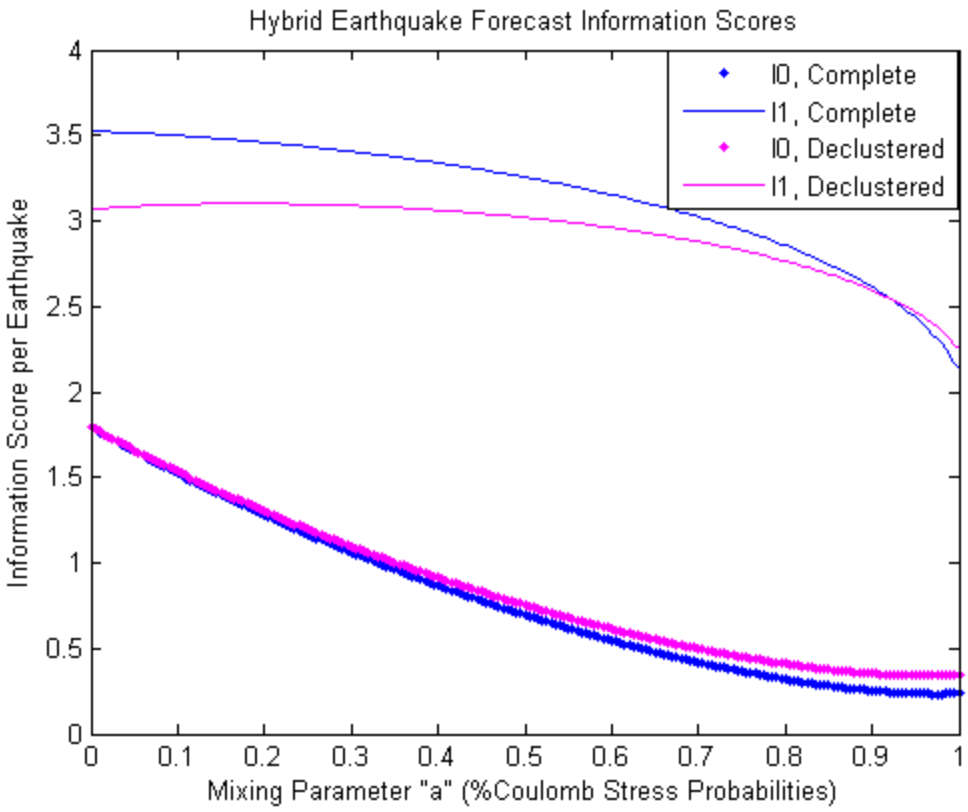

Figure 5.9: Information scores for the complete (blue curves) and declustered (magenta curves) receiver earthquake catalogs. The mixing parameter "a," which remains constant throughout the study area (not optimized), is displayed on the x-axis, and the information scores are displayed on the y-axis. The thick curves indicate I0 (specificity) values, whereas the thin curves indicate I1 (success) values.

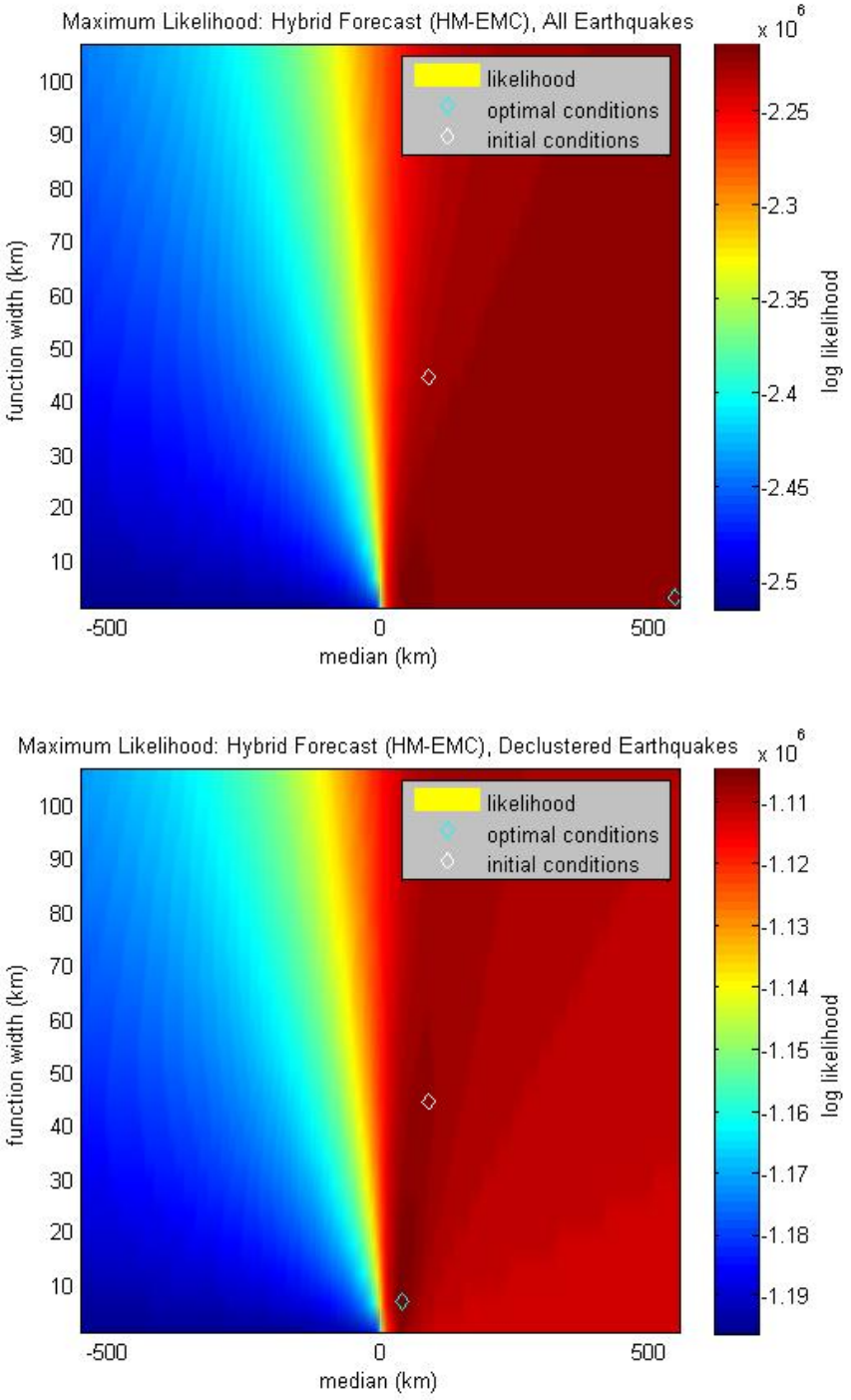

Figure 5.10: Log likelihood grids corresponding to the mixing parameter index function for the complete receiver earthquake catalog (top) and the declustered receiver earthquake catalog (bottom). The median minimum fault distance is indicated on the x-axis, and the function width on the y-axis (both in km). Initial optimization conditions, σ=89 km and d=44 km, are indicated by the white diamond. Optimal function parameters are indicated by the cyan diamond.

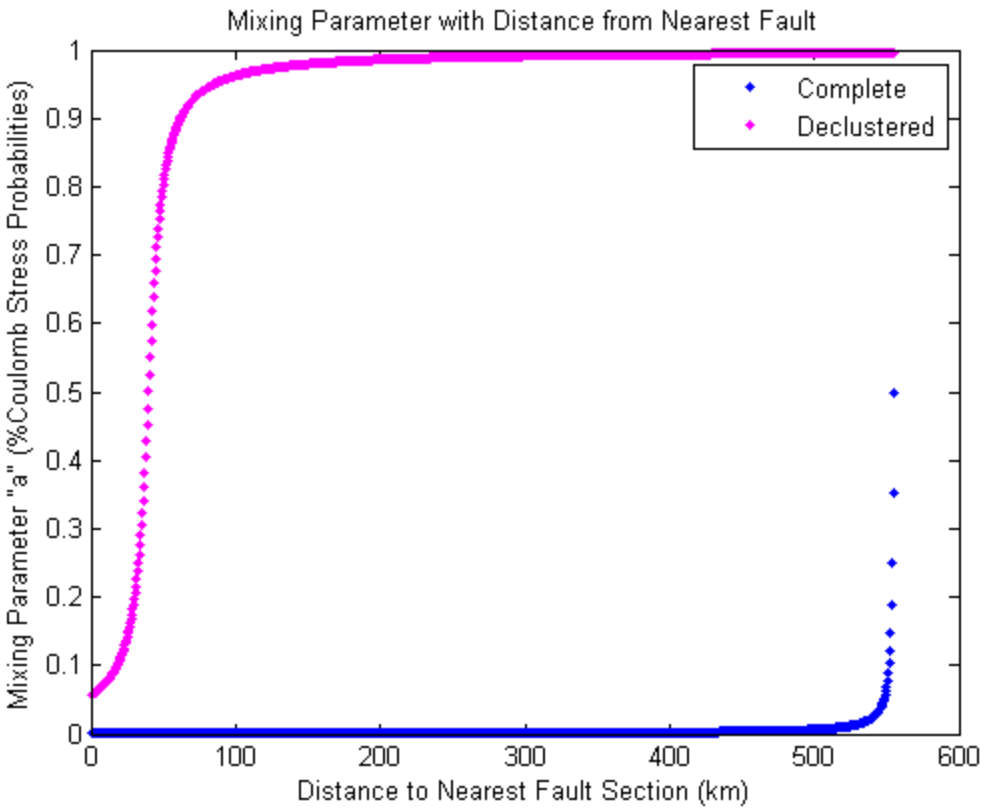

Figure 5.11: Optimal mixing parameter values as a function of minimum distance to the nearest fault section for the complete (blue curve) and declustered (magenta curve) receiver earthquake catalogs. The mixing parameter "a" was calculated from a normalized arctangent index function (Equation 63). The x-axis displays minimum cell-fault distance, and the y-axis displays the mixing parameter "a", which increases with weight given to Coulomb stress earthquake probabilities.

CHAPTER 6

Time-Dependent Earthquake Forecasts

6.1 Rate-and-State Stress Evolution: Forward Model

In previous studies, I observed that within stress-enhanced zones, earthquakes tend to nucleate in regions of recent ΔCFF elevation, suggesting postseismic stress relaxation following stress jumps. Here I introduce temporal dependence into static ΔCFF-based earthquake forecasts through rate-and-state friction. I pseudo-prospectively tested a rate-and-state ΔCFF-based earthquake forecast that allows fault strength to evolve following an earthquake, using an ETAS seismicity model as a null hypothesis with which to compare the stress-based earthquake forecast. Using the forward rate-and-state model, one may directly calculate seismicity rates as a function of Coulomb stress variation, and time elapsed since the last coseismic stress source, explained in more detail in Chapter 2. For each time-dependent earthquake forecast, I focused on seismicity within the southern California study area, during the eight weeks following the Hector Mine earthquake.

Given an assumed aftershock duration time of 500 days and $A\sigma = 1$ bar, I calculated seismicity rates from 5/28/1993 until just before the Hector Mine earthquake using rate-and-state equations described in more detail in Chapter 2. By defining the accumulation period as the six years preceding the Hector Mine earthquake, I accounted for all possible $M \geq 5$ coseismic stress sources that might have influenced seismicity rates during either the learning or target periods. I defined the learning period as the eight weeks before the Hector Mine earthquake, and the target period as the eight weeks including and after the Hector Mine earthquake. Following the Hector

Mine earthquake, I calculated expected seismicity rates at the beginning of the eight weeks following the mainshock. Like the spatially-varying, time-independent earthquake forecast, receiver earthquakes included $M \geq 2.8$ events within the entire southern California study area. Dividing the study area into 0.1°x0.1° spatial cells, I evaluated the seismicity distribution for each week, determining which cells were "activated," or contained at least one receiver earthquake. For time-dependent forecasts, variations in seismicity rates within cells containing earthquakes were considered biased due to stress singularities. Therefore, I only forecasted the probability of a given area containing earthquakes over a specific time window.

The learning period was defined as the eight-week period prior to the Hector Mine earthquake, resulting in 32000 spatiotemporal cells (4000 spatial cells and eight one-week time intervals). I calculated seismicity rates at the beginning of each week during this time, using the aforementioned rate-and-state equations (Figure 6.1). With the seismicity distribution for each week during the learning period, I determined whether each spatiotemporal cell was "activated", or contained at least one earthquake. I then sorted the resulting seismicity rates in ascending order, and categorize them into 40 quantiles, each containing 800 cells. Each quantile contained a seismicity range, and a corresponding percentage of activated cells. The percentages of activated cells were considered the probabilities of cells within the quantile's seismicity rate range containing at least one earthquake over one week. I applied the same method to derive an ETAS-based earthquake probability distribution from conditional intensity evolution during the learning period.

I applied the resulting probability distribution to the seismicity rates (Figure 6.2) within the 32000 spatiotemporal cells during the target period, or eight weeks following the Hector Mine earthquake (Figure 6.3). Each week also contained a set of ETAS-based earthquake

probabilities, derived from conditional intensity evolution following the Hector Mine earthquake (Figure 6.4). The ETAS-based earthquake probabilities (Figure 6.5) were used as a null hypothesis to evaluate the potential of quasi-static ΔCFF in forecasting future earthquake locations and times. I tested each hypothesis individually using two-tailed N- and S-tests. For each test, I simulated 1000 synthetic earthquake catalogs from the ΔCFF-based and ETAS-based earthquake probability distributions.

The N-test statistic, p, was defined as the fraction of synthetic earthquake maps containing lower numbers of activated cells than observed in the receiver earthquake catalog. At the 95% confidence interval, I rejected either forecast if $p < 0.025$ or $p > 0.975$, due to the probability distribution overestimating or underestimating the number of activated cells, respectively. I rejected both the ΔCFF-based and ETAS-based forecasts at the 95% confidence interval (Figure 6.6). For the forward rate-and-state forecast, $p = 1$, indicating that the probability distribution underestimated the area within which one observes Hector Mine aftershocks. The ETAS earthquake forecast, by contrast, overestimated the area within which the mainshock activates cells, with $p = 0$.

For the S-test, I defined a test statistic, p, as the percentage of synthetic log likelihood values exceeding the observed log likelihood. If $p < 0.025$, cell with high predicted seismicity rates are activated more frequently than anticipated. The opposite is true when $p > 0.975$, where cells with relatively low assigned probabilities experience earthquakes that a higher rate than predicted by the forecast. Therefore, in either case I rejected the earthquake forecast at the 95% confidence interval. In southern California, both forecasts failed the S-test at the 95% confidence interval (Figure 6.7), with p-values equal to zero. However, the observed likelihood

from the rate-and-state earthquake forecast is slightly greater than the observed likelihood from the ETAS forecast.

The R-test directly compares the null and alternate earthquake forecasts, by determining the probability of falsely making a decision to reject one forecast in favor of the other, and vice versa. For each synthetic earthquake map, I calculate the log likelihood using both null and alternate earthquake probabilities. The probability of a Type I error is near zero percent for both the ETAS and rate-and-state forecasts (Figure 6.8). Therefore, I reject both forecasts in favor of the other at the 95% confidence interval, indicating that the R-test is insufficient to compare the relative effectiveness of each forecast. Log likelihood residuals (Figure 6.9) indicated that the rate-and-state forecast was significantly more effective than the ETAS forecast within the Hector Mine aftershock region initially following the mainshock, but became progressively less effective later during the target period.

Both the rate-and-state and ETAS forecasts were subject to probability limitations, caused by the lack of observed seismicity, specifically triggered events, during the learning period. Because the ΔCFF range was much greater during the target period than the leaning period due to coseismic stress change from the Hector Mine earthquake, earthquake probabilities may have been inflated following the mainshock. Additionally, aftershock duration times may have varied for previous mainshocks, such as the Northridge and Landers earthquakes, that could have contributed to later seismicity rates. I assumed an aftershock duration time of 500 days, the length of time during which coseismic stress sources would be expected to contribute to the stress field, such that stress would not decay significantly within the eight week target period. However, earthquakes may have been triggered afterward the aftershock duration time, in areas with low earthquake probabilities. The aftershock duration time following the Hector Mine

earthquake may also have been lower than expected, as shown by log likelihood residuals that show the rate-and-state forecast becoming progressively less effective over time. As a result of assuming the aftershock duration time was spatially constant, earthquake probabilities did not always increase monotonically with seismicity rates calculated from rate-and-state equations, as seen in alternating regions of low and high earthquake probabilities in Figure 6.3. Similar issues resulted in probability distributions that failed to increase monotonically with conditional intensity, rendering the ETAS forecast less effective than anticipated (Figure 6.5).

The variation in rate-and-state cell activation probabilities away from faults may also have been due to the number of chosen probability quantiles. Fewer earthquakes occurred during the learning period than during the target period, and most earthquakes during the learning period were considered independent of previous seismicity. Figure 6.3 indicates that the highest cell activation probabilities occurred near active faults. However, probability failed to decrease monotonically with fault distance, instead alternating between low-moderate values in the far field. I observed similar "noise" in the cell activation probabilities from the static Coulomb stress forecast (Chapter 4, Figure 4.2). When increasing the number of quantiles, fewer earthquakes are necessary to significantly alter cell activation probabilities within each quantile. Therefore, independent earthquakes during the learning period for the time-dependent forecast may have caused the observed alternating probability patterns. To test the effect of quantile numbers on cell activation probabilities, I decreased the number of quantiles to 20, 10, and 5. I found that as the number of seismicity rate quantiles decreased, the association between cell activation probabilities and fault distance strengthened, with lower probabilities consistently observed in the far field.

6.2 Rate-and-State Stress Evolution: Inverse Model

Coulomb stress changes calculated from rectangular fault patches may effectively estimate stress evolution in the far field, but modeled stress singularities near fault sections misrepresent the actual stress state there. The forward rate-and-state model relies on such stress models when calculating seismicity rates; therefore, seismicity rates may subsequently be overestimated. Dieterich et al. (2000) presented a method, the details of which are described in Chapter 2 (Equation 36), to invert observed seismicity variations for Coulomb stress evolution and avoid such uncertainties from modeling Coulomb stress on rectangular fault sections. Because a reliable prospective forecast must effectively indicate future areas of seismic quiescence as well as areas of elevated seismicity, I modified Dieterich's Coulomb stress inversion equation to apply to areas with low or zero seismicity (Chapter 2, Equations 37-38). In areas with sufficient earthquakes to employ Dieterich's original stress inversion equation, both methods yielded similar ΔCFF.

I chose the same spatiotemporal area as in the forward rate-and-state earthquake forecast tests. For each week during the learning period (the eight weeks before the Hector Mine earthquake), I calculated the Poissonian probability of a cell being activated or deactivated, and then calculated the probability ratio for the current and previous weeks. The probability ratio yielded weekly ΔCFF evolution throughout the southern California study area (Figure 6.10). By dividing the ΔCFF distribution into quantiles and determining the fraction of activated cells within each quantile, I formulated a ΔCFF-based probability distribution that was applicable to seismicity during the target period (Figure 6.11).

Both the inverse rate-and-state and ETAS forecasts failed the two-tailed N-test at the 95% confidence interval (Figure 6.12), because both forecasts underestimated the Hector Mine aftershock area. I also rejected the null and alternate hypotheses at the 95% confidence interval

($p = 0.0$) based on two-tailed S-test results (Figure 6.13), where the observed log likelihood was significantly lower than the log likelihood values from earthquake maps constructed from each probability distribution. The observed likelihood from the inverse rate-and-state forecast exceeded the likelihood from the ETAS forecast; however, both forecasts passed the R-test at the 95% confidence interval (Figure 6.14). Because the chance of a Type I error for both the rate-and-state and ETAS forecasts was below five percent, the R-test could not provide conclusive evidence to reject one forecast in favor of the other. Log likelihood residual maps (Figure 6.15) showed that the inverse rate-and-state forecast more effectively indicated earthquake locations and times during the beginning of the target period, but the difference between the two forecasts became progressively negligible.

6.3 Rate-and-State Stress Inversion: 2014 Iquique Earthquake

The western coast of Chile is characterized by subduction of the Nazca plate underneath the South American plate, resulting in uplift of the Andes mountain range as well as active volcanism and frequent, large intraplate earthquakes. The subduction zone is bordered by the Chilean margin triple junction to the south, where the Nazca and South American plates meet the Antarctic plate, and the Panama fracture zone to the north. In the northern subduction area containing the M8.2 earthquake hypocenter, the Nazca plate subducts east-northeast at a rate of 65 mm/yr, at an angle of 25°-30° relative to the South American plate. Within central Chile, the subduction angle decreases to 10°, and subduction rates increase southwards to 80 mm/yr. The 4/1/2014 M8.2 mainshock occurred approximately 50 km west of the northern Chilean coastline, at a depth of 20.1 km, at the interface between the Nazca and South American plates.

The region in which the mainshock occurred, termed the "Iquique seismic gap" (Chlieh et al., 2004), underwent a period of seismic quiescence since 1877, when a M8.8 earthquake occurred within the gap, defined by the estimated extent of the 1877 rupture zone. In 1995, a M8.1 earthquake occurred just south of the Iquique gap in Antofagasta, rupturing a 180 km fault segment and causing surface deformation near the 8.2 mainshock epicenter. Immediately following the 1995 earthquake, aftershocks were limited to regions south of the Mejillones Peninsula, but later migrated north toward the gap region. Postseismic relaxation from the previous mainshock, as well as the series of subsequent $M \geq 6.0$ aftershocks, may have loaded the area near the 2014 mainshock, according to GPS measurements (Chlieh et al., 2004). Following the recent mainshock, the areas with maximum surface slip were to the southeast and southwest of the mainshock hypocenter, suggesting that postseismic deformation, combined with interseismic loading, may have contributed in triggering the earthquake.

Following Dieterich's stress inversion method (2000), I calculated stress evolution within areas containing sufficient seismicity from 2010-2014, and for every 500 earthquakes from 2/14/2014 until 4/9/2014. Contrary to the southern California earthquake forecast derived from inverted seismicity rates, I did not use the Poissonian probability ratio, but instead used the seismicity ratio for each pair of time intervals, N_2/N_1 (Chapter 2, Equation 36). I set the minimum number of events within a one-degree search radius at five earthquakes, not including any areas with fewer events in the stress inversion.

From 2010-2014, Coulomb stress evolution delineated the mainshock epicenter, as well as the areas within which the foreshock and aftershock sequences occurred (Figure 6.16). The 2010 M8.8 earthquake elevated coseismic Coulomb stress throughout much of the area near the 2014 M8.2 mainshock, possibly due to postseismic deformation. Seismicity following the 2010

mainshock relieved much of the stress throughout the next two years, forming a stress shadow surrounding the mainshock area during 2013. Toward the end of 2013, increased seismicity preceded the mainshock, defining an area of increased Coulomb stress which encompassed nearly all $M \geq 5.5$ earthquakes during the foreshock sequence in 2014 and migrated toward the mainshock epicenter.

Stress inversions for every 500 earthquakes between 2/14/2014 and 4/9/2014 displayed similar eastward Coulomb stress migration following the mainshock (Figure 6.17). Increased seismicity from 3/24/14 to 4/3/14 elevated stress along the areas of maximum displacement during the mainshock and M7.6 aftershock. Following the mainshock, elevated Coulomb stress persisted near the aftershock, defining the area in which most $M \geq 5.5$ aftershocks occurred. The association between aftershock location and positive Coulomb stress change suggests that the coseismic stress contribution from the mainshock may have elevated the cumulative Coulomb stress near or past the necessary threshold to trigger additional earthquakes, and illuminated areas of maximum dynamic stress transfer (Figure 6.18). However, slow-slip repeating events may have relieved stress within the creeping zone, causing an overestimation of Coulomb stress change from the inversion. Rate-and-state stress evolution predicts increased seismicity in areas corresponding to increased stress, but does not account for aseismic slip events that transfer stress to locked regions. Therefore, Coulomb stress within the seismic gap may have been elevated by stress transfer from low-frequency slip events, rather than from coseismic stress evolution. These results will be included in a publication, co-authored by Dr. Lingsen Meng, which will be submitted to Nature Geoscience.

6.4 Rate-and-State Hybrid Earthquake Forecast

Given that the forward and inverse rate-and-state southern California earthquake forecasts exhibited a trade-off in forecast reliability with cell-fault distance, I tested a pseudo-prospective hybrid forecast, with earthquake probabilities calculated from a linear combination of forward and inverse rate-and-state earthquake probabilities. I hypothesized that the inverse rate-and-state forecast more effectively forecasted earthquake locations and times near the mainshock hypocenter, given the lack of stress singularities. However, due to the inverse model's tendency to underestimate aftershock areas, I hypothesized that the forward rate-and-state forecast is more reliable in the far field (at least 50 km from active faults), where the effects of stress singularities are negligible but the seismicity rates are still significantly elevated from mainshocks.

I calculated hybrid earthquake probabilities in each spatiotemporal cell (consistent study area and target period) from a linear combination of forward and inverse rate-and-state earthquake probabilities (Chapter 2, Equation 62). Using a normalized arctangent index function, I expressed the mixing parameter, "a", as a function of the distance from a given cell to the nearest fault section (Chapter 2, Equation 63). By maximizing a log likelihood function (Chapter 2, Equation 56), I optimized the arctangent function median and width to determine the optimal influence of either forecast, given cell-fault distance (Figure 6.19). As cell-fault distance increased, the forward rate-and-state earthquake probabilities gradually contributed more to the earthquake probability distribution. The forward model exerted more influence on earthquake probabilities than the inverse model at cell-fault distances exceeding 270 km (Figure 6.20).

To test the relative influence of each ΔCFF-based earthquake probability distribution without taking into account cell-fault distance, I calculated two information statistics, I0 (specificity) and I1 (success) for multiple mixing parameter values (Chapter 2, Equations 60-61).

The optimal rate-and-state earthquake forecast was primarily influenced by the inverse rate-and-state model (Figure 6.21), with only 15% influence from the forward rate-and-state model. Therefore, the relative effectiveness of each forecast significantly depended on proximity to active faults.

6.5 Figures

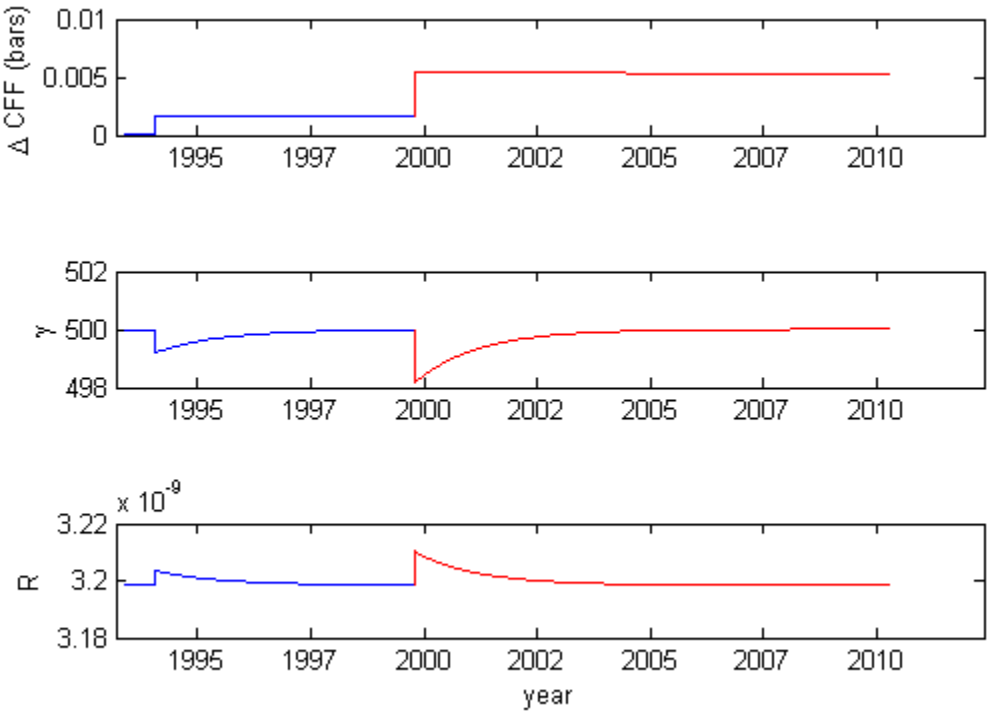

Figure 6.1: From top to bottom: Coulomb stress, state variable, and total seismicity rate evolution from 5/28/1993 to 4/4/2010. The blue curves indicate the time interval before the Hector Mine earthquake, and the red curves indicate the time including and following the Hector Mine earthquake. Increased ΔCFF corresponds to a decrease in the state variable, γ, which causes seismicity rates to increase. Seismicity rates return to the background rate over the aftershock duration time. Because ΔCFF for only one cell is displayed, not all coseismic sources significantly affect seismicity rates. Visible coseismic stress sources include the 1/17/94 Northridge earthquake, the 10/16/99 Hector Mine earthquake, and the 10/11/04 Parkfield earthquake.

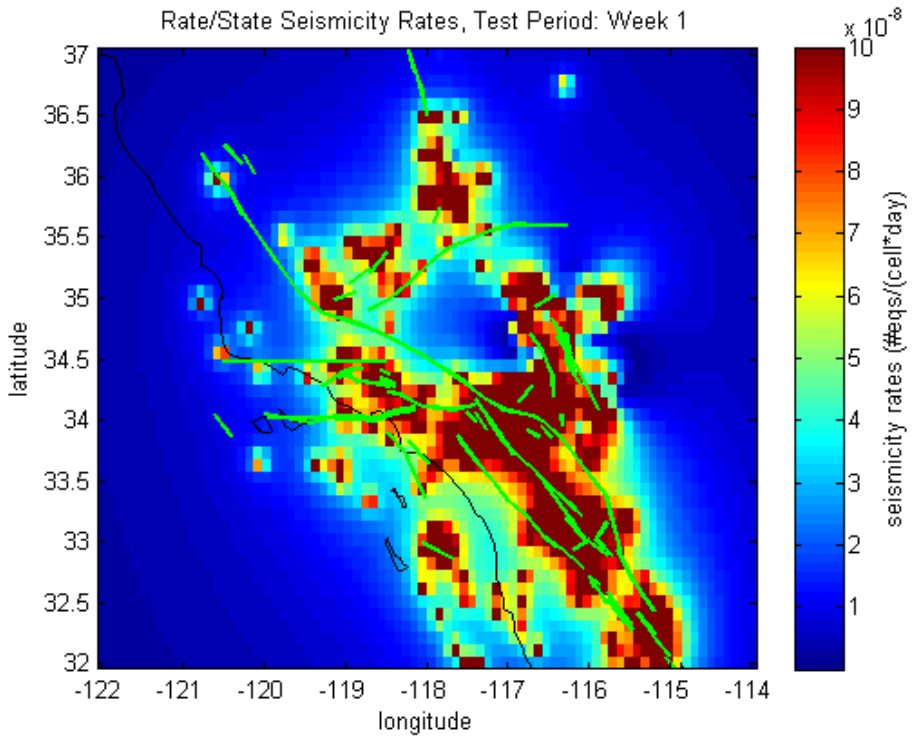
Rate/State Seismicity Rates, Test Period: Week 1
x 10^-8
10
9
8
7
6
5
4
3
2
1
seismicity rates (#eqs/(cell*day)
latitude
37
36.5
36
35.5
35
34.5
34
33.5
33
32.5
32
-122
-121
-120
-119
-118
-117
-116
-115
-114
longitude

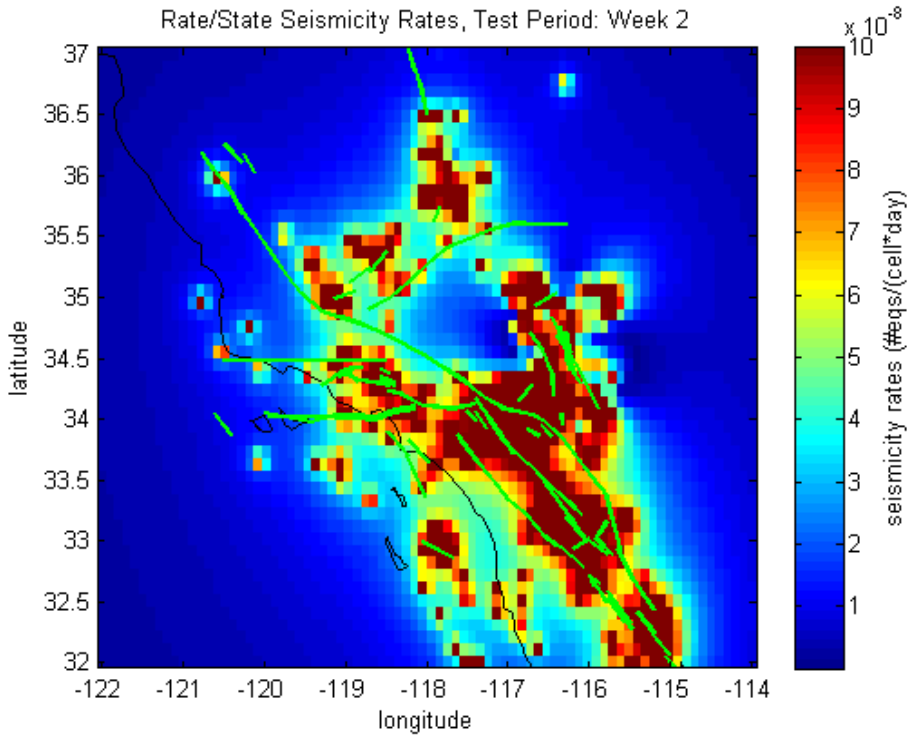
Rate/State Seismicity Rates, Test Period: Week 2
x 10^-8
10
9
8
7
6
5
4
3
2
1
seismicity rates (#eqs/(cell*day)
latitude
37
36.5
36
35.5
35
34.5
34
33.5
33
32.5
32
-122
-121
-120
-119
-118
-117
-116
-115
-114
longitude

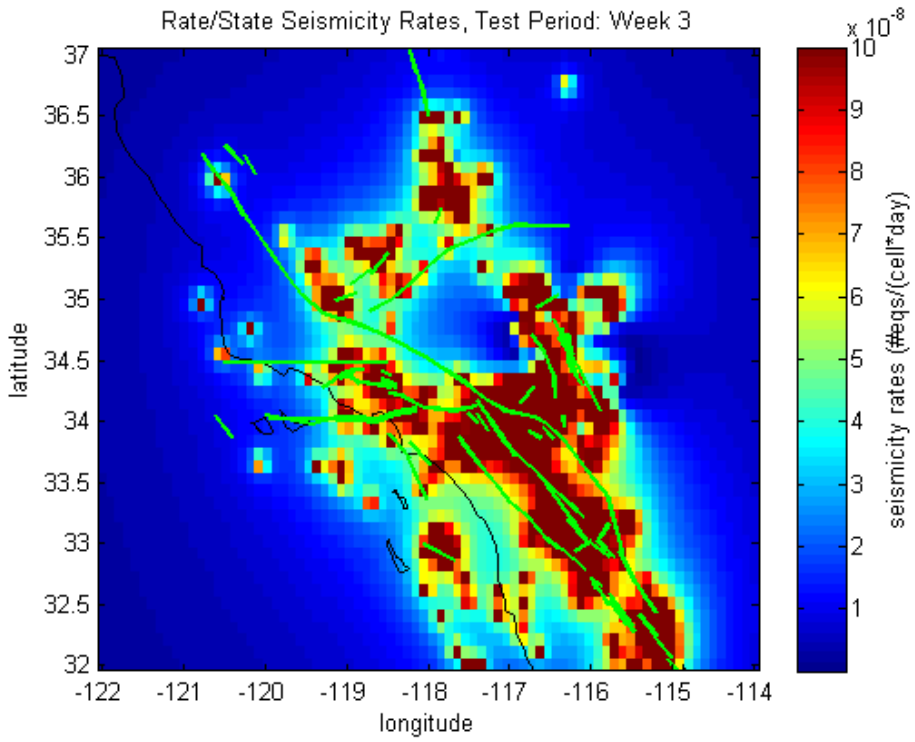
Rate/State Seismicity Rates, Test Period: Week 3
x 10^-8
10
9
8
7
6
5
4
3
2
1
seismicity rates (#eqs/(cell*day))
37
36.5
36
35.5
35
34.5
34
33.5
33
32.5
32
latitude
-122
-121
-120
-119
-118
-117
-116
-115
-114
longitude

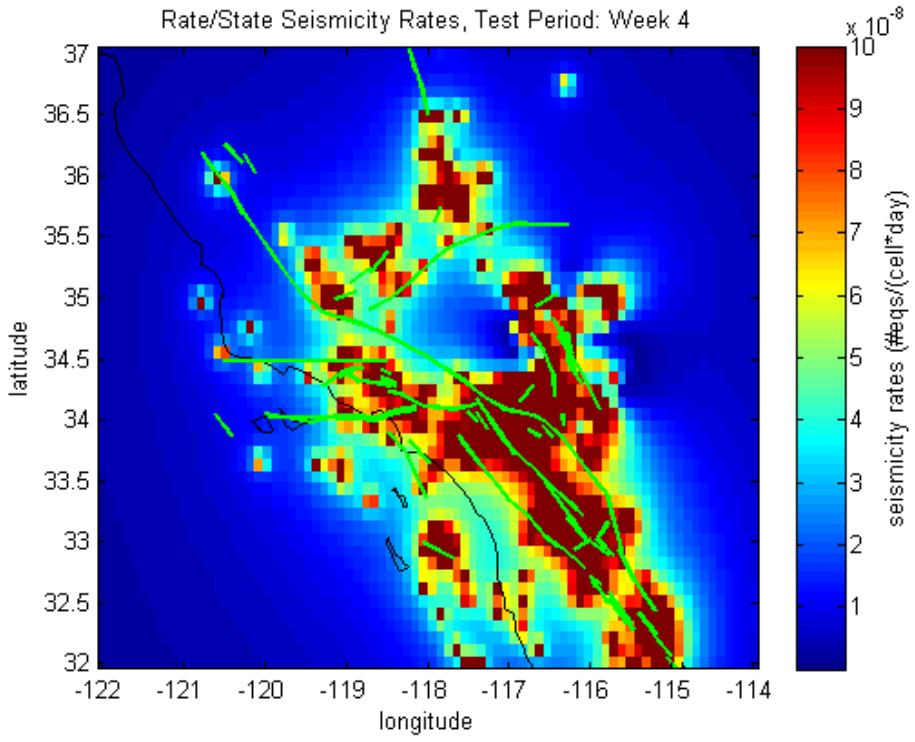
Rate/State Seismicity Rates, Test Period: Week 4
x 10^-8
10
9
8
7
6
5
4
3
2
1
seismicity rates (#eqs/(cell*day))
37
36.5
36
35.5
35
34.5
34
33.5
33
32.5
32
latitude
-122
-121
-120
-119
-118
-117
-116
-115
-114
longitude

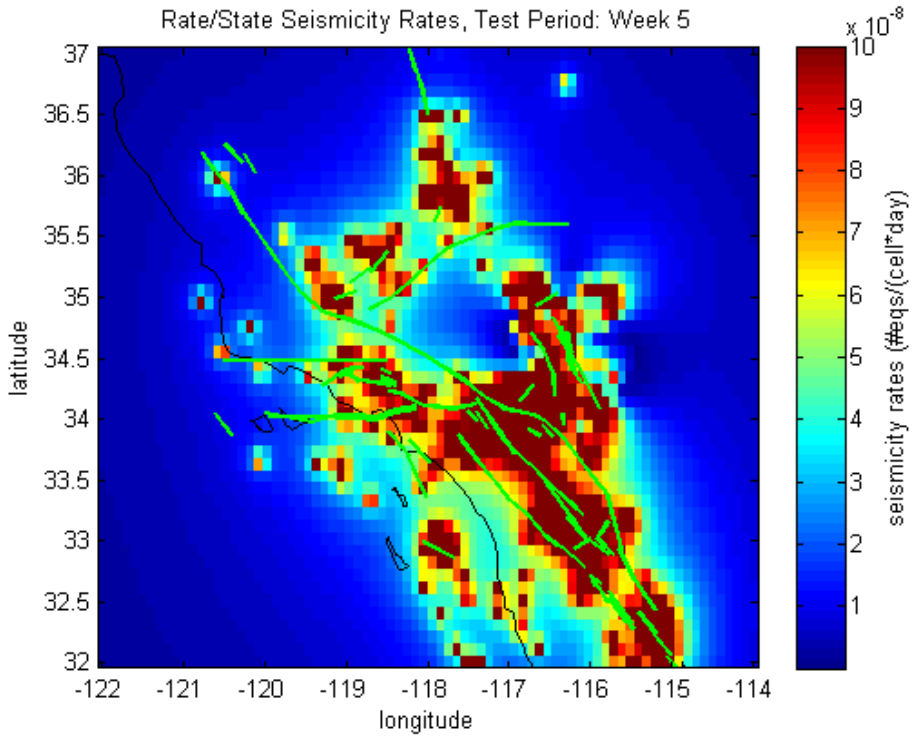
Rate/State Seismicity Rates, Test Period: Week 5
x 10^-8
10
9
8
7
6
5
4
3
2
1
seismicity rates (#eqs/(cell*day))
37
36.5
36
35.5
35
34.5
34
33.5
33
32.5
32
latitude
-122
-121
-120
-119
-118
-117
-116
-115
-114
longitude

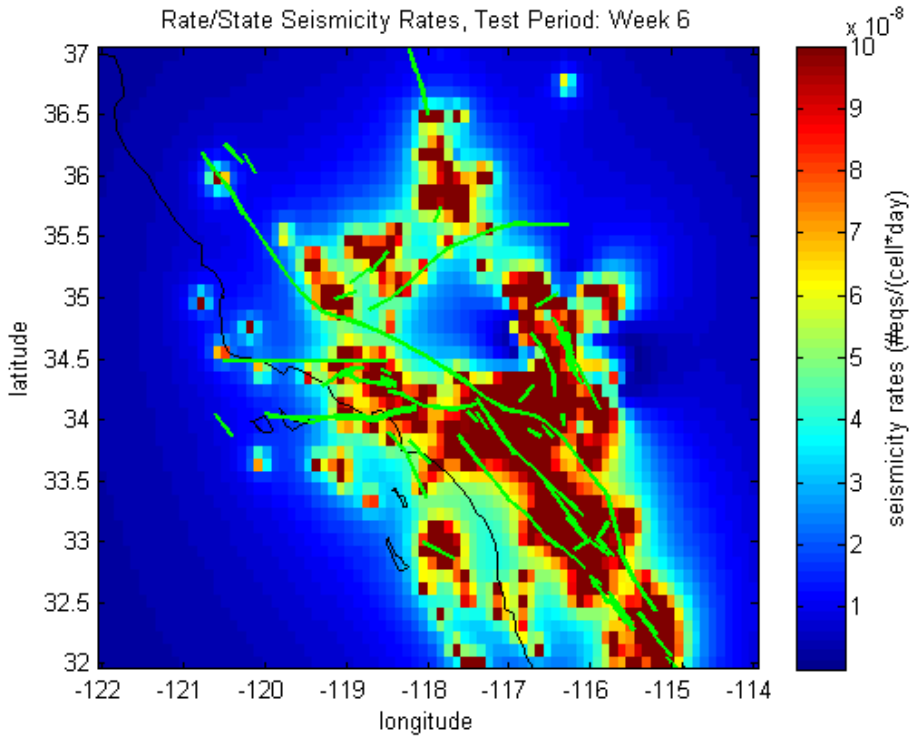
Rate/State Seismicity Rates, Test Period: Week 6
x 10^-8
10
9
8
7
6
5
4
3
2
1
seismicity rates (#eqs/(cell*day))
37
36.5
36
35.5
35
34.5
34
33.5
33
32.5
32
latitude
-122
-121
-120
-119
-118
-117
-116
-115
-114
longitude

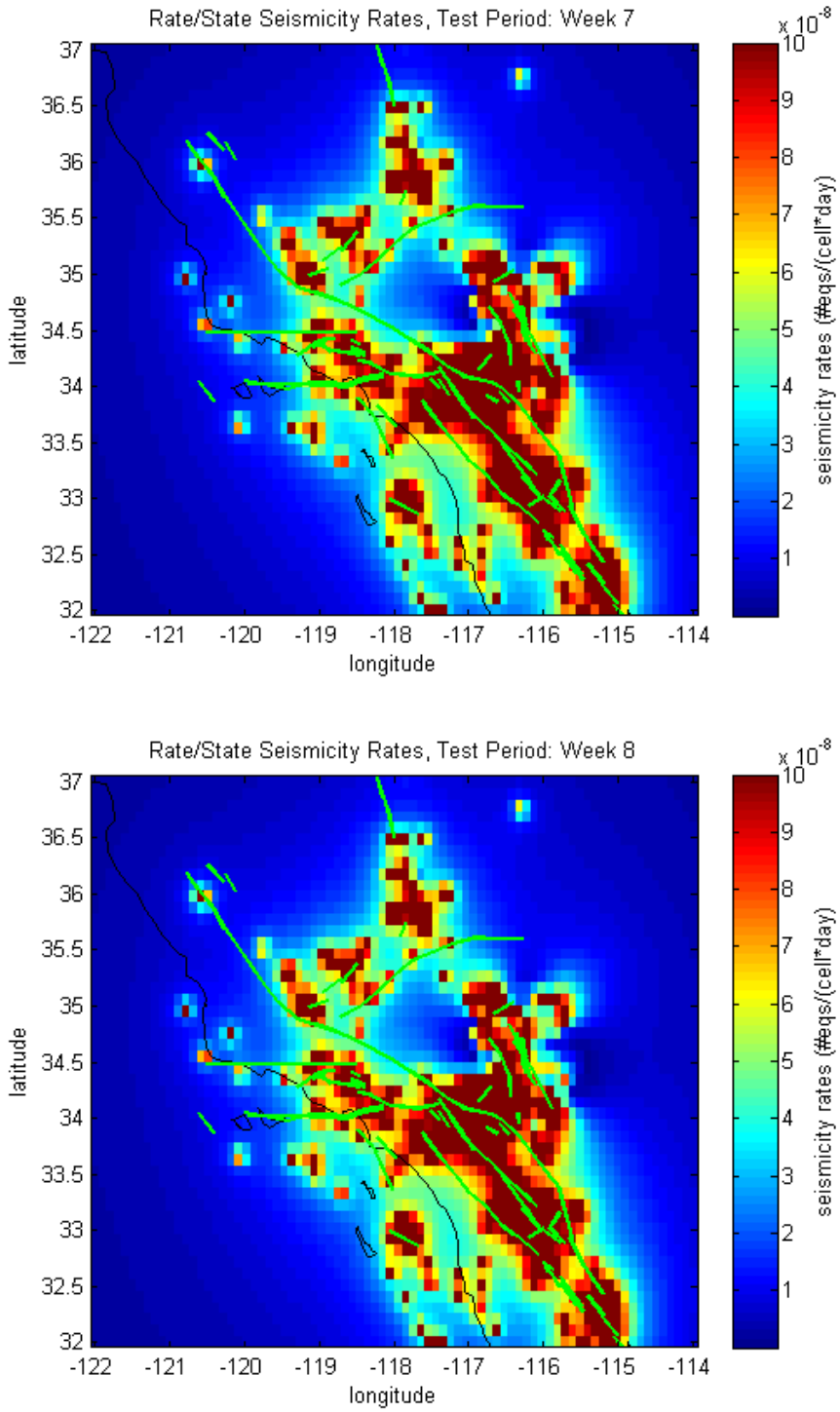

Figure 6.2: Seismicity rates, calculated from the forward rate-and-state model, at the beginning of each week during the target period, calculated from static ΔCFF evolution. Red areas indicate areas of relatively high seismicity rates, yellow and light blue areas indicate areas of moderate seismicity, and dark blue areas indicate regions with relatively low seismicity rates. Given a 500-day aftershock duration time, seismicity rates following the Hector Mine earthquake decay slowly over the eight week target period. Green lines indicate active fault sections.

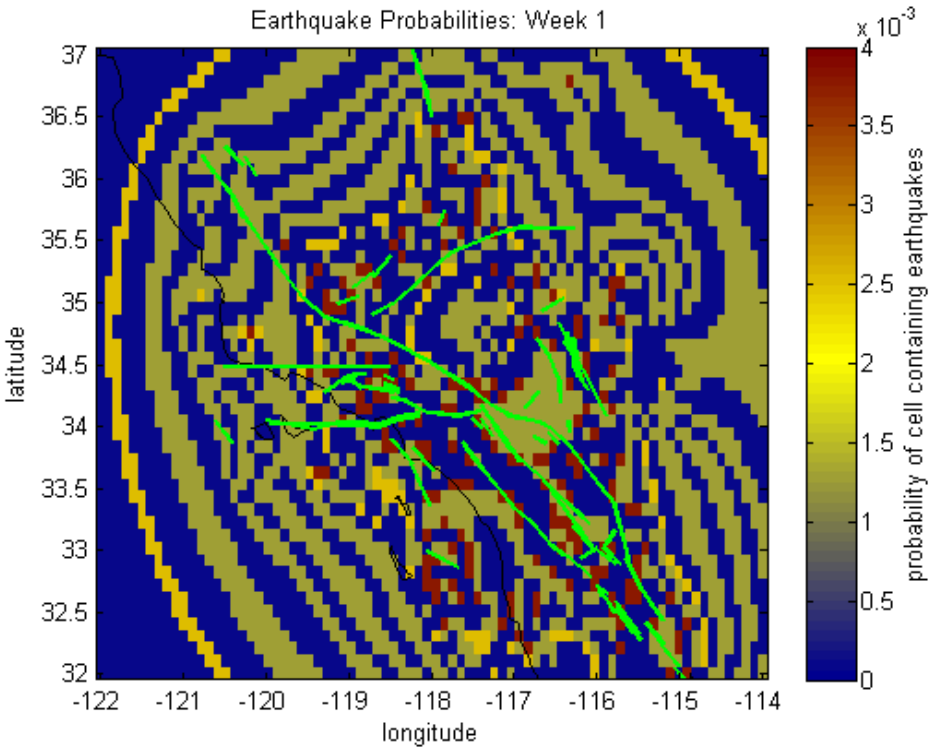
Earthquake Probabilities: Week 1
latitude
longitude
37
36.5
36
35.5
35
34.5
34
33.5
33
32.5
32
-122
-121
-120
-119
-118
-117
-116
-115
-114
x 10^-3
4
3.5
3
2.5
2
1.5
1
0.5
0
probability of cell containing earthquakes

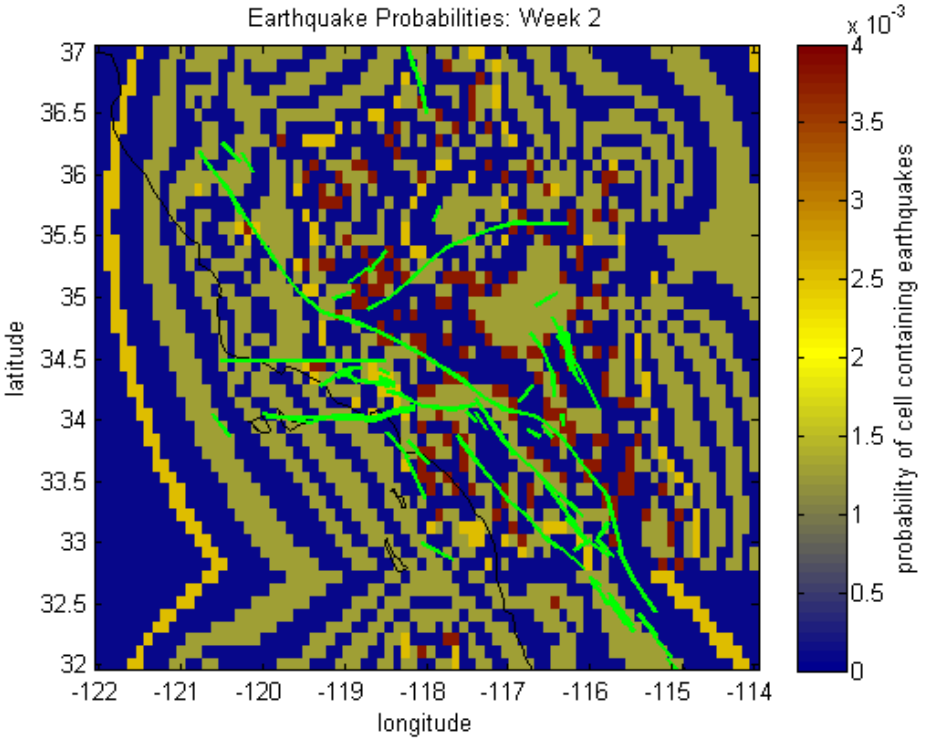
Earthquake Probabilities: Week 2
latitude
longitude
37
36.5
36
35.5
35
34.5
34
33.5
33
32.5
32
-122
-121
-120
-119
-118
-117
-116
-115
-114
x 10^-3
4
3.5
3
2.5
2
1.5
1
0.5
0
probability of cell containing earthquakes

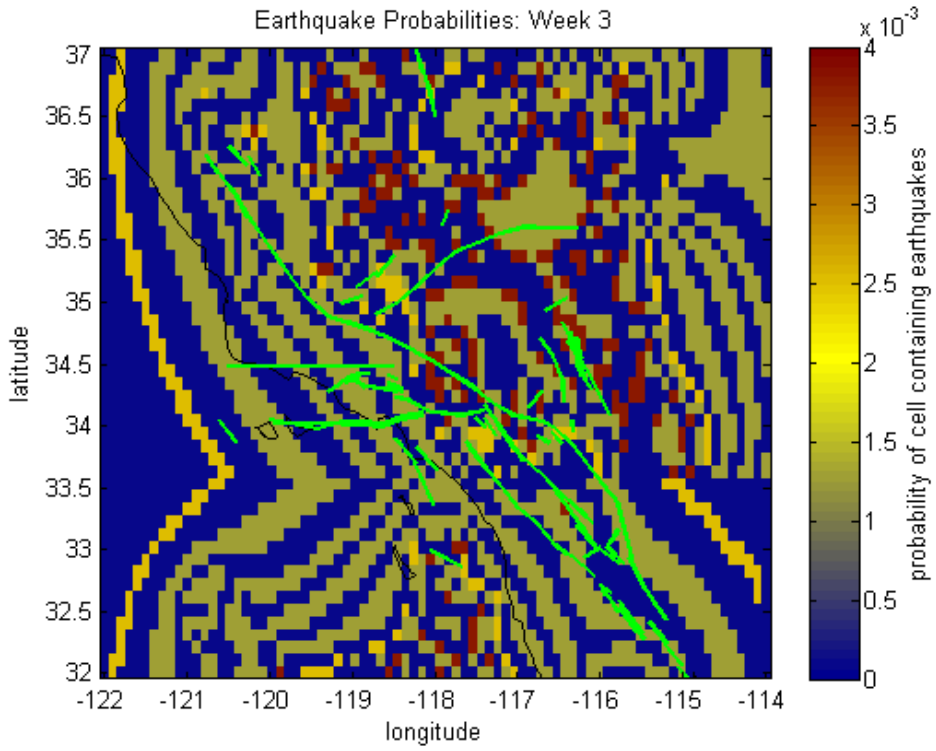
Earthquake Probabilities: Week 3
latitude
longitude
probability of cell containing earthquakes
x 10^-3
37
36.5
36
35.5
35
34.5
34
33.5
33
32.5
32
-122
-121
-120
-119
-118
-117
-116
-115
-114
4
3.5
3
2.5
2
1.5
1
0.5
0

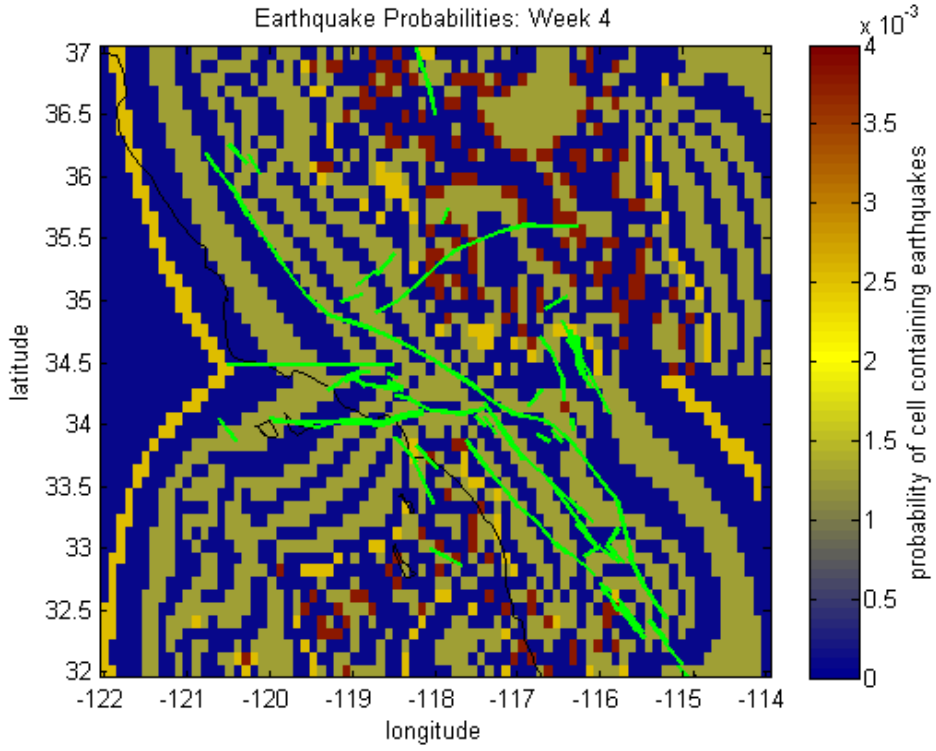
Earthquake Probabilities: Week 4
latitude
longitude
probability of cell containing earthquakes
x 10^-3
37
36.5
36
35.5
35
34.5
34
33.5
33
32.5
32
-122
-121
-120
-119
-118
-117
-116
-115
-114
4
3.5
3
2.5
2
1.5
1
0.5
0

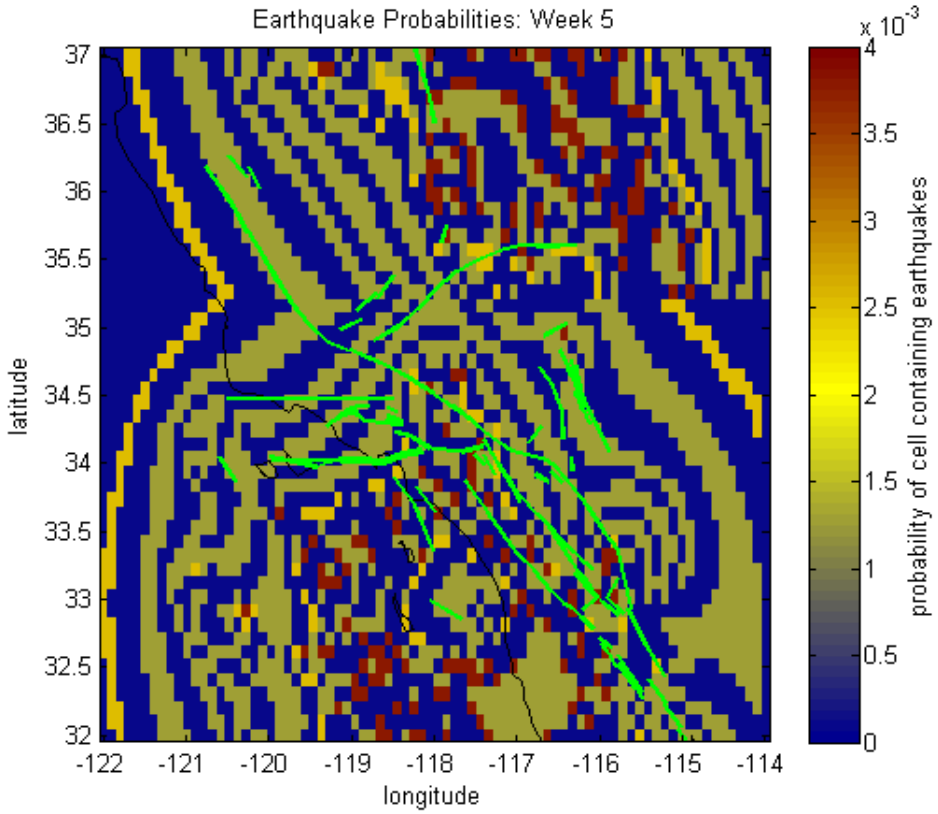
Earthquake Probabilities: Week 5
latitude
longitude
probability of cell containing earthquakes
x 10^-3
37
36.5
36
35.5
35
34.5
34
33.5
33
32.5
32
-122
-121
-120
-119
-118
-117
-116
-115
-114
4
3.5
3
2.5
2
1.5
1
0.5
0

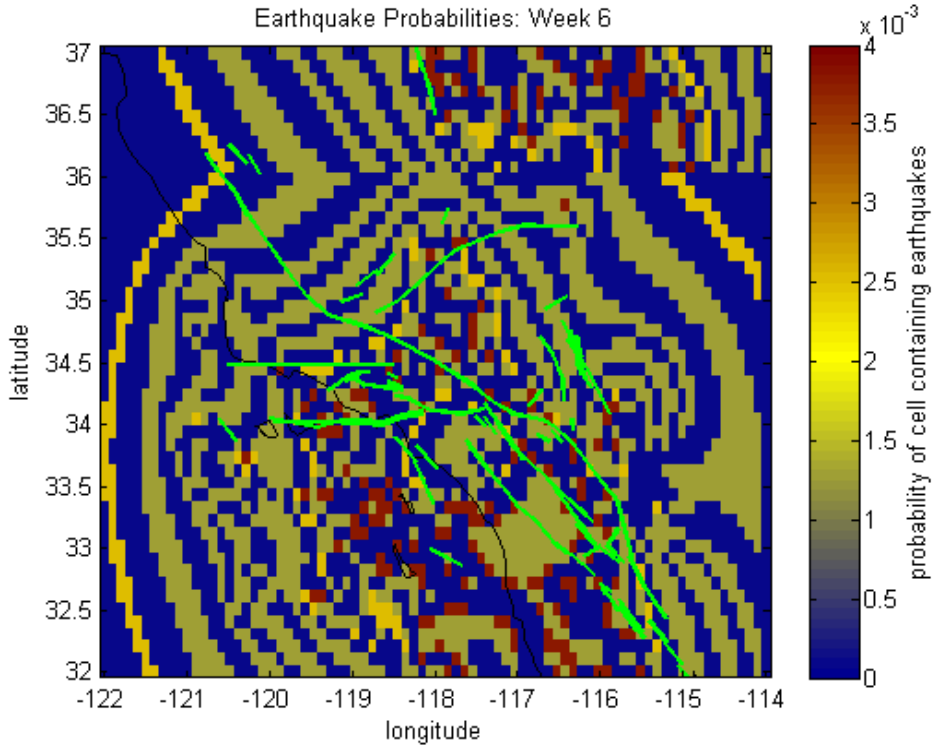
Earthquake Probabilities: Week 6
latitude
longitude
probability of cell containing earthquakes
x 10^-3
37
36.5
36
35.5
35
34.5
34
33.5
33
32.5
32
-122
-121
-120
-119
-118
-117
-116
-115
-114
4
3.5
3
2.5
2
1.5
1
0.5
0

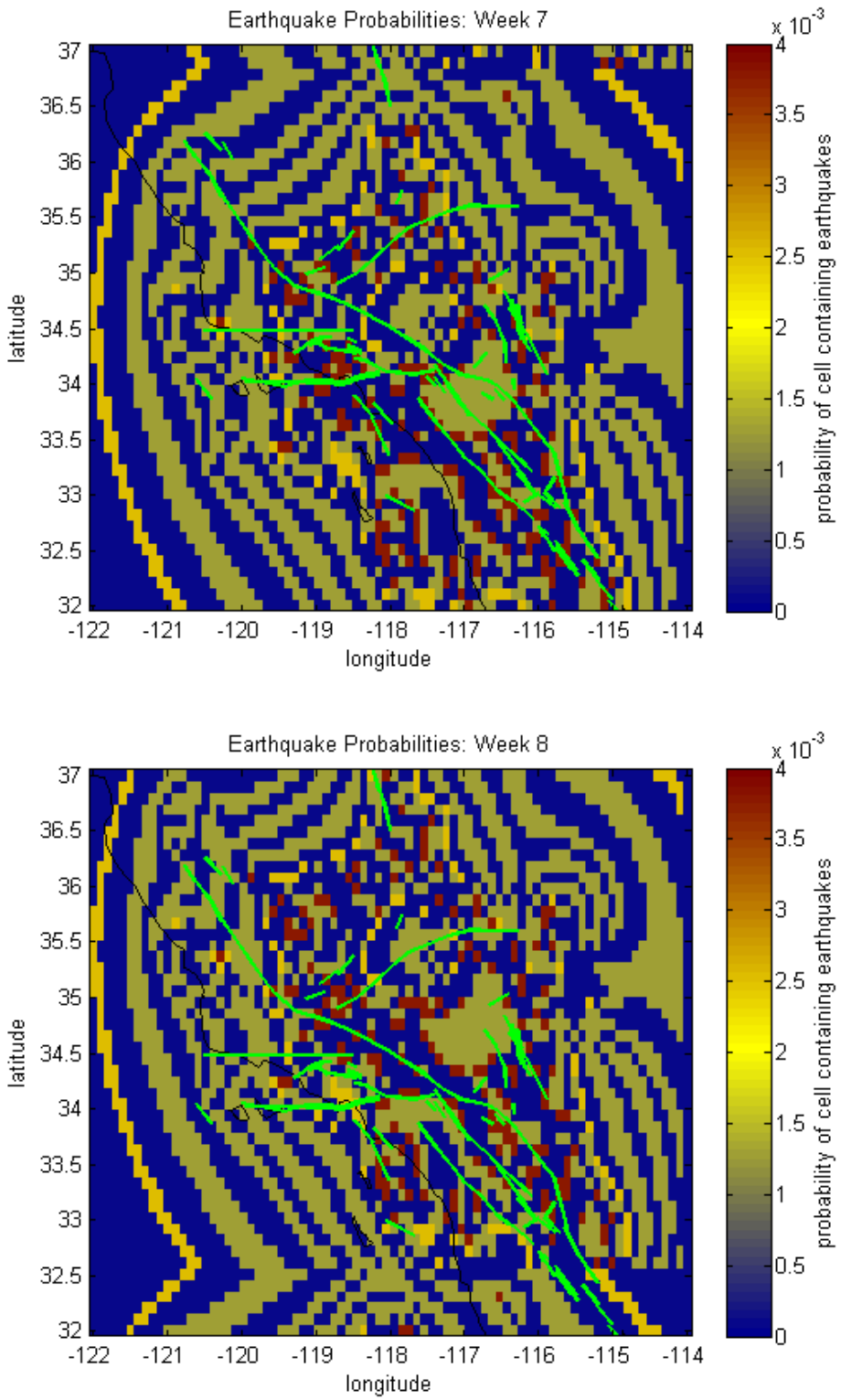

Figure 6.3: Cell activation probabilities, determined from forward rate-and-state seismicity rates, during the eight-week target period following the Hector Mine earthquake. Areas with relatively high, moderate, and low cell activation probabilities are indicated by red, yellow, and blue zones, respectively. Green lines indicate active fault sections.

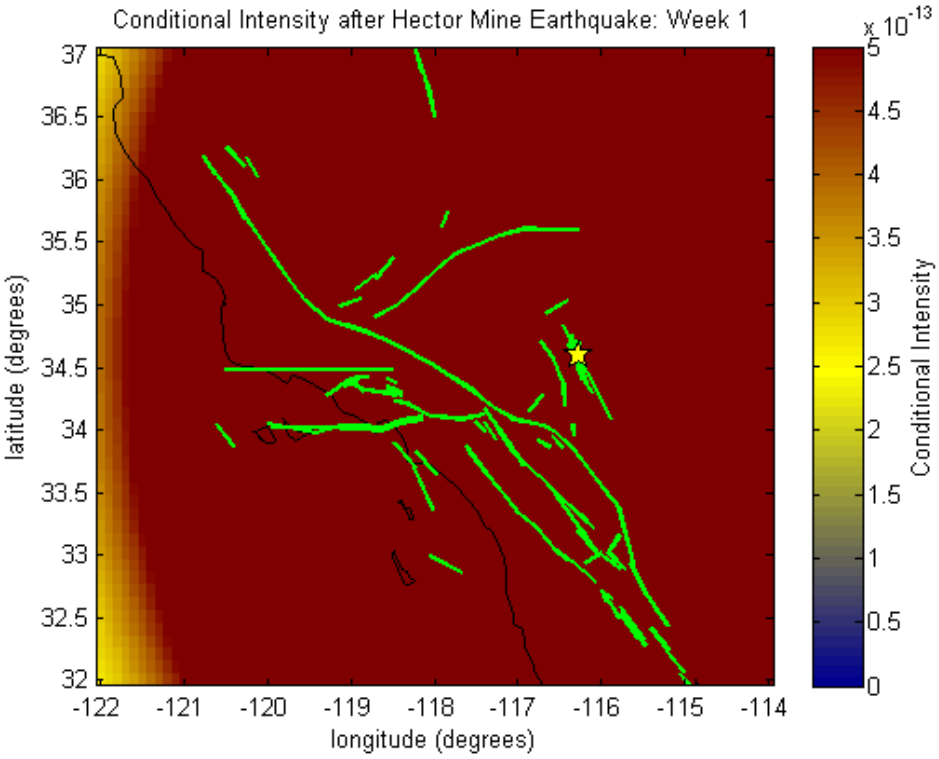
Conditional Intensity after Hector Mine Earthquake: Week 1
x 10^-13
5
4.5
4
3.5
3
2.5
2
1.5
1
0.5
0
Conditional Intensity
37
36.5
36
35.5
35
34.5
34
33.5
33
32.5
32
latitude (degrees)
-122
-121
-120
-119
-118
-117
-116
-115
-114
longitude (degrees)

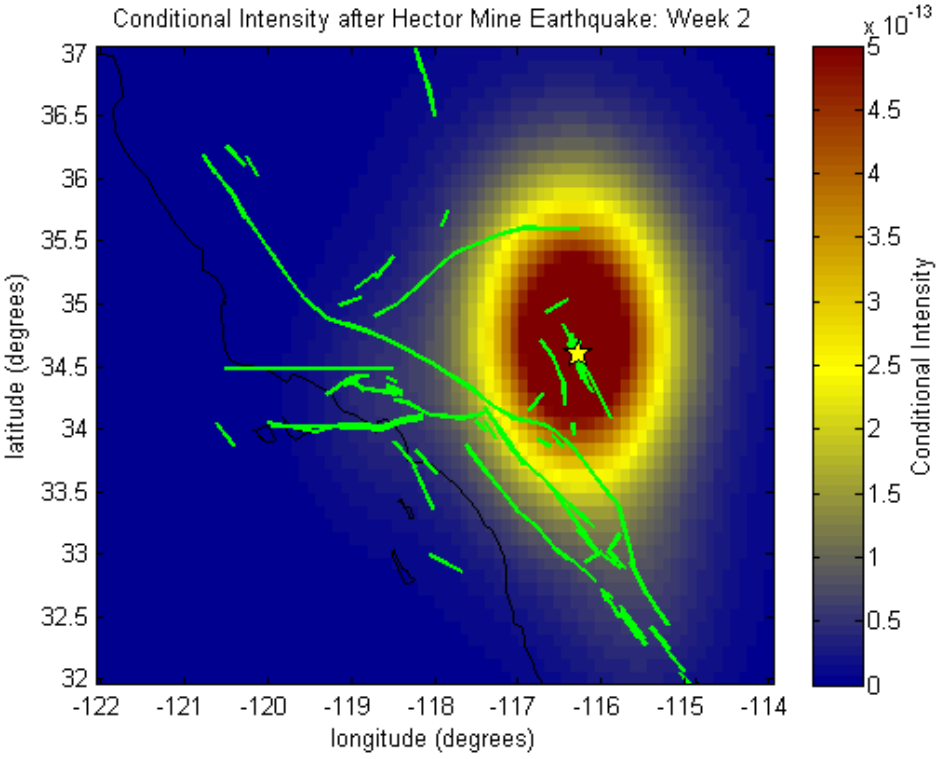
Conditional Intensity after Hector Mine Earthquake: Week 2
x 10^-13
5
4.5
4
3.5
3
2.5
2
1.5
1
0.5
0
Conditional Intensity
37
36.5
36
35.5
35
34.5
34
33.5
33
32.5
32
latitude (degrees)
-122
-121
-120
-119
-118
-117
-116
-115
-114
longitude (degrees)

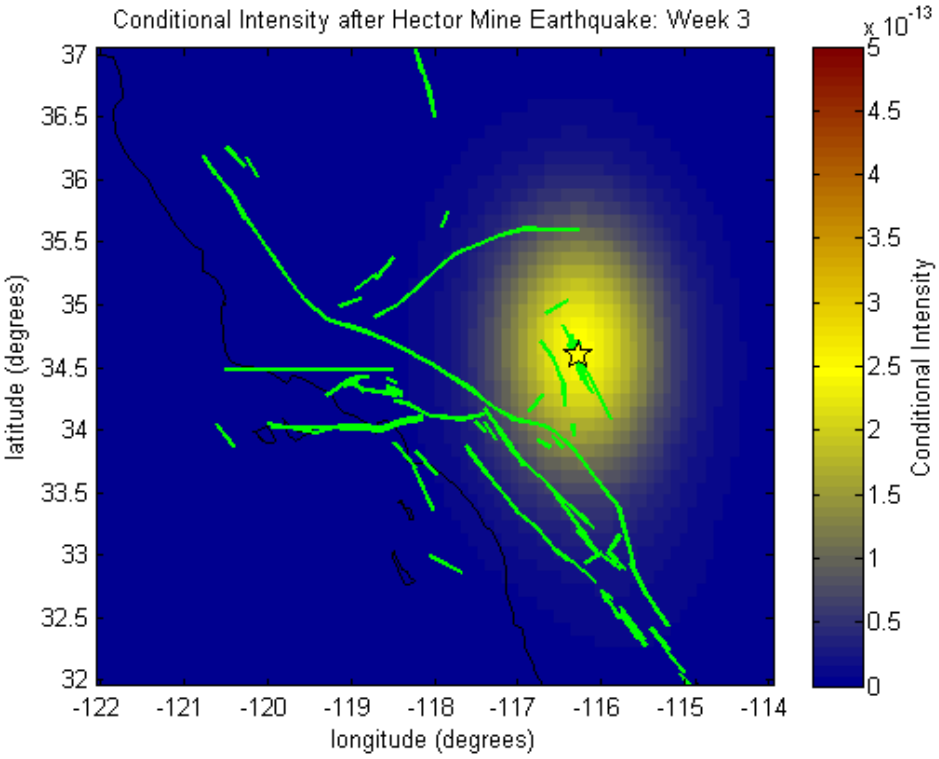
Conditional Intensity after Hector Mine Earthquake: Week 3
x 10^-13
5
4.5
4
3.5
3
2.5
2
1.5
1
0.5
0
Conditional Intensity
37
36.5
36
35.5
35
34.5
34
33.5
33
32.5
32
latitude (degrees)
-122
-121
-120
-119
-118
-117
-116
-115
-114
longitude (degrees)

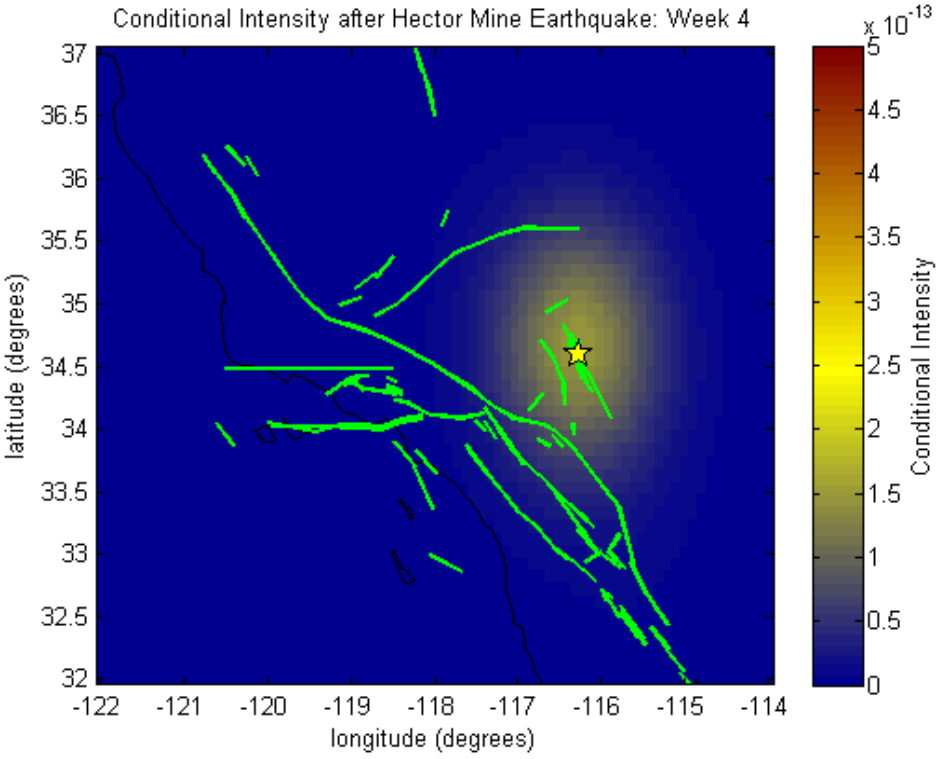
Conditional Intensity after Hector Mine Earthquake: Week 4
x 10^-13
5
4.5
4
3.5
3
2.5
2
1.5
1
0.5
0
Conditional Intensity
37
36.5
36
35.5
35
34.5
34
33.5
33
32.5
32
latitude (degrees)
-122
-121
-120
-119
-118
-117
-116
-115
-114
longitude (degrees)

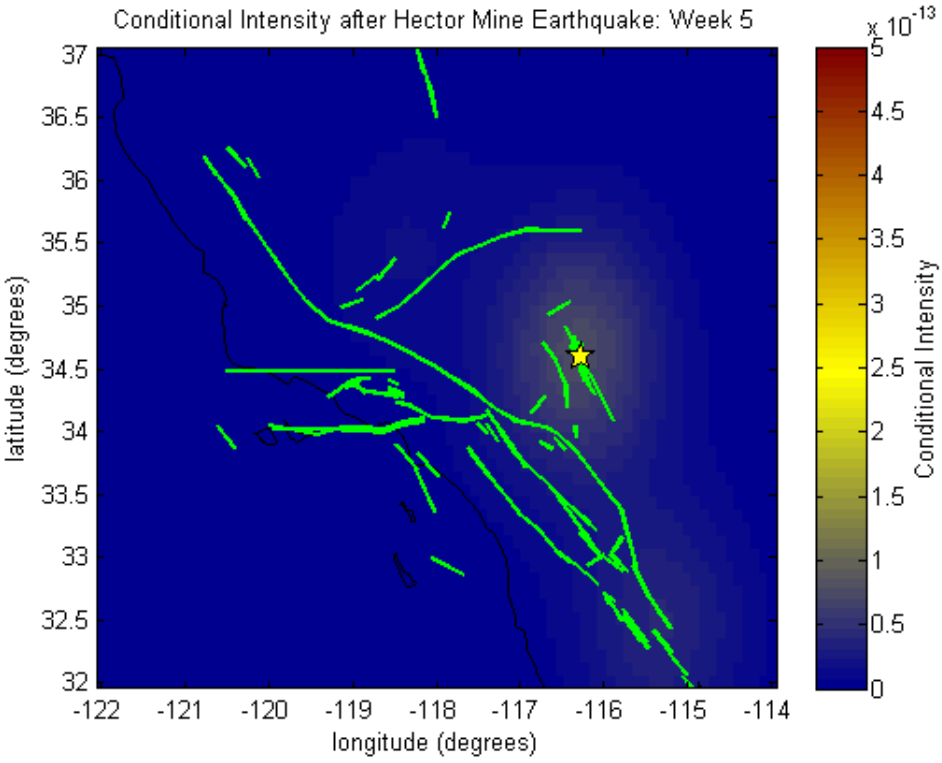
Conditional Intensity after Hector Mine Earthquake: Week 5
x 10^-13
5
4.5
4
3.5
3
2.5
2
1.5
1
0.5
0
Conditional Intensity
latitude (degrees)
37
36.5
36
35.5
35
34.5
34
33.5
33
32.5
32
-122
-121
-120
-119
-118
-117
-116
-115
-114
longitude (degrees)

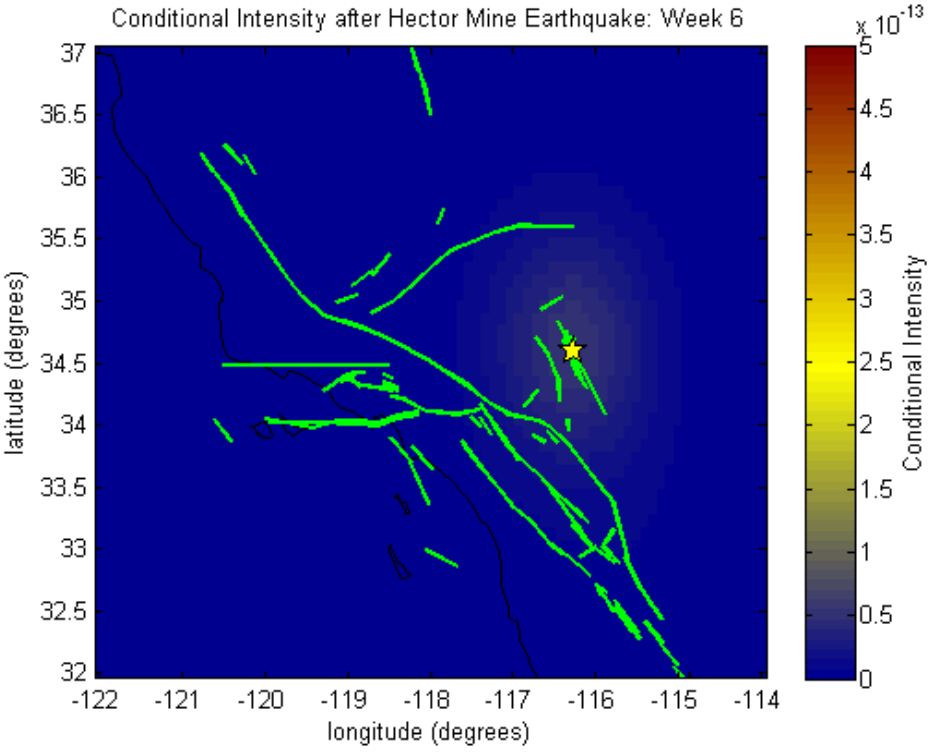
Conditional Intensity after Hector Mine Earthquake: Week 6
x 10^-13
5
4.5
4
3.5
3
2.5
2
1.5
1
0.5
0
Conditional Intensity
latitude (degrees)
37
36.5
36
35.5
35
34.5
34
33.5
33
32.5
32
-122
-121
-120
-119
-118
-117
-116
-115
-114
longitude (degrees)

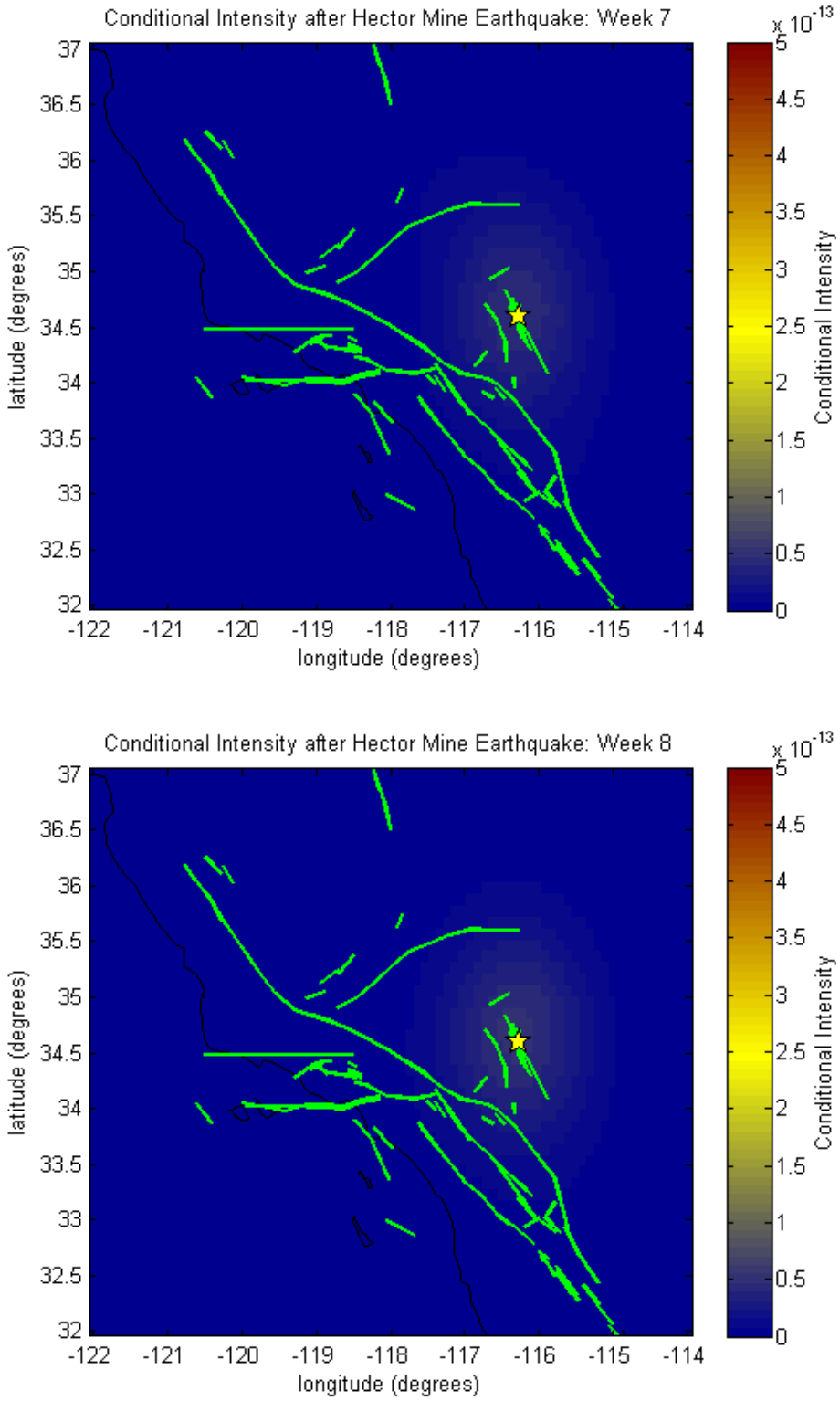

Figure 6.4: Conditional intensity (expected seismicity rates) during the eight weeks following the Hector Mine earthquake. Yellow and red regions indicate areas of elevated seismicity, whereas blue regions indicate areas of relative seismic quiescence. Green lines indicate active fault sections, and the yellow star displays the Hector Mine earthquake epicenter.

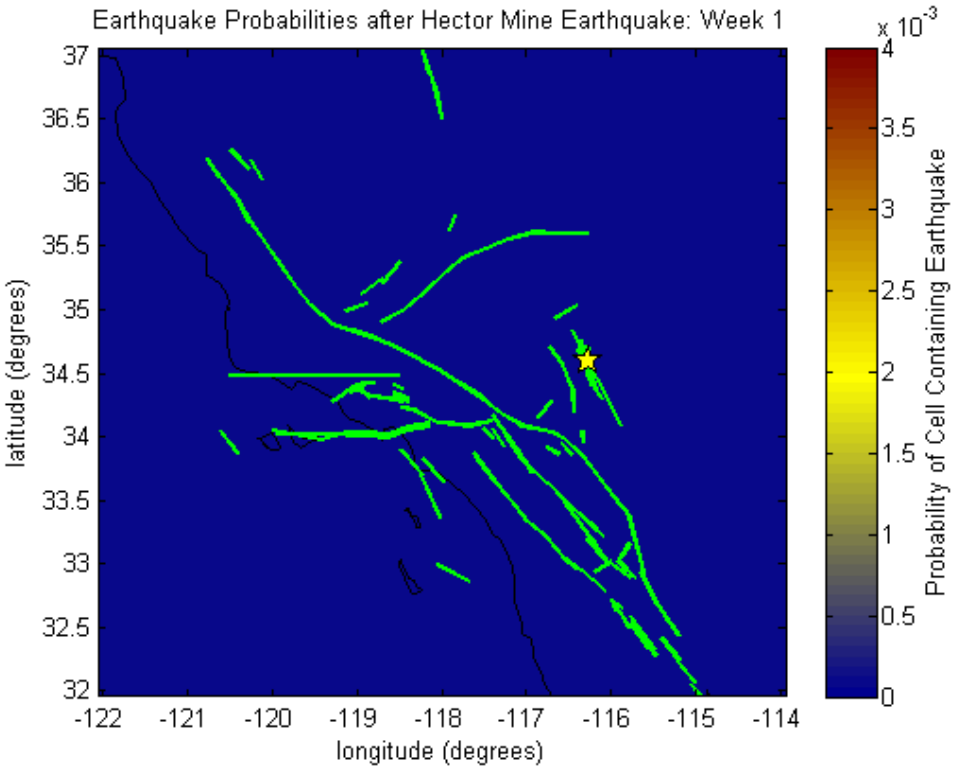
Earthquake Probabilities after Hector Mine Earthquake: Week 1
x 10^-3
4
3.5
3
2.5
2
1.5
1
0.5
0
Probability of Cell Containing Earthquake
37
36.5
36
35.5
35
34.5
34
33.5
33
32.5
32
latitude (degrees)
-122
-121
-120
-119
-118
-117
-116
-115
-114
longitude (degrees)

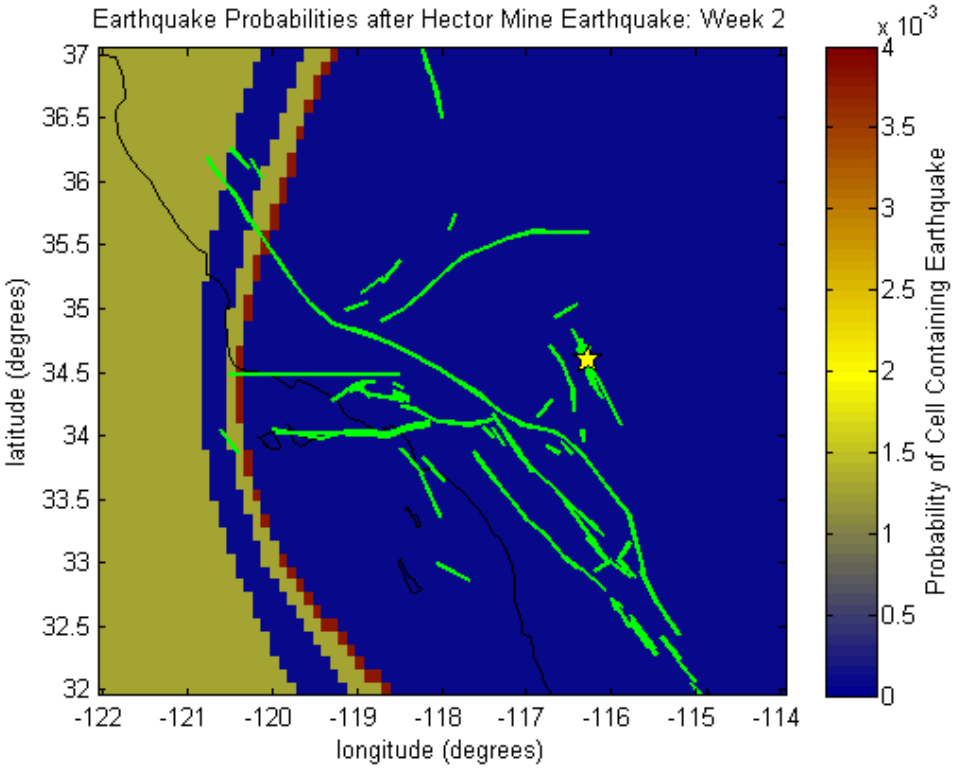
Earthquake Probabilities after Hector Mine Earthquake: Week 2
x 10^-3
4
3.5
3
2.5
2
1.5
1
0.5
0
Probability of Cell Containing Earthquake
37
36.5
36
35.5
35
34.5
34
33.5
33
32.5
32
latitude (degrees)
-122
-121
-120
-119
-118
-117
-116
-115
-114
longitude (degrees)

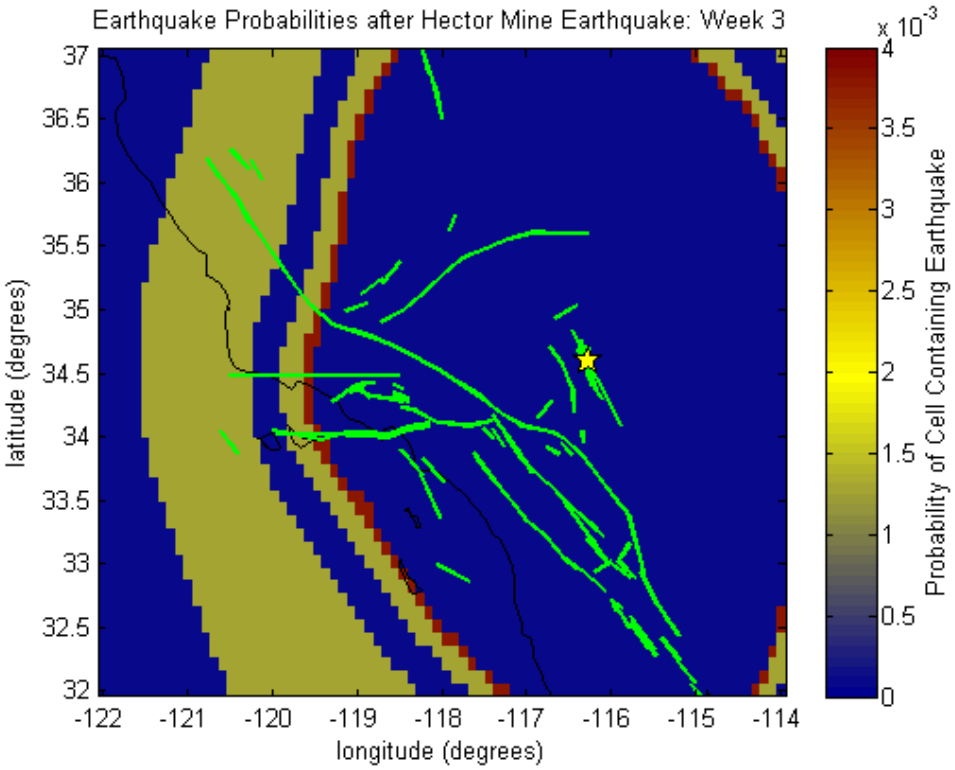
Earthquake Probabilities after Hector Mine Earthquake: Week 3
x 10^-3
4
3.5
3
2.5
2
1.5
1
0.5
0
Probability of Cell Containing Earthquake
37
36.5
36
35.5
35
34.5
34
33.5
33
32.5
32
latitude (degrees)
-122
-121
-120
-119
-118
-117
-116
-115
-114
longitude (degrees)

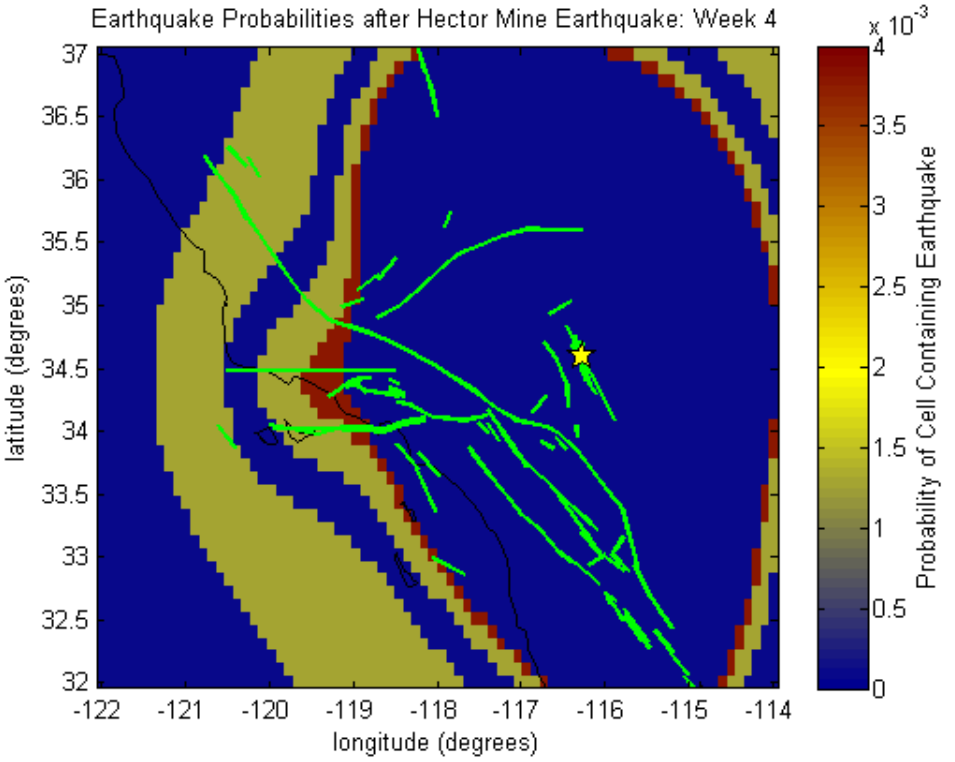
Earthquake Probabilities after Hector Mine Earthquake: Week 4
x 10^-3
4
3.5
3
2.5
2
1.5
1
0.5
0
Probability of Cell Containing Earthquake
37
36.5
36
35.5
35
34.5
34
33.5
33
32.5
32
latitude (degrees)
-122
-121
-120
-119
-118
-117
-116
-115
-114
longitude (degrees)

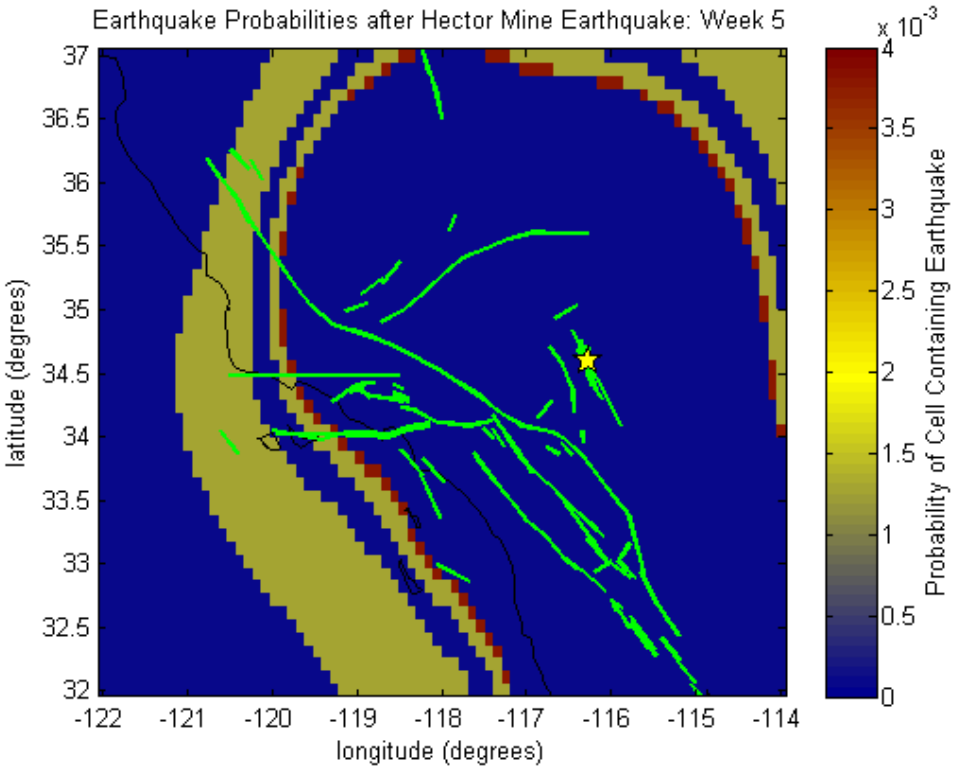
Earthquake Probabilities after Hector Mine Earthquake: Week 5
x 10^-3
4
3.5
3
2.5
2
1.5
1
0.5
0
Probability of Cell Containing Earthquake
37
36.5
36
35.5
35
34.5
34
33.5
33
32.5
32
latitude (degrees)
-122
-121
-120
-119
-118
-117
-116
-115
-114
longitude (degrees)

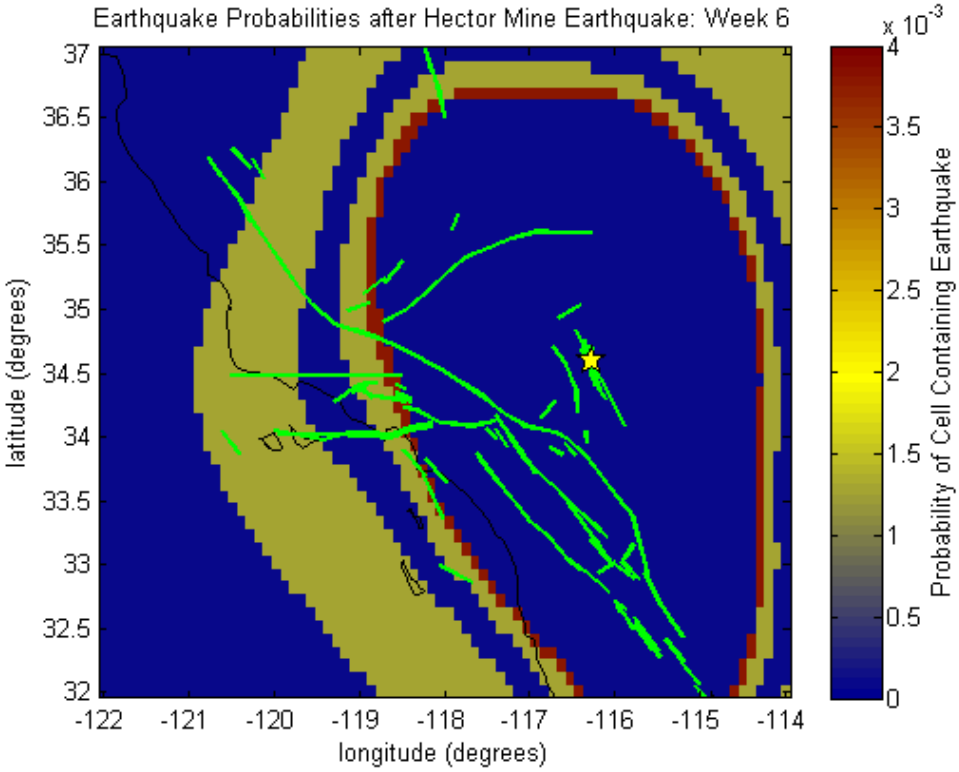
Earthquake Probabilities after Hector Mine Earthquake: Week 6
x 10^-3
4
3.5
3
2.5
2
1.5
1
0.5
0
Probability of Cell Containing Earthquake
37
36.5
36
35.5
35
34.5
34
33.5
33
32.5
32
latitude (degrees)
-122
-121
-120
-119
-118
-117
-116
-115
-114
longitude (degrees)

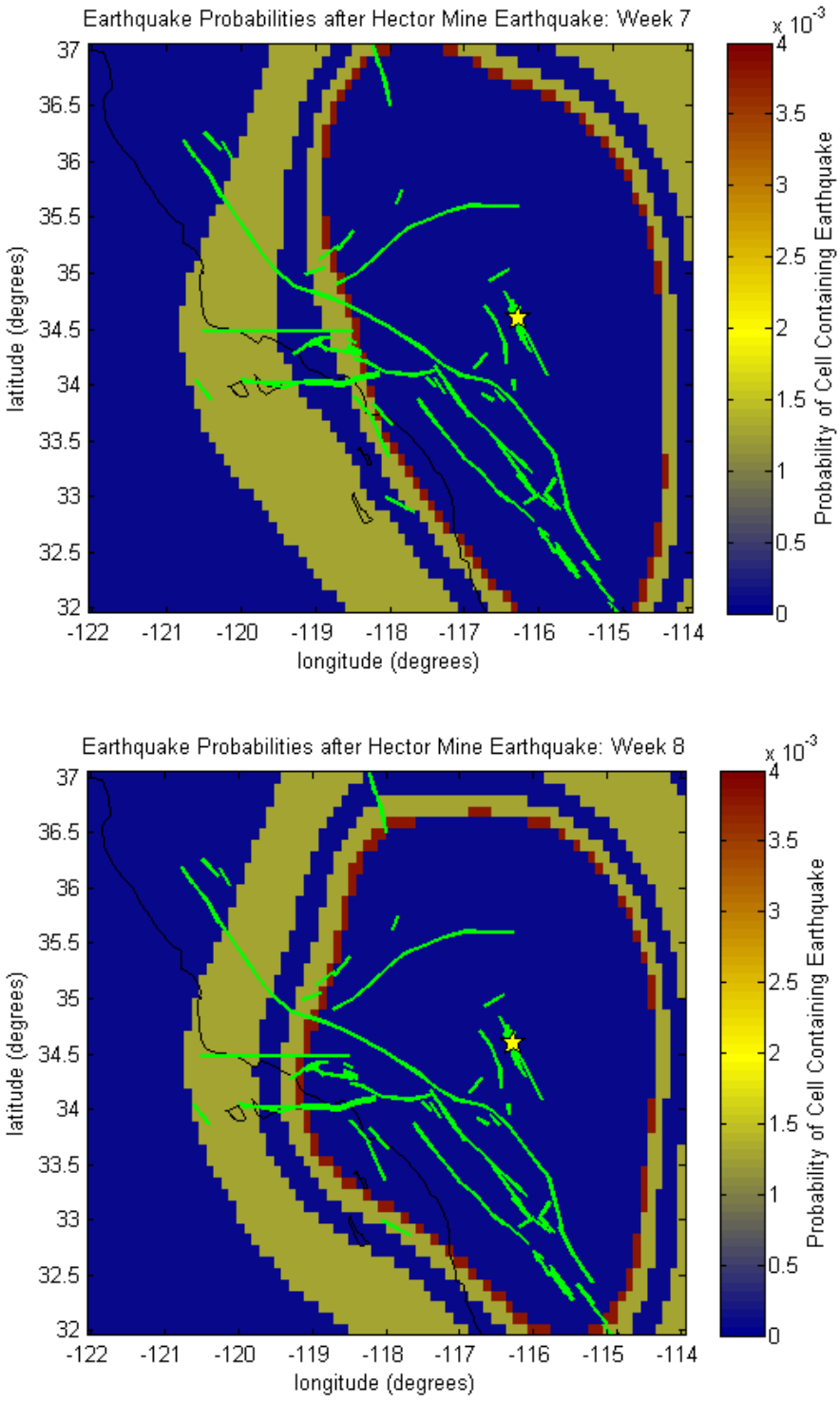

Figure 6.5: ETAS-based cell activation probabilities of each cell containing at least one earthquake during the eight weeks following the Hector Mine earthquake. Yellow and red regions indicate areas of elevated probability, whereas blue regions indicate low probability of a cell containing at least one earthquake. Green lines indicate major faults, and the yellow star indicates the Hector Mine earthquake epicenter.

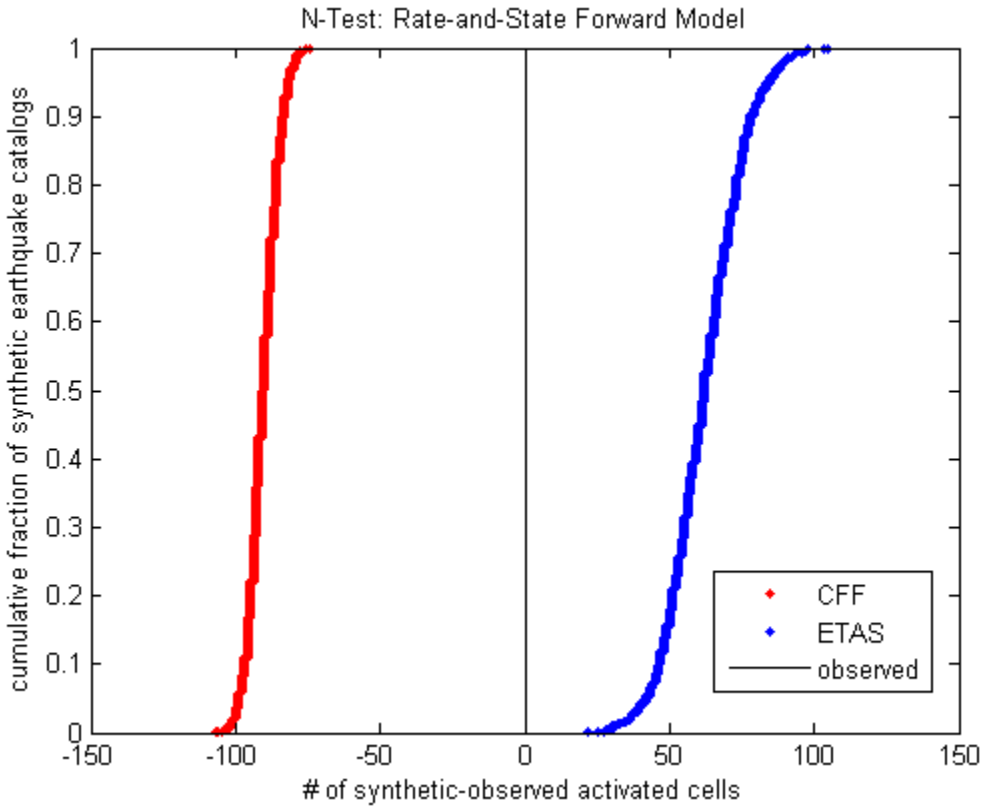

Figure 6.6: N-test results for forward model ΔCFF-based (red curve) and ETAS-based (blue curve) earthquake forecasts. The blue and red curves represent the normalized, cumulative number of synthetic seismicity distributions relative to the difference between the number of synthetic and observed filled zones. The black line indicates where the difference between the number of synthetic and observed filled zones is zero.

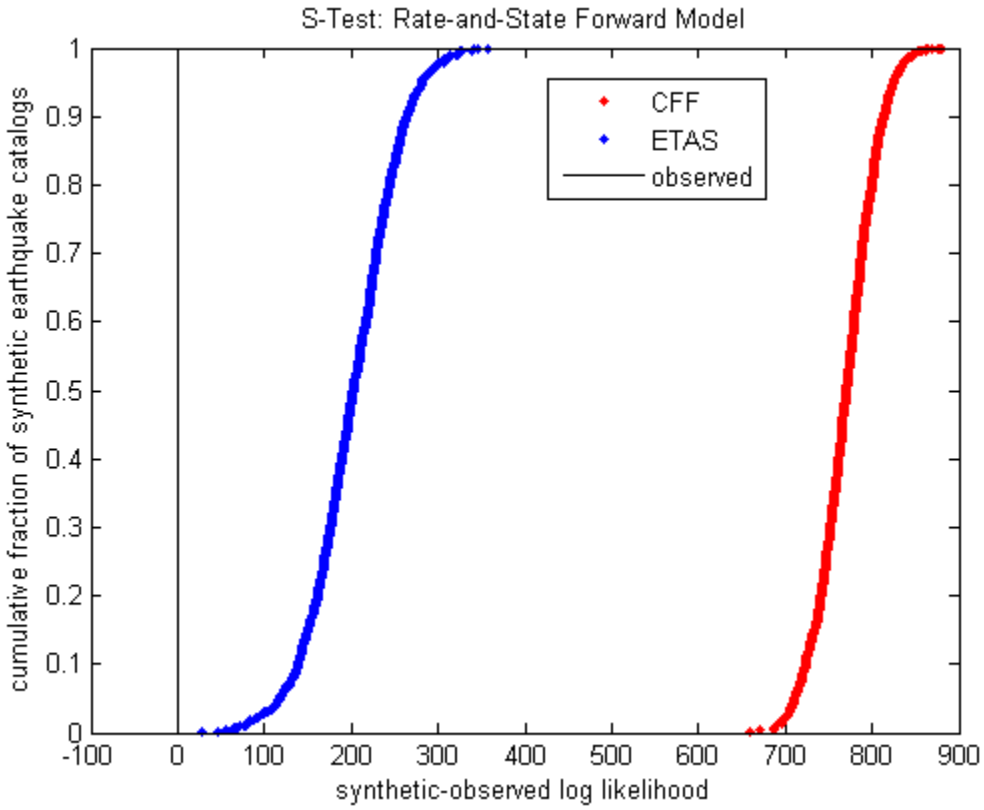

Figure 6.7: S-test results for forward model ΔCFF-based (red curve) and ETAS-based (blue curve) earthquake forecasts. The red and blue curves represent the normalized, cumulative numbers of synthetic seismicity distributions relative to the difference between the synthetic and observed log likelihood. The black line indicates where the difference between the synthetic and observed log likelihood scores is zero.

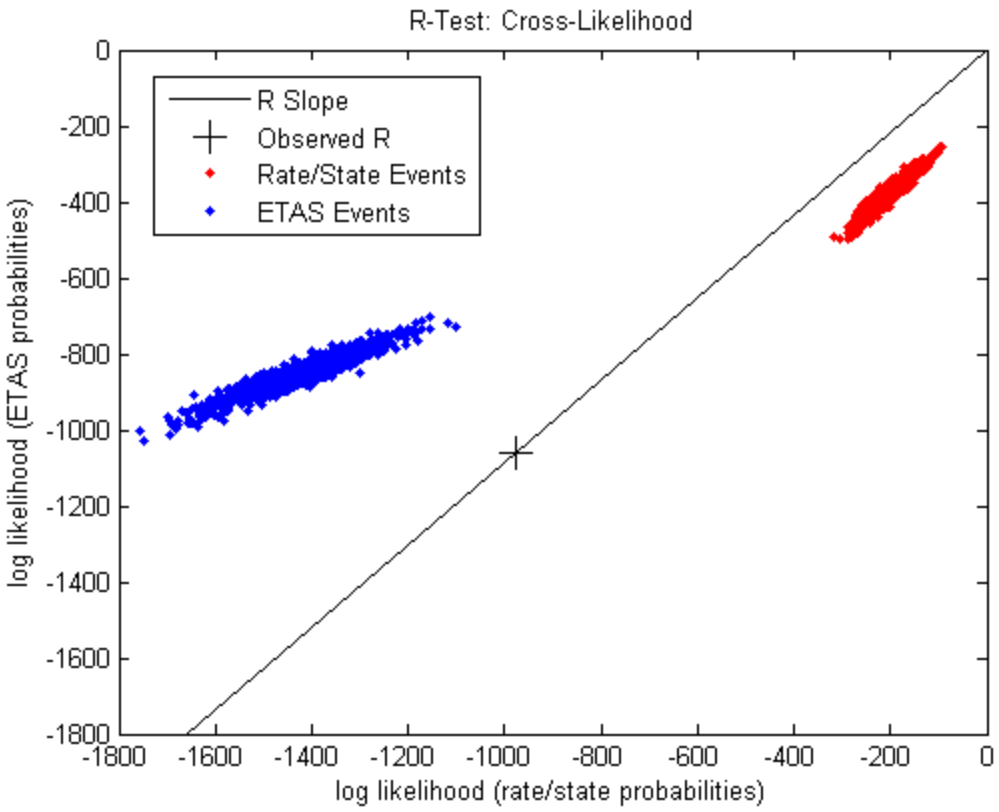

Figure 6.8: R-test cross-likelihood plot comparing the forward model ΔCFF- and ETAS-based earthquake forecasts. The red dots represent simulated log likelihood values consistent with the ΔCFF-based synthetic earthquake maps, and the blue dots represent log likelihood values consistent with ETAS. The observed R value is indicated by the black cross, and the black line includes the locus of likelihood values with the same ratio of ETAS to rate-and-state as the observed. If the rate-and-state model described the earthquake distribution well, the black cross should lie amongst the red dots.

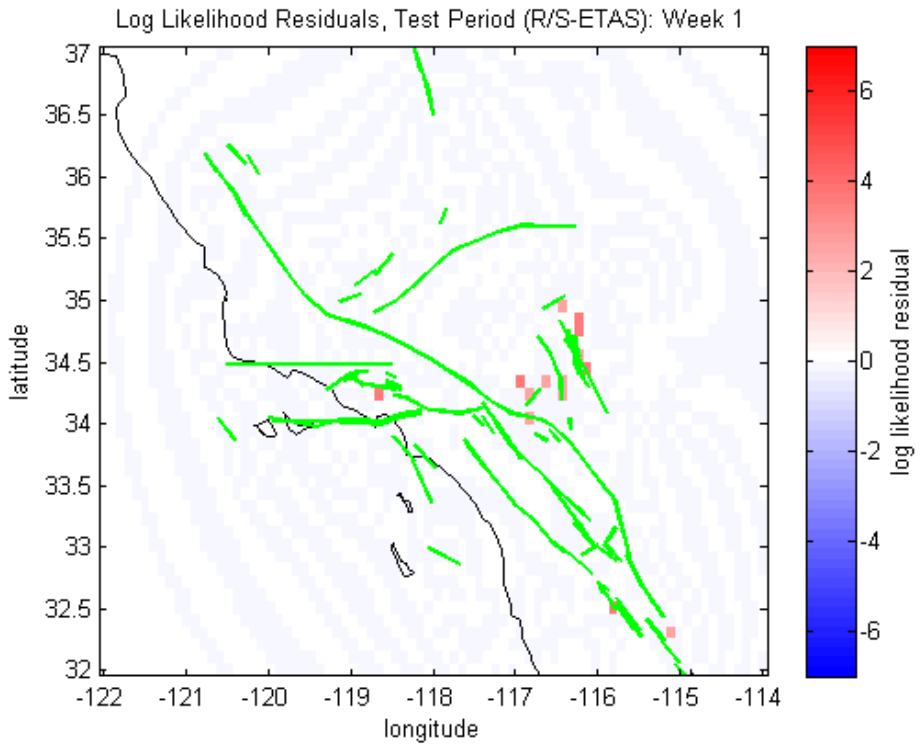
Log Likelihood Residuals, Test Period (R/S-ETAS): Week 1
latitude
longitude
log likelihood residual
37
36.5
36
35.5
35
34.5
34
33.5
33
32.5
32
-122
-121
-120
-119
-118
-117
-116
-115
-114
6
4
2
0
-2
-4
-6

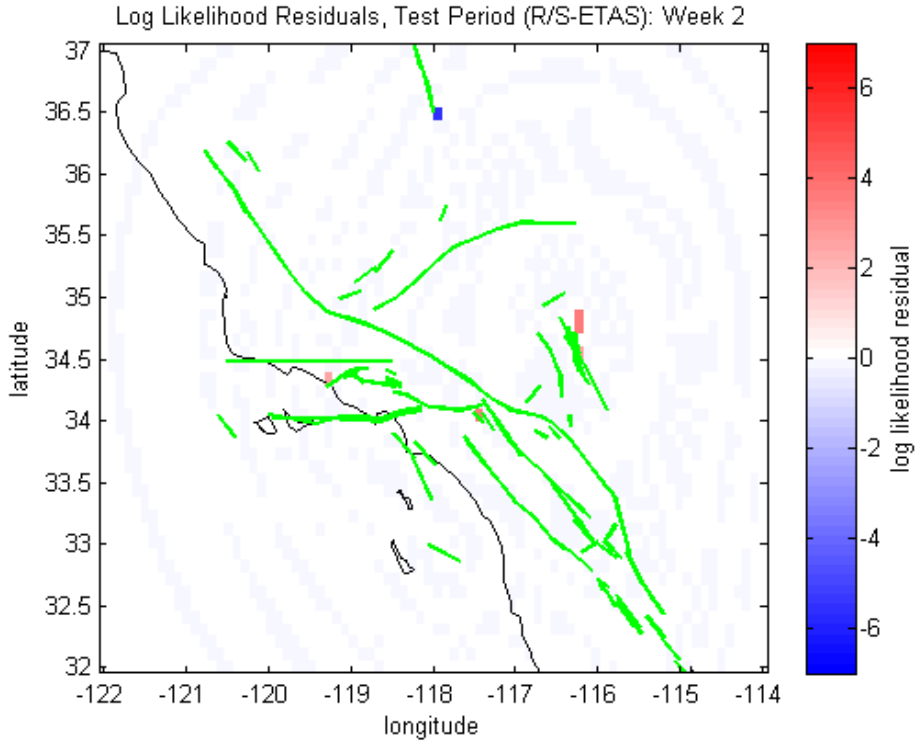
Log Likelihood Residuals, Test Period (R/S-ETAS): Week 2
latitude
longitude
log likelihood residual
37
36.5
36
35.5
35
34.5
34
33.5
33
32.5
32
-122
-121
-120
-119
-118
-117
-116
-115
-114
6
4
2
0
-2
-4
-6

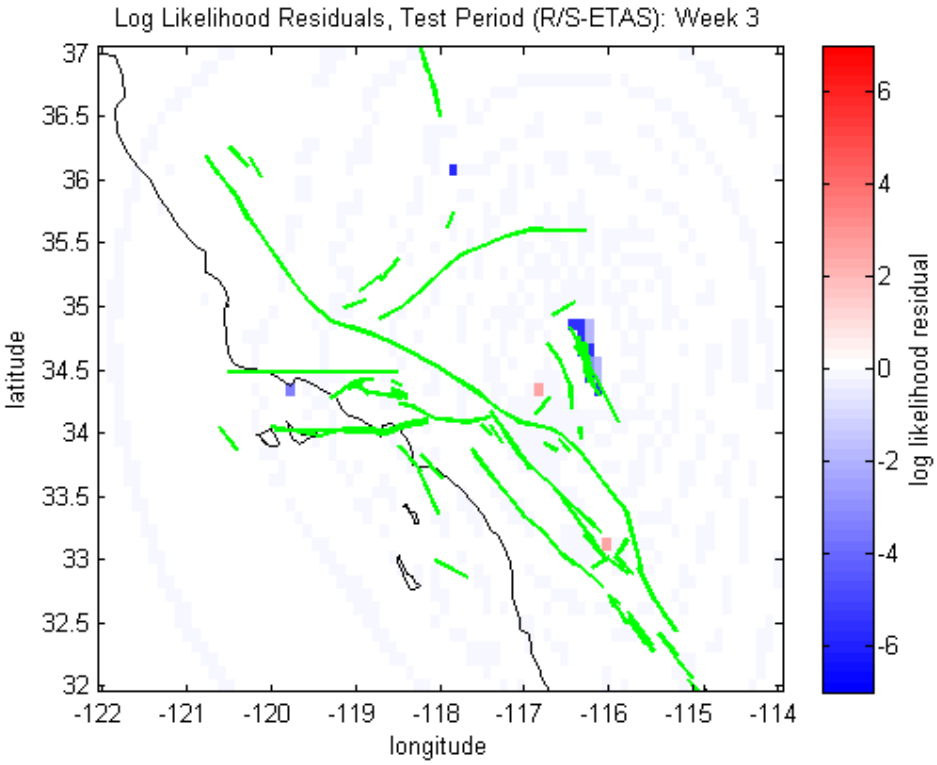
Log Likelihood Residuals, Test Period (R/S-ETAS): Week 3
latitude
longitude
log likelihood residual
37
36.5
36
35.5
35
34.5
34
33.5
33
32.5
32
-122
-121
-120
-119
-118
-117
-116
-115
-114
6
4
2
0
-2
-4
-6

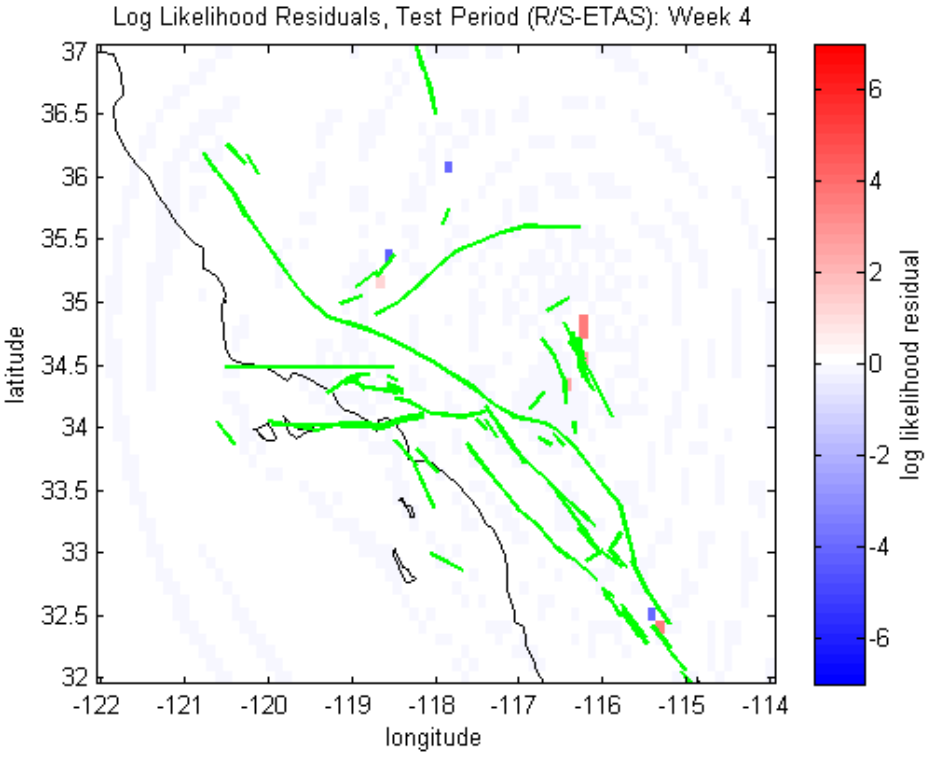
Log Likelihood Residuals, Test Period (R/S-ETAS): Week 4
latitude
longitude
log likelihood residual
37
36.5
36
35.5
35
34.5
34
33.5
33
32.5
32
-122
-121
-120
-119
-118
-117
-116
-115
-114
6
4
2
0
-2
-4
-6

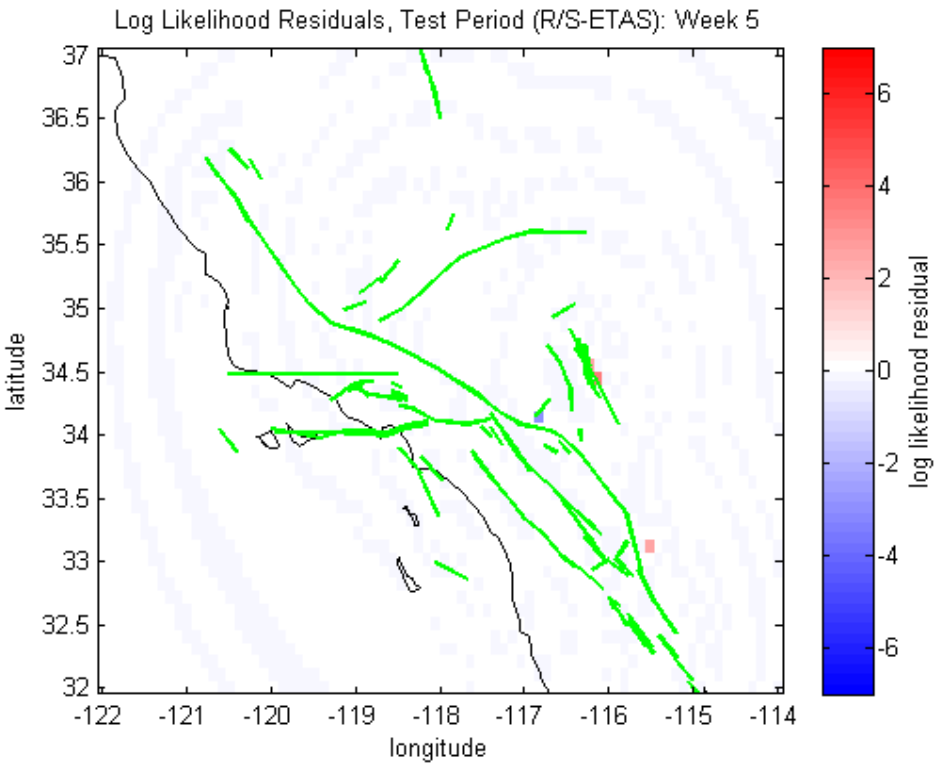
Log Likelihood Residuals, Test Period (R/S-ETAS): Week 5
latitude
longitude
log likelihood residual
37
36.5
36
35.5
35
34.5
34
33.5
33
32.5
32
-122
-121
-120
-119
-118
-117
-116
-115
-114
6
4
2
0
-2
-4
-6

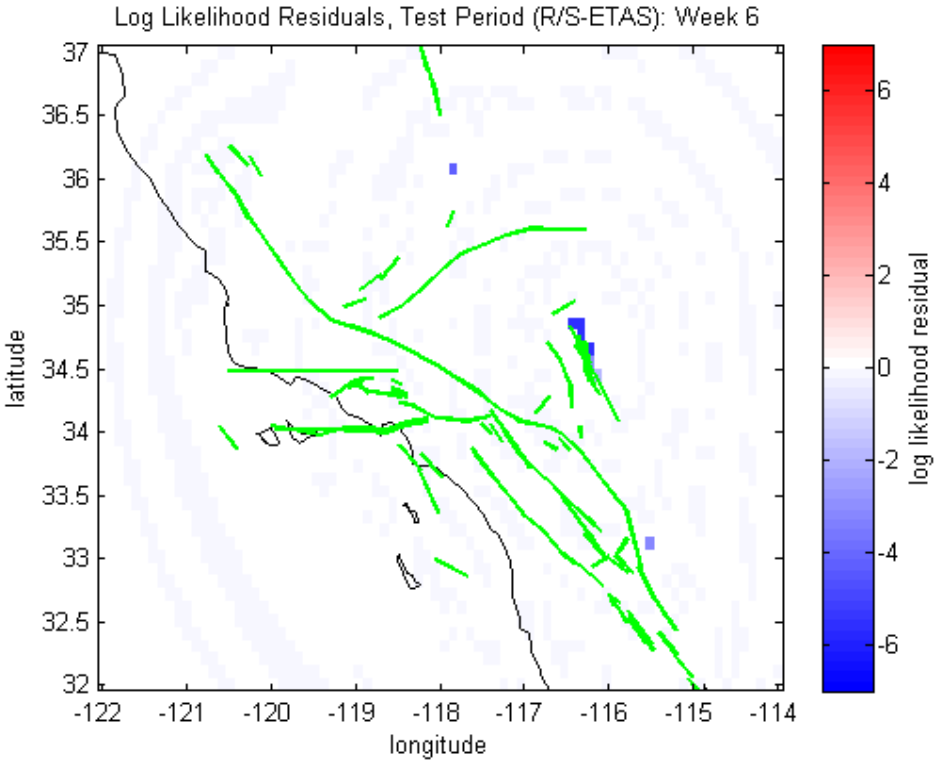
Log Likelihood Residuals, Test Period (R/S-ETAS): Week 6
latitude
longitude
log likelihood residual
37
36.5
36
35.5
35
34.5
34
33.5
33
32.5
32
-122
-121
-120
-119
-118
-117
-116
-115
-114
6
4
2
0
-2
-4
-6

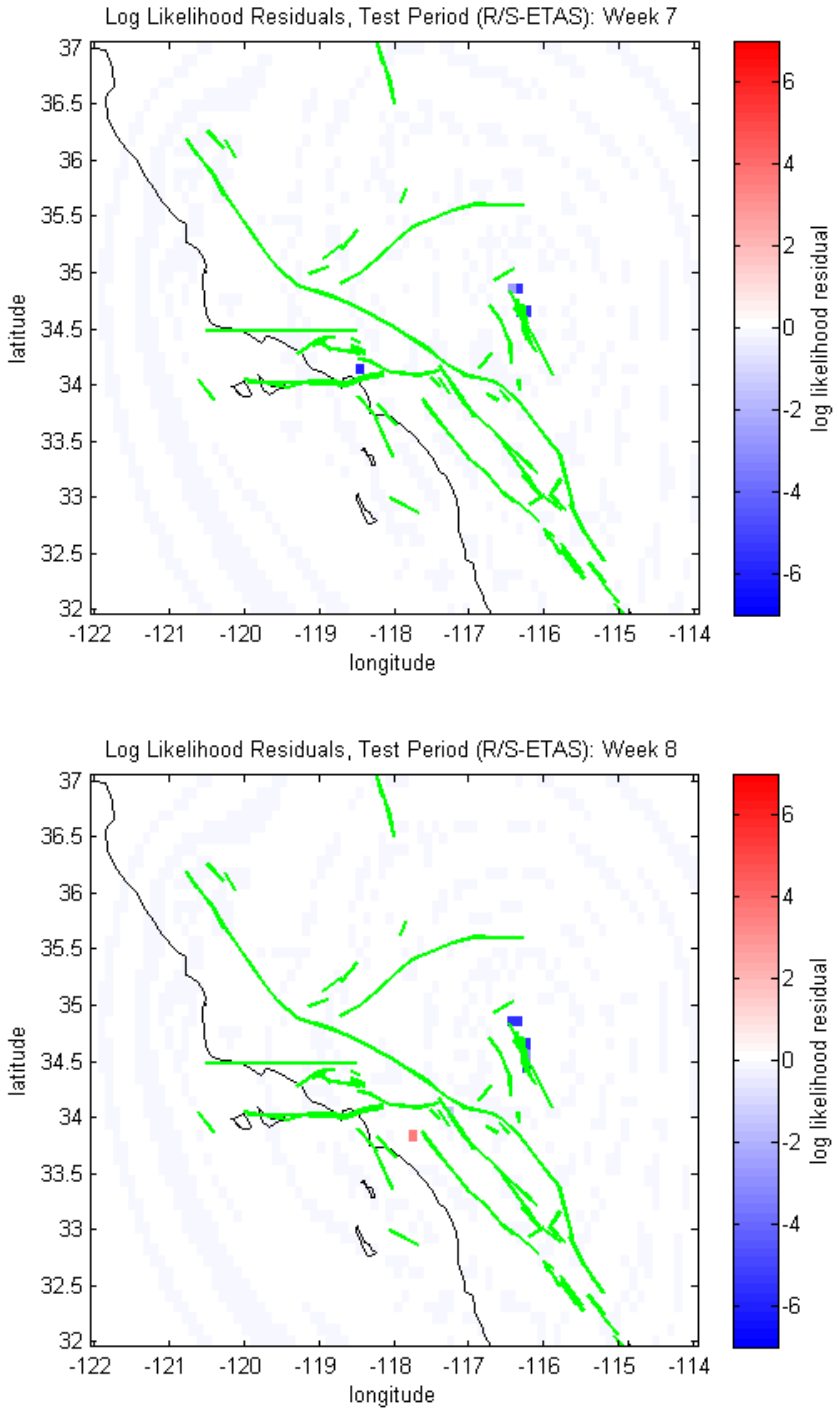

Figure 6.9: Spatial log likelihood residual map, displaying the difference between log likelihood values calculated from forward model ΔCFF- and ETAS-based earthquake forecasts. Red areas indicate where the ΔCFF-based forecast outperforms the ETAS-based forecast, and are prominent in the Hector Mine aftershock zone in the first few weeks. Blue areas display where ETAS more effectively indicates earthquake locations and times during the target period. White regions indicate a negligible difference between the two forecasts' reliability. Green lines outline active fault sections, and the yellow star indicates the Hector Mine earthquake epicenter.

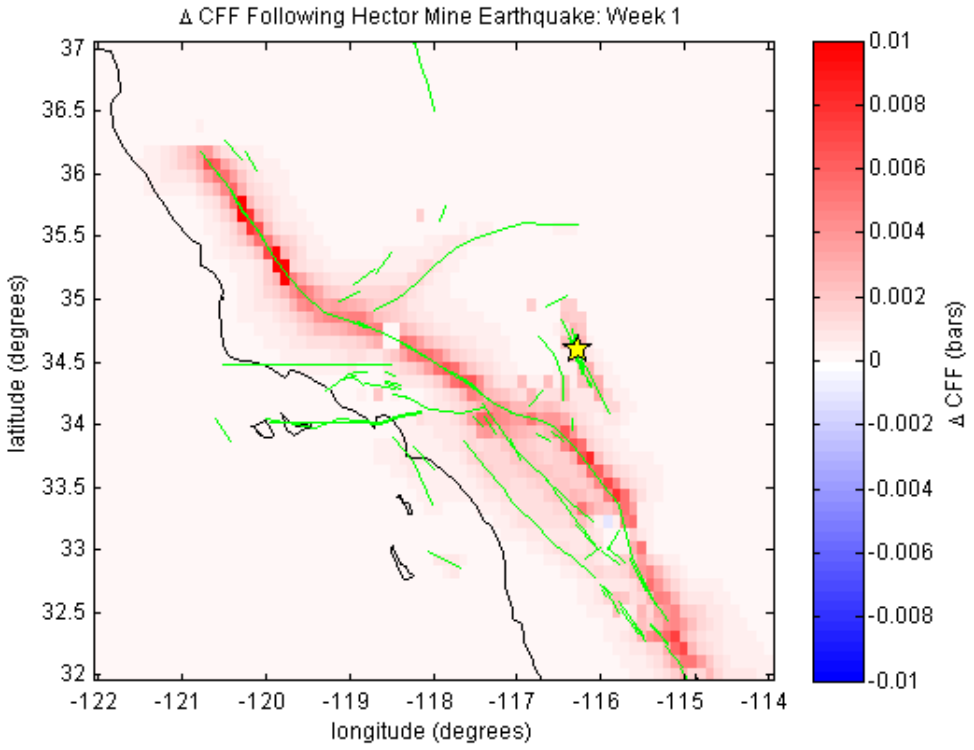
Δ CFF Following Hector Mine Earthquake: Week 1
latitude (degrees)
longitude (degrees)
Δ CFF (bars)
37
36.5
36
35.5
35
34.5
34
33.5
33
32.5
32
-122
-121
-120
-119
-118
-117
-116
-115
-114
0.01
0.008
0.006
0.004
0.002
0
-0.002
-0.004
-0.006
-0.008
-0.01

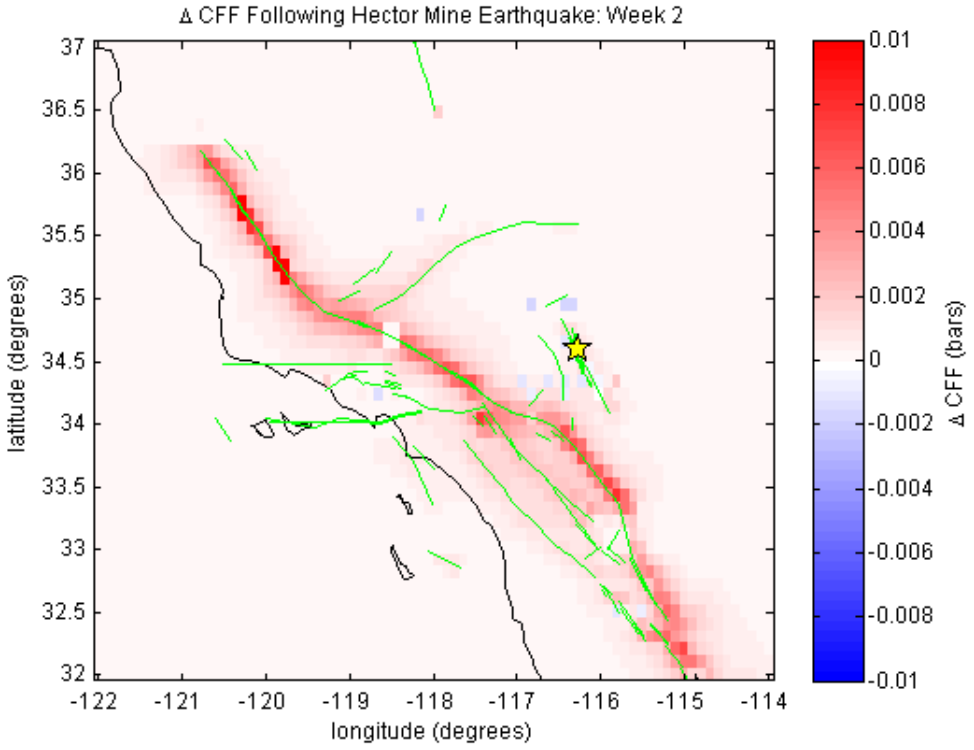
Δ CFF Following Hector Mine Earthquake: Week 2
latitude (degrees)
longitude (degrees)
Δ CFF (bars)
37
36.5
36
35.5
35
34.5
34
33.5
33
32.5
32
-122
-121
-120
-119
-118
-117
-116
-115
-114
0.01
0.008
0.006
0.004
0.002
0
-0.002
-0.004
-0.006
-0.008
-0.01

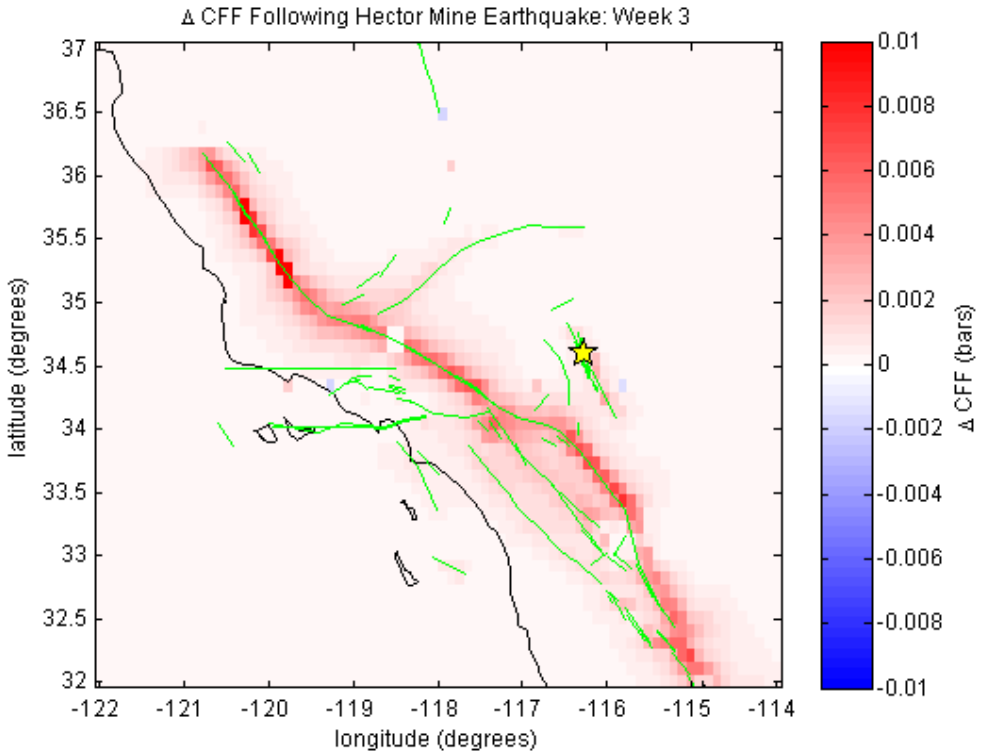
Δ CFF Following Hector Mine Earthquake: Week 3
latitude (degrees)
longitude (degrees)
Δ CFF (bars)
37
36.5
36
35.5
35
34.5
34
33.5
33
32.5
32
-122
-121
-120
-119
-118
-117
-116
-115
-114
0.01
0.008
0.006
0.004
0.002
0
-0.002
-0.004
-0.006
-0.008
-0.01

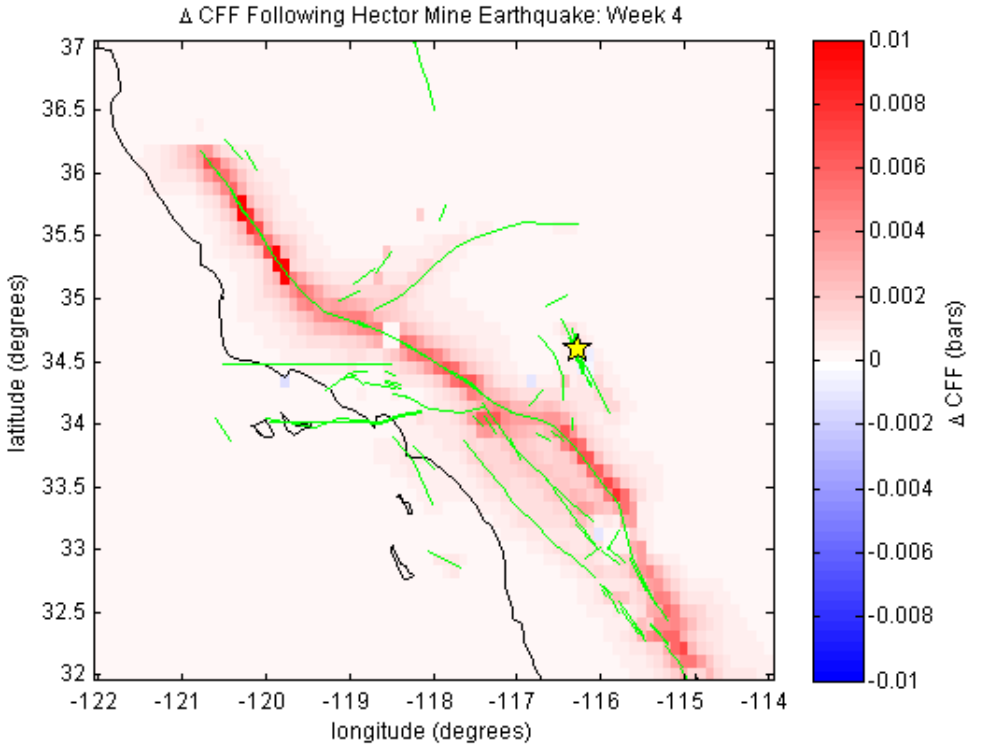
Δ CFF Following Hector Mine Earthquake: Week 4
latitude (degrees)
longitude (degrees)
Δ CFF (bars)
37
36.5
36
35.5
35
34.5
34
33.5
33
32.5
32
-122
-121
-120
-119
-118
-117
-116
-115
-114
0.01
0.008
0.006
0.004
0.002
0
-0.002
-0.004
-0.006
-0.008
-0.01

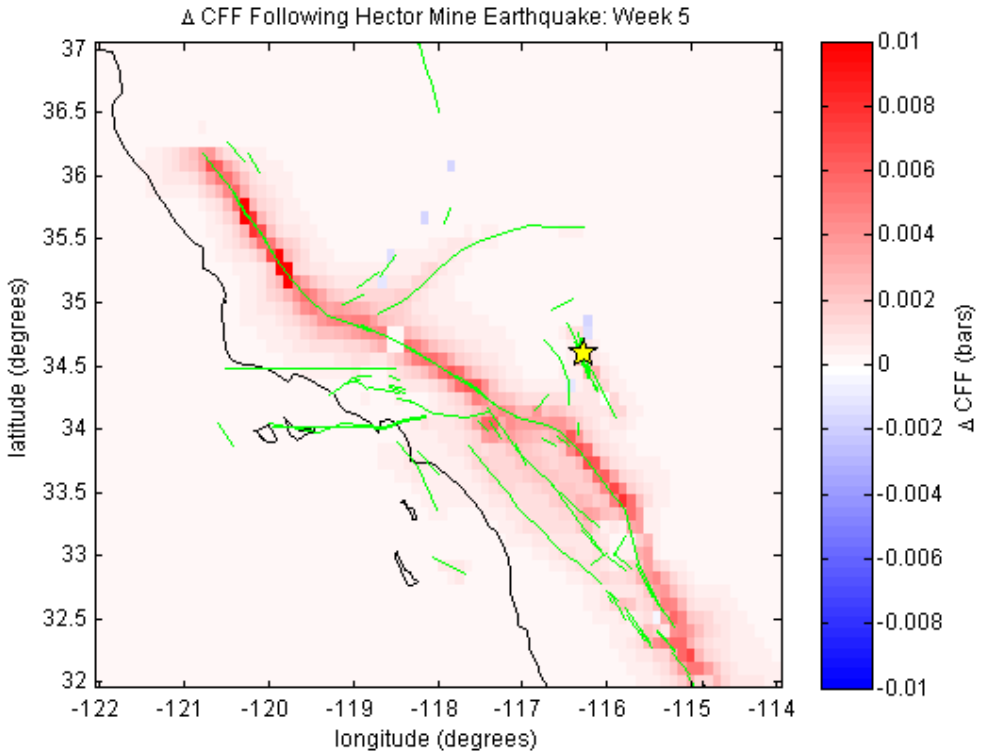
Δ CFF Following Hector Mine Earthquake: Week 5
latitude (degrees)
longitude (degrees)
Δ CFF (bars)
37
36.5
36
35.5
35
34.5
34
33.5
33
32.5
32
-122
-121
-120
-119
-118
-117
-116
-115
-114
0.01
0.008
0.006
0.004
0.002
0
-0.002
-0.004
-0.006
-0.008
-0.01

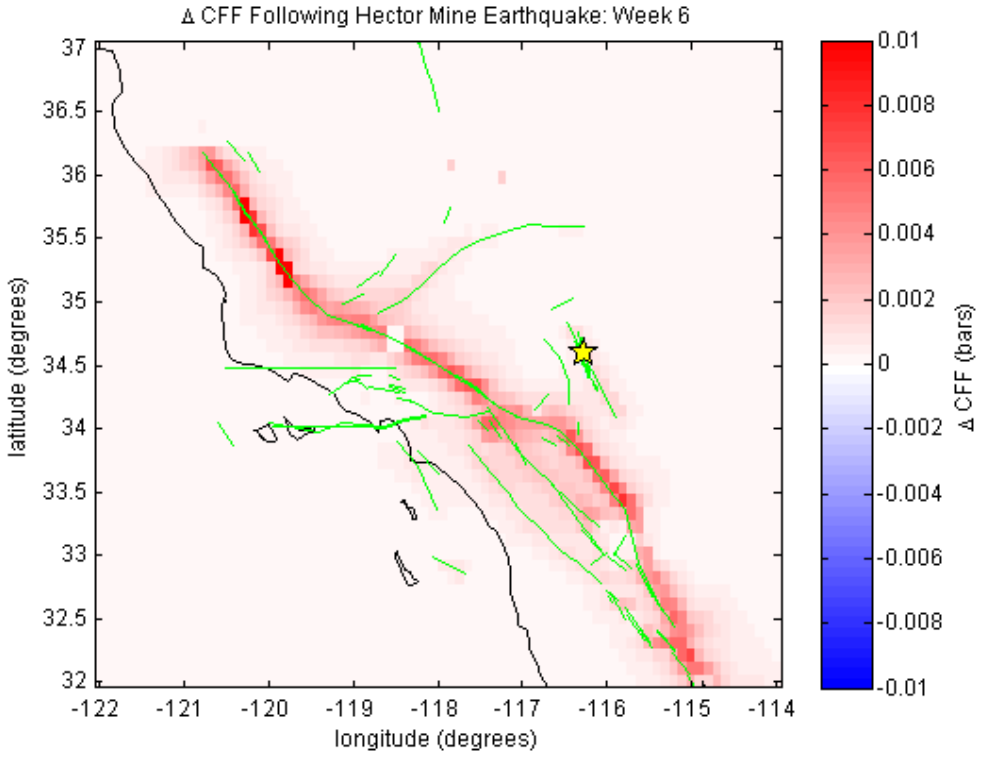
Δ CFF Following Hector Mine Earthquake: Week 6
latitude (degrees)
longitude (degrees)
Δ CFF (bars)
37
36.5
36
35.5
35
34.5
34
33.5
33
32.5
32
-122
-121
-120
-119
-118
-117
-116
-115
-114
0.01
0.008
0.006
0.004
0.002
0
-0.002
-0.004
-0.006
-0.008
-0.01

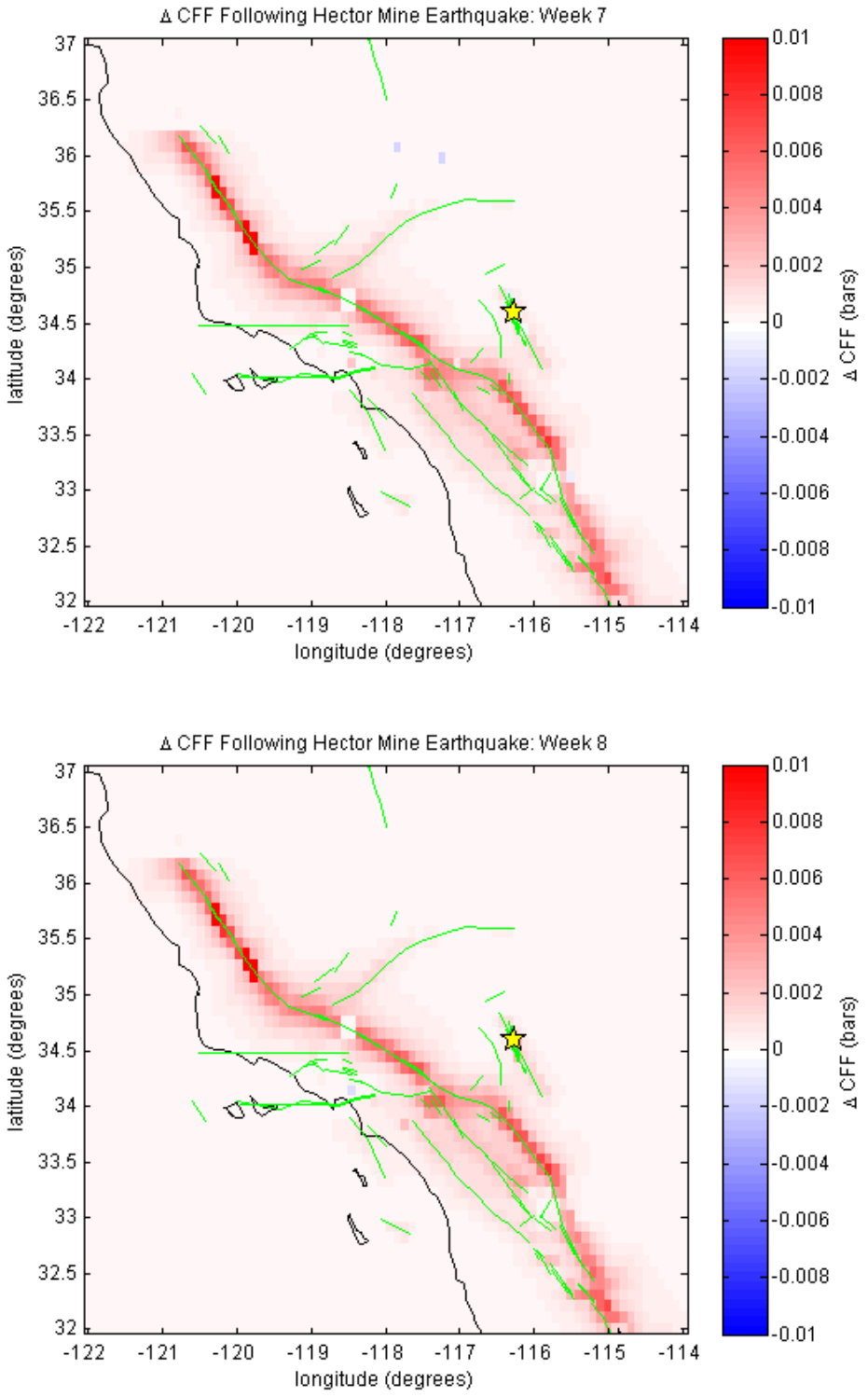

Figure 6.10: Inverse model ΔCFF evolution during the eight weeks following the Hector Mine earthquake. Red areas indicate where ΔCFF has increased, whereas blue areas delineate stress shadows. Green lines indicate active fault sections and the yellow star displays the Hector Mine earthquake epicenter.

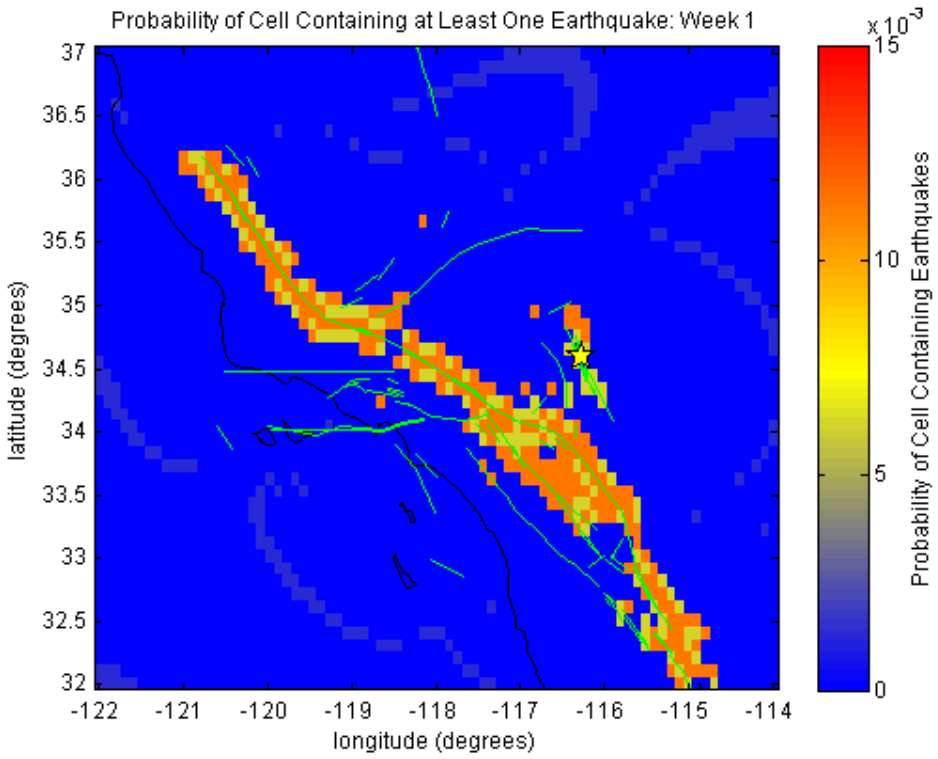
Probability of Cell Containing at Least One Earthquake: Week 1
x 10^-3
15
10
5
0
Probability of Cell Containing Earthquakes
latitude (degrees)
37
36.5
36
35.5
35
34.5
34
33.5
33
32.5
32
-122
-121
-120
-119
-118
-117
-116
-115
-114
longitude (degrees)

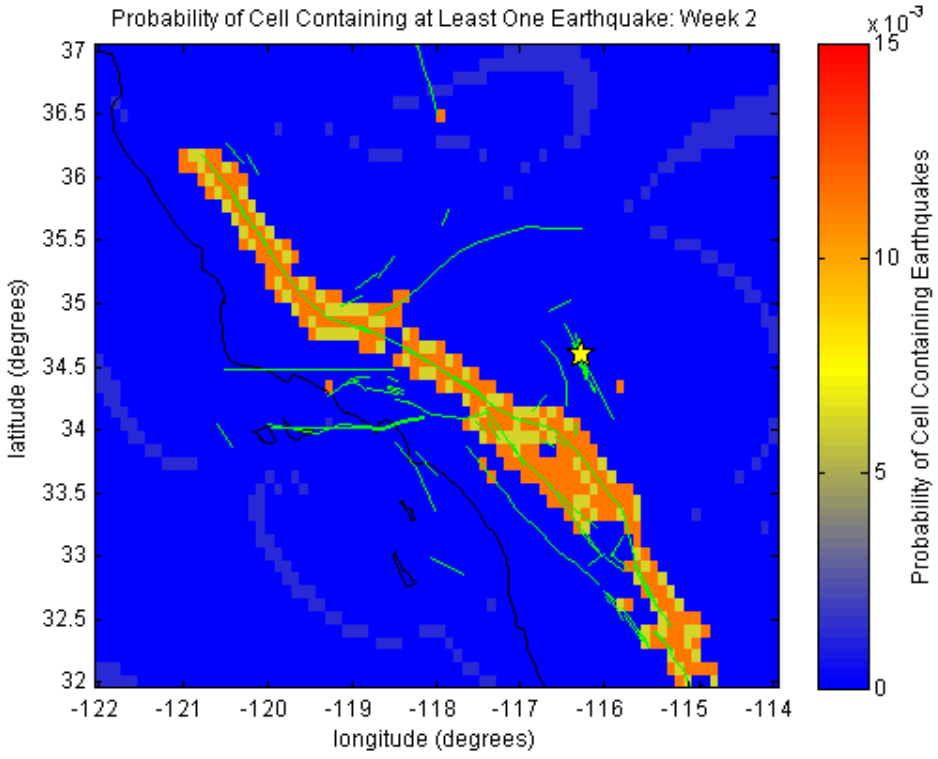
Probability of Cell Containing at Least One Earthquake: Week 2
x 10^-3
15
10
5
0
Probability of Cell Containing Earthquakes
latitude (degrees)
37
36.5
36
35.5
35
34.5
34
33.5
33
32.5
32
-122
-121
-120
-119
-118
-117
-116
-115
-114
longitude (degrees)

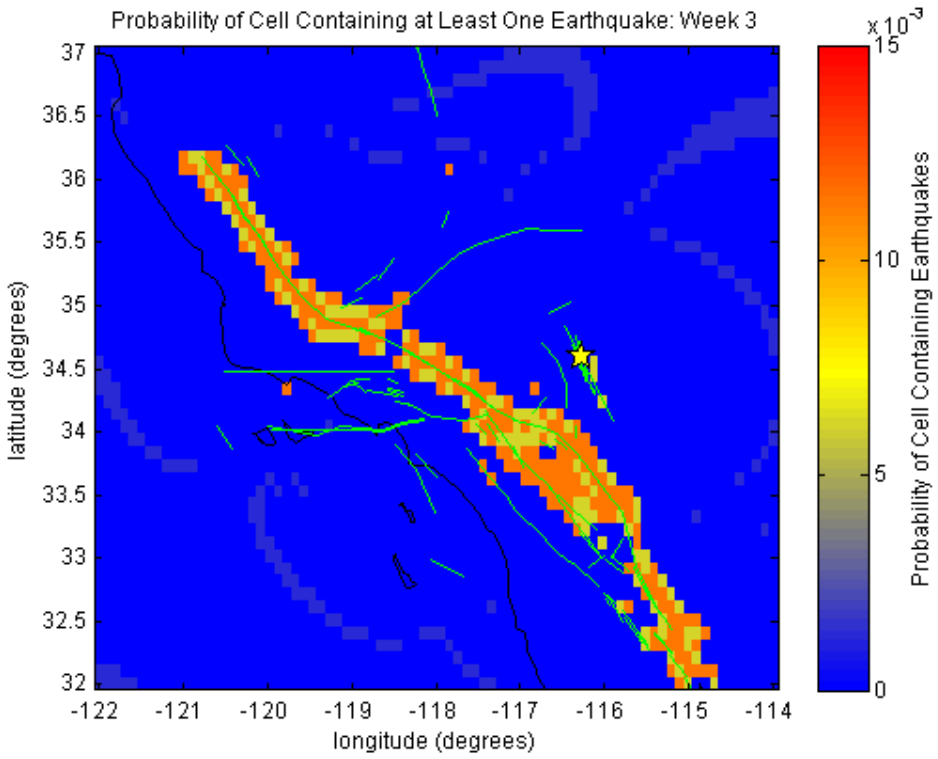
Probability of Cell Containing at Least One Earthquake: Week 3
x 10^-3
15
10
5
0
Probability of Cell Containing Earthquakes
latitude (degrees)
37
36.5
36
35.5
35
34.5
34
33.5
33
32.5
32
-122
-121
-120
-119
-118
-117
-116
-115
-114
longitude (degrees)

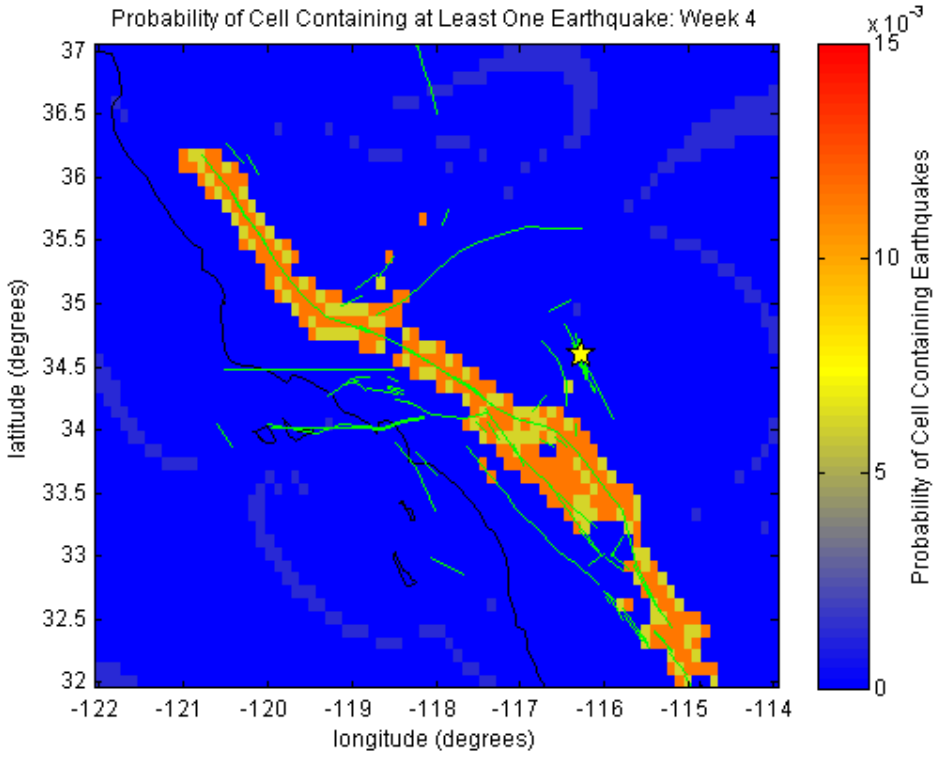
Probability of Cell Containing at Least One Earthquake: Week 4
x 10^-3
15
10
5
0
Probability of Cell Containing Earthquakes
latitude (degrees)
37
36.5
36
35.5
35
34.5
34
33.5
33
32.5
32
-122
-121
-120
-119
-118
-117
-116
-115
-114
longitude (degrees)

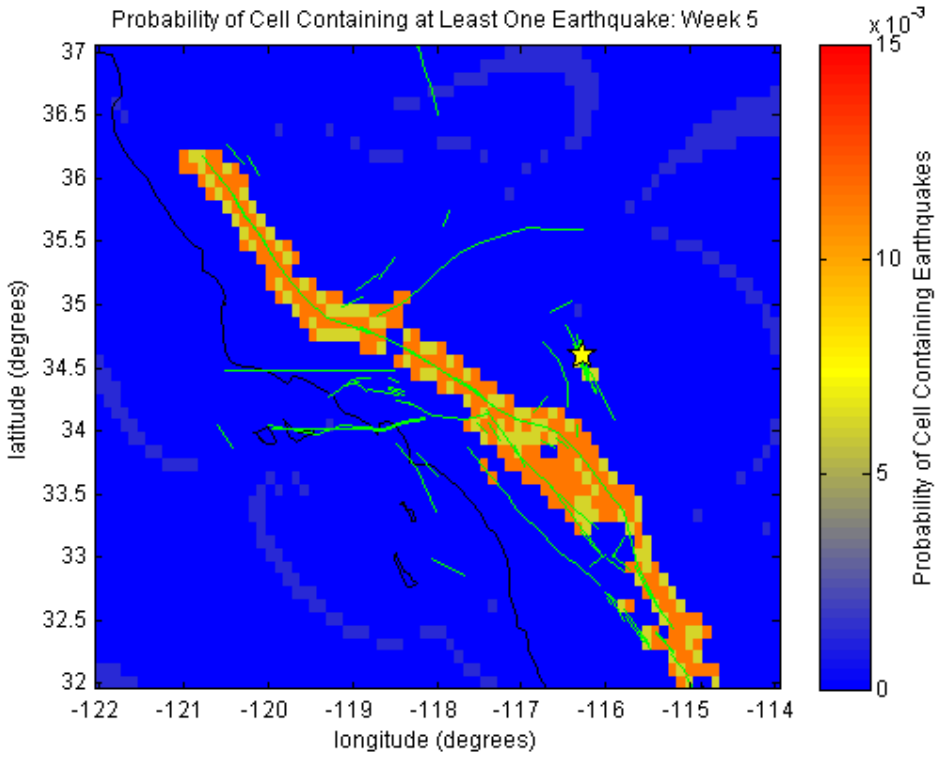
Probability of Cell Containing at Least One Earthquake: Week 5
x 10^-3
15
10
5
0
Probability of Cell Containing Earthquakes
37
36.5
36
35.5
35
34.5
34
33.5
33
32.5
32
latitude (degrees)
-122
-121
-120
-119
-118
-117
-116
-115
-114
longitude (degrees)

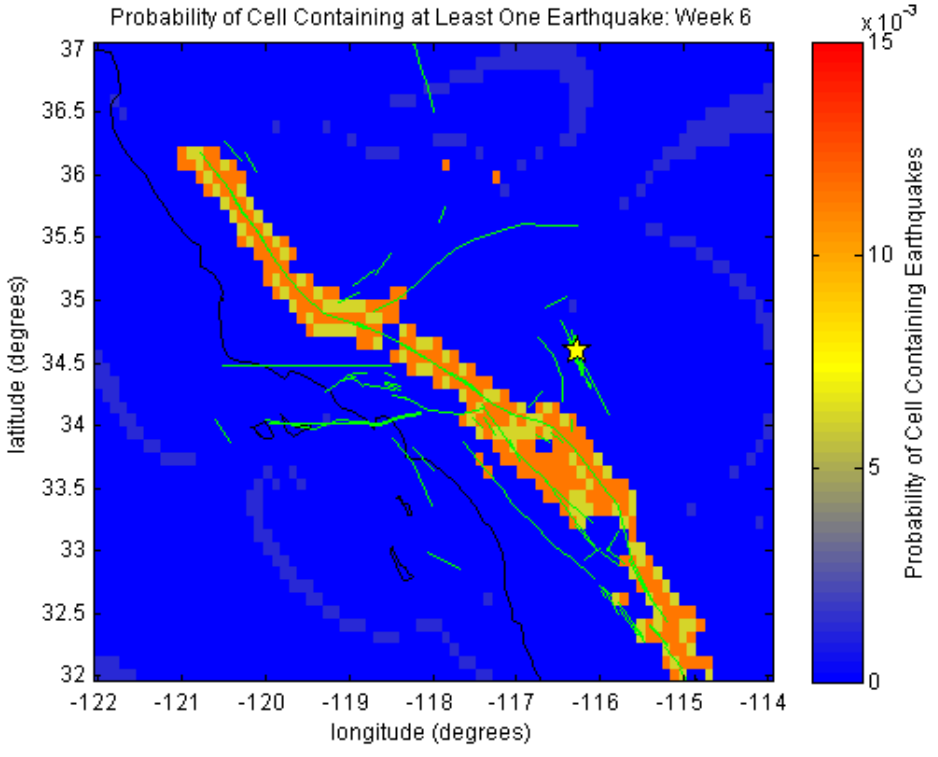
Probability of Cell Containing at Least One Earthquake: Week 6
x 10^-3
15
10
5
0
Probability of Cell Containing Earthquakes
37
36.5
36
35.5
35
34.5
34
33.5
33
32.5
32
latitude (degrees)
-122
-121
-120
-119
-118
-117
-116
-115
-114
longitude (degrees)

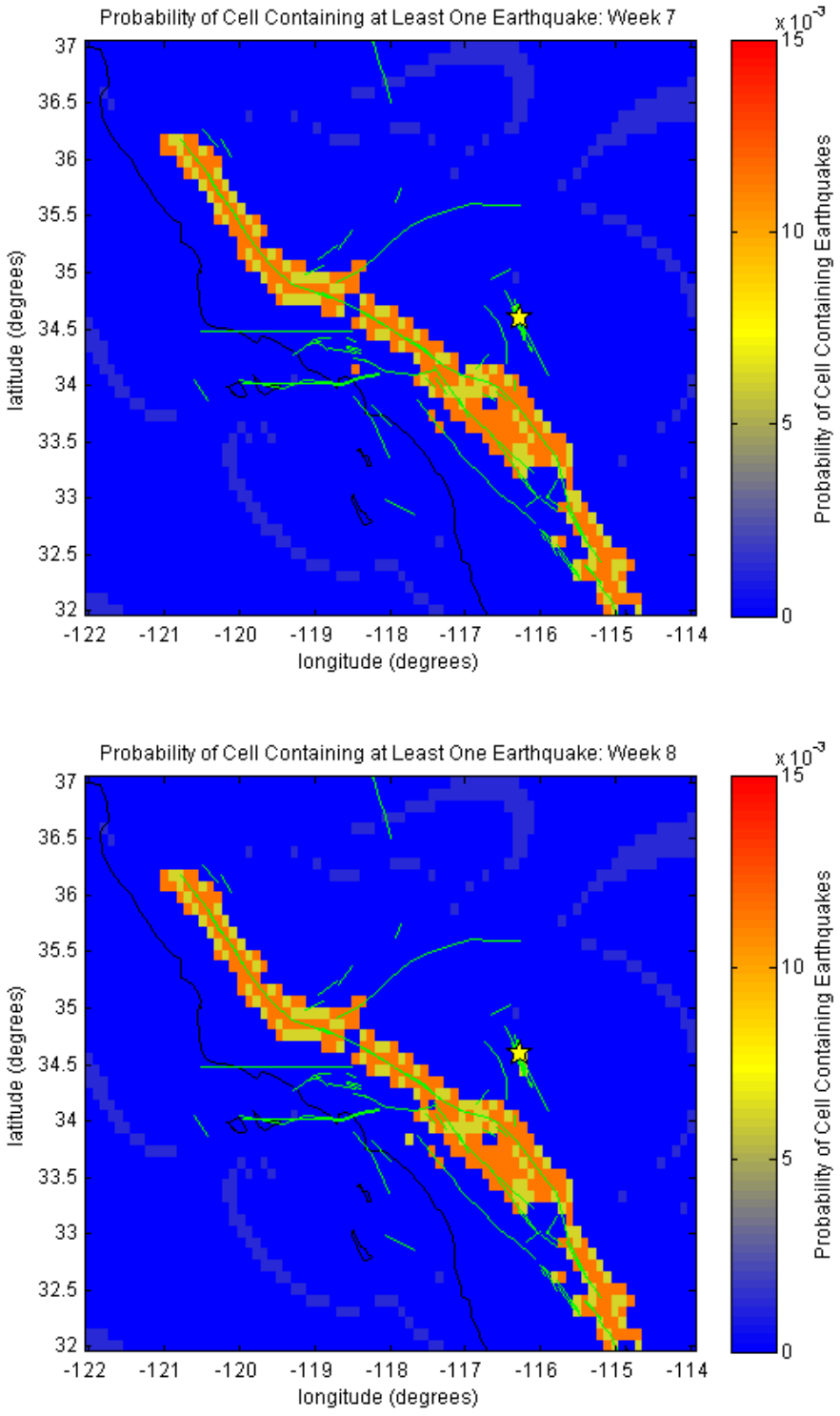

Figure 6.11: Inverse model ΔCFF-based probabilities of each cell containing at least one earthquake during the eight weeks following the Hector Mine earthquake. Yellow and red regions indicate areas of elevated probability, whereas blue regions indicate low probability of a cell containing at least one earthquake. Green lines indicate active fault sections, and the yellow star displays the Hector Mine earthquake epicenter.

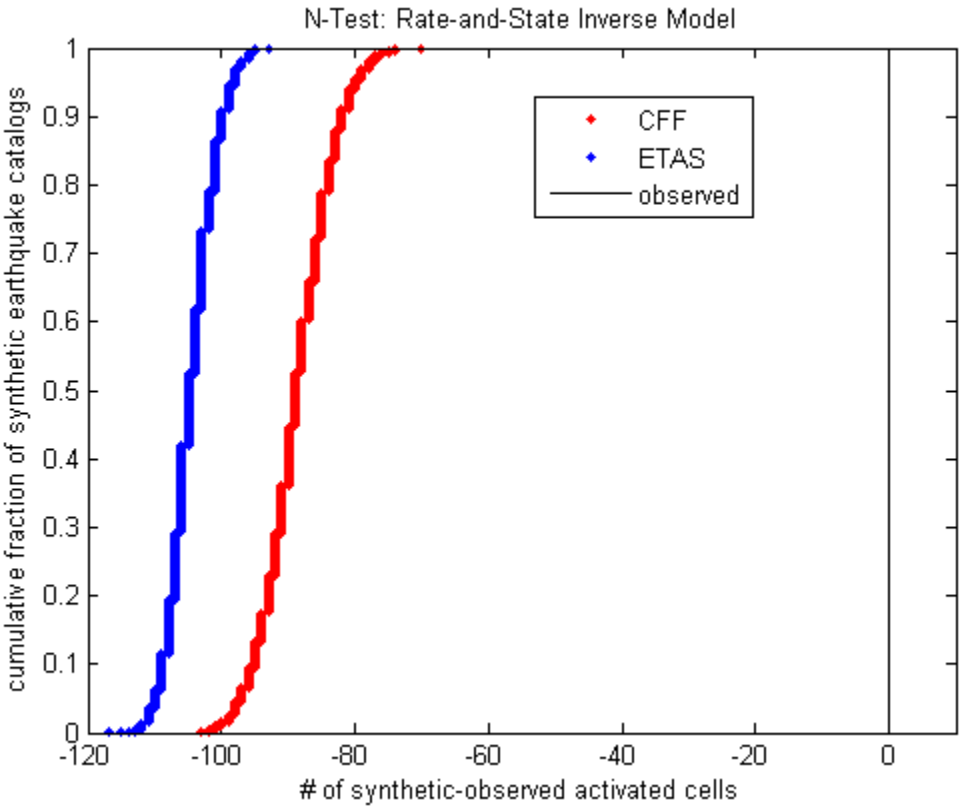

Figure 6.12: N-test results for inverse model ΔCFF-based (red curve) and ETAS-based (blue curve) earthquake forecasts. The red and blue curves represent the normalized, cumulative number of synthetic seismicity distributions relative to the difference between the number of synthetic and observed filled zones. The black line indicates where the numbers of synthetic and observed filled zones are equal.

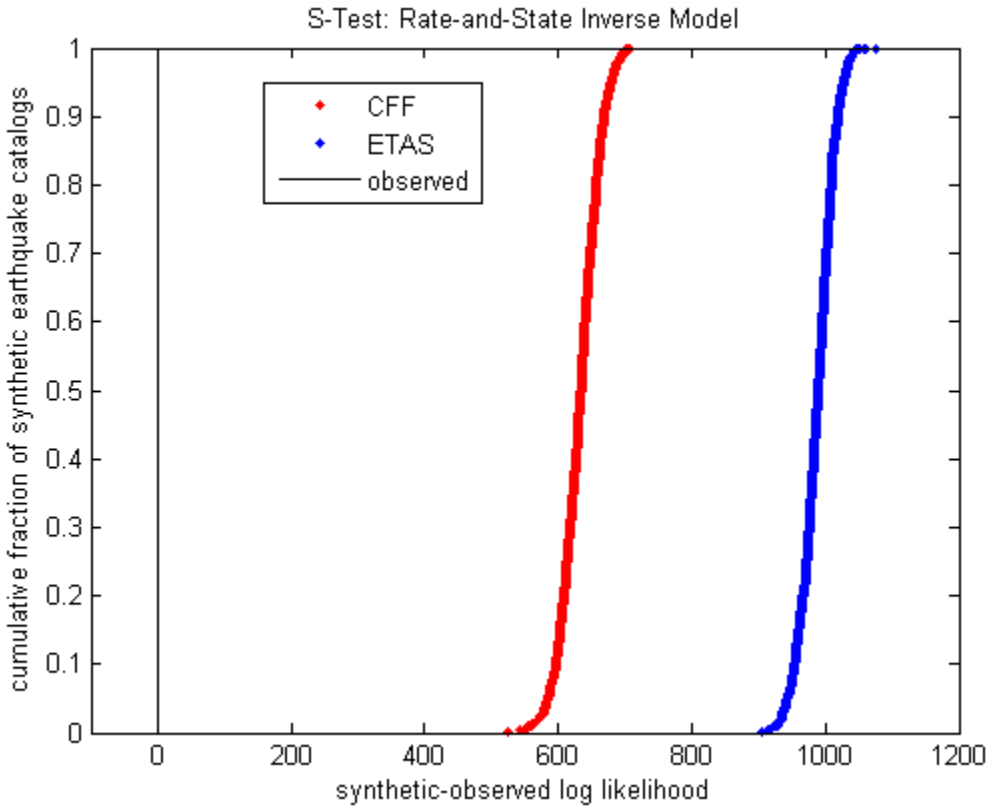

Figure 6.13: S-test results for inverse model ΔCFF-based (red curve) and ETAS-based (blue curve) earthquake forecasts. The red and blue curves represent the normalized, cumulative numbers of synthetic seismicity distributions relative the difference between the synthetic and observed log likelihood scores. The black line indicates where the synthetic and observed log likelihood scores are equal.

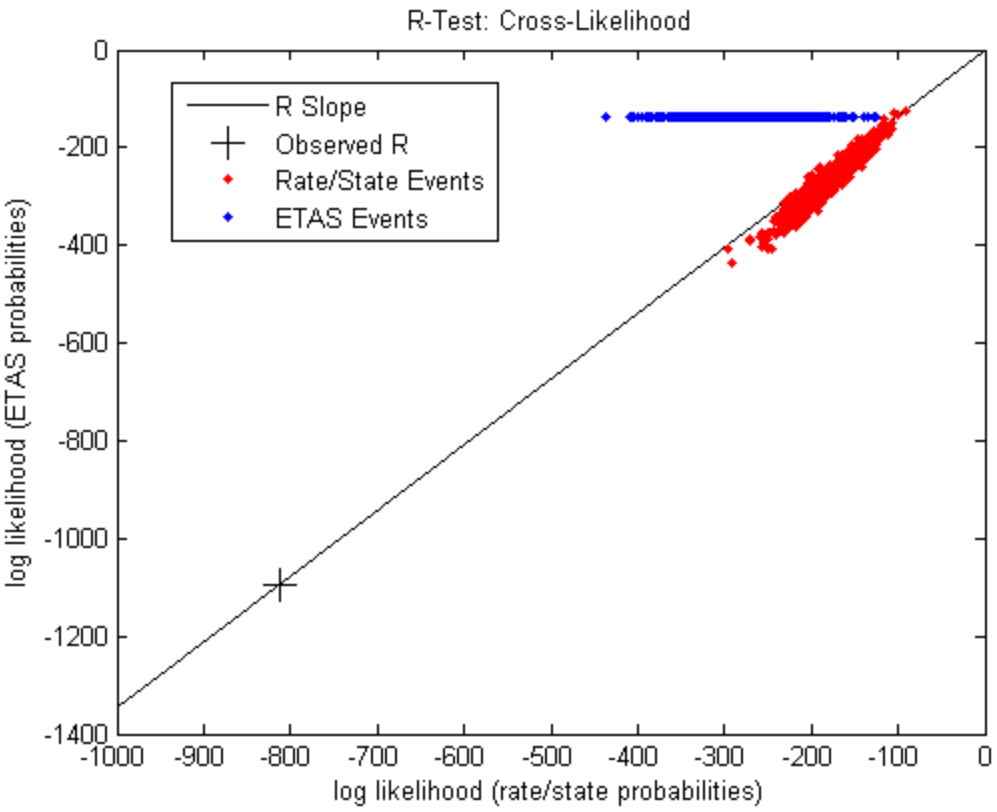

Figure 6.14: R-test cross-likelihood plot comparing the inverse model ΔCFF- and ETAS-based earthquake forecasts. The cluster of red dots represents log likelihood values from ΔCFF-based synthetic earthquake maps, and the cluster of blue dots represents log likelihood values from ETAS-based synthetic earthquake maps. The black line indicates the empirical R slope, and the observed R value is indicated by the black cross.

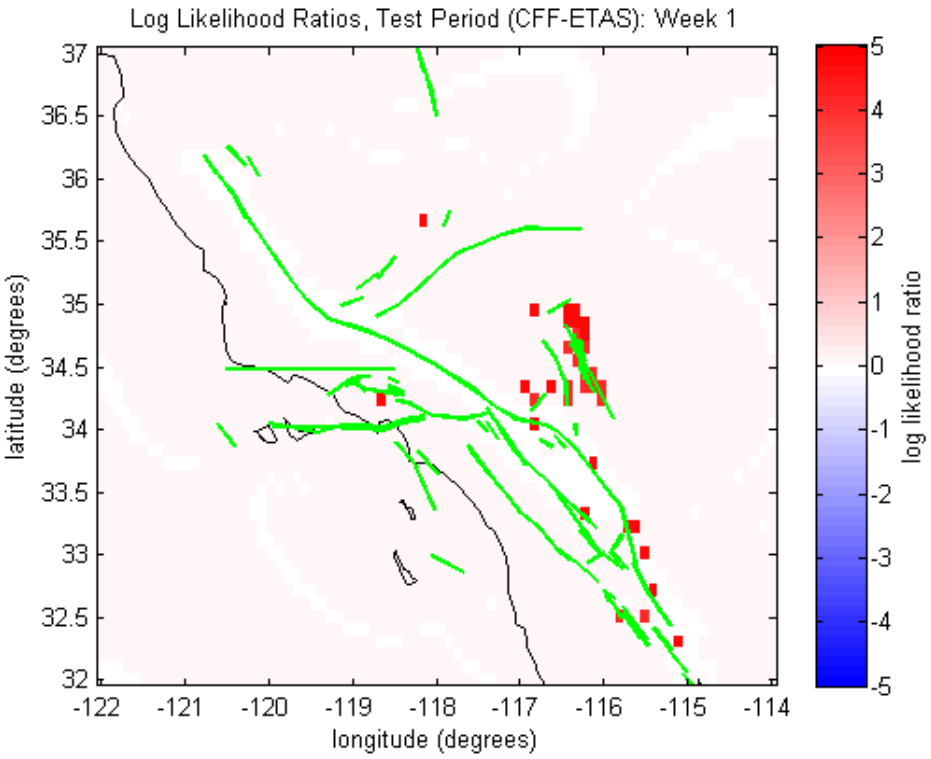
Log Likelihood Ratios, Test Period (CFF-ETAS): Week 1
latitude (degrees)
longitude (degrees)
log likelihood ratio
37
36.5
36
35.5
35
34.5
34
33.5
33
32.5
32
-122
-121
-120
-119
-118
-117
-116
-115
-114
5
4
3
2
1
0
-1
-2
-3
-4
-5

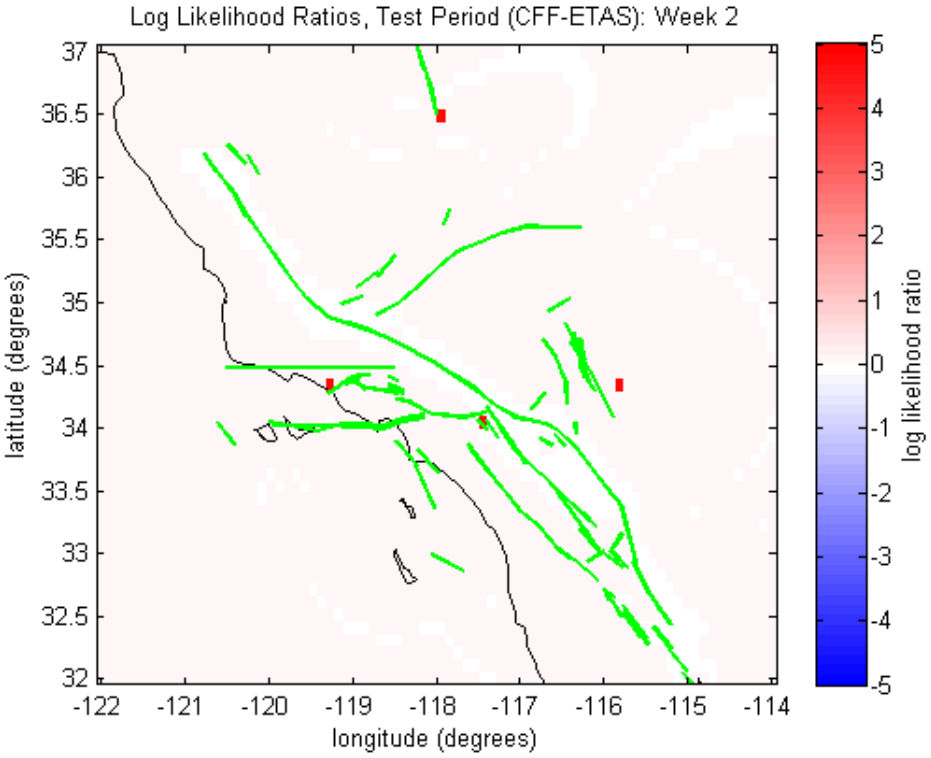
Log Likelihood Ratios, Test Period (CFF-ETAS): Week 2
latitude (degrees)
longitude (degrees)
log likelihood ratio
37
36.5
36
35.5
35
34.5
34
33.5
33
32.5
32
-122
-121
-120
-119
-118
-117
-116
-115
-114
5
4
3
2
1
0
-1
-2
-3
-4
-5

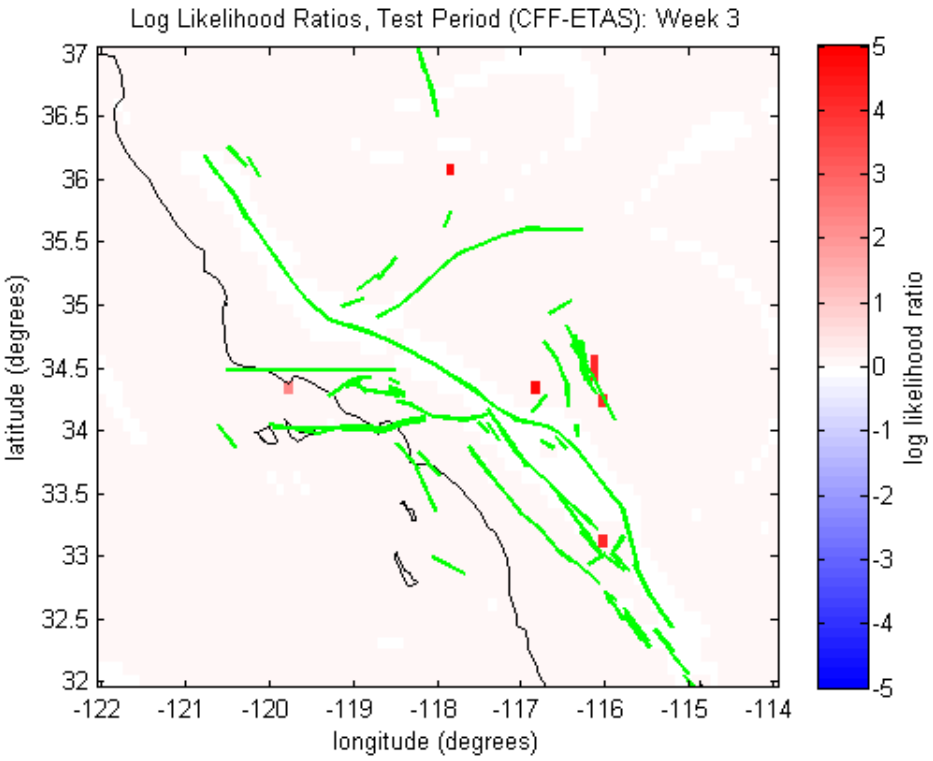
Log Likelihood Ratios, Test Period (CFF-ETAS): Week 3
latitude (degrees)
longitude (degrees)
log likelihood ratio
37
36.5
36
35.5
35
34.5
34
33.5
33
32.5
32
-122
-121
-120
-119
-118
-117
-116
-115
-114
5
4
3
2
1
0
-1
-2
-3
-4
-5

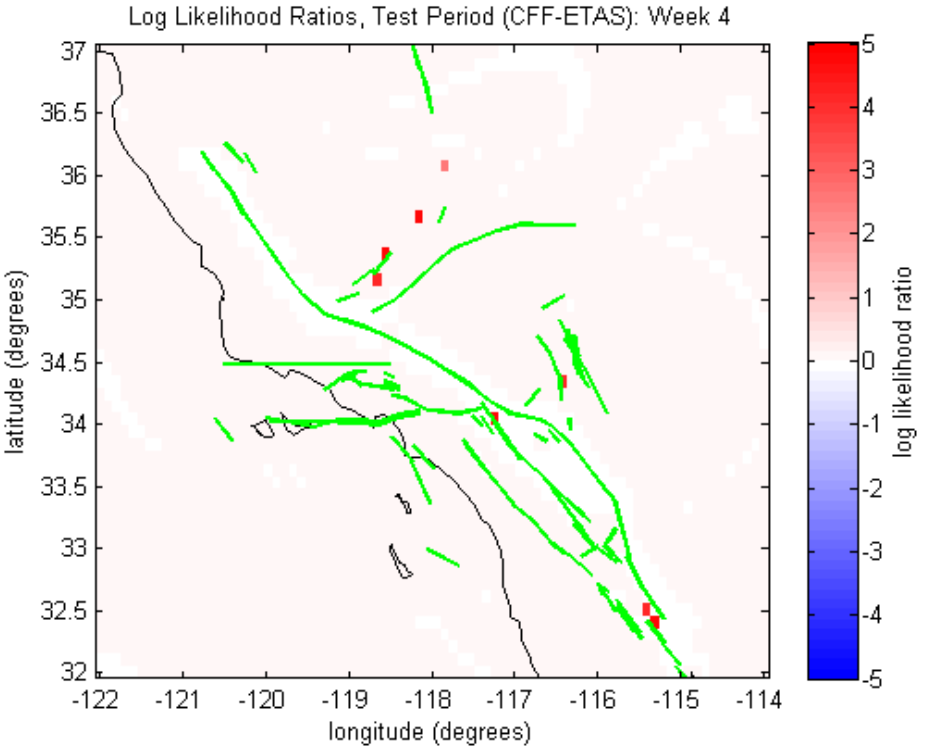
Log Likelihood Ratios, Test Period (CFF-ETAS): Week 4
latitude (degrees)
longitude (degrees)
log likelihood ratio
37
36.5
36
35.5
35
34.5
34
33.5
33
32.5
32
-122
-121
-120
-119
-118
-117
-116
-115
-114
5
4
3
2
1
0
-1
-2
-3
-4
-5

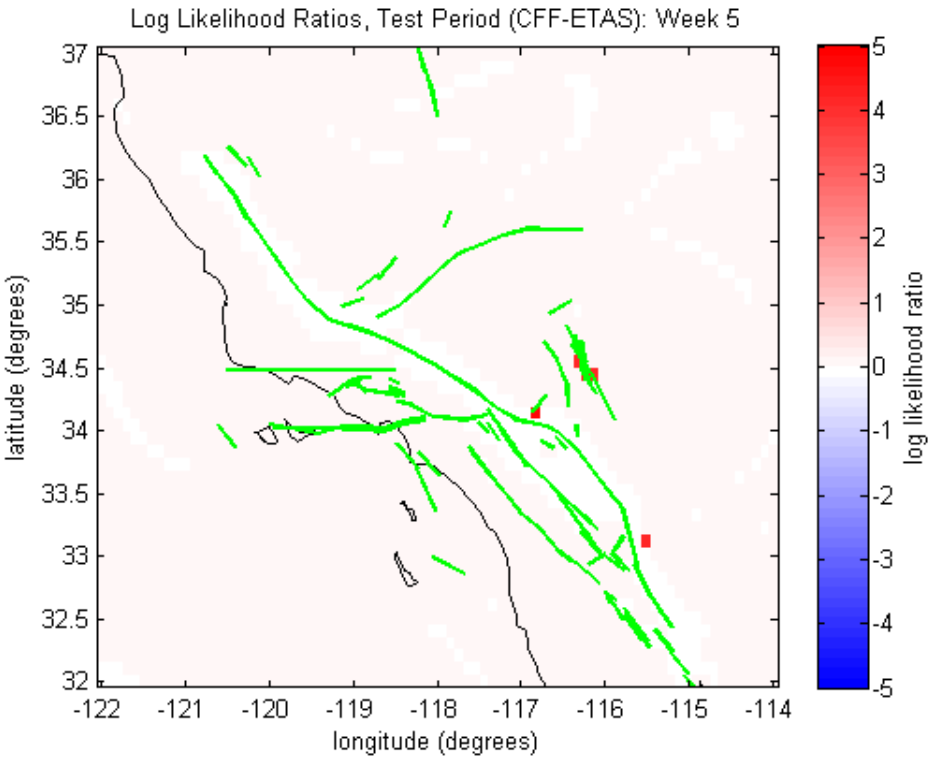
Log Likelihood Ratios, Test Period (CFF-ETAS): Week 5
latitude (degrees)
longitude (degrees)
log likelihood ratio
37
36.5
36
35.5
35
34.5
34
33.5
33
32.5
32
-122
-121
-120
-119
-118
-117
-116
-115
-114
5
4
3
2
1
0
-1
-2
-3
-4
-5

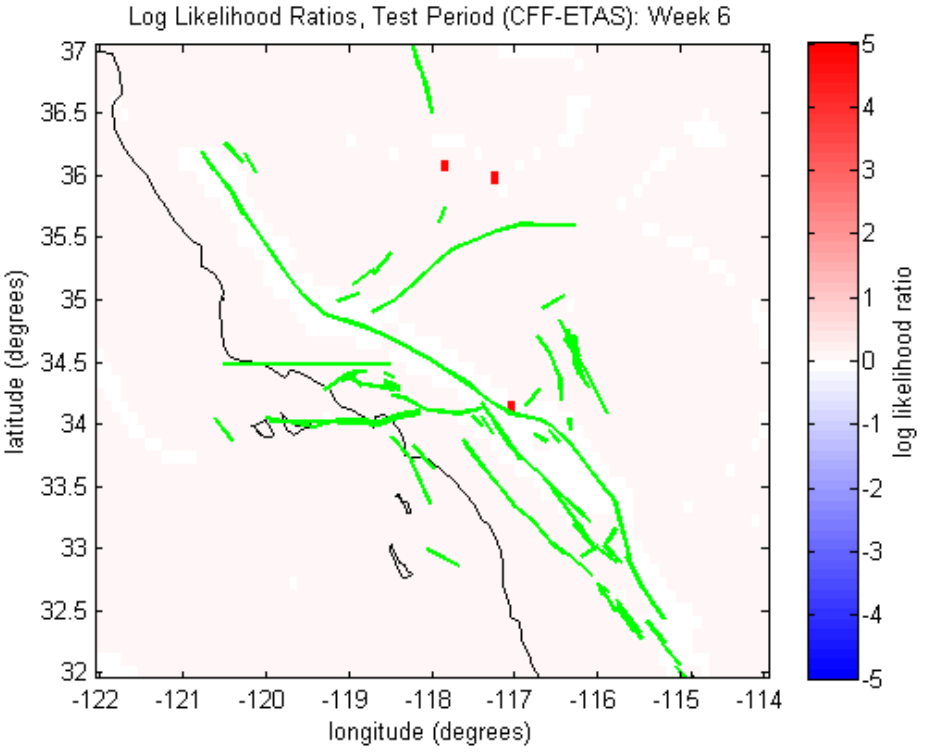
Log Likelihood Ratios, Test Period (CFF-ETAS): Week 6
latitude (degrees)
longitude (degrees)
log likelihood ratio
37
36.5
36
35.5
35
34.5
34
33.5
33
32.5
32
-122
-121
-120
-119
-118
-117
-116
-115
-114
5
4
3
2
1
0
-1
-2
-3
-4
-5

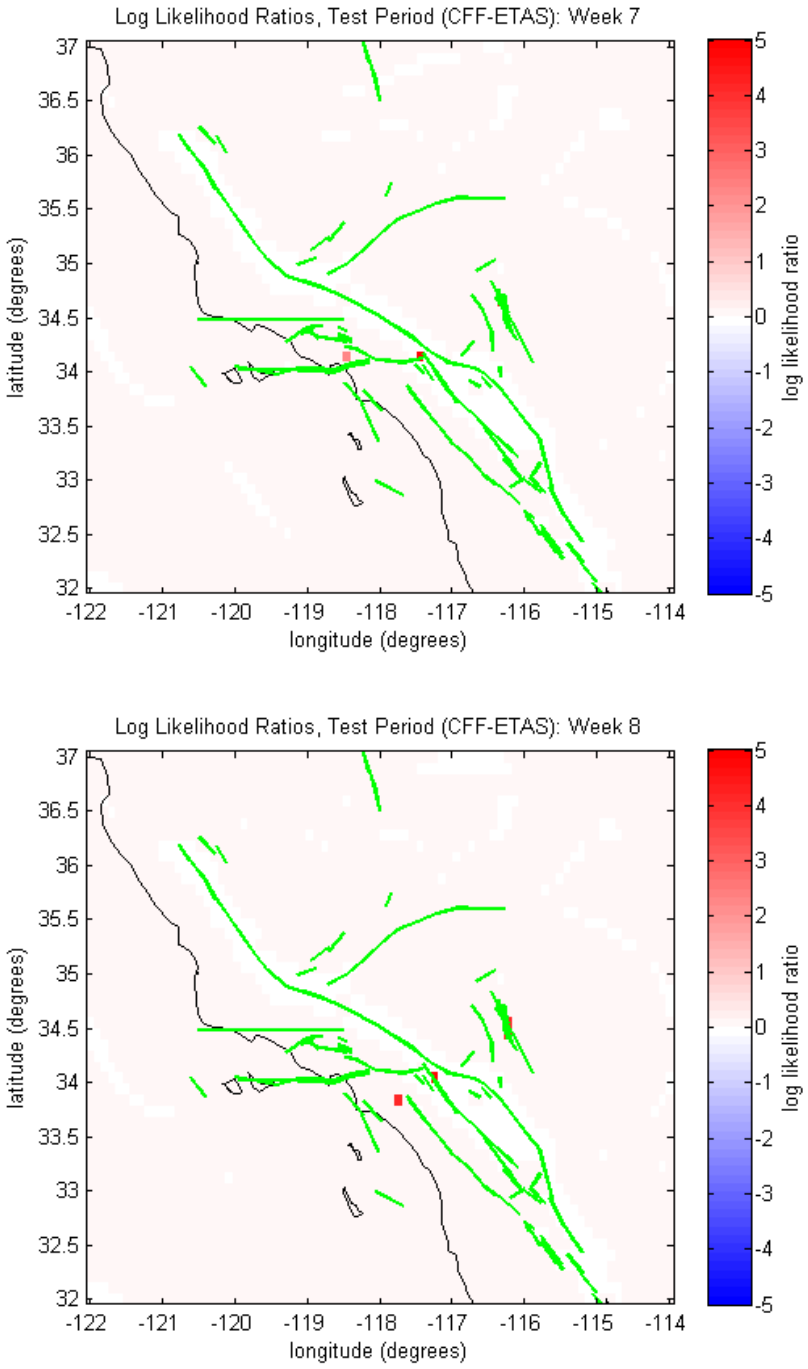

Figure 6.15: Spatial log likelihood residual maps for the eight weeks following the Hector Mine earthquake, displaying the difference between log likelihood values calculated from inverse ΔCFF- and ETAS-based earthquake forecasts. Red areas indicate where the ΔCFF-based forecast outperforms the ETAS-based forecast, and are prominent in the Hector Mine aftershock zone. Blue areas display where ETAS more effectively indicates earthquake locations during the target period. White regions indicate a negligible difference between the two forecasts' reliability. Green lines outline active faults, and the yellow star indicates the Hector Mine earthquake epicenter.

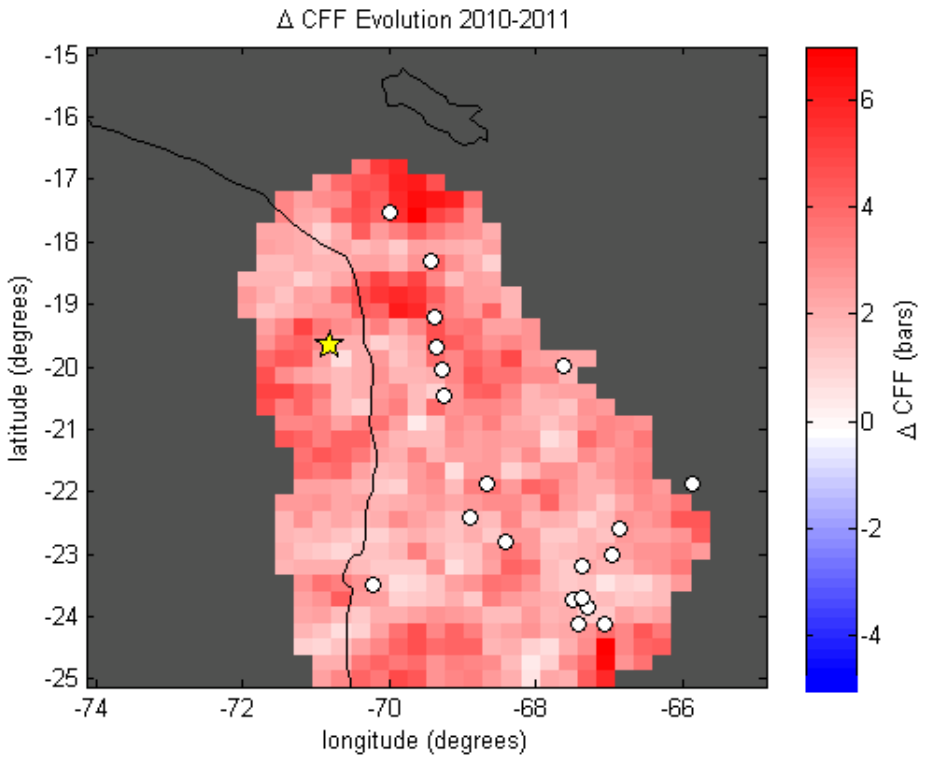
Δ CFF Evolution 2010-2011
latitude (degrees)
longitude (degrees)
Δ CFF (bars)
-15
-16
-17
-18
-19
-20
-21
-22
-23
-24
-25
-74
-72
-70
-68
-66
6
4
2
0
-2
-4

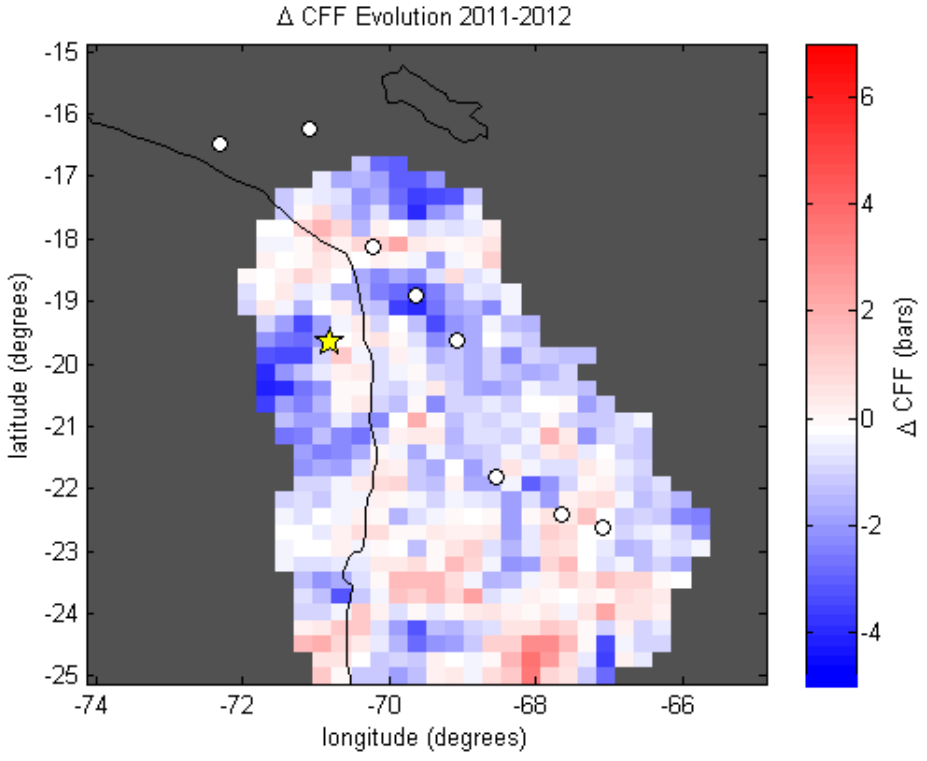
Δ CFF Evolution 2011-2012
latitude (degrees)
longitude (degrees)
Δ CFF (bars)
-15
-16
-17
-18
-19
-20
-21
-22
-23
-24
-25
-74
-72
-70
-68
-66
6
4
2
0
-2
-4

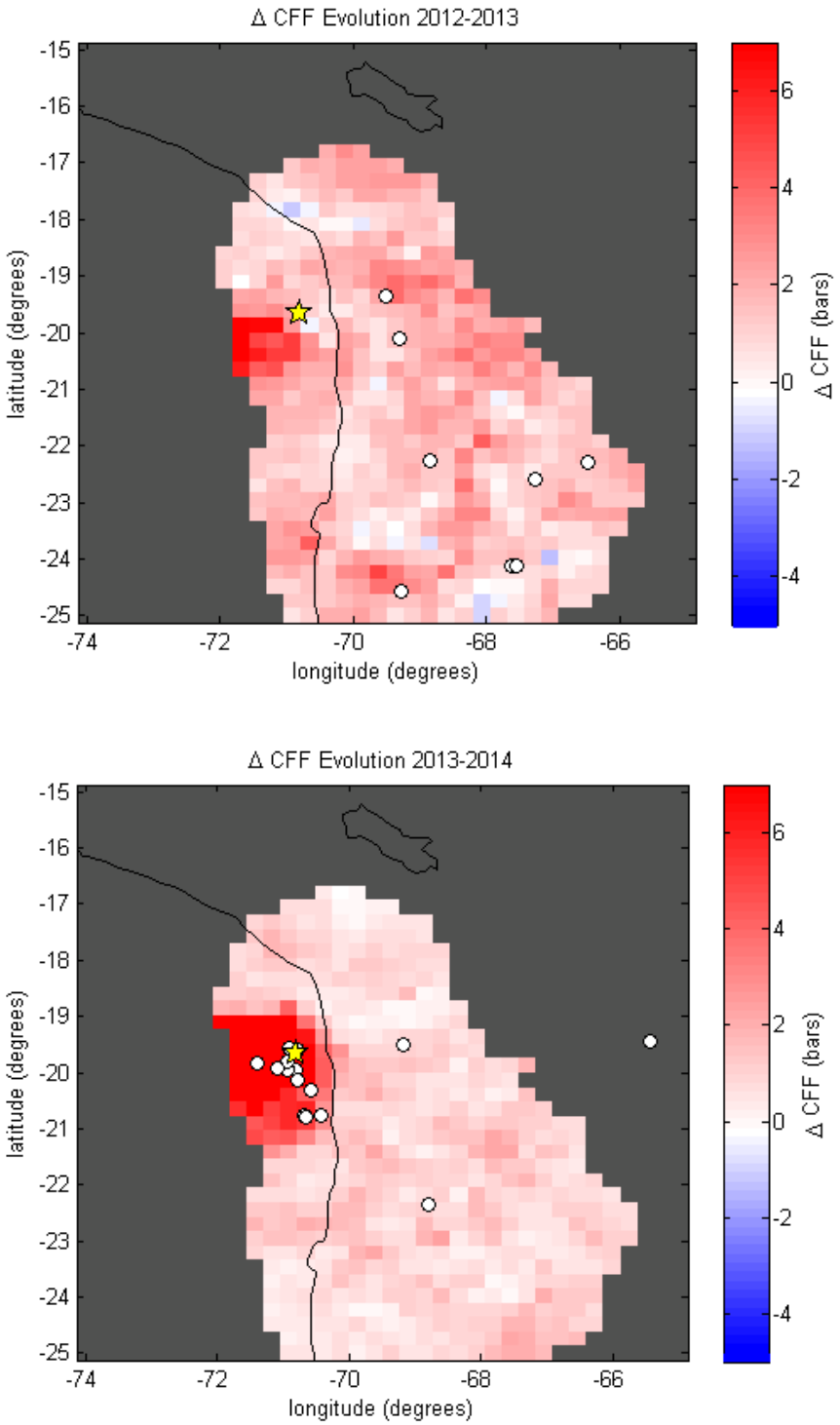

Figure 6.16: Coseismic ΔCFF evolution from 2010-2014 in the Iquique seismic gap, inferred from changes in seismicity rates. Red regions indicate areas where Coulomb stress has increased since the last time interval, and blue regions outline stress shadows. White dots show the locations of M ≥ 5.5 earthquakes occurring during the second time window in each iteration, and the yellow star indicates the mainshock epicenter.

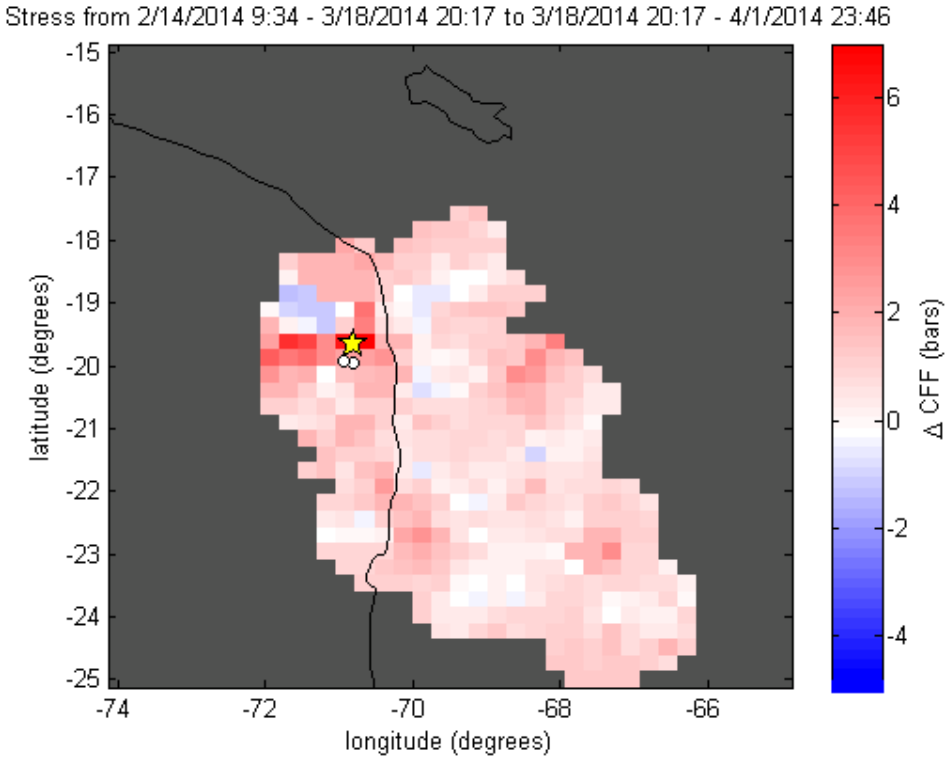
Stress from 2/14/2014 9:34 - 3/18/2014 20:17 to 3/18/2014 20:17 - 4/1/2014 23:46
latitude (degrees)
-15
-16
-17
-18
-19
-20
-21
-22
-23
-24
-25
longitude (degrees)
-74
-72
-70
-68
-66
Δ CFF (bars)
6
4
2
0
-2
-4

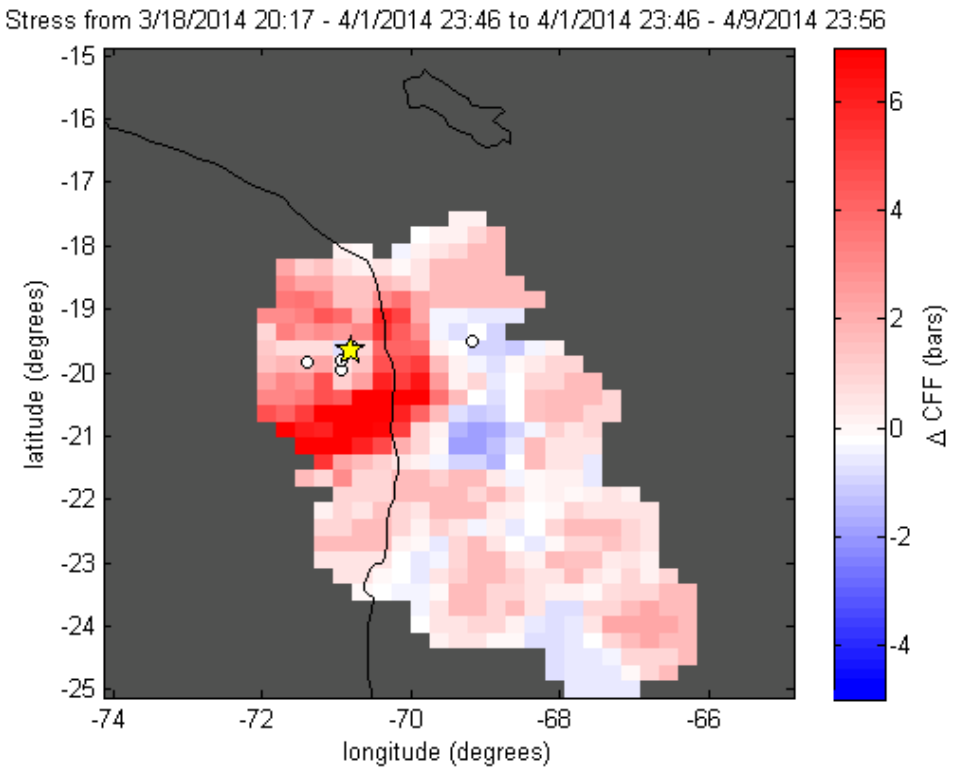

Figure 6.17: Coseismic ΔCFF, inferred by inverting seismicity rates for every 500 earthquakes from 2/14/2014 until 4/9/2014. Red regions indicate areas where Coulomb stress has increased since the last time interval, whereas blue regions delineate stress shadows. White dots show $M \geq 5.5$ epicenter locations during the second time window for each iteration, and the yellow star displays the mainshock epicenter location.

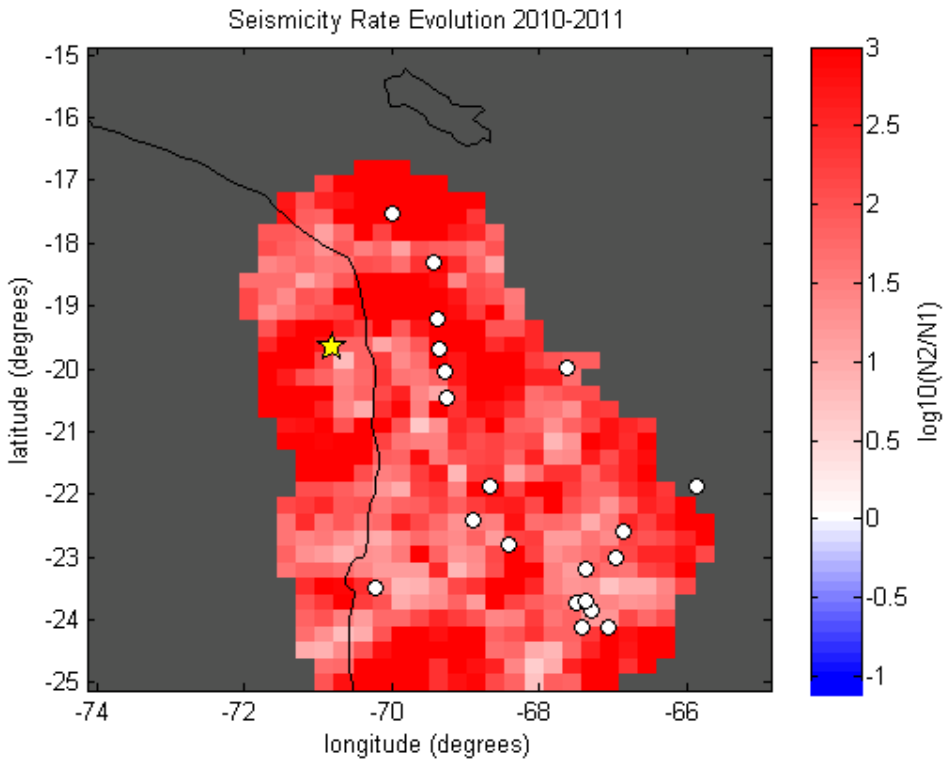
Seismicity Rate Evolution 2010-2011
latitude (degrees)
longitude (degrees)
log10(N2/N1)
-15
-16
-17
-18
-19
-20
-21
-22
-23
-24
-25
-74
-72
-70
-68
-66
3
2.5
2
1.5
1
0.5
0
-0.5
-1

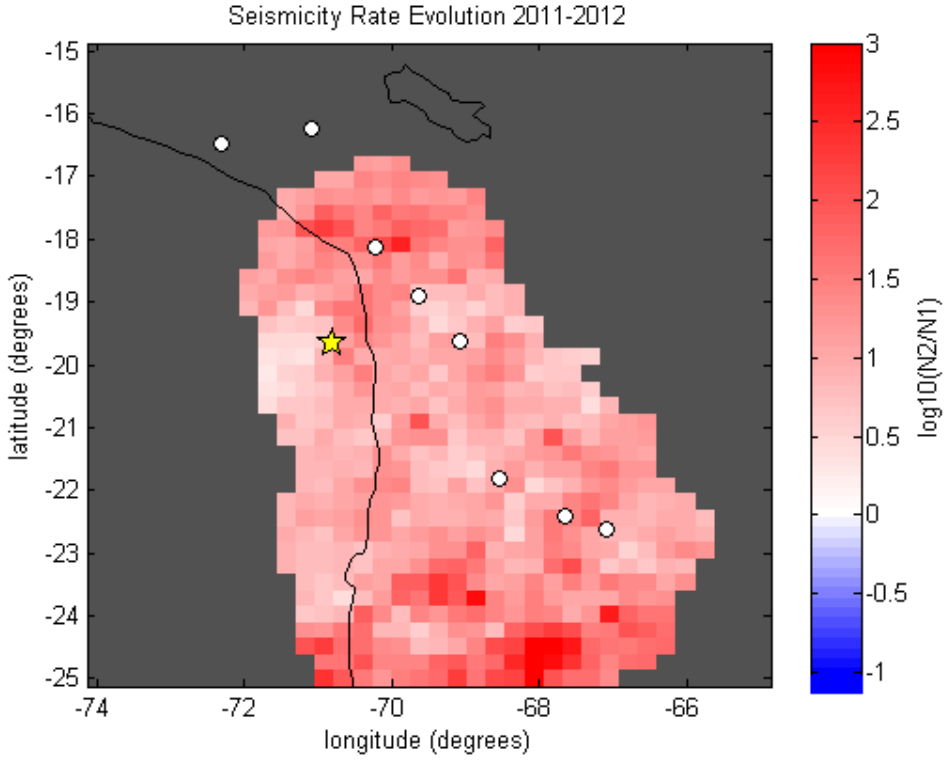
Seismicity Rate Evolution 2011-2012
latitude (degrees)
longitude (degrees)
log10(N2/N1)
-15
-16
-17
-18
-19
-20
-21
-22
-23
-24
-25
-74
-72
-70
-68
-66
3
2.5
2
1.5
1
0.5
0
-0.5
-1

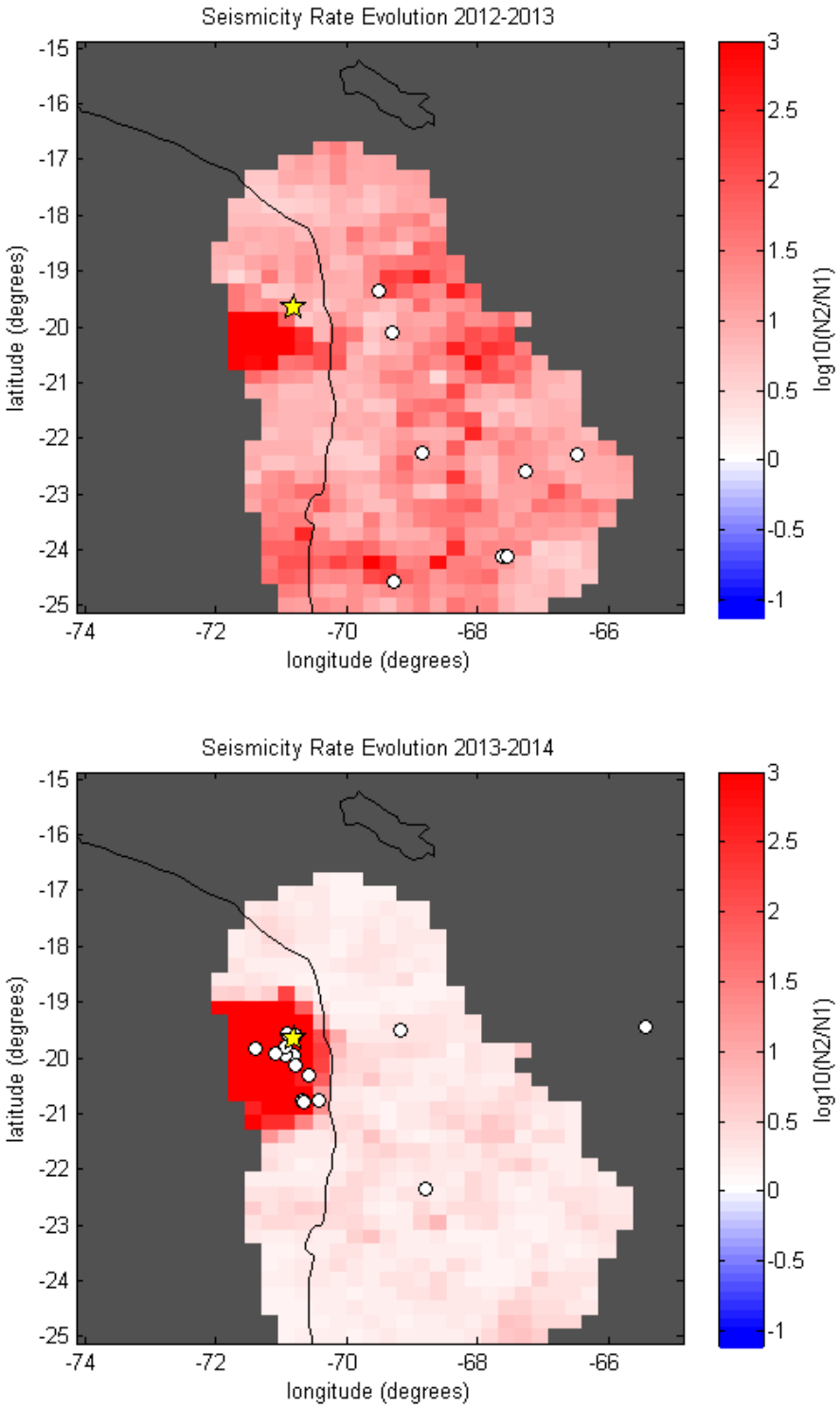

Figure 6.18: Seismicity rate changes (N_2/N_1) from 2010-2014, which were inverted to obtain the ΔCFF evolution shown in Figure 16. Red areas indicate regions where seismicity increases from one year to the next, whereas blue regions denote areas where seismicity decreased. White dots show $M \geq 5.5$ earthquake epicenters during the second year in each time window, and the yellow star displays the mainshock epicenter location.

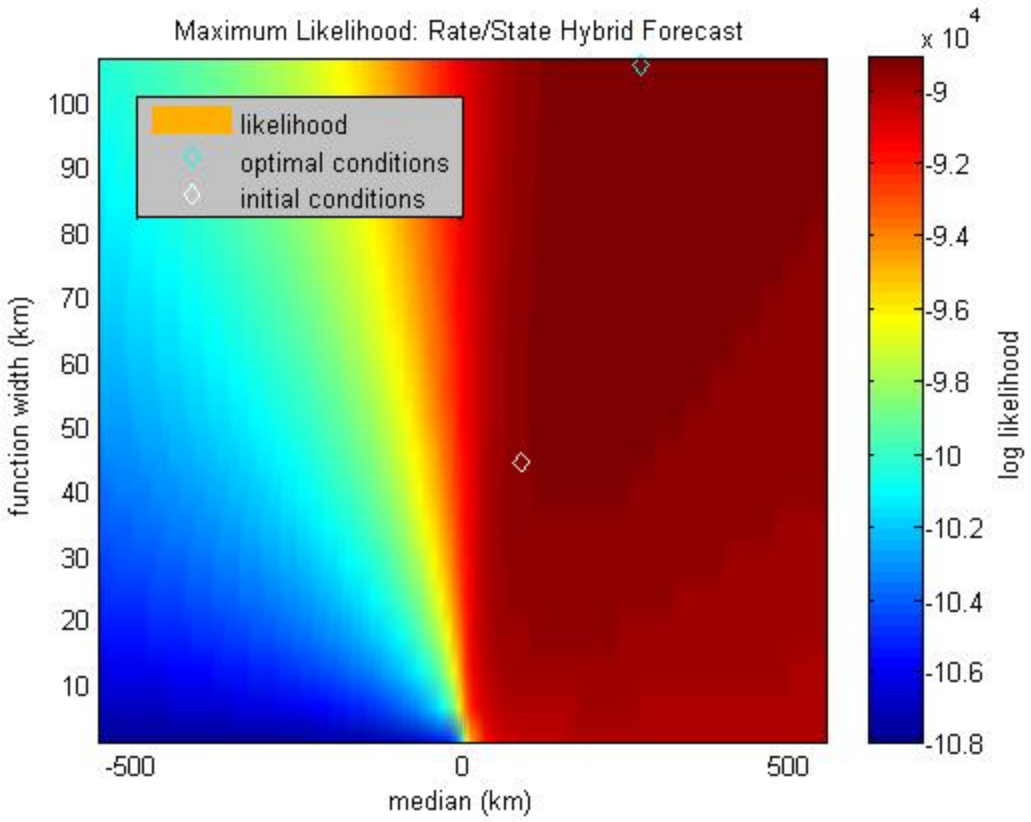

Figure 6.19: Log likelihood grid corresponding to the mixing parameter index function for the hybrid forward/inverse rate-and-state earthquake forecast. The median minimum fault distance is indicated on the x-axis, and the function width on the y-axis (both in degrees). Initial optimization conditions, $\sigma = 89$ km and $d = 44$ km, are indicated by the white diamond. Optimal function parameters are indicated by the cyan diamond.

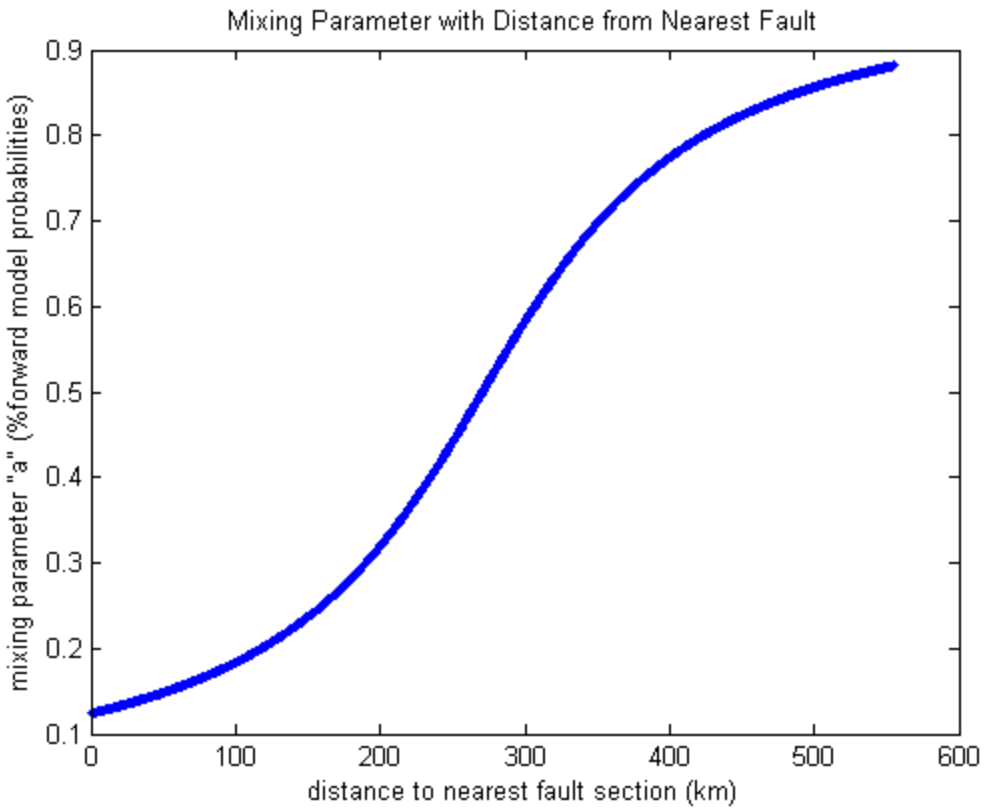

Figure 6.20: Mixing parameter values as a function of minimum distance to the nearest fault section. The x-axis displays minimum cell-fault distance, and the y-axis displays the mixing parameter "a", which increases with weight given to the forward rate-and-state probability model.

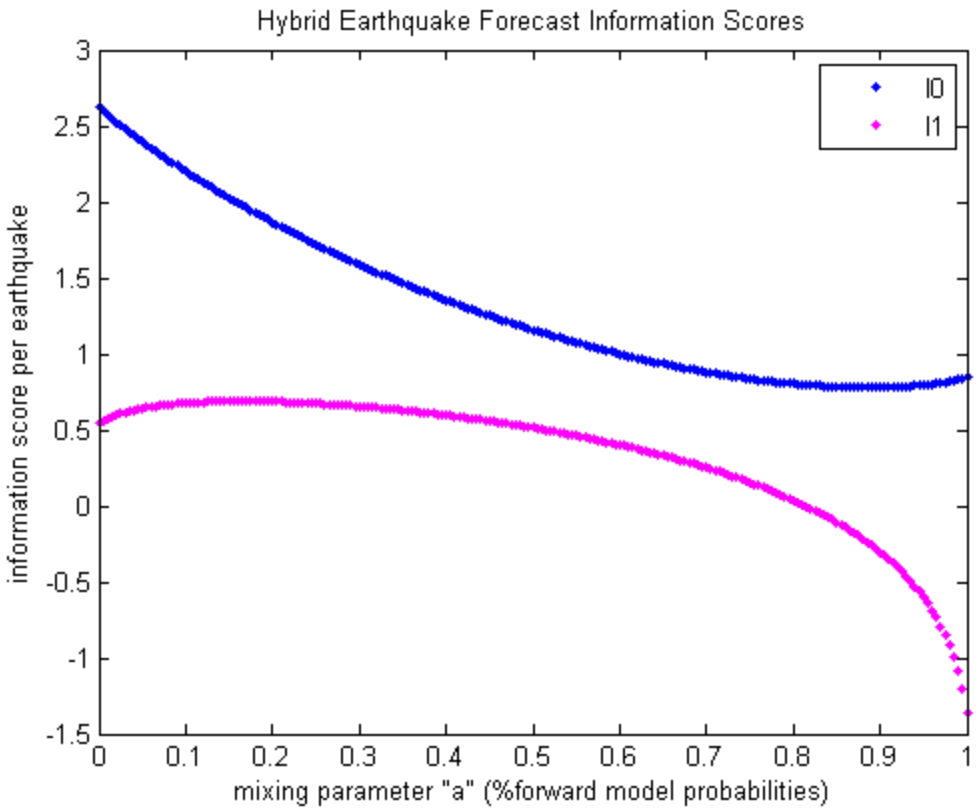

Figure 6.21: Information scores I0 (specificity) and I1 (success). The mixing parameter "a" is displayed on the x-axis, and the information scores are displayed on the y-axis. The blue curve shows I0, and the magenta curve shows I1 as a function of the mixing parameter.

CHAPTER 7

Discussion and Future Work

At the 95% confidence interval, the pseudo-prospective spatially-dependent static ΔCFF-based forecast significantly improved upon smoothed seismicity-based earthquake forecasts, but all tested rate-and-state forecasts failed to improve upon ETAS forecasts. All ΔCFF calculations involved a multitude of simplifying assumptions that may have overlooked variations in mechanical fault properties that could have altered crustal stress states. For all tests I conducted except for the inverse rate-state forecast, I assumed uniform slip distribution on each fault section. Because strain tensor components were calculated from derivatives of displacement components, discontinuities between fault sections yielded stress singularities. Such areas, common within detailed earthquake displacement models such as the Hector Mine coseismic slip model, may imply stress changes that are physically unreasonable. Additionally, most receiver earthquakes may be considered aftershocks, but not necessarily nucleate close to the modeled edges of fault sections. Therefore, modeled stress singularities may skew mean stress change at earthquake hypocenters, even when modified to physically realistic quantities.

Alternatives to applying constraints on stress changes include limiting the area, or receiver earthquakes, for which Coulomb stress changes are applicable in prospective earthquake forecasts. Static stress changes decay exponentially, on the order of r^3, with distance from faults (Okada, 1992). Therefore, I do not expect modeled stress singularities to significantly impact far-field Coulomb stress changes, defined as areas outside of most aftershock clustering. Stein et al. (1997) imposed a 5km constraint around fault sections, within which Coulomb stress changes

and receiver earthquake locations are not included in forecast results. Alternatively, declustering the receiver earthquake catalog may remove most aftershocks, which are most likely to occur near or within fault sections with uncertain Coulomb stress changes. However, such methods severely limit the potential reliability of earthquake forecasts, as most mainshocks occur on or near major faults included in my displacement model. Additionally, most receiver earthquakes, regardless of magnitude, nucleate near fault sections in aftershock clusters that would be eliminated through declustering.

Time-dependent earthquake forecasts, such as the tested rate-and-state forecasts, highlight uncertainties in stress evolution over time, as well as variations in crustal properties throughout the study area. While aftershocks from events occurring before the aftershock duration time influenced seismicity during the learning period just before the Hector Mine earthquake, the Hector Mine aftershock sequence failed to persist for the same length of time. The forward rate-and-state model's tendency to overestimate aftershock rates implies that rate-and-state forecasts are limited to indicating aftershock areas, but not seismicity rate magnitudes. Likewise, one expects seismicity to delineate the stress field, as earthquakes are directly triggered by inter-, co- and postseismic stress changes. However, short-term seismicity distributions may not provide a complete explanation of stress evolution, as shown by the inverse rate-and-state forecast results which underestimate aftershock areas. One possible improvement to rate-and-state forecasts is to combine them with statistical seismicity-based forecasts, such as ETAS, to expand expected aftershock areas to match observed areas.

I observed the strongest association between static stress change and earthquake location when resolving Coulomb stress onto uniformly oriented planes and the set of nodal planes with greater ΔCFF. However, I have not yet compared results from resolving stress onto optimally

oriented planes with the aforementioned plane orientations. Previous studies suggest that, for predominately strike-slip environments such as the southern California study area, optimally oriented planes yield the strongest correlation between static Coulomb stress change and aftershock distribution, compared to focal mechanisms or uniformly oriented planes (Steacy et al., 2005). Despite the uncertainty of the regional stress field, incorporating regional stress in areas that are not tectonically complex tends to improve association between static Coulomb stress change and earthquake location. For areas with primarily strike-slip tectonics, such as southern California, the correlation coefficient has been shown to be particularly sensitive to the intermediate principal regional stress.

For pseudo-prospective tests I conducted, only stress sources within the study area were included in my stress model. Therefore, the total stress field and tectonic stress rates might have been incomplete at the edges of the study area, misrepresenting expected seismicity rates. To determine the extent to which extraneous stress contributions affect earthquake forecast reliability, in future work I will define a region within the study area surrounded by an auxiliary window (Wang et al., 2010). Receiver earthquakes occurring within this window would not be considered when testing earthquake forecasts, but any static stress contributions would be included in seismicity rate calculations. Spatially-variant earthquake forecasts, and to some extent rate-and-state forecast results, provide evidence that Coulomb stress contributes most to seismicity rates in the far field, which encompasses many regions near study area boundaries. Through varying the width of the auxiliary stress window, I will determine the distance at which Coulomb stress impact on seismicity rates appears to be negligible. A similar test is possible for smoothed seismicity-based earthquake forecasts, as earthquakes occurring near but outside of study area boundaries may also contribute to earthquake triggering within the area. Time-

dependent earthquake sequences, such as those simulated from ETAS, may require additional temporal and magnitude windows to determine thresholds at which source earthquakes trigger future events. Similarly, the duration of stress evolution may be varied to further examine whether or not recent static stress changes impact seismicity distribution more than older earthquakes. Given that the complete stress field is unknown and that displacement distributions may be poorly constrained for older earthquakes, such a result would lower uncertainties in future seismicity distributions.

Stress field completeness also depends on the source earthquake magnitude threshold. Although stress perturbations from large earthquakes tend to affect wider areas than those from small earthquakes, smaller earthquakes are much more frequent and therefore expected to comprise a significant amount of the coseismic static stress field. Additionally, aftershock sequences concentrate much of the stress field from smaller earthquakes, which may in turn trigger future aftershocks. There exists a tradeoff from lowering the source earthquake magnitude threshold, in that adding fault sections to the displacement model will increase the number of stress singularities, as well as the amount of area they affect. While static stress changes in areas at least tens of kilometers away from fault sections may become more accurate, the area within which Coulomb stress may reliably indicate future earthquake locations and times will decrease. I will use a maximum-likelihood test to determine the optimal magnitude threshold at which I include coseismic slip in the displacement model. Likewise, I will vary the receiver earthquake magnitude threshold to determine the magnitude range at which Coulomb stress-based forecasts are most reliable, and to evaluate effectiveness when forecasting large ($M \geq 6$) source events.

Throughout all previously conducted tests, I assumed that the crust within the study area was homogeneous and isotropic, and that the coefficient of friction was constant. This simplification may misrepresent variations in stress release throughout the southern California study area. Additionally, no Coulomb stress fields used in my previously conducted tests take pore fluid pressure into account. A positive change in pore fluid pressure decreases effective confining pressure and theoretically brings faults closer to failure. Beeler et al. (2000) suggest that changes in pore fluid pressure, and therefore, the apparent coefficient of friction, are functions of mean stress changes. The apparent coefficient of friction is therefore dependent upon location, tectonic loading, coseismic stress changes, and fault plane orientation.

Overall, static Coulomb stress shows significant potential in prospectively forecasting future earthquake locations, but has not yet proven a reliable indicator of future earthquake times over short time intervals. The strong association between earthquake locations and ΔCFF, described in Chapter 3, persists over time intervals of at least eleven years, allowing for reliable, long-term prospective earthquake forecasts. However, rate-and-state forecasts fail to indicate earthquake locations over shorter time intervals, such as several weeks. Simplifying assumptions, such as assuming a homogeneous, isotropic crust with no pore fluid pressure variation, may have contributed to the rate-and-state forecasts' poor performance compared to ETAS by masking changes in crustal properties caused by mainshocks.

Dynamic and viscoelastic stress transfer also were not represented by the rate-and-state model, which describes fault strength evolution following coseismic ΔCFF. Stress sources from $M < 5$ earthquakes triggered secondary aftershocks, which were not anticipated by rate-and-state stress evolution. While the ΔCFF inversion forecast avoids stress singularities resulting from fault dislocation patches in the forward model, it neglects variations in the Gutenberg-Richter

earthquake magnitude distribution, which change the coseismic ΔCFF as a function of seismicity rate. In order to extend Coulomb stress-based earthquake forecasts to different time intervals and tectonic settings, a more detailed understanding of crustal properties and fault asperities is necessary. To eliminate stress singularities, fault displacement may be modeled as elliptic instead of uniform, ensuring uniform stress drop along faults. Fault asperities may also be relocated by inverting observed seismicity for a higher resolution displacement model, which places stress singularities in regions with elevated seismicity. Variation in aftershock duration times for southern California mainshocks may be taken into account in the forecast through calculating stress changes using an elastic-viscoelastic coupling model, allowing for three-dimensional deformation beyond immediate changes in fault strength (Freed et al., 2007).

BIBLIOGRAPHY

Aki, K., and P. G. Richards (2002), *Quantitative Seismology Second Edition*, W. H. Freeman and Company, New York.

Beeler, N. M., Simpson, R. W., Hickman, S. H., and D. A. Lockner (2000), Pore fluid pressure, apparent friction, and Coulomb failure, *Journal of Geophysical Research, 105*, 25,533-25,542.

Chlieh, M., de Chabalier, J. B., Ruegg, J. C., Armijo, R., Dmowska, R., Campos, J., and K. L. Feigl (2004), Crustal deformation and fault slip during the seismic cycle in the North Chile subduction zone, from GPS and InSAR observations, *Geophysical Journal International, 158*, 695-711.

Cocco, M., S. Hainzl, F. Catalli, B. Enescu, A. M. Lombardi, and J. Woessner (2010), Sensitivity study of forecasted aftershock seismicity based on Coulomb stress calculation and rate-and-state dependent frictional response, *Journal of Geophysical Research, 115*, doi:10.1029/2009JB006838.

Daniel, G., E. Prono, F. Renard, F. Thouvenot, S. Hainzl, D. Marsan, A. Helmstetter, P. Traversa, J. L. Got, L. Jenatton, and R. Guiget (2011), Changes in effective stress during the 2003-2004 Ubaye seismic swarm, France, *Journal of Geophysical Research, 116*, doi:10.1029/2010JB007551.

Deng, J., and L. R. Sykes (1997a), Evolution of the stress field in southern California and triggering of moderate-size earthquakes: a 200-year perspective, *Journal of Geophysical Research, 102*, 9859-9886.

Deng, J., and L. R. Sykes (1997b), Stress evolution in southern California and triggering of moderate-, small-, and micro-size earthquakes, *Journal of Geophysical Research, 102*, 24411-24435.

Dieterich, J. H., and B. Kilgore (1996), Implications of fault constitutive properties for earthquake prediction, *Proceedings of the National Academy of Sciences, 93*, 3787-3794.

Du, W. X., and L. R. Sykes (2001), Changes in frequency of moderate-size earthquakes and Coulomb failure stress before and after the Landers, California, earthquake of 1991, *Bulletin of the Seismological Society of America, 91*, 725-738.

Freed, A. M., S. T. Ali, and R. Burgmann (2007), Evolution of stress in southern California for the past 200 years from coseismic, postseismic and interseismic stress changes, *Geophysical Journal International, 169*, 1164-1179.

Ghisetti, F. (2000), Slip partitioning and deformation cycles close to major faults in southern California: evidence from small-scale faults, *Tectonics, 19*, 25-43.

Hainzl, S., G. B. Brietzke, and G. Zoller (2010), Quantitative earthquake forecasts resulting from static stress triggering, *Journal of Geophysical Research, 115*, doi:10.1029/2010JB007473.

Hainzl, S., G. Zoller, and R. Wang (2010), Impact of the receiver fault distribution on aftershock activity, *Journal of Geophysical Research, 115*, doi:10.1029/2008JB006224.

Hainzl, S., and Y. Ogata (2005), Detecting fluid signals in seismicity data through statistical earthquake modeling, *Journal of Geophysical Research, 110*, doi: 10.1029/2004JB003247.

Harris, R. A. (2000), Earthquake stress triggers, stress shadows, and seismic hazard, *Current Science, 79,* 1215-1225.

Harris, R. A. (1998), Introduction to special section: stress triggers, stress shadows, and implications for seismic hazard, *Journal of Geophysical Research – Solid Earth, 103,* 24347-24358.

Harris, R. A., and R. W. Simpson (1998), Suppression of large earthquakes by stress shadows: a comparison of Coulomb and rate-and-state failure, *Journal of Geophysical Research – Solid Earth, 103,* 24439-24451.

Harris, R. A., and R. W. Simpson (1996), In the shadow of 1857 – the effect of the great Ft. Tejon earthquake on subsequent earthquakes in southern California, *Geophysical Research Letters, 23,* 229-232.

Hetherington, A., and S. Steacy (2007), Fault heterogeneity and earthquake scaling, *Geophysical Research Letters, 34,* doi:10.1029/2007GL030365.

Hiemer, S., D. D. Jackson, Q. Wang, Y. Y. Kagan, J. Woessner, J. D. Zechar, and S. Wiemer (2013), A stochastic forecast of California earthquakes based on fault slip and smoothed seismicity, *Bulletin of the Seismological Society of America, 103,* No. 2A, 799-810.

Jackson, D. D., and Y. Y. Kagan (2006), The 2004 Parkfield earthquake, the 1985 prediction, and characteristic earthquakes: lessons for the future, *Bulletin of the Seismological Society of America, 96,* No. 4B, S397-S409.

Ji, C., D. J. Wald, and D. V. Helmberger (2002), Source description of the 1999 Hector Mine, California earthquake, part I: Wavelet domain inversion theory and resolution analysis, *Bulletin of the Seismological Society of America,92*, 1192-1207.

Kagan, Y. Y. (2009), Testing long-term earthquake forecasts: likelihood methods and error diagrams, *Geophysical Journal International, 177*, 532-542.

Kagan, Y. Y., and D. D. Jackson (1998), Spatial aftershock distribution: effect of normal stress, *Journal of Geophysical Research, 103*, 24453-24467.

King, G. C. P., M. Cocco (2001), Fault interaction by elastic stress changes: new clues from earthquake sequences, *Advances in Geophysics, 44*, 1-38.

Lin, J., and R. S. Stein (2004), Stress triggering in thrust and subduction earthquakes and stress interaction between the southern San Andreas and nearby thrust and strike-slip faults, *Journal of Geophysical Research, 109*, B02303, doi:10.1029/2003JB00267.

Luo, G., and M. Liu (2012), Multi-timescale mechanical coupling between the San Jacinto fault and the San Andreas fault, southern California, *Lithosphere, 4*, 221-229.

Marzocchi, W., and J. Selva (2003), On the long-term interaction among earthquakes: some insight from a model simulation, *Bulletin of the Seismological Society of America, 98*, 1102-1112.

Newman, W. I. (2012), *Continuum Mechanics in the Earth Sciences*, Cambridge University Press, Massachusetts.

Nostro, C., A. Piersanti, and M. Cocco (2001), Normal fault interaction caused by coseismic and postseismic stress changes, *Journal of Geophysical Research – Solid Earth, 106*, 19391-19410.

Ogata, Y., K. Katsura, G. Falcone, K. Nanjo, and J. Zhuang (2013), Comprehensive and topical evaluations of earthquake forecasts in terms of number, time, space, and magnitude, *Bulletin of the Seismological Society of America, 103,* No. 3, 1692-1708.

Ogata, Y., L. M. Jones, and S. Toda (2003), When and where the aftershock activity was depressed: contrasting decay patterns of the proximate large earthquakes in southern California, *Journal of Geophysical Research, 108*, doi: 10.1029/2002JB002009.

Okada, Y. (1992), Internal deformation due to shear and tensile faults in a half-space, *Bulletin of the Seismological Society of America, 82*, 1018-1040.

Papadimitriou, E. E. (2002), Mode of strong earthquake recurrence in the central Ionian Islands (Greece): possible triggering due to Coulomb stress changes generated by the occurrence of previous strong shocks, *Bulletin of the Seismological Society of America, 92*, 3293-3308.

Papdimitriou, E. E., and L. R. Sykes (2001), Evolution of the stress field in the North Aegean Sea (Greece), *Geophysical Journal International, 146*, 747-759.

Papadimitriou, E. E., V. G. Karakostas, and B. C. Papazachos (2001), Rupture zones in the area of the 17.08.99 Izmit (NW Turkey) large earthquake (M-w 7.4) and stress changes caused by its generation, *Journal of Seismology, 5*, 269-276.

Parons, T., and M. Segou (2014), Stress, distance, magnitude, and clustering influences on the success or failure of an aftershock forecast: the 2013 M6.6 Lushan earthquake and other examples, *Seismological Research Letters, 85*, No. 1, doi:10.1785/0220130100.

Parsons, T., Y. Ogata, J. Zhuang, and E. L. Geist (2012), Evaluation of static stress change forecasting with prospective and blind tests, *Geophysical Journal International,* doi:10.1111/j.1365-246X.2011.05343.x.

Parsons, T. (2002), Global Omori law decay of triggered earthquakes: large aftershocks outside the classical aftershock zone, *Journal of Geophysical Research, 107*, doi: 10.1029/2001JB000646.

Parsons, T., R. S. Stein, R. W. Simpson, and P. A. Reasenberg (1999), Stress sensitivity of fault seismicity: a comparison between limited-offset oblique and major strike-slip faults, *Journal of Geophysical Research, 104*, 20183-20202.

Robinson, R. (2004), Potential earthquake triggering in a complex fault network: the Northern South Island, New Zealand, *Geophysical Journal International, 159*, 734-738.

Rong, Y., D. D. Jackson, and Y. Y. Kagan (2003), Seismic gaps and earthquakes, *Journal of Geophysical Research, 108,*No. B10, 2471, doi:10.1029/2002JB002334.

Selva, J., and W. Marzocchi (2005), Variations of southern California seismicity: empirical evidence and possible physical causes, *Journal of Geophysical Research – Solid Earth, 110*, B11306, doi: 10.1029/2004JB003494.

Smith, D. E., and J. H. Dieterich (2010), Aftershock sequences modeled with 3-D stress heterogeneity and rate-state seismicity equations: implications for crustal stress estimation, *Pure and Applied Geophysics, 167*, 1067-1085.

Steacy, S., S. N. Suleyman, and J. McCloskey (2005), Onto what planes should Coulomb stress perturbations be resolved?, *Journal of Geophysical Research, 110*, doi:10.1029/2004JB003356.

Stein, R. S., A. A. Barka, and J. H. Dieterich (1997), Progressive failure on the north Anatolian fault since 1939 by earthquake stress triggering, *Geophysical Journal International, 128*, 594-604.

Strader, A., and D. D. Jackson (2014), Near-prospective test of Coulomb stress triggering, *Journal of Geophsyical Research – Solid Earth, 119*, doi: 10.1002/2013JB010780.

Toda, S., and B. Enescu (2011), Rate/state Coulomb stress transfer model for the CSEP Japan seismicity forecast, *Earth Planets Space, 63*, 171-185.

Toda, S., R. S. Stein, V. Sevilgen, and J. Lin (2011), Coulomb 3.3 graphic-rich deformation and stress-change software – user guide: U. S. Geological Survey open-file report 2011-1060, XX p.

Toda, S., R. S. Stein, K. Richards-Dinger, and S. B. Bozkurt (2005), Forecasting the evolution of seismicity in southern California: animations built on earthquake stress transfer, *Journal of Geophysical Research, 110*, doi:10.1029/2004JB003415.

Viti, M., F. D'Onza, E. MAntovani, D. Albarello, and N. Cenni (2003), Post-seismic relaxation and earthquake triggering in the southern Adriatic region, *Geophysical Journal International, 153*, 645-657.

Wang, Q., D. D. Jackson, and J. Zhuang (2010), Missing links in earthquake clustering models, *Geophysical Research Letters, 37*, doi:10.1029/2010GL044858.

Wang, W. H., and C. H. Chen (2001), Static stress transferred by the 1999 Chi-Chi, Taiwan, earthquake: effects on the stability of the surrounding fault systems and aftershock triggering with a 3D fault-slip model, *Bulletin of the Seismological Society of America, 91*, 1041-1052.

Yang, W., E. Hauksson, and P. Shearer (2012), Computing a large refined catalog of focal mechanisms for southern California (1981-2010): Temporal stability of the style of faulting, *Bulletin of the Seismological Society of America, 102*, 1179-1194.

Zhuang, J., Y. Ogata, and D. Vere-Jones (2002), Stochastic declustering of space-time earthquake occurrences, *Journal of the American Statistical Association, 97*. No. 458, 369-380.

Ziv, A., and A. M. Rubin (2000), Static-stress transfer and earthquake triggering: no lower threshold in sight?, *Journal of Geophysical Research – Solid Earth, 105*, 13631-13642.